Modelling Stargardt Disease Using iPSC-Derived Retinal Organoids: Insights into Pathology and Genotype/Phenotype Correlations

Avril Watson

A thesis submitted to Newcastle University for the degree:
Doctor of Philosophy (PhD)

Biosciences Institute
Faculty of Medical Sciences
Newcastle University

September 2023

Abstract

Stargardt disease (STGD1) is an inherited retinopathy affecting approximately 1:8000 individuals. It is characterised by biallelic mutations in *ABCA4* and encodes a vital protein for the recycling of retinaldehyde in the retina. Despite its prevalence and impact, there are currently no treatments available for this condition. Furthermore, 35% of STGD1 cases remain genetically unsolved. Efforts have been directed towards comprehending the fundamental disease mechanisms and identifying all disease-causing variants in the extensive 128kb gene, to better aid with the development of effective therapeutic strategies.

In this study, we generated iPSC lines from two monoallelic (PT1 & PT2), late-onset STGD1 cases with the heterozygous complex allele - c.[5461-10T>C;5603A>T]. We differentiated these cells alongside a biallelic affected control (AC) - c.4892T>C, and c.4539+2001G>A, to retinal organoids (ROs) allowing us to investigate cellular and molecular characteristics associated with STGD1. We hypothesised that the missing inheritance in our monoallelic cases is due to an RNA defect. Consequently, we utilised a myriad of sequencing strategies including WGS, single-cell RNA sequencing (scRNAseq) and long-read RNA sequencing (LRS) to address this.

ROs were grown for 230 days and developed all key retinal neurons with photoreceptor outer segments capable of ABCA4 expression. We observed patient-specific disruption to lamination with OPN1MW/LW^{+} cone photoreceptor retention in the RO centre during differentiation. Retention was more severe in the AC case affecting both cones and rods, suggesting a genotype/phenotype correlation. scRNAseq suggests retention may be due to the induction of apoptosis in photoreceptors. WGS successfully identified the missing alleles in both cases; PT1 reported c. 5603A>T in homozygous state and PT2 uncovered a rare hypomorph - c.4685T>C. Furthermore, ROs were able to recapitulate the retina-specific splicing defect in PT1 as shown by LRS data.

Collectively, these results highlight the suitability of ROs in STGD1 modelling. Their ability to display genotype-phenotype correlations enhances their utility as a platform for therapeutic development. Importantly, both PT1 and PT2 cases were genetically resolved in this study, providing two more individuals with their confirmed genetic diagnosis.

Acknowledgements

"Nothing in life is to be feared, it is only understood.
Now is the time to understand more, so that we may fear less".
– ***Marie Curie***

My PhD was a wonderful experience, filled with many ups and downs - tears and laughter. It was challenging both professionally and personally and has truly shaped me as a person and a scientist. It would not have been possible without my supportive team of supervisors, friends, and family.

I would especially like to extend my deepest gratitude to ***Prof. Majlinda Lako*** for all of her support, mentorship, kindness and understanding during my studentship. She has always had my best interests at heart as her student and afforded me the experience of a lifetime in the Lako lab. My gratitude extends to my secondary supervisors - **Prof. Lyle Armstrong** and **Dr. Valeria Chichagova** for their support and guidance on various elements of my project.

I'd like to thank **all** members of the Lako & Armstrong research groups for fostering a fun and collaborative environment. You will always be my Newcastle Family. I want to particularly acknowledge **Dr. Birthe Dorgau** and **Dr. Agata Rozanska** for their friendship, in addition to their day-to-day support and advice on key elements of this study and future career perspectives.

Thank you to our collaborators for their input into this study, especially **Dr. Rachel Queen, Dr. Michael McCorkindale, Dr. Jonathan Coxhead** and **Rafiqul Hussain** at Newcastle University, **Prof. Frans Cremers** at Radboud University (NL), **Dr. Andrew Nelson** at Northumbria University, and **Dr. Ana Conesa** and **Dr. Luís Ferrandez** at the University of Valencia (Spain). Thank you also to the core staff at the Centre for Life for being so kind and helpful always, especially **Lisa Hodgson, Lisa Embleton** and **Tony Riley.**

Thank you to the Marie Curie ITN Network StarT for funding this research and providing excellent scientific support through training workshops, collaboration, and mini-conferences.

It is rare to meet a diverse group of people who individually add so much value to your life. We've shared our PhD experiences, our hopes and fears, our successes and failures. We've travelled together and survived a pandemic and Brexit! Thank you for all of the memories.

I am grateful to have spent the last 3-4 years with you
Maria Georgiou, Robert Atkinson, Sarah Bassim Hammadi, Sally Harwood, Marina Moya Molina, Rodrigo Cerna Chavez, Jack Thornton, Elena Tasinato, Anastassia Kostenko and Madeleine Carter

Thank you to my family and future in-laws for all of their support and encouragement over the years. My parents, **Anne** and **Billy**, brother **Shane** and grandad **Gus**, and all of my home friends – for always believing in me.

To my fiancé **Jordan**, for the last decade you have been my biggest supporter by far. Thank you for always being there for me – through thick and thin. For encouraging me to follow my dreams and move abroad to carry out this research. For the countless hours lost in airports to come visit me, for never once complaining. I couldn't have done any of this without you. ♡

In an extension to my acknowledgements, I've been fortunate to be surrounded by strong women in my life who have continually inspired and motivated me to chase my dreams. I can't refer to them all but as this thesis is one of my biggest achievements to date, I wanted to document some of the key women who have empowered me to get to this stage.

First and foremost, my mam **Anne.** I know life has not always been easy, and the cards have often been stacked against you. No one has taught me more that your circumstances do not define you or your abilities. Thank you for giving me all the opportunities you never had, for making so many sacrifices for me and for always being my biggest supporter. The older I get, the more that I see.

My secondary school Maths teacher – the late **Ms. Maria Broderick**, my first role model in STEM. I'll never forget your tales of travelling to the all-boys school as a young girl to have the chance to study maths and science. Your tenacity and dedication, even later in life, are still such an inspiration to me. I am so grateful to have had the chance to reconnect and tell you that. You left too soon but your impact has reached far beyond what you could ever imagine.

Finally, my PhD supervisor and mentor **Prof. Majlinda Lako** – the woman who never stops. Your insatiable curiosity, unwavering ambition and unparalleled determination are truly inspiring. Not only have you achieved tremendous success in your career, but you have also managed to raise a beautiful family, proving that hard work can lead to a fulfilling life in both personal and professional aspects. Your willingness to provide opportunities for exciting research has been transformative for me. I will cherish the knowledge and experience gained under your guidance, which has undoubtedly shaped me as a researcher and as an individual. Thank you for being an excellent role model. Your influence in my life will have a lasting impact and I hope our paths will cross many more times in the future.

Stem Cell Lab
(2019-2023)

Contents

List of Figures

List of Tables

List of Abbreviations

AOSLO	Adaptive Optics Scanning Laser Ophthalmoscopy
AAV	Adeno-Associated Virus
AMD	Age-Related Macular Degeneration
ASE	Allele-Specific Expression
AC	Amacrine Cell
AON	Antisense Oligonucleotide
ABCA4	ATP-Binding Cassette Subfamily A Member 4
BCVA	Best-Corrected Visual Acuity
BSU	Bioinformatics Support Unit
BMP	Bone Morphogenetic Protein
CNS	Central Nervous System
CPC	Chromatic Pupil Campimetry
CDS	Coding Sequence
cDNA	Complementary DNA
CM	Conditioned Medium
CRD/CORD	Cone-Rod Dystrophy
CCS	Consensus Circularised Sequence
CN	Copy Number
CNV	Copy Number Variation
CF	Counting Fingers
cGMP	Cyclic Guanosine Monophosphate
DNA	Deoxyribonucleic Acid
DE	Differential Expression
DEG	Differentially Expressed Genes
DHA	Docosahexaenoic Acid
DMEM/F12	Dulbecco's Modified Eagle Medium: Nutrient Mixture F-12
EB	Embryoid Body
EC	Embryonal Carcinoma
ESC	Embryonic Stem Cell
ELM	External Limiting Membrane
FBS	Foetal Bovine serum
ffERG	Full-Field Electroretinogram
FAF	Fundus Autofluorescence
GCPR	G Protein-Coupled Receptor
Gα-GTP	G-alpha Guanosine Triphosphate
GOF	Gain of Function
GCF	Genomics Core Facility
HM	Hand Motion
HC	Horizontal Cell
hESC	Human Embryonic Stem Cell
iPSC	Induced Pluripotent Stem Cell
IPA	Ingenuity Pathway Analysis

ICM	Inner Cell Mass
INL	Inner Nuclear Layer
IPL	Inner Plexiform Layer
IS	Inner Segment
IGF-1	Insulin-Like Growth Factor 1
IKNM	Interkinetic Nuclear Migration
IRBP	Interphotoreceptor Retinoid-Binding Protein
iMEF	Irradiated Mouse Embryonic Feeder Cells
KOSR	KnockOut Serum Replacement
LCA	Leber Congenital Amaurosis
L-DOPA	Levodopa
LUBEC	Linear Ubiquitin Chain Assembly Complex
LRS	Long-Read RNA Sequencing
LOF	Loss of Function
MAC	Membrane Attack Complex
mESC	Mouse Embryonic Stem Cell
MCO	Multi Characteristic Opsin
MEAs	Multi-Electrode Arrays
DAPT	N-[N-(3,5-Difluorophenacetyl)-L-alanyl]-S-phenylglycine t-butyl ester
A2E	*N*-retinylidene-*N*-retinylethanolamine
A2PE	*N*-retinylidene-*N*-retinylphosphatidylethanolamine
NRPE	N-retinylidene-phosphatidylethanolamine
NGS	Next-Generation Sequencing
NGS	Normal Goat Serum
NFW	Nuclease Free Water
OKSM	Oct4, Sox2, Klf4, and cMyc
OMIM	Online Mendelian Inheritance in Man
ORF	Open Reading Frame
OV	Optic Vesicle
ONL	Outer Nuclear Layer
OPL	Outer Plexiform Layer
OS	Outer Segment
PFA	Paraformaldehyde
PSI	Percentage Spliced In
PBMCs	Peripheral Blood Mononuclear Cells
PBS	Phosphate Buffer Saline
PCs	Proliferating Cells
PE	Phosphatidylethanolamine
PDE	Phosphodiesterase
POS	Photoreceptor Outer Segment
PPC	Photoreceptor Precursor Cell
PCR	Polymerase Chain Reaction
PVS	Predicted Very Severe
PMEF	Primary Mouse Embryonic Feeder Cells
PCs	Proliferating cells

qPCR	Quantitative Polymerase Chain Reaction
RORA	*RAR Related Orphan Receptor A*
RGC	Retinal Ganglion Cell
RO	Retinal Organoid
RPE	Retinal Pigment Epithelium
RPC	Retinal Precursor Cell
RP	Retinitis Pigmentosa
RA	Retinoic Acid
RDH12	Retinol Dehydrogenase 12
RDH5	Retinol Dehydrogenase 5
RDH8	Retinol Dehydrogenase 8
RT-qPCR	Reverse Transcription Quantitative PCR
ROCKi	Rho-associated Coiled-coil Protein Kinase Inhibitor
RNA	Ribonucleic Acid
RIN	RNA Integrity Number
SeV	Sendai Virus
SAE	Serious Adverse Effects
SNP	Single Nucleotide Polymorphism
scRNA-Seq	Single-Cell RNA Sequencing
smMIP	Single-Molecule Molecular Inversion Probe
SD-OCT	Spectral Domain Optical Coherence Tomography
SOP	Standard operating procedure
STGD1	Stargardt Disease 1
TER/TEER	Transepithelial/Transendothelial Electrical Resistance
TGFβ	Transforming Growth Factor Beta
T3	Triiodothyronine
UTR	Untranslated Region
WGS	Whole genome sequencing
XLRS	X-Linked Retinoschisis

Chapter 1 Introduction

1.1 The retina – structure and function

The retina is a highly specialised, complex neural tissue situated at the back of the eye. It is comprised of a variety of specialised neurons that work together with the visual cortex to facilitate the recognition and conversion of light photons to electrical signals. These signals are decoded by the brain as real-time images of the surrounding environment, enabling visual perception.

1.1.1 Retinal physiology

The retina hosts a diverse repertoire of cells. Approximately 55 separate neuronal cell types have been identified - of which 5 neuronal classes are essential for vision (Masland, 2001). These include the photoreceptor cells, bipolar cells, amacrine cells (ACs), horizontal cells (HCs) and retinal ganglion cells (RGCs). These cells are laminated along an apical-basal axis to form an intricate network of cells that can relay information from one cell type to another for the overall purpose of phototransduction **(Figure 1.1).**

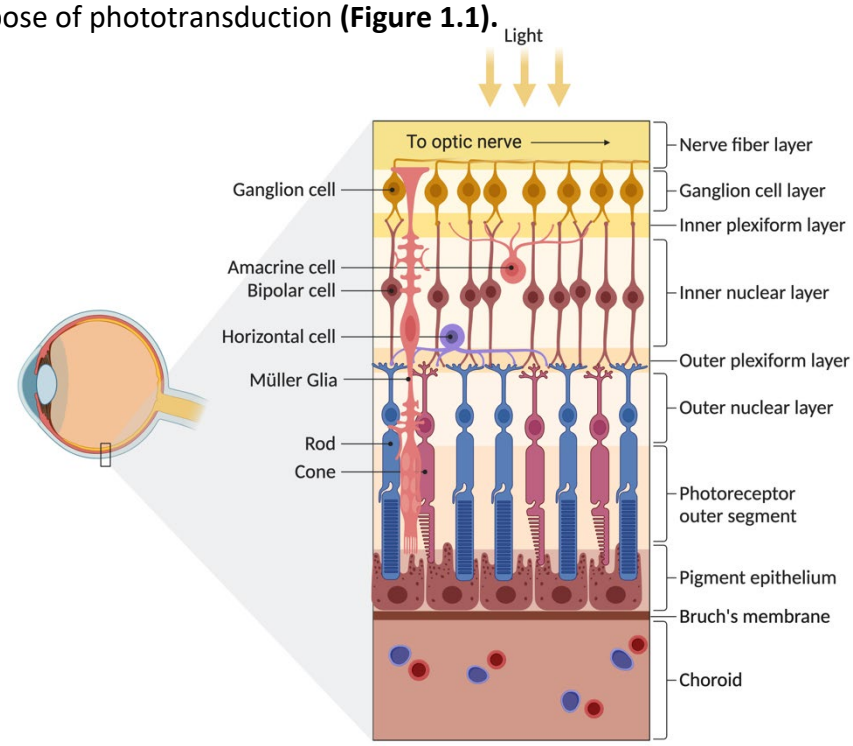

Figure 1.1 The retina.

Light entering the eye is focused by the lens onto the retina, stimulating photoreceptors (rods and cones) to generate electrical signals. These signals are transmitted through a neural circuit involving bipolar cells, RGCs, HCs and ACs, ultimately reaching the optic nerve as action potentials, which are then sent to the visual cortex in the brain. The retina's outermost layer - the RPE, supports photoreceptors and prevents light backscattering, while the choroid supplies the retina with oxygen and nutrients through Bruch's membrane.

Humans have two main classes of photoreceptor cells – the cones and the rods. Rods are specialised neurons known for their sensitivity but lower visual acuity. They are highly adapted for low-light conditions and suited for night vision. In contrast, cone photoreceptors have less sensitivity, thereby requiring high levels of light for activation. Cone photoreceptors provide high acuity vision through three distinct subclasses of cells: blue, green, and red cones, which can absorb light at varying wavelengths (short, medium, and long respectively) within the visible light spectrum **(Figure 1.2)**.

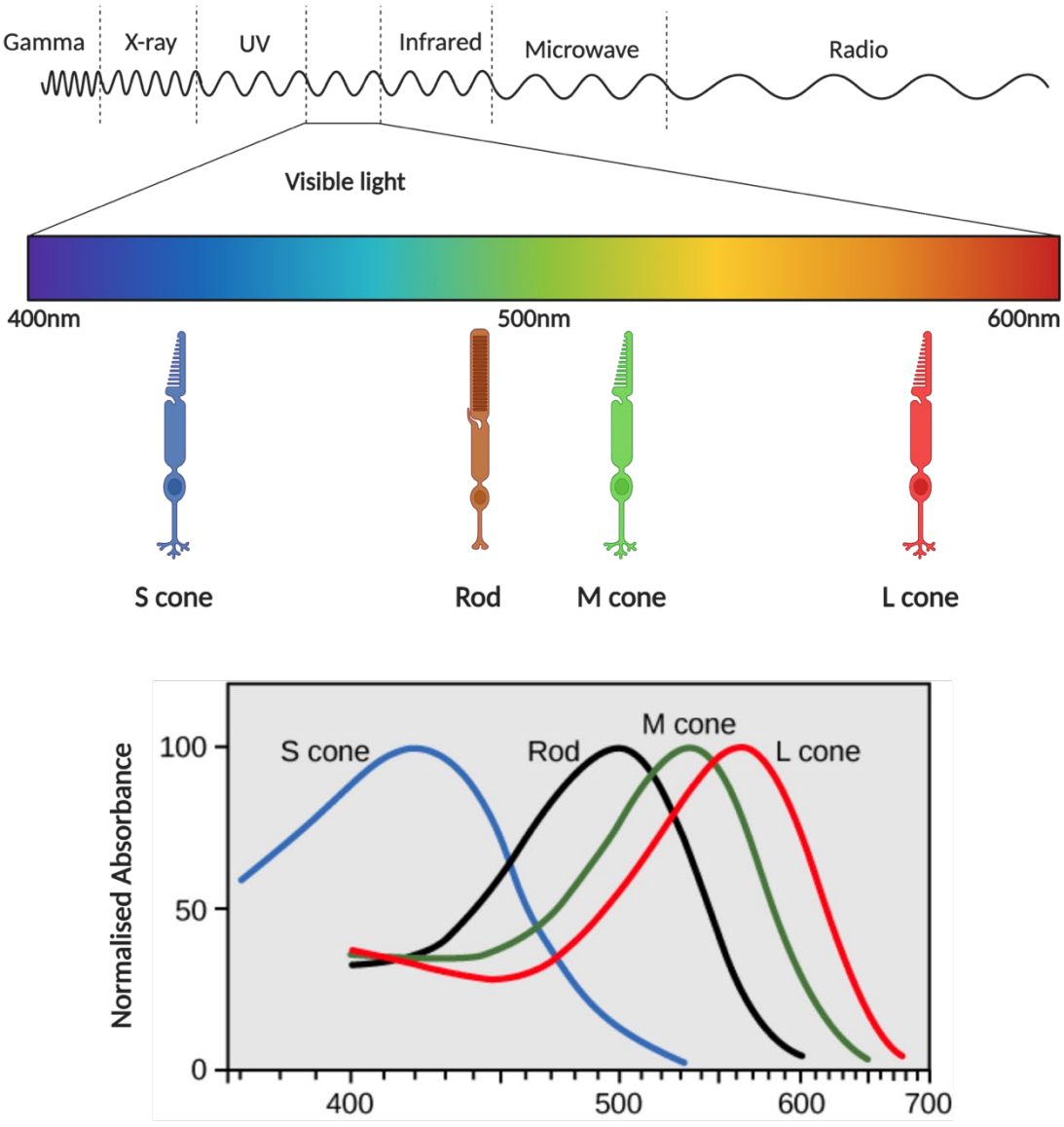

Figure 1.2 Visible light spectrum.

The electromagnetic spectrum is depicted, highlighting the visible portion ranging from approximately 400 to 600nm. Different wavelengths of light are represented by various colours to which specific photoreceptor subtypes are responsive to. Rod cells are sensitive to lower wavelengths, primarily in the blue and green regions, around 400-550nm. The three subtypes of cone cells are each tuned to different wavelengths: S-cones (blue-sensitive, 400-500nm), M-cones (green-sensitive, 500-600nm), and L-cones (red-sensitive, 600-700nm). This selective sensitivity allows the visual system to perceive a wide range of colours and shapes in the environment.

The human retina is largely dominated by rod photoreceptors occurring at a 20:1 ratio to cone photoreceptors. However, the distribution of these cells is not equal across the retina. Within the central region of the retina, called the macula, there is a pit in the tissue where a dense population of cone photoreceptors are located (Curcio *et al.*, 1990) **(Figure 1.3).** This region is called the fovea and the cluster of cone cells that reside there permit high quality vision with sharp resolution, necessary for tasks such as object recognition, reading, writing and chromatic vision. To facilitate such high acuity, the macula is structured in a way where second order neurons are pushed aside to reduce the distortion of light associated with the passing through of them, as is the case in the periphery. Thereby, this structural adaption ensures that light can be focused by the lens and projected directly on cone photoreceptors in an unperturbed manner. To further assist in the provision of high acuity vision, the ratio of bipolar cell to cone cell is reduced to 1:1, ensuring clear and effective transmission of the electrical impulses generated by the photoreceptor to second order neurons (Purves D, 2001).

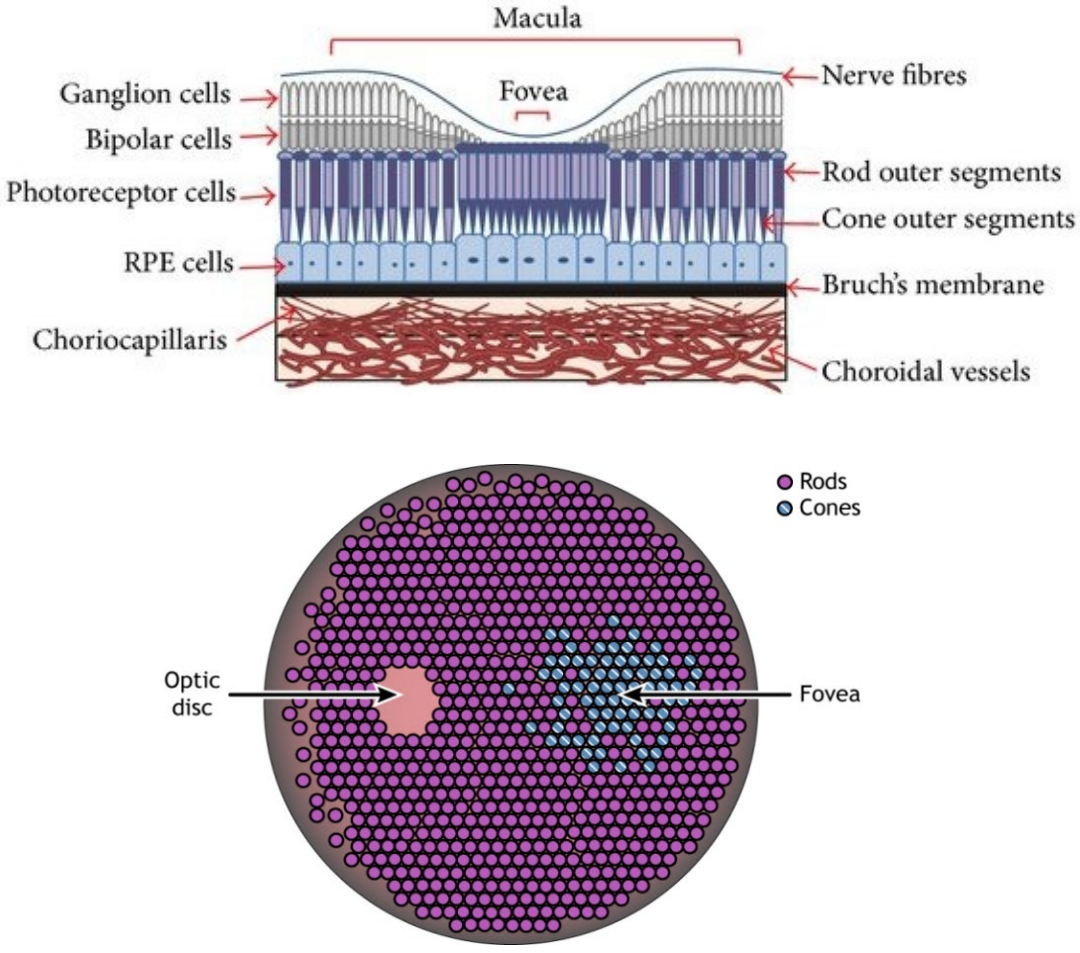

Figure 1.3 Structure of the macula, and distribution of rod and cone photoreceptors in the retina.

In the macula, a central region of the retina, second-order neurons, such as bipolar cells and ganglion cells, are pushed aside, allowing for direct absorption of photons by cone photoreceptors. This arrangement enhances visual acuity and detail in the central visual field. Cone photoreceptors, responsible for colour vision and high acuity, are concentrated within the macula, particularly in the fovea, where colour discrimination is most acute. In contrast, the peripheral regions of the retina are dominated by rod photoreceptors, which excel in low-light conditions and peripheral vision. This distribution of photoreceptors across the retina optimises visual function for various lighting and spatial requirements in the visual field.

Figure adapted from Henly (2021) and Al Gwairi *et al.* (2016).

Rod photoreceptors are mainly located outside of the macula, in the peripheral retina. Despite their high sensitivity, the ratio of rod to bipolar cell is significantly increased (50-100 rods:1 bipolar cell) the further these cells are situated from the macula. This corresponds to an approximate 75% reduction of visual acuity when compared with cone photoreceptors (Forrester *et al.*, 2016).

As an instigator of the phototransduction cascade, photoreceptors are arguably one of the most important cells in this system, but they do not work in isolation. There is a series of neurons that play a role in propagating the initial electrical impulse generated by the photoreceptor cells to higher processing centres in the brain. The bipolar cell is the 'messenger' in this system, linking the photoreceptor cell to the RGC, which is the output neuron of the retina. In response to light, photoreceptors alter their neurotransmitter release, and this is picked up by bipolar cells, decoded and transmitted to RGCs in the form of spikes.

Although more than 10 subclasses of bipolar cells exist, they are generally comprised of two functional types: OFF bipolar and ON bipolar cells. These cells directly recognise and respond to membrane potential changes in the photoreceptor cell via neurotransmitter release. The neurotransmitter released by photoreceptor cells is glutamate (Euler *et al.*, 2014). This neurotransmitter is excitatory to OFF bipolar cells which carry ionotropic glutamate receptors on their cell surface. The activation of these receptors enables sodium influx into the cell triggering depolarisation. In the presence of light, photoreceptors reduce glutamate release. This causes the ionotropic receptors of OFF bipolar cells to inactivate (Kolb, Fernandez and Nelson, 1995). Contrary to this, glutamate is inhibitory to ON bipolar cells. In the dark, metabotropic receptors on the cell surface are activated which trigger associated G-proteins to close cation channels in the membrane preventing sodium and calcium influx leading to hyperpolarisation of the cell. In the light, decreased glutamate release from photoreceptors

is insufficient to activate the metabotropic receptors and thus cation influx is permissible and results in depolarisation of the photoreceptor (Popova, 2014).

In the context of cone photoreceptors, bipolar cells transmit spikes from photoreceptors directly to RGCs. In cones specifically, OFF bipolar cells contact OFF-centre RGCs and ON bipolar cells with ON-centre RGCs. In response to light, ON bipolar cells depolarise whilst OFF bipolar cells hyperpolarise. Consequently, ON-centre RGCs are excited and generate an action potential, whereas OFF-centre RGCs are inhibited. This signal is then propagated to the visual cortex in the brain via their axon fibres which converge and form the optic nerve. A similar mechanism exists for rod bipolar cells except that RGCs are not categorised into distinct ON and OFF subtypes as clearly as in the cone pathway. Instead, they often exhibit a graded response to light, which means they are active across a range of light levels. This differential response is a fundamental aspect of visual processing that helps detect contrasts in the visual scene (Nelson and Connaughton, 2012).

This is the most direct pathway of neuronal communication in the retina. However, this pathway can also function through the inhibitory interneurons – HCs and ACs, in the outer and inner plexiform layers, respectively. HCs are important for both colour opponency and enhancing contrast (Chapot, Euler and Schubert, 2017). ACs play an important role in detecting changes in light intensity and relay this information via the generation of transient responses to RGCs (Roska, Nemeth and Werblin, 1998).

However, the critical functions of these interneurons are to finetune the light signal propagated from the photoreceptor through lateral inhibition. This is a process in which an excited neuron can dampen the response of neighbouring neurons such as photoreceptors and other bipolar cells to reduce their activity. This defines the region of receptivity in the retina, often denoted as the receptive field. The receptive field varies in size across the retina in accordance with the density and subtype of photoreceptor cell present. In the fovea, the receptive field is the smallest which permits high acuity vision. On the other hand, in the peripheral retina the receptive field is much larger, and vision is less acute (Chaya *et al.*, 2017).

There are additional elements to this system that are critical for overall visual function. Adjacent to the photoreceptor layer outside of the neural retina lies a specialised monolayer of pigmented, hexagonal cells called the retinal pigment epithelium (RPE). This tissue is located in close proximity to both neural retina and the choriocapillaris and has a key role in maintaining the blood-retina barrier. Moreover, it is crucial for the sustenance and viability of

the overlying photoreceptor cells. The microvilli of RPE cells interdigitate with the photoreceptor outer segments (POS), which are diurnally shed and phagocytosed by the adjacent RPE cell. The RPE is also responsible for the recycling and provision of molecules and nutrients important for vision. Due to its dark pigment, excessive light is easily absorbed and prevented from the process of backscattering. This contributes to improved visual acuity in the retina (Boulton and Dayhaw-Barker, 2001).

Another important element for the structure and function of neural retina is Müller glia. These cells provide structural support by forming tight barriers, which create the outer and inner limiting membranes (ONL and INL respectively) and contribute to blood-retina barrier integrity. Despite residing in the INL, they extend processes throughout the entire retina to reach all cell layers, maintaining overall retinal architecture. They also contribute to tissue stability by releasing neurotrophic factors and metabolites, and they assist in phagocytosis of spent photoreceptor outer segments alongside the RPE in cones specifically (Reichenbach and Bringmann, 2013). In cases of retinal damage, Müller glial cells are pivotal. They undergo reactive gliosis, multiplying and enhancing neuroprotective substance release, preventing neuronal cell death and supporting retinal recovery (Bringmann et al., 2009).

1.1.2 Retinogenesis

In utero retinogenesis begins with the establishment of the eye field from the medial anterior neural plate **(Figure 1.4).** This is facilitated by the expression of key transcription factors including *Pax6, Rax, Six3, Six6* and *Lhx2,* among others to specify eye field fate. These transcription factors are also involved in forebrain development. A critical stage in this process is the separation of eye field from diencephalon, the caudal region of the forebrain. This is achieved by indentation within the neural fold to generate optic grooves, which evaginate bilaterally from the diencephalon to form optic vesicles (OVs). OVs continue to grow towards the surface ectoderm, which upon contact forms the lens placode. The resulting optic stalk attaching the OVs to the forebrain later becomes the optic nerve (Quinn and Wijnholds, 2019). Invagination of the lens placode and OVs split the eye field in two and generates double-layered optic cups. The lens placode continues to develop into the lens vesicle at the surface ectoderm, whilst the iris and the ciliary body begin to form at the anterior of the optic cup. At the posterior, the outer layer of the optic cup becomes RPE, the aforementioned monolayer of hexagonal, pigmented cells. Within the inner layer of the posterior optic cup, retinal progenitor cells (RPCs) proliferate to form the intricate network of sensory neurons

responsible for the process of phototransduction (O'Hara-Wright and Gonzalez-Cordero, 2020). The laminated ordering of the cells present in the retina corresponds to their sequential birth order. RGCs are the first to be generated and the Müller glial cells are the last. Asymmetrical division from RPCs produce both post-mitotic neurons, that migrate to their site of function, whilst newly generated RPCs continue to populate the retina with a diverse set of retinal neurons (Heavner and Pevny, 2012).

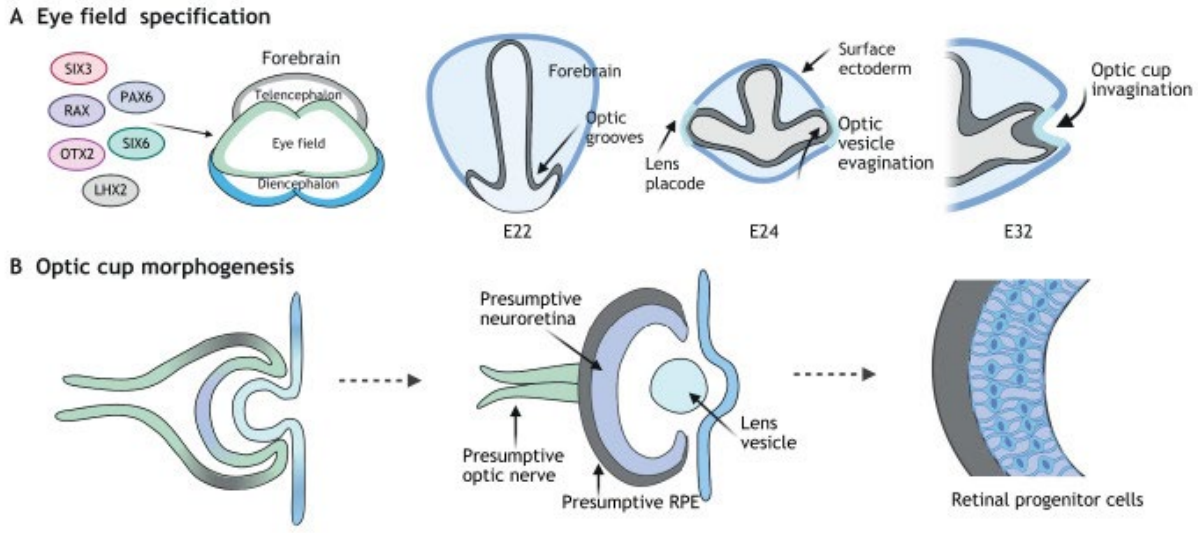

Figure 1.4 Human retinogenesis

In vivo, eye field transcription factors (SIX3, RAX, PAX6, OTX2, SIX6, and LHX2) specify eye fate from forebrain. By human embryonic day 22 (E22), optic grooves appear on both sides of the diencephalon in the neural fold. These grooves transform into optic vesicles by E24, which contact the surface ectoderm where the lens will form (lens placode). By E32, invagination of the optic vesicle creates the bilayered optic cup. The inner layer becomes the presumptive neuroretina, while the outer layer becomes the presumptive RPE. The optic stalk, a hollow connection, links the optic vesicles to the forebrain, eventually forming the optic nerve. The lens vesicle separates from the surface ectoderm, and in the presumptive neuroretina, multipotent RPCs initiate differentiation into various retinal cell types.

Figure adapted from O'Hara-Wright and Gonzalez-Cordero (2020).

1.1.3 Phototransduction Cascade

Phototransduction is a biochemical process that involves the absorption and conversion of photons to electrical signals in the retina. These electrical impulses provide meaningful information that can be decoded into visual images by the visual cortex in the brain. This process begins in the POS where light-sensitive conjugates of the chromophore 11-*cis*-retinal and the relevant photopigments exist. Whilst both rod and cone photoreceptors function in a similar manner, the phototransduction cascade is best described in the context of rod photoreceptors.

Rhodopsin is the photopigment found in rod POS and functions as a G-coupled protein receptor (GCPR). It is a highly sensitive photopigment responsive to a maximum of 480nm of light emission in dimly lit conditions (Palczewski, 2006). In its inactive form, rhodopsin is bound to light-sensitive 11-*cis*-retinal. In response to a light stimulus, the chromophore undergoes photoisomerisation to all-*trans*-retinal which triggers a conformational change in the rhodopsin protein, thereby activating and converting it to metarhodopsin II. This kickstarts the phototransduction cascade to propagate and amplify the initial response to light for downstream cortical processing.

Once photobleached, all-*trans*-retinal dissociates from metarhodopsin II and enters the visual cycle where light-responsive 11-*cis*-retinal is regenerated. In the meantime, metarhodopsin II binds with transducin, a G-protein found in the cell membrane, triggering a nucleotide exchange of GDP for GTP. The active alpha subunit of Transducin (G_{α}-GTP) dissociates from metarhodopsin II to activate the next protein in the cascade. Metarhodopsin II remains active and can continuously activate several transducin proteins thereafter. G_{α}-GTP binds with phosphodiesterase (PDE), however PDE requires two G_{α}-GTP subunits to bind with its inhibitory y-subunits for full activation (Lamb and Pugh, 2006).

In the resting photoreceptor in the dark, there is constitutive activity of PDE, facilitating a balance of cyclic GMP (cGMP) synthesis and its hydrolysis by PDE. This maintains a transient concentration of cGMP in the POS to keep ion channels open, allowing for the influx and efflux of ions within the cell. This keeps resting photoreceptors in a depolarised state at a voltage of -40mV.

In response to light, PDE becomes fully activated and hydrolysis rates significantly increase. Consequently, cGMP levels significantly drop causing ion channels in the cell membrane to

snap shut. Decreased Na^+ ion influx results in hyperpolarisation of the cell to -70mV, this alters neurotransmitter release from the cell which in turn generates the electrical signal to be propagated in this cascade (Purves D, 2001).

The phototransduction cascade terminates via phosphorylation of metarhodopsin II via an opsin kinase called arrestin. Transducin is inactivated via intrinsic GTPase activity supported by a G-protein signalling regulator RGS9. The inactivation of transducin directly inactivates PDE via its dissociation from the molecule. Guanylate cyclase restores cGMP levels in the photoreceptor allowing for the membrane potential to depolarise and return to -40mV (Kandel *et al.*, 2000).

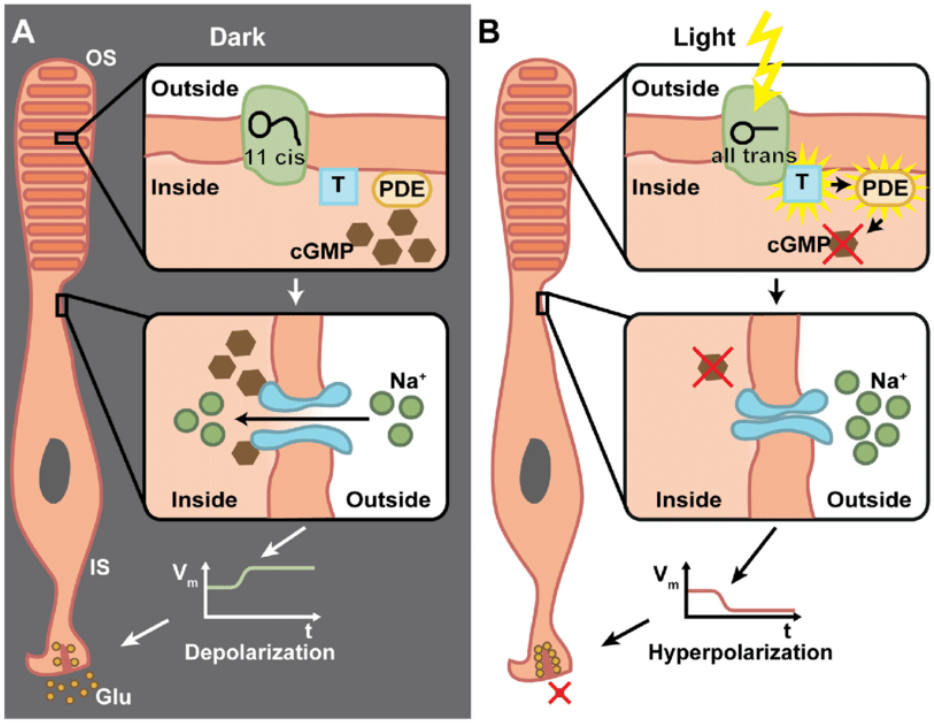

Figure 1.5 Phototransduction cascade in rod photoreceptor cells (dark versus light).

Dark Condition (Left): In the absence of light, the photopigment rhodopsin contains 11-*cis*-retinal, maintaining sodium (Na+) channels in an open state. Consequently, the cell remains depolarised, continuously releasing the neurotransmitter glutamate onto bipolar cells. The presence of cyclic guanosine monophosphate (cGMP) ensures the sodium channels remain open by inhibiting phosphodiesterase (PDE) activity. Transducin molecules remain in their inactive state.

Light Condition (Right): Upon exposure to light, photons activate rhodopsin, leading to the conversion of 11-*cis*-retinal to all-*trans*-retinal. All-*trans*-retinal dissociates from rhodopsin, triggering rhodopsin's activation. Rhodopsin then activates transducin, initiating the phototransduction cascade. This activation prompts PDE to break down cGMP into GMP. Reduced cGMP levels result in the closure of sodium channels, preventing sodium ions (Na+) from entering the cell. Consequently, the cell undergoes hyperpolarisation as its membrane potential becomes more negative. This decrease in glutamate release signals a change in neurotransmission to bipolar cells, conveying the presence of light. This highly orchestrated cascade enables the rod photoreceptor cell to convert light stimuli into electrical signals, facilitating the detection and processing of visual information.

Figure source: Klapper *et al.* (2016)

1.1.4 Visual Cycle

Once rhodopsin has been photobleached and undergone its conformational change to metarhodopsin II, all-*trans*-retinal dissociates from the photopigment to enter the visual cycle for the regeneration of light-responsive 11-*cis*-retinal. This is facilitated via a series of enzymatic reactions that occur in the POS and adjacent RPE cell. This process holds significant importance because retinal, a derivative of vitamin A, is not naturally synthesised by the body and must be acquired through dietary sources.

All-*trans*-retinal is a highly reactive molecule, and upon its release, it undergoes rapid transformation in one of two ways: it is either swiftly converted into all-*trans*-retinol by retinal dehydrogenase enzymes (atRDH) in the cytoplasm or it is sequestered to the POS disc membrane via conjugation with phosphatidylethanolamine (PE) to generate *N*-retinylidene-phosphatidylethanolamine (NRPE) (Haeseleer *et al.*, 1998). Cytoplasmically facing NRPE can be metabolised by reducing enzymes in the cytoplasm surrounding the discs in the POS, whilst NRPE molecules with the all-*trans*-retinal group orientated towards the inner leaflet become a substrate for ABCA4 protein. This protein functions as 'flippase' to transport NRPE complexes trapped inside the disc to the cytoplasmic leaflet, enabling their access to the cytosolic enzymes for further metabolism (Quazi, Lenevich and Molday, 2012). An estimated 30% of all-*trans*-retinal molecules are processed via the ABCA4 pathway (Lamb and Pugh, 2004) and so this pathway is crucial in ensuring effective clearance of NRPE and avoidance of toxic bisretinoid generation (Sparrow *et al.*, 2010).

Once reduced, all-*trans*-retinol is bound by the interphotoreceptor retinoid binding protein (IRBP) and shuttled out of the POS to distal RPE cells. Here, all-*trans*-retinol is esterified by LRAT to all-*trans*-retinyl esters which are selectively hydrolysed and isomerised by RPE65 to 11-*cis*-retinol (Moiseyev *et al.*, 2005). Finally, retinal dehydrogenase 5 (11-cRDH) oxidises 11-*cis*-retinol to 11-*cis*-retinal. This renewed light-sensitive molecule is transported to the POS once again by IRBP and is ready to bind with rhodopsin again to form a functional chromophore for participation in another round of phototransduction (Rando, 2001).

A cone-specific visual cycle also exists which occurs independent of RPE. Instead, Müller glia play a crucial role in the regeneration of visual cycle proteins and supply them exclusively to cone photoreceptors. This is a much faster process when compared with RPE visual protein regeneration, which although it does supply 11-*cis*-retinal to rods and cones, cannot meet the

high demand of cone photoreceptors when under bright light conditions (Wang and Kefalov, 2011).

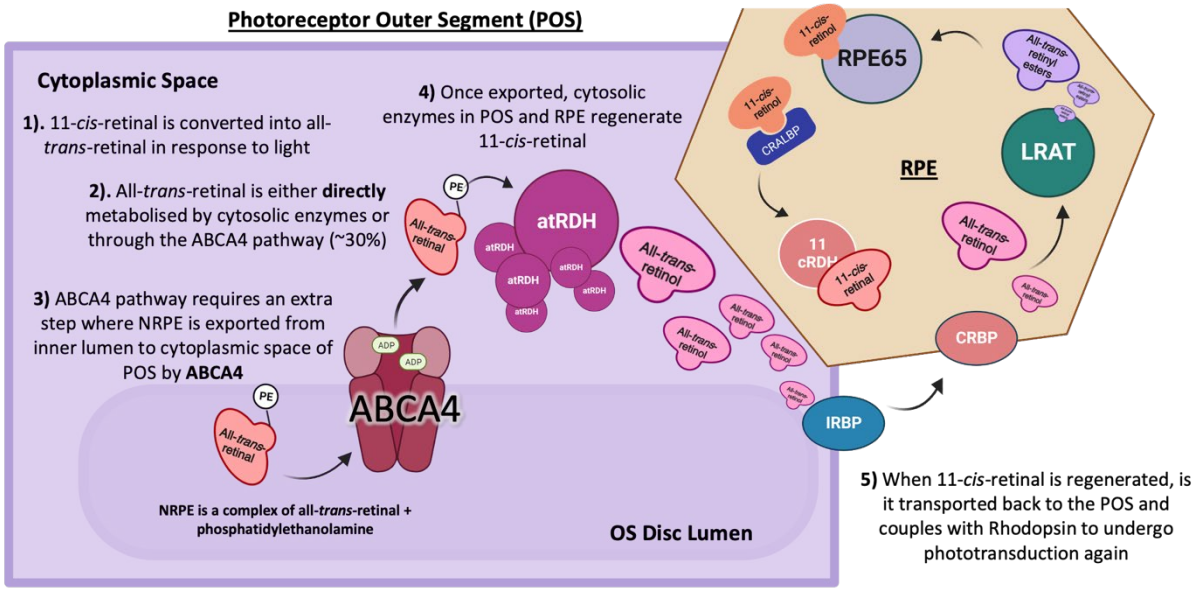

Figure 1.6 Visual Cycle.

This figure illustrates the biochemical pathway responsible for the regeneration of 11-*cis*-retinal from spent all-*trans*-retinal in rod photoreceptors. The process begins in the photoreceptor when 11-*cis*-retinal, conjugated to Rhodopsin, is activated in response to light. Once spent, all-*trans*-retinal is dissociated from Rhodopsin and reduced to all-*trans*-retinol via atRDH, an enzyme found in the cytoplasm of the photoreceptor outer segment. IRBP translocates the molecule to the RPE where it encounters three enzymes; LRAT, RPE65 and RDH5 which process the molecule back to 11-*cis*-retinal. IRBP translocates the molecule back to the photoreceptor outer segment where it can be used again in the phototransduction cascade.

1.1.5 Dysfunction in the retina

With the retina being a highly complex and ordered tissue, dysregulation of any elements within the system can severely compromise individual cell types resulting in local neurodegeneration and subsequent vision loss.

A substantial proportion of retinal degenerations are attributable to genetic factors and are heritable. These so-called inherited retinal degenerations (IRDs) are currently the leading cause of blindness in working aged individuals in the UK (Liew, Michaelides and Bunce, 2014). IRDs account for a significant portion of the 350,000 registered blind cases in the UK and impose a substantial socioeconomic burden on those affected, their families, and the UK economy, with estimated annual costs exceeding £25 billion (Dewing, Lotery and Ratnayaka, 2023). On a global scale, IRDs affect approximately 5.5 million people, with an overall incidence of 1 in 1,380 individuals (Ben-Yosef, 2022). Despite this high incidence, most IRDs lack approved treatments or therapies to slow or halt disease progression.

IRDs encompass a diverse collection of rare blinding disorders, displaying considerable clinical and genetic heterogeneity - such that individual IRD cases are rare in incidence. While the molecular causes of disease may differ between disorders, the ultimate outcome in nearly all IRDs is the loss of photoreceptor cells and/or RPE cells, leading to blindness.

Retinitis pigmentosa (RP), the most common IRD, has an overall incidence of 1:4,000 (Pagon, 1988; Hartong, Berson and Dryja, 2006), followed by STGD1 with an incidence of 1:8,000–10,000 (Blacharski, 1988). Some IRDs present syndromically, with visual impairment accompanied by other comorbidities. Approximately 18% of RP cases are Usher Syndrome (Toms, Pagarkar and Moosajee, 2020) where blindness presents alongside varying degrees of deafness. This condition affects roughly 1:10,000 individuals (Boughman, Vernon and Shaver, 1983; Kimberling *et al.*, 2010). These three conditions are the most diagnosed forms of IRDs.

With over 280 genes implicated in the development of IRDs (RetNet at https://sph.uth.edu/Retnet/, accessed on 1st September 2023), recent years have seen a plateau in the discovery of novel genes **(Figure 1.7),** suggesting that the majority of IRD-associated genes are known. However, despite this, the genetic solve rate of IRD cases following next-generation sequencing (NGS), using gene target capture panels and whole genome sequencing (WGS), remains at 50-70% (Stone *et al.*, 2017; Carss *et al.*, 2017; Dockery *et al.*, 2017; Whelan *et al.*, 2020; Del Pozo-Valero *et al.*, 2022). It is likely that causative

mutations for these undiagnosed cases exist within the known cohort of IRD genes but may have been overlooked due to technical limitations or misinterpretation of called variants.

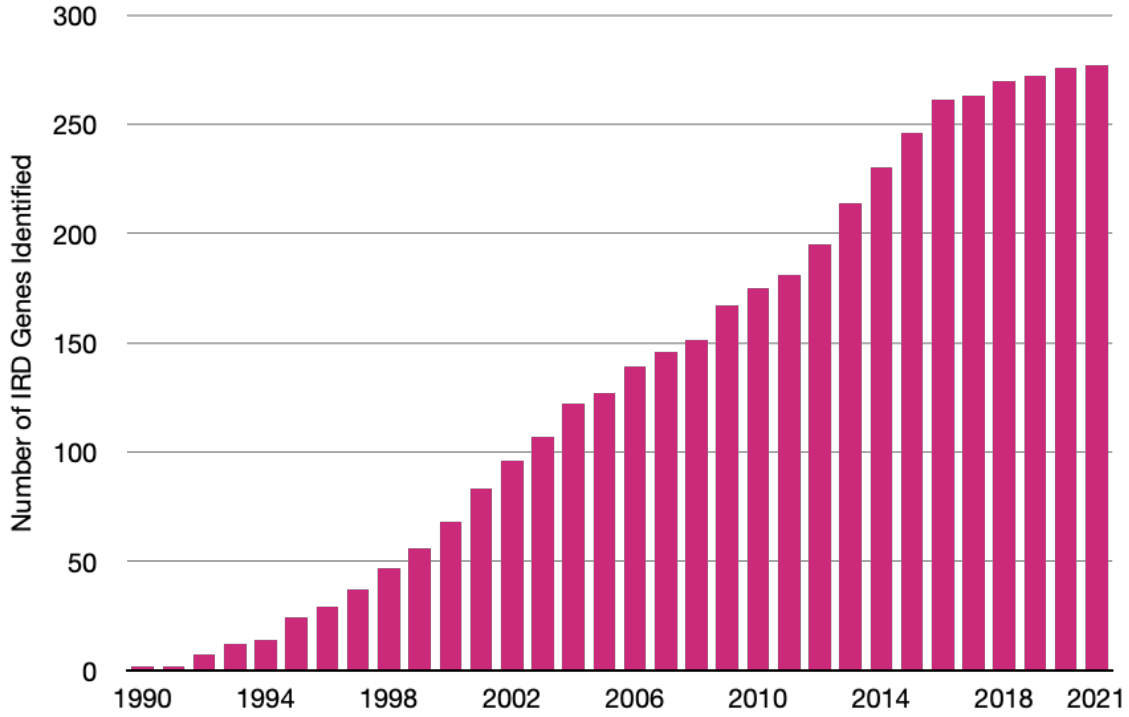

Figure 1.7 Genes identified in IRD conditions.

This histogram depicts the number of genes identified as causative of IRDs between the years 1990 and 2021. Gene discovery has grown steadily over this period owing to the advancements made in genetic diagnostics. Gene discovery has plateaued in the last 5 years, indicating that most disease-causing genes have thus far been identified.

Graph generated from data on RetNet (2023).

Given the considerable heterogeneity of IRDs, accurate diagnosis based solely on clinical presentation can be challenging. This underscores the importance of genetic diagnoses for individuals with heritable blindness. Such diagnoses provide access to genetic counselling, prognostic insights on disease progression, guidance on managing the condition and eligibility for participation in relevant clinical trials – the latter being an especially critical consideration given the limited therapeutic options currently available for IRD treatment.

1.2 Stargardt Disease

STGD1 (OMIM: 248200) is the most commonly inherited maculopathy affecting an estimated 1 in 10,000 individuals globally (Blacharski, 1988). It is a monogenic disease caused by biallelic mutations in the *ATP-binding Cassette Subfamily A Member 4 gene* (*ABCA4)* gene (Allikmets *et al.*, 1997b). Akin to other IRDs, STGD1 displays a high degree of allelic and phenotypic heterogeneity which impacts the age of onset, disease penetrance, rates of progression and ultimate extent of vision loss. Importantly, these variations correlate with the severity of mutation in *ABCA4* (van Driel *et al.*, 1998a).

1.2.1 Clinical Presentation and Diagnosis of STGD1

"Classic" STGD1 is described as a juvenile maculopathy which becomes apparent within the first two decades of life. German ophthalmologist Karl Stargardt first described the disorder in 1901 after identifying specific phenotypes in two families with macular degeneration (Stargardt, 1909). As a macular condition, bilateral central vision is mostly affected. Initial symptoms include decreased visual acuity, defects with chromatic vision and photophobia, which cannot be aided by corrective eyewear (Rotenstreich, Fishman and Anderson, 2003). Despite continued progression of central vision loss over time, peripheral vision tends to be completely spared in STGD1.

Initial fundus examinations may not reveal any visible defect in STGD1 retinas. The presence of irregularly shaped yellow-white flecks around the fundus is a key indicator of disease and signifies early lipofuscin accumulation **(Figure 1.8).** Occasionally, mild retinal abnormalities are detected – such as RPE depigmentation overlying the macula, or loss of foveal reflexes (Lambertus *et al.*, 2015). However, the lack of obvious disease phenotypes at early stages often leads to a delay in diagnosis of STGD1. In general, STGD1 is diagnosed based on the presence of three key phenotypic indicators - macular affection, presence of fundus flecks and peripapillary sparing (Cremers *et al.*, 2020).

These phenotypes can be observed using non-invasive imaging platforms such as fundus autofluorescence (FAF) imaging combined with spectral-domain optical coherence tomography (SD-OCT). FAF imaging is particularly useful for the identification of abnormal lipofuscin accumulation and RPE atrophy (Schmitz-Valckenberg *et al.*, 2021), which are common features of STGD1. This technology is also useful for the continued monitoring of STDG1 progression in affected individuals. SD-OCT provides a cross-section of the retina to

visualise the overarching structure of the retina and its layers, in addition to the anterior segment of the eye (Yaqoob, Wu and Yang, 2005). This gives ophthalmologists greater insights into any structural retinal defects that may be present in individuals with STGD1.

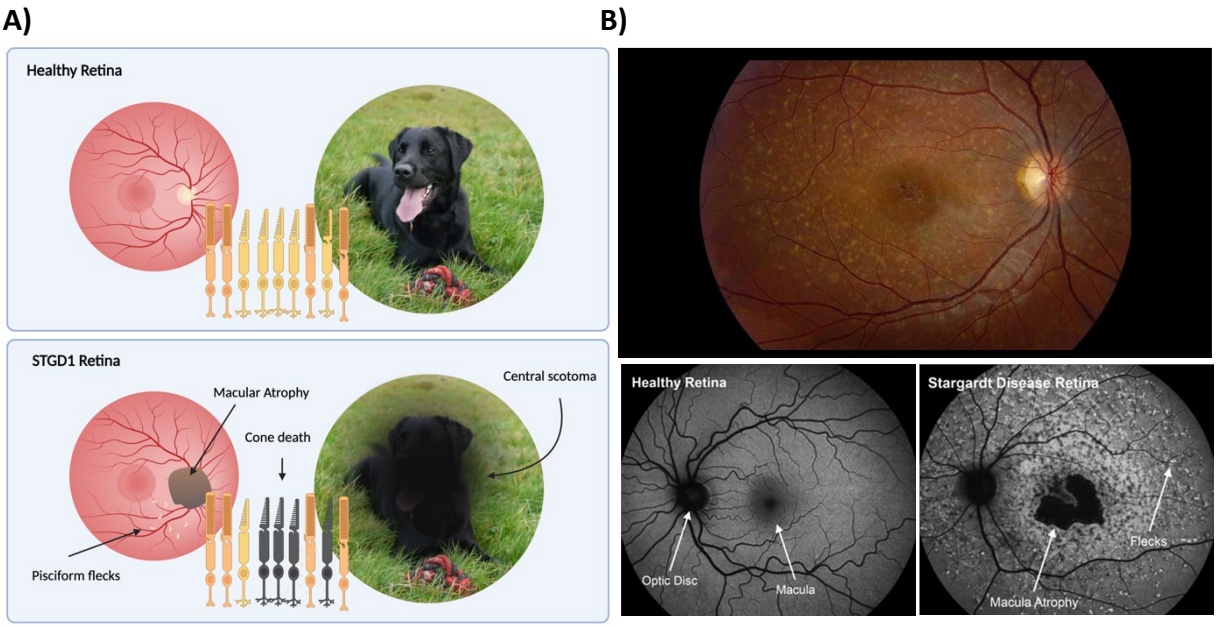

Figure 1.8 Classic Phenotypes of STGD1.

A) STGD1 retinas often display characteristic macular atrophy which causes death of central cone photoreceptors. The is due to the build-up of lipofuscin in the retina (which can be seen as pisciform flecks by fundus imaging). Death of cone photoreceptors in the macula results in central vision loss. These scotomas prevent affected individuals from recognising family members, reading books, driving etc, demonstrating the debilitating nature of this condition. **B)** Top panel is a fundus image from a patient with classic STGD1 symptoms, with pisciform lipofuscin accumulation around the macula, extending to peripheral retina. Lower panels are fundus autofluorescent (FAF) images comparing images of healthy and STGD1 retina. Photosensitive properties of lipofuscin are apparent with this method. Hyperfluorescent lipofuscin flecks are seen surround the retina. A decreased signal over the macular region is indicative of tissue atrophy.

Lipofuscin is a metabolic waste product comprised of undigested lipids and proteins that naturally accumulate in RPE cells as a result of daily photoreceptor turnover and oxidative stress. It has autofluorescent properties under specific wavelengths of light (mainly 488nm; blue/short-wave) - a characteristic which is exploited by FAF imaging to gain insights into retinal health in affected individuals (Schmitz-Valckenberg *et al.*, 2008). Areas with normal RPE function typically display a background level of autofluorescence, while regions with lipofuscin accumulation may appear as brighter spots or speckles. In STGD1, FAF reveals characteristic autofluorescent flecks or granules in the macula or extending far across the posterior pole in more advanced stages (Cideciyan *et al.*, 2015; Chen *et al.*, 2019). Regions with reduced autofluorescence suggest a loss of photoreceptors, while the absence of autofluorescence signifies the complete loss of RPE (Lois *et al.*, 2004). Flecks and the sparing of the peripapillary region are frequently observed (Cukras *et al.*, 2012) and represent specific features, although they may not be present in all cases, such as late-onset STGD1 cases (Runhart *et al.*, 2019).

Evidently, FAF is a highly valuable technique in the diagnosis and monitoring of STGD1, demonstrating significant advantages over standard fundus imaging. However, the earliest indications of STGD1 may be more effectively identified using SD-OCT. Thickening of the external limiting membrane (ELM) has been observed in STGD1 patients via SD-OCT and has been attributed to gliosis of Müller glial cells in response to stress elicited by ABCA4-deficiency in photoreceptor cells (Lee *et al.*, 2014). Furthermore, ELM thickening has also been observed in a patient with biallelic pathogenic *ABCA4* variants presenting with no visual deficits and normal fundus (Burke *et al.*, 2013). In addition to this, the ellipsoid zone, a band associated with photoreceptor cells, shows features of regression prior to RPE cells on SD-OCT (Ergun *et al.*, 2005). This demonstrates the fidelity of SD-OCT in the early diagnosis of STGD1, which will undoubtedly play a considerable role in the treatment of this disease in the future.

As STGD1 advances over time, flecks and atrophy gradually spread outward from the vascular arcades. Depending on the severity of disease, which correlates with age of onset, prognoses of ABCA4 disease differs significantly. Early-onset cases generally have a poorer prognosis where pan-retinal degeneration is often observed towards end stage of the disease. This is characterised by unrecordable responses from cone and rod cells using full-field electroretinogram (ffERG), extensive chorioretinal atrophy and pigmentary changes resembling RP (Cremers *et al.*, 2020).

A matrix has been devised to classify the variable prognostic outcomes of ABCA4-mediated retinal disease (Lee *et al.*, 2021). This study used a pool of 112 unrelated patients ≥50 years of age with biallelic resolution for pathogenic *ABCA4* variants causative of disease **(Figure 1.9).**

Prognosis 1 represents the mildest disease outcome of *ABCA4* mutation and is defined as discrete foveal/parafoveal atrophy and the absence of pisciform flecks. Central scotomas are present but often sized <10° and relatively good retention of vision is observed with normal ffERG responses in cone and rod photoreceptors. Prognosis 2 correlates with more progressed disease phenotypes but in individuals with a later onset of disease symptoms overall. This is often due to the phenomenon of foveal sparing (Runhart *et al.*, 2019). Advanced chorioretinal atrophy is observed but confined to the macula and pisciform flecks are apparent beyond the vascular arcades. Central scotoma size varies between 10° - 15° and ffERG responses vary between normal vision and attenuated cone responses. Prognosis 3 defines the "classic" form of STGD1 where age of onset is typically young but can vary dramatically. It is characterised by multifocal regions of chorioretinal atrophy and highly confluent flecks widespread throughout the retina. Scotoma size varies between 10° - 20° with ffERG responses between normal and attenuated cone responses depending on the degree of macular atrophy. Prognosis 1 through 3 correspond to individuals with the highest Best-corrected visual acuities (BCVA) owing to the sparing of peripheral retinal tissue. Prognosis 4 represents the worst possible outcome of ABCA4-disease. These cases tend to present very early in childhood and progress rapidly. Phenotypically, large atrophic regions extending past the macula are observed in these cases. Atrophic regions often coalesce across the entire posterior pole. Scotoma size is >20° and ffERGs display attenuated responses from cone and rod photoreceptor cells.

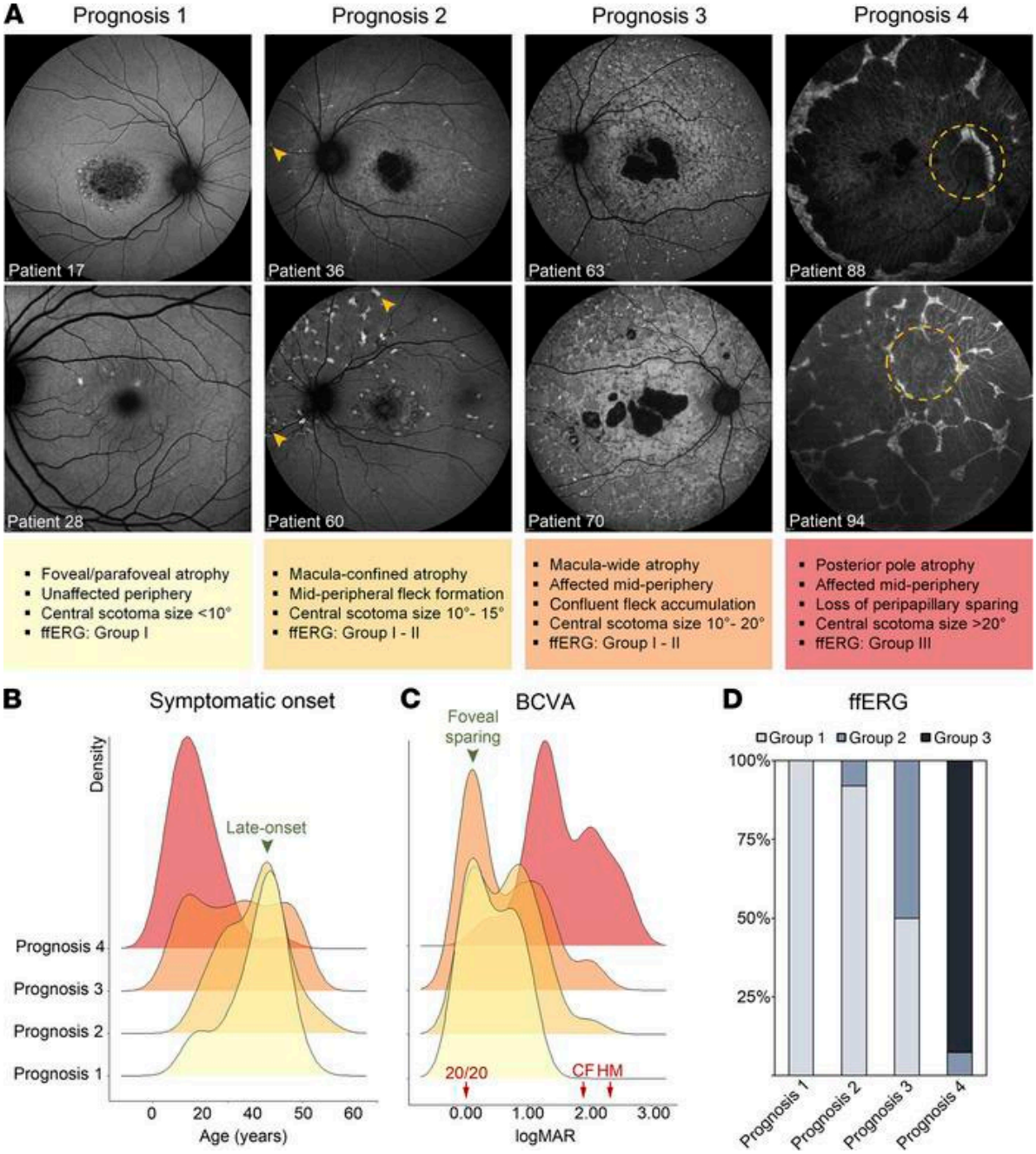

Figure 1.9 Four prognostic outcomes of mutated ABCA4.

In 112 patients aged 50 years or older with ABCA4 disease, four distinct prognostic outcomes were observed based on observable spatial disease progression features during their most recent visit. (A) Representative autofluorescence images and clinical descriptions illustrate each prognosis category. Prognosis 2 displays extramacular flecks (indicated by yellow arrowheads), with the optic nerve position outlined by a dotted yellow line. Autofluorescence image fields of view are 55° except for P28 (30°). (B) Ridgeline plots show the ages at which visual symptoms first appeared in patients across each prognosis category. (C) Density plots present the best-corrected visual acuity (BCVA) of the least-affected eye for all patients, including Snellen equivalents (20/20, counting fingers [CF], and hand motion [HM], denoted by red arrows). (D) The proportion of ffERG groupings is displayed for each prognosis category. Group 1 indicates normal responses, group 2 signifies cone response attenuation, and group 3 implies attenuation of both cone and rod responses. BCVAs are presented in logMAR units.

Figure source: Lee *et al.* (2021)

1.2.2 Pathophysiology

Often referred to as the rim protein, ABCA4 is most dominantly expressed in both rod and cone photoreceptor outer segments of the retina (Weng *et al.*, 1999; Sun, Molday and Nathans, 1999; Molday, Rabin and Molday, 2000). As previously discussed in **Section 1.1.4,** it serves as a flippase within the visual cycle, playing a critical role in the transportation of NRPE molecules from the inner leaflet of the POS disc membrane. This transportation is essential for these molecules to access cytoplasmic enzymes required for the regeneration of 11-*cis*-retinal from all-*trans*-retinal. ABCA4 is also expressed in RPE cells where it likely also plays a role in retinaldehyde recycling and could further contribute to STGD1 pathology (Lenis *et al.*, 2018)

The classical hypothesis for STGD1 pathology suggests that photoreceptor degeneration occurs secondarily to RPE cell loss **(Figure 1.10).** It is attributed to inefficient clearance of NRPE molecules from the POS, which results in the phagocytosis of diretinoid-pyridinium-phosphatidylethanolamine (A2PE)-laden POS discs and subsequent lipofuscin generation within the RPE cells. This outcome is directly associated with *ABCA4* mutations, which diminish or completely disrupt the protein's overall function. Consequently, an accumulation of NRPE molecules takes place within the inner disc membrane due to the ongoing turnover of retinal molecules following phototransduction. This accumulation facilitates the dimerisation of all-*trans*-retinal groups within NRPE complexes, ultimately forming A2PE (Quazi, Lenevich and Molday, 2012)

POSs are naturally shed during the daily maintenance of photoreceptor cells and are subsequently phagocytosed by neighbouring RPE cells. In the context of ABCA4-disease, the acidic environment of the phagolysosome in the RPE causes hydrolysis of A2PE to the highly toxic metabolite A2E, after which no further metabolic degradation can occur. This results in the accumulation of A2E (Sparrow *et al.*, 2003; Sparrow *et al.*, 2010; Sparrow *et al.*, 2012)

A2E is a frequently identified component of the characteristic lipofuscin deposits observed in patients with STGD1 (Rozet *et al.*, 1998). Several *in vitro* studies have reported the toxic effects of A2E on the RPE including decreased lysosomal function, inhibition of cytochrome c oxygenase and mediation of further light-induced damage due to the inherent photosensitising abilities of the molecule (Iriyama *et al.*, 2008). Whilst the presence of lipofuscin in the retina is typically associated with normal ageing tissue, in cases of *ABCA4*-

mediated retinopathies, premature and excessive lipofuscin deposits cause significant cellular stress. This results in the apoptosis of RPE cells and consequential atrophy of the overlying photoreceptor cells in the macula. The fovea tends to be the most affected region of the retina due to the high density of cone photoreceptors. As the tissue continues to atrophy over time, an overall loss of central vision occurs (Molday, Zhong and Quazi, 2009; Molday, 2007).

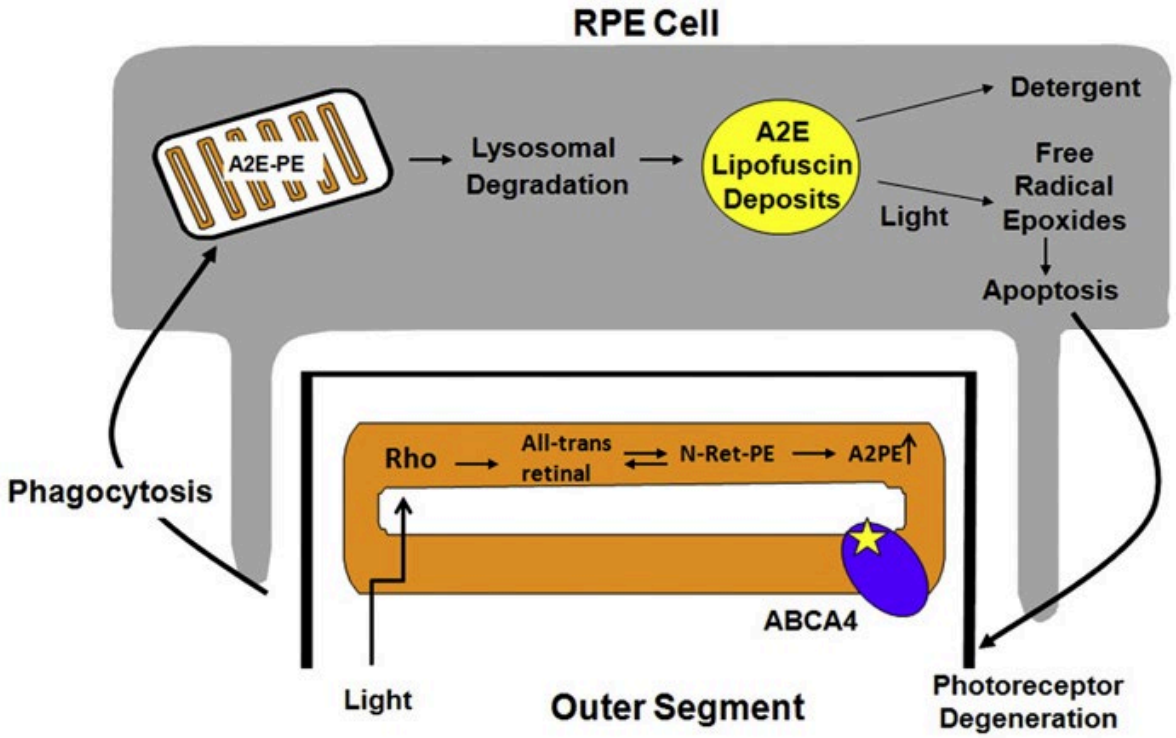

Figure 1.10 Dysfunctional ABCA4 causes A2E Lipofuscin deposits.

ABCA4 plays a crucial role in relocating luminally-oriented NRPE from the inner leaflet to the cytoplasmic side of the outer segment. Mutations in *ABCA4* reduce its ability to perform this function, leading to the build-up of NRPE within the outer segment lumen. This accumulation allows for the secondary formation of toxic bisretinoids. These harmful compounds are absorbed by the RPE during the phagocytosis of diurnally-shed outer segments. Within the RPE phagolysosome, bisretinoids cannot be metabolised and start accumulating, resulting in the formation of lipofuscin. These deposits are detrimental to the RPE, causing cellular stress and eventual apoptosis. Consequently, this leads to the compromise and degeneration of the photoreceptor cells that overlay the RPE.

Figure source: Molday (2007)

1.2.3 Genetics of ABCA4

ABCA4 is a 128-kb transcript which boasts an expansive and ever-growing list of genetic variation. >1,000 pathogenic/likely-pathogenic mutations have thus far been reported in both coding and non-coding regions of the gene. In addition to this, there is a large degree of polymorphism in the gene with an overall carrier incidence of 5% in the general population (Maugeri *et al.*, 1999a; Jaakson *et al.*, 2003; Cornelis *et al.*, 2017) such that it is a rare occurrence for anyone to be homozygous for the consensus sequence of *ABCA4.* This highlights a major issue of allelic heterogeneity for STGD1 which can complicate genetic diagnoses of STDG1 (Webster *et al.*, 2001).

The matter is further complexed with the implication of *ABCA4* in other retinopathies, such as cone-rod dystrophy (CRD), RP and age-related macular degeneration (AMD). This phenotypic heterogeneity is somewhat explained by a genotype-phenotype correlation model (van Driel *et al.*, 1998b) **(Figure 1.11).** According to this model, an individual with two severe disease alleles in *ABCA4* will result in a significantly enhanced disease phenotype like RP and CRD. Those who carry milder mutations tend to exhibit symptoms much later in life and are more akin to AMD. Classical STGD1 criteria lie in the middle of these extremes with combinations of either two moderately severe mutations or a mild and severe mutation in *ABCA4*, resulting in overall reduced function of the protein but not complete loss of function in both alleles (Cremers *et al.*, 1998; Martínez-Mir *et al.*, 1998). However, this model does not account for the phenotypic heterogeneity observed within families with similar *ABCA4* mutations and related genetic composition which suggests that the resulting phenotype could further be influenced by external environmental factors and genetic modifiers (Burke *et al.*, 2012; Michaelides *et al.*, 2007; Runhart *et al.*, 2019; Lee *et al.*, 2021).

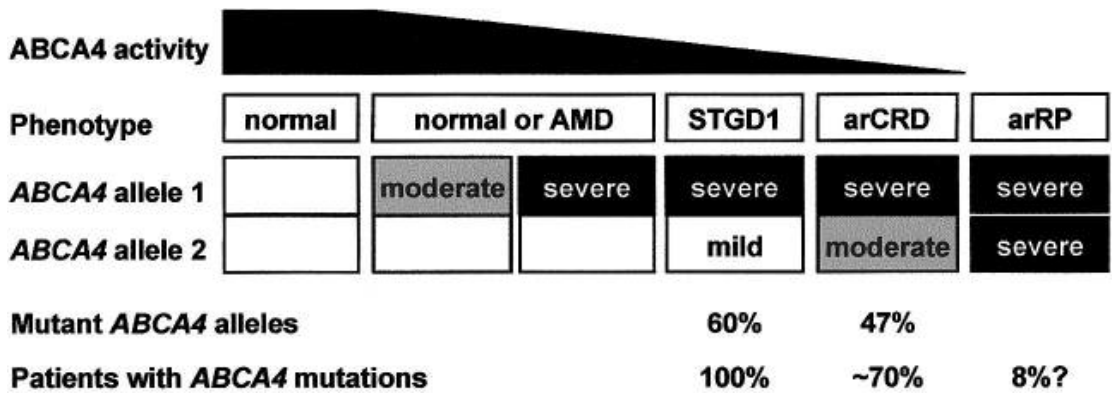

Figure 1.11 Genotype-Phenotype Correlation Matrix.

This model delineates an inverse connection between the remaining function of ABCA4 protein and the severity of the associated disease. More severe retinal conditions like RP and CRD are linked to a substantial reduction in ABCA4 function. In contrast, STGD1 phenotypes result from a significant but less severe decline in protein function, allowing for the preservation of central vision while preventing peripheral vision loss. AMD represents the mildest phenotype among ABCA4-related retinopathies and has a later onset of development, primarily due to the minimal impact on ABCA4 function.

Figure source: van Driel *et al.* (1998a).

At present, obtaining a genetic diagnosis for STGD1 is relatively straightforward in identifying biallelic pathogenic mutations in the coding regions of *ABCA4*. With the use of cost-effective target panel capture systems with NGS (Zernant *et al.*, 2011) and the development of single molecule molecular inversion probes (smMIPs) for WGS of *ABCA4 (Khan et al., 2019)*, the solve rate has stabilised for STGD1 diagnosis at ~95%, if including monoallelic cases with strong phenotypic indicators of STGD1 (Cremers *et al.*, 2020).

However, ~15-20% of all STGD1 cases remain unsolved with just one or no pathogenic *ABCA4* mutations identified, despite strong clinical indicators of STGD1. It was originally hypothesised that late-onset STGD1 cases were intrinsically monoallelic, however this was disproven with the realisation of the common allele c.5603A>T functioning as a hypomorphic variant, only penetrant when *in trans* with a null allele (Zernant *et al.*, 2017). Another source of missing variation in these cases proved to be in the non-coding regions of *ABCA4* resulting in pathogenic RNA defects (Runhart *et al.*, 2018; Sangermano *et al.*, 2019). Could the remaining 5% of unresolved cases also harbour hypomorphic alleles or RNA defects pertinent to ABCA4-pathology?

An updated genotype-phenotype correlation matrix has been recently published to account for the more variable phenotypes observed in ABCA4-mediated retinopathy and reflects the advancements made in molecular diagnostics, linking mutational severity with prognostic outcomes, as illustrated in **Section 1.2.1** (Lee *et al.*, 2021) **(Figure 1.12).**

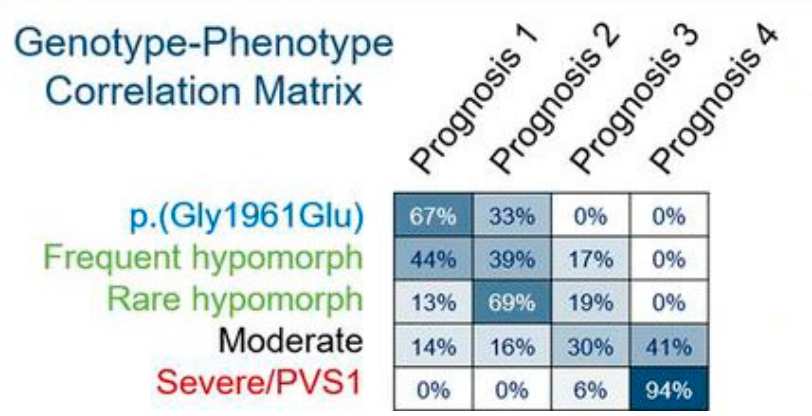

Figure 1.12 Updated genotype-phenotype correlation matrix.

Following from the previous model described by van Driel (1998), an updated model has been generated to reflect the advancements made in ABCA4 disease over the last 20+ years. The model now includes the hypomorphic variants, and other mutations that always display the same clinical phenotype (p.Gly1961Glu = bullseye maculopathy phenotype). This figure links in with Prognoses 1-4 in **Figure 1.9**.

Figure source: Lee *et al.* (2021).

1.2.4 Existing models of STGD1

Animal models:

The most widely used *in vivo* model for STGD1 is the *ABCA4* knockout mouse. This model has provided valuable insights into the role of ABCA4 in the visual cycle, and how it contributes to STGD1 pathology when mutated. In the absence of ABCA4, this model demonstrated increased deposition of A2E and other lipofuscin fluorophores in RPE cells - potentiating a link between ABCA4 and the transport of NRPE across the POS disc membrane (Weng *et al.*, 1999; Charbel Issa *et al.*, 2013). Lipofuscin flecks could be observed by FAF imaging and delayed dark adaptation was also present in the model, akin to human phenotypes. Interestingly, the ABCA4 knockout model was also able to demonstrate increased all-*trans*-retinaldehyde and accumulated NRPE following UV light exposure (Weng *et al.*, 1999) and Vitamin A supplementation (Radu *et al.*, 2008). This led to the provision of STGD1 individuals with UV-blocking sunglasses and avoiding diets rich in Vitamin A (Tanna *et al.*, 2017). Evidently, this model has taught us a lot of what we know so far in STGD1 disease pathogenesis. However, like any model, the ABCA4 knockout model has limitations, such as the absence of a macula (the primary affected retinal region in STGD1), in addition to an overall slower disease progression which could be due attributed to the short life span of mice. Taken together, these limitations can affect the translation of these findings to human.

Other animal models have been investigated which could better recapitulate human STGD1 pathology, such as the pig model (Trapani *et al.*, 2019) which shares many biological similarities with regard to retinal structure. However, little information has been published thus far on the characterisation of this model. A naturally occurring STGD1 canine model has also been reported (Mäkeläinen *et al.*, 2019), but again, limited information is available on its utility for studying STGD1.

Cell models:

Photoreceptor precursor cells (PPCs) derived from pluripotent stem cells (PSCs) have proven valuable for modelling STGD1 at the transcript level and for evaluating putative splicing variant candidates *in vitro* (Sangermano *et al.*, 2016; Albert *et al.*, 2018). They have also served as a platform to test antisense oligonucleotides (AONs) as a therapeutic to correct *ABCA4* splicing defects. Since ABCA4 is uniquely expressed in the retina, these models offer the opportunity to investigate the gene's splicing patterns within its native genomic context. This extends to

PSC-derived ROs which not only exhibit ABCA4 expression at both the transcriptomic and protein levels but also provide a platform for studying STGD1-related processes (Kaltak *et al.*, 2023b; Kaltak *et al.*, 2023a)

However, it is important to note that these cell models do not manifest phenotypic defects analogous to those observed in humans, possibly due to a lack of comprehensive characterisation across the developmental timeline of these differentiated cell models or inherent limitations to the models themselves.

In contrast, PSC-derived RPE models of ABCA4 deficiency have undergone more thorough characterisation throughout their development. These models have displayed intracellular autofluorescence-lipofuscin accumulation and heightened complement C3 activity. Consequently, this has led to the deposition of the membrane attack complex (MAC) on the surfaces of RPE cells and a decline in trans-epithelial electrical resistance (TEER) scores, indicative of compromised barrier function in RPE cells, ultimately culminating in RPE cell death (Ng *et al.*, 2022). Another study using PSC-RPE deficient in ABCA4 exhibits autonomous lipid deposits and impaired POS digestion due to disruptions in lysosomal function. This underscores the potential contribution of defective ABCA4 in the RPE to the pathogenesis of STGD1, even in the absence of POS laden with A2E (Farnoodian *et al.*, 2022).

1.2.5 Treatment Strategies

STGD1 is evidently an extremely debilitating disease which renders people legally blind at a relatively young age. This maculopathy significantly reduces the quality of life for affected individuals, who lose their ability to perform everyday tasks like reading, writing, watching TV, driving and recognising faces. Unfortunately, to date there is still no effective cure for STGD1. However, all hope is not lost as numerous therapies are under consideration for this condition. These therapies fall under the categories of gene therapy, cell-replacement therapy and compound administration therapy.

Gene Therapy:

Gene replacement therapy is designed to preserve viable photoreceptors, and ideally halt or slow the progression of retinal degeneration. It is imperative for early intervention for the promise of optimal outcomes. This is where the importance of genetic diagnoses comes into play. This strategy has shown success for RPE65-mediated retinal degeneration by delivering functional copies of *RPE65* to dysfunctional cells of individuals with Lebers Congenital Amaurosis (LCA) and RP (Press Release | FDA, 2018).

AAVs are often the preferred viral vector for delivery of replacement genes but due to limited cargo size, they are not suitable for *ABCA4* gene delivery. This 128-kb gene exceeds the capacity of AAV vectors and has represented a limitation for gene therapy strategies for STGD1. An alternative vector to use is lentiviruses which have the cargo capacity to match the size of *ABCA4*. Already in pre-clinical trials, they have shown reduced levels of lipofuscin accumulation in murine models of ABCA4 disease (Kong *et al.*, 2008). Recent reports of a Phase I/II clinical trial investigating lentiviral delivery of *ABCA4* cDNA (SAR422459 – EIAV-ABCA4) in patients with STGD1 have been published and reported that the treatment was well tolerated and safe (Parker *et al.*, 2022). However, this trial has since been terminated with no exact reason known.

Cell replacement therapy

hESC-derived RPE holds significant promise in the field of regenerative medicine, especially for treating maculopathies characterised by RPE atrophy. In a prospective clinical trial aimed at assessing safety and tolerance, a mixed population of 9 patients with STGD1 and 9 with advanced AMD, received subretinal injections of hESC-derived RPE sheets which successfully integrated into the host RPE without any signs of rejection during a four-month monitoring

period. Concerns about potential tumorigenicity when introducing hPSC-derived tissues into the host were dispelled as no hyperproliferation was observed in the treated patients (Schwartz *et al.*, 2012). Subsequent dose-escalation studies involving nine individuals further supported the safety of this approach, with an apparent improvement in BCVA in the treated eyes compared to the contralateral eye. Adverse events were primarily associated with vitreoretinal surgery and immunosuppression, rather than the hESC-RPE product itself (Schwartz *et al.*, 2015).

These findings suggest that transplanting hESC-derived RPE could be a viable treatment option for this disease. However, as ABCA4 is predominantly expressed in photoreceptors, this raises questions about the long-term effectiveness of replacing atrophic RPE tissue, as lipofuscin accumulation could still occur in the regenerated tissue. Yet, if ABCA4-mediated pathology is also linked to mutational defects in the RPE tissue, as proposed by Farnoodian *et al.* (2022), this therapeutic approach may indeed yield beneficial outcomes. A comprehensive understanding of the exact ABCA4 pathomechanism in human would substantially aid with the development of future therapeutics.

Compound administration therapy

An alternative to the previous two approaches is the use of various compounds to target physiological or pathological pathways. A variety of compounds have been tested in human patients and have shown limited promise. Saffron and docohexaenoic acid (DHA) were administered orally but did not show significant short-term visual improvement (Piccardi *et al.*, 2019; MacDonald and Sieving, 2018). 4-methylpyrazole (4-MP) and ALK-001 aimed to prevent lipofuscin formation, but results for 4-MP are unpublished, while ALK-001 has been shown to slow the growth rate of atrophic lesions, however no improvement in BCVA was noted (Scholl *et al.*, 2022). Despite this, Alkeus Pharmaceuticals plans to launch a new drug application for ALK-001 (gildeuretinol) in 2024 following their successful fundraising of $150 million (Press Release | Alkeus Pharmaceuticals Inc, 2023). Overall, these compounds appear safe but have not demonstrated strong therapeutic effects. Further research is needed to optimise delivery routes, concentrations, and treatment regimens for potential benefits.

1.3 Pluripotent Stem Cells (PSCs)

PSCs are a unique, unspecialised, cell type that intrinsically possesses the capability to differentiate into any cell of the three embryonic germ layers: endoderm (e.g., digestive system, respiratory system), mesoderm (e.g., muscle, bone, and blood cells), and ectoderm (e.g., neurons, skin cells). Recently, these cells have also been shown to be capable of differentiation to trophectodermal lineage (e.g. placenta) (Mischler *et al.*, 2021). They are capable of self-renewal ensuring an enduring source of identical daughter pluripotent cells that retain genetic stability and the expression of specific pluripotency markers like OCT4, NANOG, and SOX2. Further to this, these cells can be cultured for indefinite periods of time *in vitro*. PSCs are typically subcategorised into embryonic stem cells (ESCs) and induced pluripotent stem cells (iPSCs). Whilst derived through different means, these ESCs and iPSCs overlap in transcriptomic and epigenetic profiles (Zakrzewski *et al.*, 2019).

Due to their pluripotent nature, these cells form teratomas when transplanted into appropriate hosts, validating their capacity to differentiate into numerous different cell types. ESCs are derived from the inner cell mass (ICM) of blastocysts, whilst iPSCs can be derived by reprogramming differentiated somatic cells. Both types of PSCs represent a powerful tool for personalised medicine and disease modelling. Their adaptability in culture, immune privilege (particularly for ESCs), and capacity for genetic manipulation make PSCs indispensable for elucidating developmental processes, investigating disease mechanisms, and exploring the frontiers of regenerative medicine (Puri and Nagy, 2012) **(Figure 1.13).**

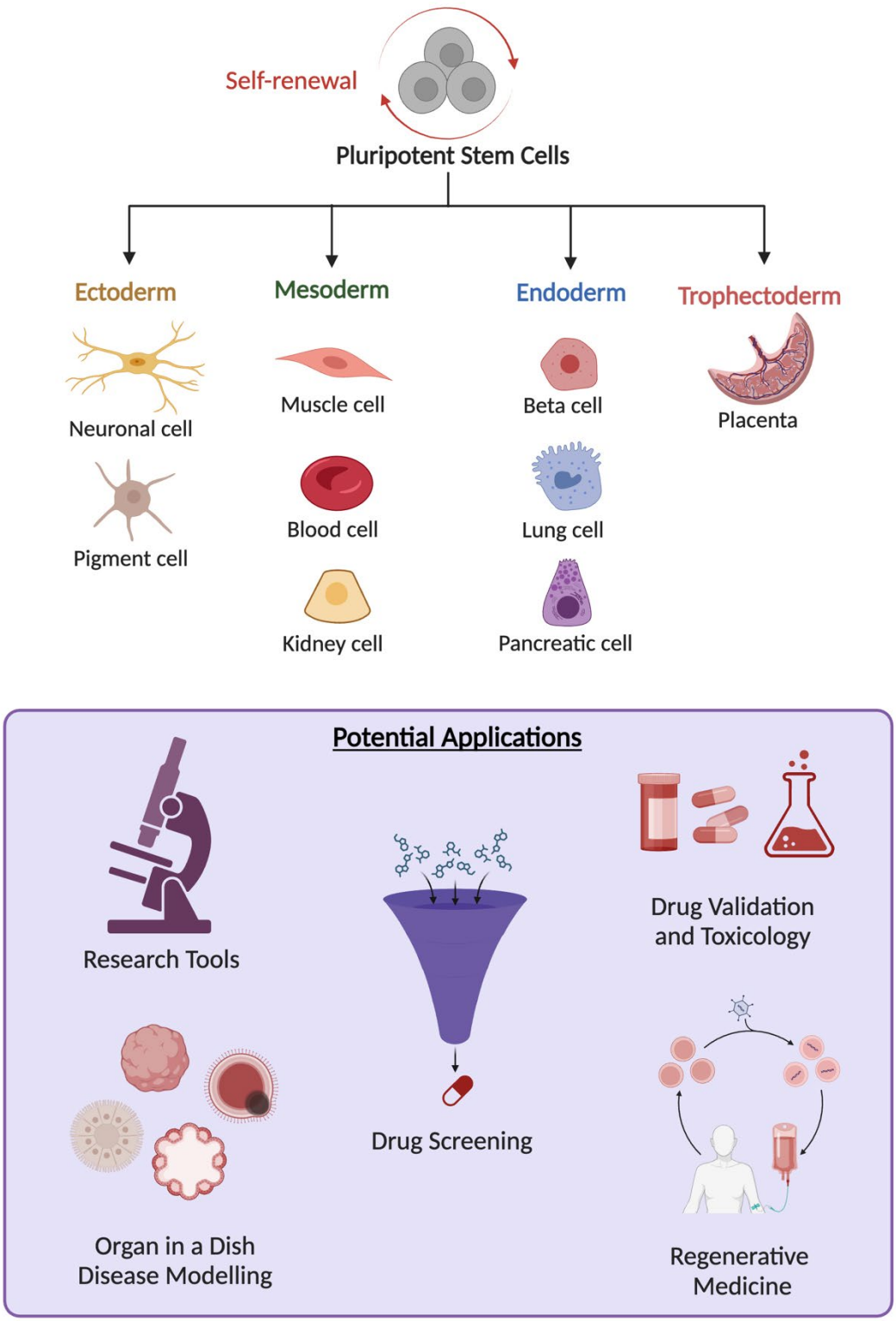

Figure 1.13 Characteristics of PSCs and their potential applications.

PSCs possess the remarkable ability to self-renew, ensuring their sustained propagation, while also displaying pluripotency by differentiating into cell types from all three germ layers —ectoderm, mesoderm, endoderm, in addition to those of trophectodermal lineage. These characteristics make PSCs invaluable research tools. They serve as the foundation for creating "organs in a dish" or organoids, offering insights into disease mechanisms, drug responses, and tissue development. PSCs are instrumental in high-throughput drug screening, validating drug candidates, and assessing toxicity, reducing the need for animal models. Additionally, they hold immense promise for regenerative medicine, as they can be guided to become patient-specific cell types, offering potential treatments for degenerative diseases and injuries. PSCs have revolutionised biomedical research and continue to drive advancements in various fields.

1.3.1 Discovery of Embryonic Stem Cells

The discovery of stem cells began in the 1950s, with the finding that a particular inbred strain of laboratory mice (129 family) had a predisposition for the development of testicular cancer. In 1% of the mice, they developed an aggressive form of germ cell tumour called a teratoma. Teratomas are typically made up of various tissue/cell types that are not typically found in the location of origin. They can contain any tissues that arise from the three germ layers of an embryo including hair, nails, teeth, fat, skin, muscle etc. (Stevens and Little, 1954). The so-called embryonic carcinoma (EC) cells derived from the tumour could be propagated and cultured *in vitro*. Subsequently, it was shown that the injection of just a single EC cell into a donor mouse facilitated the development of another teratoma *in vivo*.

It was hypothesised that these cells were PSCs that could self-renew and generate a vast number of different cell types (Pierce and Dixon, 1959). It wasn't until the 1980s that the true link between EC cells and ESCs was made. It was observed that teratoma formation could be recapitulated via the transplantation of early post-implantation mouse embryos into adult mice at stages prior to neurulation (Damjanov and Solter, 1974). The race to find these pluripotent cells within the embryo was on.

Traditional stem cells are derived from the ICM of an embryonic blastocyst at the pre-implantation stage between 3-5 days old **(Figure 1.14).** Mouse ESCs (mESCs) were first derived in 1981 (Evans and Kaufman, 1981; Martin, 1981), representing a major breakthrough in human disease modelling. As a result, this was a partial Nobel prize winning feat that was awarded in 2007 to Sir Martin J. Evans, Mario R. Cappechi and Oliver Smithies for their combined efforts in the field of ESC and mouse genetics research.

It wasn't until 1998 that the first human ESCs were isolated, thanks to James Thomson, who defined his own culture medium and generated protocols for the *in vitro* culturing of hESCs. Thomson's method involved culturing blastocyst cells on mitotically inactivated mouse embryonic fibroblasts, supplemented with foetal calf serum (Thomson *et al.*, 1998). However, later hESC culture was adapted to feeder-free conditions (Ludwig *et al.*, 2006). In a significantly understated conclusion, Thomson wrote, "These cell lines should be useful in human developmental biology, drug discovery and transplantation medicine".

Despite the potential to revolutionise the way scientific research was conducted, this pioneering technology stirred significant controversy and ethical concerns, mainly due to the need for early-stage embryo destruction to obtain ESCs. To address these ethical concerns and circumvent restrictions, researchers have sought alternative approaches. One such approach is the development of induced pluripotent stem cells (iPSCs).

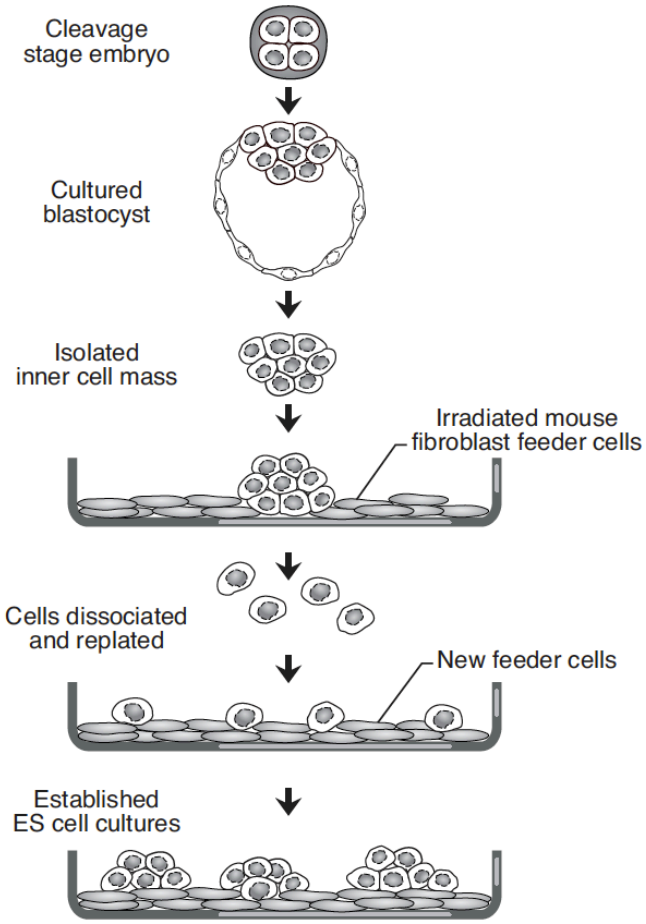

Figure 1.14 Derivation of ESCs.

Embryos developed via *in vitro* fertilisation are cultured to blastocyst stage. At this point, ESCs are surgically removed from the ICM of the embryo. These cells are then cultured *in vitro* on mitotically inactive mouse embryonic fibroblasts. Through continuous culturing, ESC lines are established and can grow for an indefinite period.

Figure adapted from Sullivan *et al.* (2007)

1.3.2 The generation of induced pluripotent stem cells

The ground-breaking discovery of iPSCs by Shinya Yamanaka in 2006 has fundamentally altered the landscape of stem cell research, opening unprecedented opportunities in disease modelling, drug screening and regenerative medicine (Takahashi and Yamanaka, 2006). Building from the work of stem cell biologists before him, Yamanaka was motivated to devise a method for reprogramming mature, differentiated adult cells into PSCs, similar to ESCs, while circumventing the ethical complexities associated with embryonic sources.

With iPSC technology, adult somatic cells undergo cellular reprogramming via the expression of a defined set of transcription factors characteristic of ESCs. This resets the cell's epigenetic and transcriptional signatures, reverting the cell to a pluripotent state. These iPSCs behave similarly to ESCs such that they can differentiate into any cell type or tissue specified, whilst eliminating any previous ethical concerns with the generation of hESCs.

The seminal discovery of iPSCs occurred first in 2006 with mice (Takahashi and Yamanaka, 2006) and later in 2007, with humans (Takahashi *et al.*, 2007). Initially exploring an extensive list of candidate genes with potential pluripotency-inducing properties, Yamanaka and his team encountered limited success. However, a pivotal turning point emerged with the identification of a specific quartet of transcription factors: Oct3/4, Sox2, Klf4, and c-Myc (OSKM). Through the introduction of these factors into adult mouse fibroblast cells via retroviruses, Yamanaka's team remarkably observed the emergence of iPSCs possessing pluripotent characteristics akin to ESCs. Subsequent validation, characterisation, and refinement of the reprogramming process further solidified the potential of iPSCs. This landmark discovery not only revolutionised stem cell research but also unlocked new avenues for regenerative medicine, disease modelling, and personalised therapeutic approaches.

Shinya Yamanaka was honoured with the Nobel Prize in Physiology or Medicine in 2012, alongside John B. Gurdon, acknowledging their seminal contributions to cellular reprogramming and pluripotent stem cell science (The Nobel Assembly at Karolinska Institutet, 2012).

Several different platforms for cellular reprogramming exist today, each with their own advantages and disadvantages as outlined in **Table 1.1** (Rao and Malik, 2012).

Method	Integration	Duration (Days)	Efficiency (%)	Advantages	Disadvantages
Retroviral (Takahashi and Yamanaka, 2006; Takahashi *et al.*, 2007)	Yes	25–35	0.02–0.08	• Good efficiency • Easy strategy • Multiple cell types	• Retained genetic footprint
Lentiviral (Sommer *et al.*, 2009)	Yes	20–30	0.02–1	• Good efficiency • Easy strategy • Multiple cell types	• Retained genetic footprint
Lentiviral (miRNA) (Anokye-Danso *et al.*, 2011)	No	18–26	10.4–11.6	• High efficiency • Short time frame	• Retained genetic footprint • Only validated in one cell type
miRNA (direct transfection) (Fan *et al.*, 2020)	No	20	0.002	• Zero genetic footprint • Short time frame	• Low efficiency • Only validated in one cell type
Adenoviral (Zhou and Freed, 2009)	No	25–30	0.0002	• Zero genetic footprint	• Low efficiency • Only validated in one cell type • Technically challenging
Sendai virus (Ban *et al.*, 2011; Chichagova *et al.*, 2016)	No	25	0.5–1.4	• Zero genetic footprint • High efficiency • Multiple cell types • Kits are commercially available	• Expensive commercially • Technically challenging to make in-house • Potential licencing/patent issues

mRNA (Warren *et al.*, 2010)	No	20	0.6–4.4	• Zero genetic footprint • High efficiency • Short time frame • Multiple cell types • Kits are commercially available	• Expensive commercially • Technically challenging to make in-house • Labour intensive • Only validated in one cell type
Protein (Cho *et al.*, 2010)	No	56	0.001	• Zero genetic footprint	• Low efficiency • Technically challenging • Long time frame • Only validated in one cell type
Episomal (Okita *et al.*, 2011)	No	30	0.0006–0.02	• Zero genetic footprint • Mostly good efficiency • Multiple cell types	• Low efficiency in some cell types
PiggyBac (Woltjen *et al.*, 2009)	Yes	14–28	0.02–0.05	• Zero genetic footprint • Good efficiency • Short time frame	• Only validated in one cell type • No confirmation of transposon excision • Potential licencing/patent issues
Minicircles (Jia *et al.*, 2010)	Non-Integrative	14–16	0.005	• Zero genetic footprint	• Low efficiency • Only validated in one cell type

Table 1.1 Overview of Reprogramming Methods

Generated using data from Rao and Malik (2012).

1.3.3 Advantages of iPSCs

iPSCs have fundamentally reshaped the landscape of disease modelling. With more streamlined protocols in place, the creation of patient-specific or disease-specific models has become more accessible than ever before. The inherent characteristics of iPSCs including their indefinite culture periods and capacity for self-renewal, make these cells amenable to gene editing techniques such as CRISPR (Jinek *et al.*, 2012). This facilitates the generation of isogenic iPSC lines to elucidate the effect of specific mutations on disease pathogenesis, in the absence of confounding patient genetic backgrounds (Bassett, 2017).

iPSCs have been differentiated into many cell types and complex tissues over the last two decades including brain (Lancaster *et al.*, 2013; Lancaster and Knoblich, 2014), heart tissue (Giacomelli *et al.*, 2020), liver (Takebe *et al.*, 2014) and retina (Eiraku *et al.*, 2011b; Nakano *et al.*, 2012; Flamier, Barabino and Bernier, 2016; Gozlan *et al.*, 2023) - to name a few **(Figure 1.15).** The generation of these iPSC-derived tissue models has given researchers novel and unparalleled insights into human biology, particularly in the context of disease. With these models, underlying mechanisms of human disease can be interrogated, such that new therapeutic targets are discovered, and treatments developed. One key feature of iPSC-derived models is their human origin, making them inherently more physiologically pertinent compared to traditional *in vivo* animal models. In extension to this, these models serve as a crucial foundation for drug screening and toxicological investigations and demonstrate immense utility in pre-clinical trials (Sequiera *et al.*, 2022). This leads to a decreased need for animal models in proof-of-concept studies, consistent with the principles outlined in the NC3R's strategy for research involving animals (O'Connor, 2013; Kim, Che and Yun, 2019).

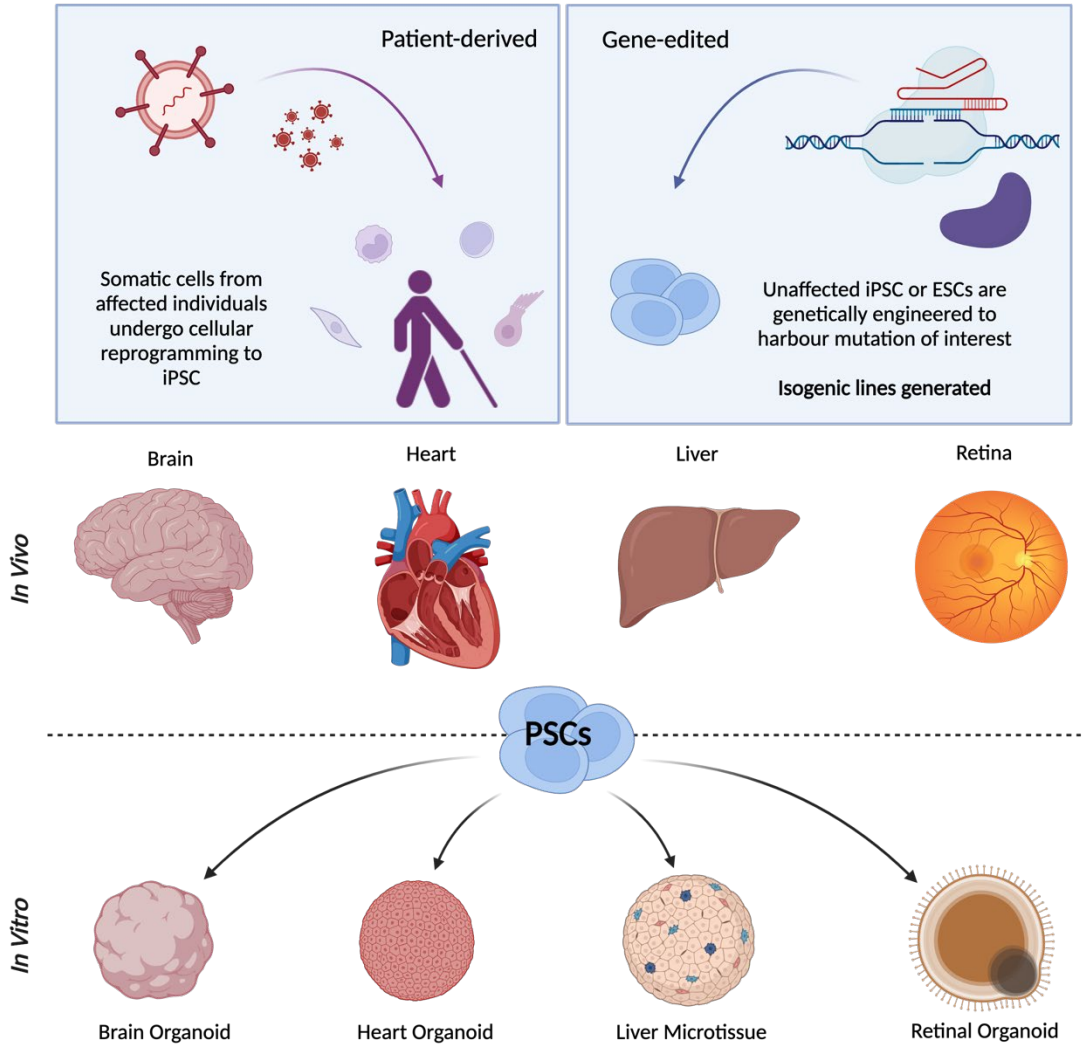

Figure 1.15 Disease modelling with PSCs.

This figure illustrates the generation of disease-specific iPSCs or ESCs through cellular reprogramming or CRISPR engineering to generate isogenic lines respectively. These engineered PSC lines carry disease-associated mutations, allowing them to serve as valuable models for studying various pathologies. Moreover, these diseased PSCs can be utilised to recreate organ models *in vitro*, including brain, heart, liver, and retina. These "organ in a dish" models faithfully recapitulate features of their *in vivo* tissue counterparts, providing invaluable platforms for disease modelling, drug screening, and regenerative medicine research.

1.3.4 Limitations of iPSCs

While the advantages brought by iPSC technology to biological research are indisputable, it does come with several limitations. These limitations primarily revolve around genetic and epigenetic variations between iPSC lines, incomplete reprogramming, genetic instability, and low reprogramming efficiencies (Yoshihara, Hayashizaki and Murakawa, 2017).

Both ESCs and iPSCs display clonal differences in their propensities to differentiate into specific lineages (Osafune *et al.*, 2008; Yokobayashi *et al.*, 2017; Wang *et al.*, 2018). They also often display chromosomal aberrations (Taapken *et al.*, 2011), particularly subchromosomal copy number variations (CNVs) which are associated with the long-term culture of these cells (Laurent *et al.*, 2011; Martins-Taylor *et al.*, 2011; Hussein *et al.*, 2011). However, iPSCs experience additional factors that influence their variability and differentiation capacity. One major factor is attributed to the retention of somatic cell epigenetic signatures (Marchetto *et al.*, 2009; Ghosh *et al.*, 2010) which can ultimately bias the differentiated fate of the cells. iPSCs may also exhibit incomplete cellular reprogramming, where they have not undergone the full genetic and epigenetic alterations to become true pluripotent cells. Consequently, these cells may have limited capacity to undergo directed differentiation to all cell lineages (Chan *et al.*, 2009).

Originally, iPSC generation was facilitated by retro- and lentiviral delivery of pluripotency transgenes to the target cells (Takahashi and Yamanaka, 2006). These vectors are known for their high transduction efficiencies but display high rates of host genome integration, demonstrating the potential for insertional mutagenesis and genome instability. This raises significant safety concerns, especially for potential clinical applications of iPSCs. Non-integrating methods for pluripotency transgene delivery are more favourable due to risk reduction of genomic integration. These include episomal plasmid-mediated and Sendai (SeV) viral-mediated cellular reprogramming (Schlaeger *et al.*, 2015). However, as seen in **Table 1.1,** reprogramming efficiencies are relatively low across all non-integrative methods. Despite these challenges, iPSCs remain a powerful tool with immense potential for advancing biomedical science and healthcare.

1.4 Retinal Organoids

iPSC-derived ROs introduce a notable advancement in vision research, offering a distinctive avenue for acquiring insightful biological knowledge that more closely emulates human physiology. This sets them apart from traditional *in vitro* 2D models and animal models, which may not fully capture the complexities of human retina function and development. These ROs are a suitable proxy for human tissue enabling insights into retinal diseases and potential avenues for therapeutic intervention.

1.4.1 Features of ROs

ROs are three-dimensional structures that recapitulate many aspects of the natural architecture of the human retina **(Figure 1.16).** Within these organoids, a stratified neuroepithelium is established, featuring apical-basal polarity (Nakano *et al.*, 2012; Phillips *et al.*, 2012). All major retinal neurons are present including rod and cone photoreceptors (S and M/L-opsin containing), bipolar cells, RGCs, ACs, HCs, and Müller glia. What is particularly fascinating is that these neurons possess the intrinsic ability to arrange themselves into distinct layers within the organoid, mirroring the native configuration observed *in vivo*. Specifically, photoreceptors form an outer nuclear layer (ONL) situated along the apical edge of the RO, interneurons occupy the inner nuclear layer (INL) at the neuroepithelium's centre, and the RGCs cluster within the ganglion cell layer (GCL), positioned at the RO's innermost boundary (Watson and Lako, 2023).

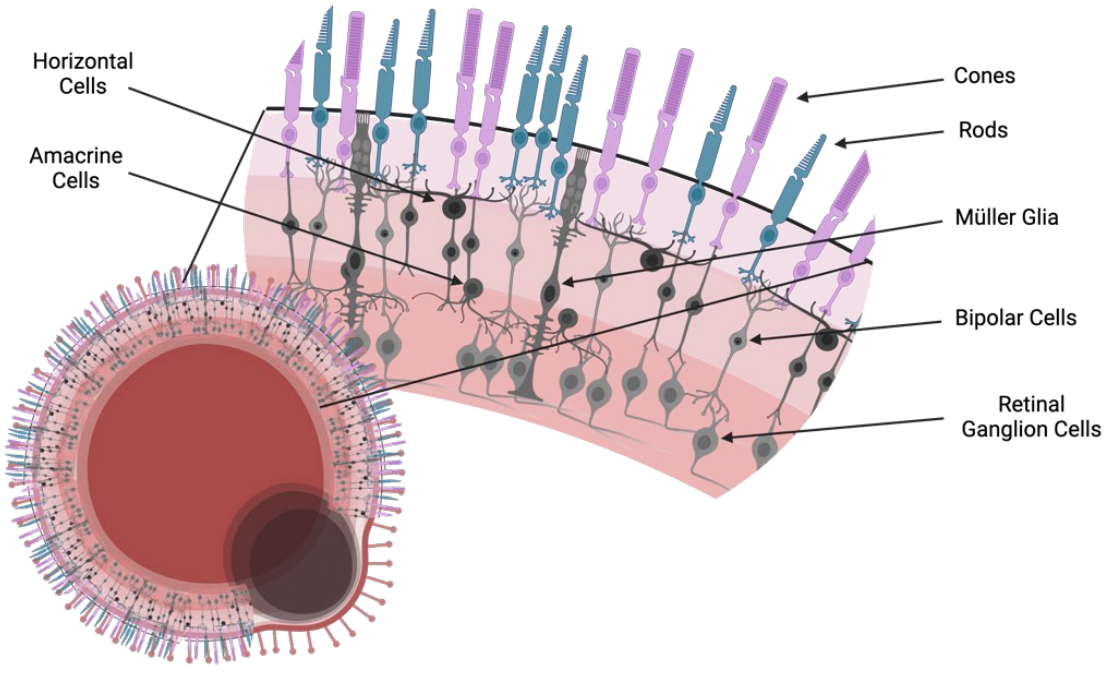

Figure 1.16 ROs replicate features of *in vivo* retinal architecture.

ROs demonstrate a remarkable resemblance to the intricate architecture of *in vivo* retinal tissue. The figure showcases a RO structure with a magnified view that allows for a detailed examination of the retinal layers. In this view, all essential retinal neurons are accurately arranged in their correct sequence, and laminated as observed in living retinal tissue, highlighting the fidelity of ROs in replicating the *in vivo* retinal structure.

The developmental timelines of RO differentiation from PSCs largely follow the observed rates of retinogenesis *in utero* with retinal neurons mirroring the birth order of those observed in developing foetal retina (Collin *et al.*, 2019), but also with some differences in the abundance and temporal emergence of some cell types (Dorgau *et al.*, 2023). Interestingly, transcriptomic profiles of ROs and foetal retina converge significantly, demonstrating that iPSC-derived retinal tissue is highly reminiscent of nascent retina (Cowan *et al.*, 2020).

ROs undergo a progressive maturation process often spanning more than 210 days, during which distinct phases of development are marked by the presence of specific cell subgroups. One study has classified the development and maturation of ROs into three discernible stages (Capowski *et al.*, 2019) **(Figure 1.17).**

At Stage 1, a phase-bright neuroepithelial layer is present in the RO. This layer is positive for markers of neuroepithelial cells (SOX2, PAX6, NESTIN, OTX2, VSX2) which give rise to several neurons that populate the retina. Immature RGCs (BRN3A, POU4F1, TUJ1) are also present at this stage. Stage 2 represents a mid-stage of RO development where photoreceptor cells (Recoverin, CRX, RXRɣ, NRL) emerge to form the ONL. The outer plexiform layer (OPL) begins to form as these photoreceptors continually mature and establish synaptic connections. Bipolar cells (PKCα) and other interneurons (Calbindin, PROX1, AP2α) become apparent (Collin *et al.*, 2019). Stage 3 corresponds to the most mature stage of RO development. Photoreceptors express mature markers (OPN1SW, OPN1MW/LW, RHOD, ARRESTIN) and contain inner and outer segments. All other cell types appear in a laminated manner. Evidence of retinal connectivity has been observed at this point with nascent light responses in photoreceptor cells (Zhong *et al.*, 2014; Hallam *et al.*, 2018).

	Stage	Morphological features	Molecular markers	Fetal retina epoch
Day 60 – Day 90	Stage 1 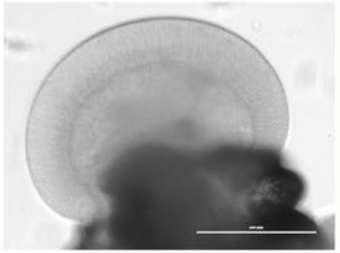	○ Phase-bright neuroepithelium ○ Often columnar organization visible ○ Cup-like shape ○ Rapid growth ○ Several weeks post isolation	○ Retinal progenitors: RAX, VSX2, PAX6 ○ Neurogenesis: ASCL1, NEUROD1, NEUROG1, ATOH1 ○ Ganglion and Starburst amacrine cells: BRN3A/B, SNCG, HuC/D, CHAT, NEFL	○ **First epoch** ○ Mitosis and retinal progenitor genes (*FGF19*, *LIN28B*, *PRTG*, *SFRP2*) ○ Retinal ganglion cell genes (*ATOH7*, *DLX2*, *POU4F2*)
Day 120 – Day 180	Stage 2 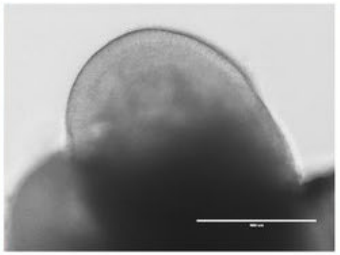	○ Phase dark core develops ○ Grown together tend to merge forming multi-lobular aggregates ○ May remain at this stage	○ Interneurons: ONECUT1/2, TFAP2A/C, CALB2 ○ Photoreceptor precursors: OTX2, CRX, NRL, NR2E3, THRB2, RXRG ○ Synaptogenesis: VAMP2, SNAP25, STX3, SYP, SYT1, CPLX3, PCLO	○ **Second epoch** ○ Horizontal and amacrine cell genes (*PROX1, ASCL1*) ○ Synapse genes (*NRXN1/3*, *SCN2A*, *CACNA1C*)
Day 180+	Stage 3 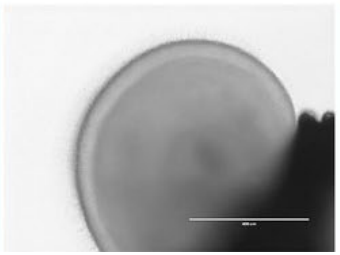	○ Outer lamina clearly defined ○ Brush-like apical protrusions at the rim ○ Center dense and opaque ○ Arise around 15-20 weeks post-isolation	○ Opsins: OPN1SW, OPN1MW, RHO ○ Phototransduction: GNAT1/2, GNGT1/2, SAG, ARR3, CNGB1/3 ○ Outer segment: ROM1, ABCA4, PRPH2, RPGR ○ Müller glia: RLBP1, VIM	○ **Third epoch** ○ Photoreceptor and bipolar cells genes (*OTX2*, *NRL*, *RCVRN*, *TULP1*, *GNAT1/2*, *GRM5/6/7/8*)

Figure 1.17 Staging of RO Development.

Staging of ROs is based on histological characteristics and the expression of molecular markers identified through transcriptome studies of the organoids. These developmental stages closely align with specific molecularly defined periods in human foetal retina development. The left side of the figure displays bright-field images illustrating retinal tissue within the organoids at each of these developmental stages, with a scale bar of 400µm. Additionally, the accompanying table provides a summary of the principal morphological traits, molecular markers, and the corresponding developmental stages in human foetal development that correlate with each stage of organoid differentiation.

Figure source: Kruczek and Swaroop (2020)

1.4.2 Generation of ROs

Yoshiki Sasai and his group at the RIKEN Institute in Japan were leading pioneers in the development of 3D retina with their seminal 2011 study reporting self-organising 3D optic cup structures from mESCs (Eiraku *et al.*, 2011b).

Throughout the process of *in vitro* optic cup development, they observed the organisation of retinal cells in a laminar arrangement, which occurred autonomously and in a stepwise manner. The optic cups exhibited clear apical-basal polarity, mirroring the natural process of retinogenesis *in vivo.* Through immunohistochemistry, they demonstrated that the optic cups expressed markers for all major retinal cell types. Adjacent RPE structures were also observed in the optic cups. Notably, rod photoreceptors greatly outnumbered cone photoreceptors, resulting in an overall phenotype resembling peripheral retina. The authors proposed that the self-organizing capacity of these optic cups stemmed from the spontaneous activation of intrinsic factors, possibly triggered by the initial dissociation and reaggregation of mESCs. This hypothesis found support using exogenous signalling factor combinations, including inhibitors of Wnt, Nodal, and Notch signalling pathways.

This was later reproduced from hESCs to develop human retinal cups (Nakano et al., 2012). These optic cups exhibited similar features to those derived from mESCs in terms of cellular composition and apical-basal polarity. However, hESC-derived optic cups were considerably larger than their mESC-derived counterparts. Culturing periods differed substantially between mESC and hESC differentiation to ROs, with 30 days for mESC-ROs and up to 210 days for hESCs. Furthermore, neural retina exhibited increased thickness in hESC-derived optic cups, consistent with species-specific morphological variations *in vivo* and inherent differences in developmental biology between mice and humans.

In the past decade, extensive research efforts have been dedicated to advancing and enhancing current protocols, while also innovating new methods for obtaining RO from PSCs (Zhong *et al.*, 2014; Mellough *et al.*, 2015; Gonzalez-Cordero *et al.*, 2017; Hallam *et al.*, 2018; Capowski *et al.*, 2019; Zerti *et al.*, 2020; Cowan *et al.*, 2020; West *et al.*, 2022). A brief summary of these protocols can be observed in **Table 1.2.**

Method	Year	Description	Citation
3D Retina Modelling with hESCs and hiPSCs	2009	The Gamm lab differentiated hESC and hiPSC lines using a differentiation medium targeted for neural fate. By culturing in suspension, they obtained optic vesicle-like (OV-like) structures from neural rosettes expressing markers for retinal precursor cells and showing anterior neuroectodermal origins.	(Meyer *et al.*, 2009)
Generation of 3D Optic Cup Structures from mESCs	2011	The Sasai group achieved self-organising 3D optic cup structures from mouse ESCs, featuring a laminated structure reminiscent of the native retina. The optic cups displayed clear apical-basal polarity and expressed markers of major retinal cells. The development of these structures was linked to intrinsic factors and exogenous signalling pathway inhibitors	(Eiraku *et al.*, 2011a)
3D Optic Cup Formation from hESCs	2012	Similar to mESCs, hESCs were used to generate 3D optic cups with laminated retinal cell ordering and apical-basal polarity. These hESC-derived optic cups were larger and thicker than mESC-derived ones.	(Nakano *et al.*, 2012)
Laminated 3D Retinal Tissue from Human PSCs	2012	The Gamm group produced laminated 3D retinal tissue from human PSCs, expressing key markers for synaptogenesis. They used established protocols, involving suspension culture, EB formation, and neurosphere generation. Unlike previous methods, their approach did not require exogenous factors.	(Phillips *et al.*, 2012)
Functional Retinal Organoids	2014	The Canto-Soler group achieved fully stratified retinal organoids with rudimentary outer segments and photosensitivity. Their protocol, based on earlier work, included foetal bovine serum, taurine, and retinoic acid support for long-term culture.	(Zhong *et al.*, 2014)
BMP-4 Supplementation Enhances Retinal Organoid Development	2015	Sasai group developed a method to generate a ciliary margin-like stem cell niche from self-organizing human retinal tissue. This niche had characteristics reminiscent of the ciliary margin zone and provided insights into retinal tissue development. The addition of BMP-4 (Bone Morphogenetic Protein 4) supplementation was a key component of their protocol. BMP-4 played a crucial role in enhancing the generation and organisation of retinal organoids, contributing to their development. It acted as a signalling factor that promoted specific cellular responses necessary for retinal tissue formation and organisation	(Kuwahara *et al.*, 2015)

Robust and High-Throughput Retinal Organoids	2015	The Lako group developed a protocol involving IGF1 supplementation, resulting in the orchestration of retinal cell development and lamination, along with the development of lens/corneal tissue. Photoreceptors exhibited inner and outer segments, synapses, and photosensitivity. IGF1 was crucial for development, survival, and maturation	(Mellough *et al.*, 2015)
Matrigel-Free Retinal Organoids	2018	Another method by the Lako group, based on the Sasai protocols (Nakano *et al.*, 2012; Kuwahara *et al.*, 2015) but avoided Matrigel and used BMP4 supplementation. Culturing in a 96-well U-bottom plate format improved scalability, and organoids exhibited cilia, photoreceptor outer segments, and robust formation. This protocol simplifies production but can vary in efficiency.	(Hallam *et al.*, 2018)
Disease-Recapitulating Retinal Organoids	2018, 2022	The Lako group's protocol for ROs was effective in recapitulating disease phenotypes. They facilitated the study of an autosomal dominant form of retinitis pigmentosa (adRP) (PRPF31-mediated) and discovered location-specific RNA transcripts, offering insights into disease mechanisms. ROs demonstrate accumulation of harmful protein aggregates which could be reversed by the activation of autophagy.	(Buskin *et al.*, 2018; Georgiou *et al.*, 2022)
Optimising Cone and Rod Photoreceptor Development in Retinal Organoids	2020	The Lako group developed a simple method to enhance the generation of cone and rod photoreceptors in pluripotent stem cell-derived retinal organoids. They investigated techniques to improve the efficiency of photoreceptor generation, with a focus on enhancing both cone and rod photoreceptor populations. The study involved modifications to the differentiation protocol including additions of T3 hormone, DAPT and retinoic acid to achieve this enhancement.	(Zerti *et al.*, 2020)
Improvement of Photoreceptor Outer Segments	2022	2D/3D culture approach using a checkerboard scraping method to isolate OVs from 2D monolayers of differentiated PSCs and transfer to 3D suspension culture. Antioxidant and lipid supplementation in PSC-derived retinal organoids led to significant improvements in the development of photoreceptor outer segments, resulting in more structurally mature and organised outer segments in the organoids	(West *et al.*, 2022)

Table 1.2 Summary of of key RO-derivation methods.

Included in this list are several papers from our own research group, demonstrating our success in the generation of robust and reliable ROs in a high throughput manner. These organoids have shown great utility in disease modelling (Buskin *et al.*, 2018; Georgiou *et al.*, 2022; Rozanska *et al.*, 2022) and in *in vitro* toxicology (Dorgau *et al.*, 2022)

Our earliest work in the development of PSC-derived ROs investigated the role of insulin-like growth factor (IGF1) in retinogenesis (Mellough *et al.*, 2015). This constituted a simple protocol involving continuous supplementation with IGF1 and yielded ROs with neural retina, RPE and lens/corneal tissue – a unique outcome compared to previous methods. Photoreceptors developed inner and outer segments with evidence of connectivity to RGCs through synapse-related markers Synaptophysin 1, VGLUT1 and TUJI1. Furthermore, increased evidence of functionality was observed in the photoreceptors via their response to cGMP stimulation during later developmental stages. These findings highlight the effectiveness of the approach employed by the Lako group. Importantly, when IGF1 was absent from cultures, optic cup formation and development of ROs were significantly impaired, emphasizing the vital role of IGF1 in the development, survival, and maturation of ROs.

RO protocols continually evolve through ongoing research. Since the original derivation of the IGF1-dependent protocol, our group has made modifications to enhance the development of different photoreceptor cell populations in ESC-derived ROs **(Figure 1.18).** This is achieved via the addition of ɣ-secretase inhibitor [(N-[N-(3,5-difluorophenacetyl)-L-alanyl]-S-phenylglycine t-butyl ester, DAPT], dopamine agonists such as levodopa (L-DOPA) or hormones such as Triiodothyronine (T3) at particular stages during the differentiation process. This is in addition to retinoic acid (RA), vitamin A derivatives used to promote differentiation and maturation of rod and cone photoreceptors (Zerti *et al.*, 2020). These molecules are added in varying concentrations temporally throughout the differentiation period to alter the fate of developing photoreceptors. DAPT treatment results in a higher number of M/L cones at the expense of rod photoreceptors. Whereas T3 combined with RA promotes the formation of rod and S-cone photoreceptors. This advancement moves us closer to creating RO models that better replicate the diversity and structure of the retina's various regions, such as the macula which primarily consists of M/L cones and relatively few rods.

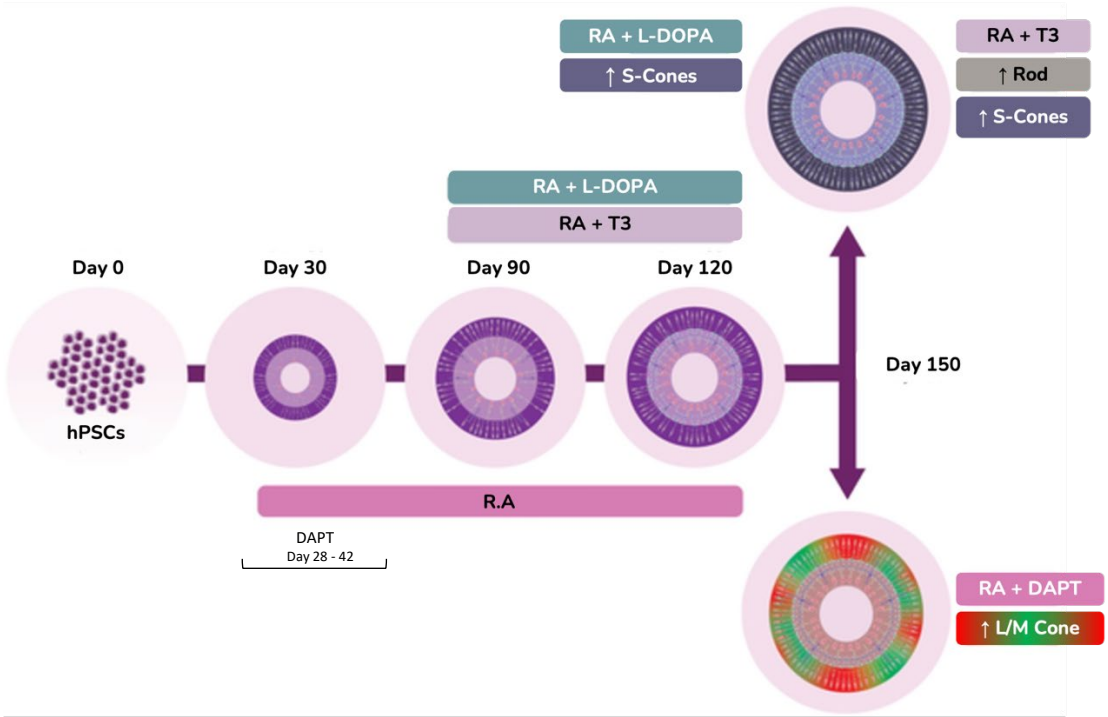

Figure 1.18 RO differentiations can be optimised to yield varying populations of cone photoreceptors.

The stage-specific additions of various compounds, including retinoic acid (RA), 9-*cis*-retinal, 11-*cis*-retinal, l-DOPA, T3 and DAPT greatly impacts the generation of rod and cone photoreceptors. The introduction of RA + T3 between days 90 to 120 of the differentiation process enhances the formation of rod and S-cone photoreceptors. Conversely, when DAPT is combined with RA from days 28 to 42 and with just RA until day 120 of differentiation, it promotes the generation of L/M-cones at the expense of rod photoreceptors. Additionally, the concurrent addition of l-DOPA and RA between days 90 to 120 of differentiation fosters the emergence of S-cones while diminishing the population of rod photoreceptors. The ability to precisely control the generation of rod and cone photoreceptors in vitro is a significant step towards better disease modelling, drug development, personalised medicine, and potential vision restoration strategies for individuals with retinal disorders.

Figure source: Zerti *et al.* (2020).

Our group has also adapted existing protocols based on Sasai's work (Eiraku *et al.*, 2011a; Nakano *et al.*, 2012; Kuwahara *et al.*, 2015) to generate high throughput ROs by increasing scalability and decreasing variability (Hallam *et al.*, 2018). These adaptions included the removal of Matrigel, which has inherent batch-to-batch variability in addition to the adaption to 96 U-bottom well plate culturing formats. This enabled streamlining of the differentiation process with an optimised seeding density of 7,000 cells per well. This adaptation allows for the production of significantly higher numbers of ROs with reduced hands-on maintenance. Consequently, it serves as an ideal platform for drug screening and toxicology testing, enabling more robust statistical analysis. These protocol modifications developed ROs akin to previously developed organoids, with improved RGC responses. In a proof-of-concept study, the ROs in this format were used to assay the effects of Moxifloxacin, a drug known to be toxic to the ONL when administered to mouse models. Through immunohistochemistry and gene expression assays, they demonstrated that akin to *in vivo* models, the photoreceptors and ACs in ROs were the primary cell types affected by the toxicity of this drug (Hallam *et al.*, 2018).

It has been widely accepted that a large degree of variability in differentiated cultures is a consequence of variability in iPSCs themselves, as discussed in **Section 1.3.4.** Consequently, many groups are now looking at ways to reduce iPSC variability. One approach is to adopt automated strategies to generate iPSCs from patient fibroblasts, clonal expansion, and retinal organoid differentiation (Bohrer *et al.*, 2023; Cooke *et al.*, 2023) which controls for technical variability. The development of such automated systems will prove invaluable for the production of autologous PSCs for clinical application.

1.4.3 Disease modelling with ROs

One of the greatest advantages of RO technology is the ability to generate disease models in a patient-specific or even mutation-specific manner using cellular reprogramming or gene editing strategies. This is particularly useful for the modelling of individual IRDs that may present with overlapping clinical phenotypes but have distinct underlying mechanisms implicating different genes, offering novel insights into the effects of mutated retinal genes during retinogenesis (Watson and Lako, 2023).

For instance, take RP, a condition linked to mutations in over 70 genes, characterised by significant phenotypic diversity and variable disease onset, ranging from infancy to adulthood (Hartong, Berson and Dryja, 2006). In recent years, numerous RO models have been established to study RP resulting from mutations in *USH2A* (Guo et al., 2019; Sanjurjo-Soriano et al., 2023)*, RP2* (Lane et al., 2020)*, CRB1* (Buck et al., 2023)*, Rho* (Zhou et al., 2023; Kandoi et al., 2023*), IMPG2 (*Mayerl et al., 2022)*, PDE6B* (Gao et al., 2020), *RPGR* (Chahine Karam et al., 2022) and *PRPF31* (Rodrigues et al., 2022; Buskin et al., 2018; Georgiou et al., 2022).

Interestingly, overlapping phenotypes have been observed in these retinal models, closely resembling the *in vivo* situation. These shared characteristics encompass specific rod defects (correlating with night blindness in patients) and heightened stress responses, including impaired autophagy and increased oxidative stress, which align with animal models of RP (Trachsel-Moncho *et al.*, 2018). This highlights the fidelity of these models in their ability to recapitulate features of human retinal disease.

From our group's own studies on PRPF31-mediated RP (RP11) using ROs, we have shown that photoreceptor cells from RP11-ROs display altered morphology with a 150% increase in apoptotic nuclei compared with controls, indicating increased cell death. These photoreceptors also contained stress vacuoles which is a characteristic feature of adaptive survival and had not previously been reported. Photoreceptor cilia also appeared defective with a bulbous morphology and misaligned microtubules. Reduced RGC activity was also reported in the RP11-ROs which exhibited a reduced spiking rate in response to GABA in multi-electrode arrays (MEAs) indicating potential retinal network connectivity issues in a disease-specific manner (Buskin *et al.*, 2018). Notably, global splicing defects were observed in RP11-ROs and iPSC-RPE consequential to *PRPF31* mutation, but not blood cells or fibroblasts demonstrating the retina-specific effect of *PRPF31* mutations, despite its ubiquitous

expression in the body. iPSC-derived RPE was also cultured in parallel to RP11-ROs and demonstrated the most significant disease phenotype affected by *PRPF31* mutation. This corroborated previously published results in *in vivo* mouse models (Farkas *et al.*, 2014). The disease phenotype of these cells was characterised by the loss of apical-basal polarity as described by impaired tight epithelial barriers, deformed microvilli which were both shorter and fewer in incidence, defective phagocytic function, and the occurrence of large basal deposits **(Figure 1.19).**

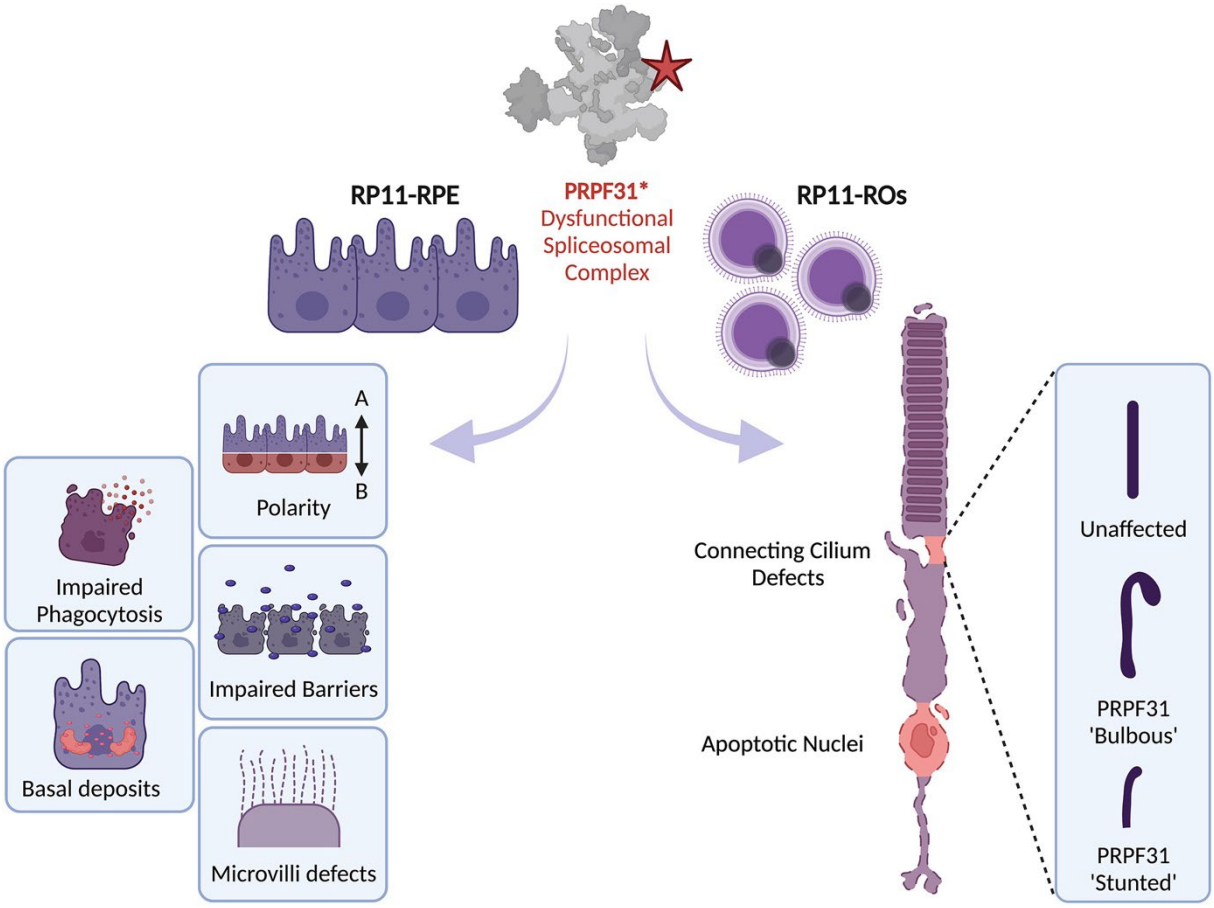

Figure 1.19 Features of PRPF31-mediated RP are recapitulated in iPSC-derived retinal tissues *in vitro.*

Summary of disease phenotypes observed in stem cell-derived RP11-retinal tissues. *PRPF31* mutations negatively impact spliceosome assembly leading to global splicing dysregulation. RP11-RPE and RP11-ROs were derived from patient iPSCs and revealed defects in molecular structures. RP11-RPE reveals several defects including disrupted apical/basal polarity and tight junctions, altered microvilli morphology, defective phagocytotic function and the appearance of basal deposits. RP11-ROs harboured photoreceptor cells with apoptotic nuclei and altered connecting cilium.

Figure source: Watson and Lako (2023).

Building upon this work, we recently showed activation of autophagy in RP11-ROs, likely as a response to protein aggregation and misfolding (Georgiou *et al.*, 2022). However, the RP11-RPE was better suited for the understanding of the potential disease mechanisms at play in RP11 (**Figure 1.20).** Autophagy is a cellular process for clearing misfolded proteins and damaged organelles. An impairment of this process was noted in RP11-RPE. Specifically, late-stage autophagy was blocked, as indicated by the upregulation of proteins such as p62 and LC3-II. These are conventionally associated with an inhibition of autophagosome degradation. This was confirmed by flux assays in the presence of Bafilomycin, a drug that inhibits autophagosome-lysosome fusion *in vitro*. This can cause the accumulation of cellular aggregates resulting in RPE cell degeneration and ultimately photoreceptor death. However, culturing RP11-RPE with Rapamycin, an mTOR pathway inhibitor, for 7 days was sufficient to activate autophagy. This significantly reduced the burden of cytoplasmic aggregates in RP11-RPE and significantly reduced caspase-3 activation, thereby demonstrating a potential therapeutic application of Rapamycin for RP11 disease (Watson and Lako, 2023).

These models have provided fresh insights into the molecular mechanisms underlying RP11, pinpointing the precise location of cell aggregates within the cytoplasm and elucidating defective processes contributing to the build-up and clustering of misfolded proteins. Consequently, this discovery has opened new avenues for targeting autophagy activation and expediting the removal of cytoplasmic aggregates. Notably, this marks the inaugural instance of an *in vitro* RP11 model that faithfully replicates human physiology, serving as an invaluable asset for unravelling the pathogenic mechanisms of this poorly understood retinal degenerative condition and truly demonstrates the unlimited possibilities of PSC-derived retinal models in understanding molecular signatures of retinopathies.

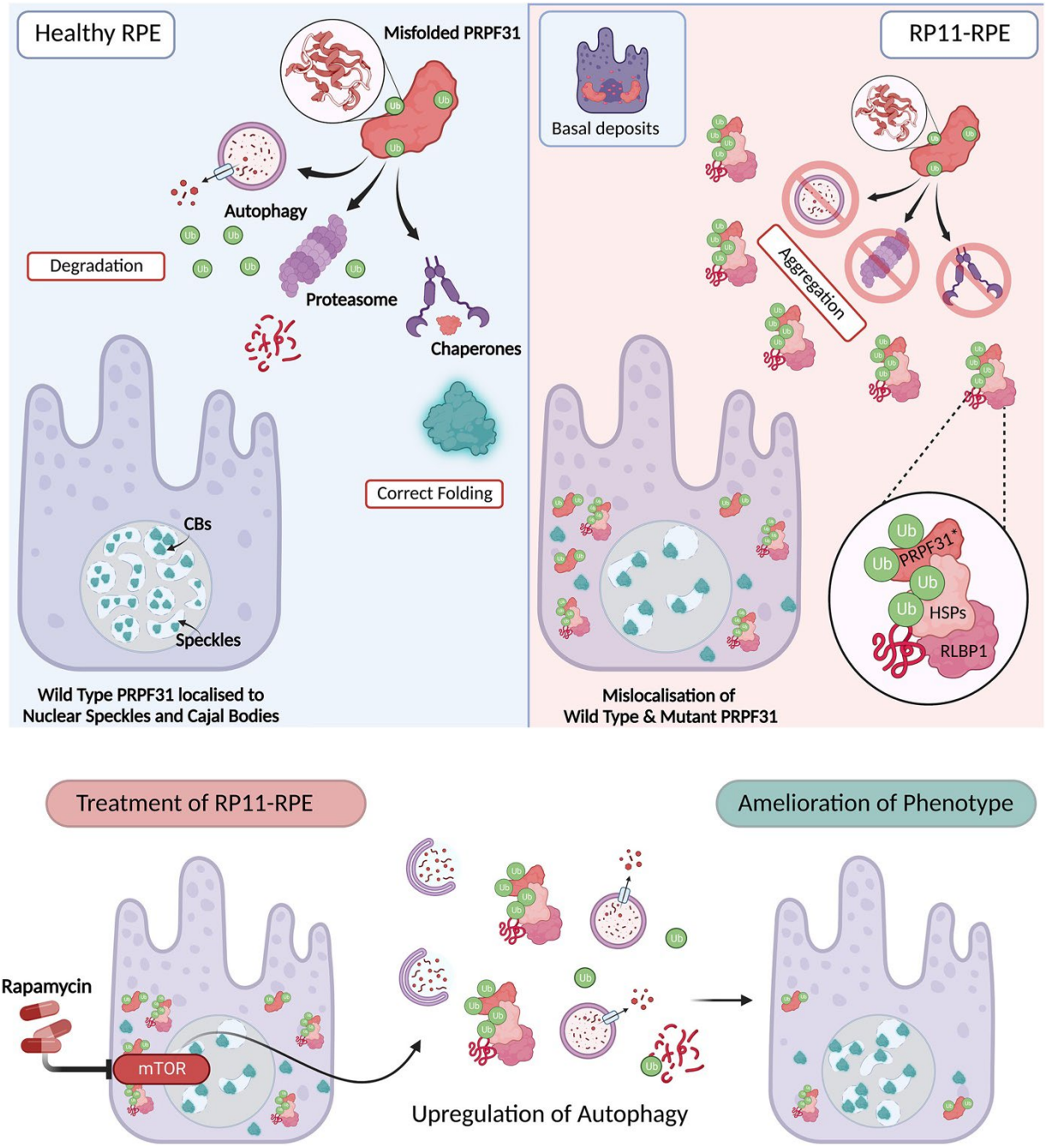

Figure 1.20 Mechanism of Aggregate Formation in RP11-RPE and Treatment with Rapamycin.

In healthy RPE cells, responses to misfolded proteins involve molecular chaperones like heat shock proteins (HSPs) aiding in protein stabilisation and correct conformation. Severely misfolded proteins are tagged with ubiquitin molecules, targeting them for degradation via proteasomal or autophagic pathways, recycling their components. In RP11-RPE, impaired unfolded protein response (UPR) pathways, likely due to mis-splicing events from defective PRPF31 protein, lead to cytoplasmic aggregate formation. These aggregates contain mutant PRPF31, HSPs, and other mutant retinal proteins, negatively impacting cell health and directing the cytoplasmic localisation of both mutant and wild-type PRPF31. Treatment with rapamycin inhibits the mTOR pathway, upregulating autophagy, which enhances misfolded PRPF31 degradation, resulting in reduced cytoplasmic aggregates, mutant PRPF31, and improved wild-type PRPF31 localisation.

Figure source: Watson and Lako (2023).

1.4.4 Limitations of ROs

The previous discussion of PRPF31-mediated retinal disease highlights the limitations of studying IRDs solely in ROs and the necessity for looking at the disease in the context of both neural retina and RPE. Whilst ROs do technically contain RPE cells, it is not functional and is generally attached to ROs in clumps and not as a monolayer as seen *in vivo*. Even still, the presence of RPE clusters is not guaranteed as it appears to be protocol and cell-line-specific (Chichagova *et al.*, 2020).

This is perhaps the biggest limitation of the model as RPE is known to contribute to the development and maintenance of photoreceptor cells. Thereby, without functional RPE tissue, RO models may not accurately recapitulate the full extent of disease processes. The lack of RPE also likely contributes to the incomplete maturation of photoreceptors and their outer segments. The outer segment structures observed in ROs display improperly stacked membranous stacks (O'Hara-Wright and Gonzalez-Cordero, 2020). This also contributes to the poor light responses exhibited by photoreceptors in ROs (Zhong *et al.*, 2014; Dorgau *et al.*, 2019; Hallam *et al.*, 2018).

Hence, there is an ongoing challenge to generate iPSC-derived retina where both the neural retina and RPE can exist in proximity and function together. Investigations into using microfluidic culturing chambers may facilitate the co-culture of these tissues and generate retina-on-a-chip platforms, however success to date is limited as the system provides only limited contact between spheroidal neural retina and two-dimensional RPE monolayers (Achberger *et al.*, 2019).

Another important missing feature of ROs is the lack of vascularisation and immune-related cells. This is particularly important for the modelling of multifactorial retinal diseases such as AMD to understand the effects of the peripheral immune system in retinopathy. Efforts have been made to incorporate immune cells such as microglia via co-culture and have shown some success in retinal invasion following endotoxin challenge (Chichagova *et al.*, 2023). The outer blood-retinal barrier has also been modelled *in vitro* using RPE cells, in addition to endothelial cells to form vasculature (Arık *et al.*, 2021). In the future, perhaps assembloid models will be generated that encompass vascularised retinal tissue with RPE to better replicate *in vivo* physiology.

1.5 Research Aims

This project aims to model and characterise STGD1 with ROs throughout retinogenesis and uncover the missing inheritance in two monoallelic late-onset STGD1 cases.

There are 3 key elements to this study, simplified in **Figure 1.21** but in detail as follows:

1) Reprogram cells from Patient 1 (PT1) and Patient 2 (PT2) samples to iPSC and characterise these cells using qPCR, pluripotency and karyotypic assays.
2) Differentiate these cells to iPSC lines to ROs alongside a biallelic STGD1 iPSC line as an affected control (AC) and a wild-type iPSC line (WT2) as an unaffected control. Characterise the development of these ROs over a period of 220 days and phenotype any disease-specific effect that arises using ICC, Western Blotting, and scRNA-Seq.
3) Identify the missing inheritance of PT1 and PT2 cases using a myriad of sequencing techniques including WGS and LRS using *ABCA4.*

These aims on based on 3 main hypotheses for this research:

1) **The missing inheritance** is attributed to the presence of a deep-intronic variant or hypomorph previously undetected by traditional sequencing methods.
2) **ROs can effectively model STGD1** and exhibit distinct phenotypic and molecular features reflective of the disease.
3) **The genotype/phenotype correlation** for specific mutations will be observable in STGD1 ROs on a molecular level.

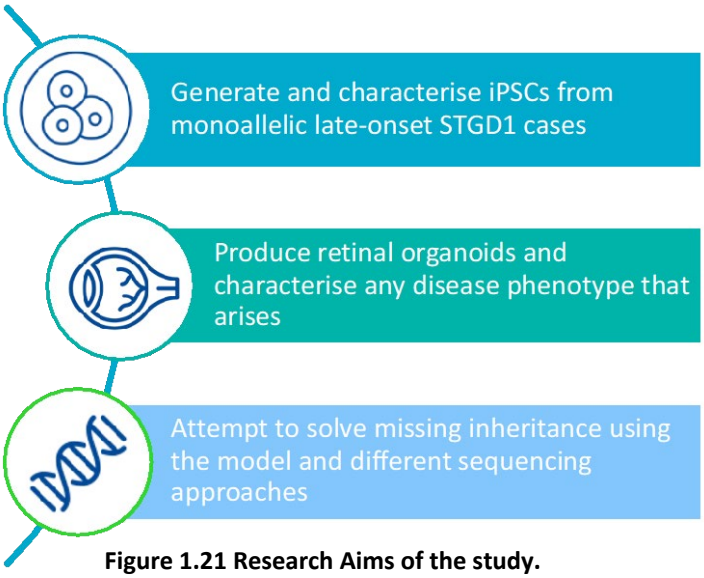

Figure 1.21 Research Aims of the study.

Chapter 2 Materials & Methods

2.1 Patient Information & Ethics

The two participants (PT1 & PT2) **(Table 2.1)** in this research study were identified and enlisted by Prof. Frans Cremers of Radboud University Medical Centre (RUMC) in Nijmegen, NL as part of the collaborative Marie-Curie Innovative Training Network – StarT (Grant no: 813490). PT1 & PT2 are of Dutch/Belgian descent and were enlisted in this study as cases of monoallelic late-onset STGD1. These individuals have undergone prior ethical approval for their participation in this study.

Case:	Diagnosis	Age:	Gender	iPSC Source	Mutation:	
Information Provided by RUMC Collaborators					Classified Severe	Classified Mild/Moderate
Genotype						
PT1	Late-onset STGD1	30 yrs	Male	Fibroblast	Allele 1:	c.[5461-10T>C; 5603A>T] p.[Thr*13, Thr1821Aspfs*6; Asn1868Ile]
					Allele 2:	?
PT2	Late-onset STGD1	44 yrs	Male	PBMC	Allele 1:	c.[5461-10T>C; 5603A>T] p.[Thr*13, Thr1821Aspfs*6; Asn1868Ile]
					Allele 2:	?
AC	Classic STGD1/CRD	12 yrs	Female	Fibroblast	Allele 1:	c.4539+2001G>A p.[Arg1514Leufs*36,=]
					Allele 2:	c.4892T>C p.(Leu1631Pro)
WT2	Healthy	31	Female	Fibroblast	Allele 1:	c.4539+2001G>A p.[Arg1514Leufs*36,=]
					Allele 2:	c.4892T>C p.(Leu1631Pro)
WT3	Healthy	68	Male	Fibroblast	Allele 1:	Wild-Type
						Wild-Type
					Allele 2:	Wild-Type
						Wild-Type
PT1	**At diagnosis**	Age:	30 years			
		BCVA:	Not available			
		Fundus:	Large region of atrophy with foveal sparing, fundus flecks			
		ffERG:	Not available			
PT2	**At diagnosis**	Age:	44 years			
		BCVA:	Not available			
		Fundus:	Large region of atrophy surrounding preserved fovea			
		ffERG:	Not available			
AC	**At last visit:**	Age:	48			
		BCVA:	20/400			
		Fundus:	Large atrophic regions in RPE			
		ffERG:	Photopic severely reduced, scotopic normal			

Table 2.1 Information about patients provided by collaborators at RUMC

Details for wild-type cells are published in supplementary data of Buskin *et al.* (2018)

2.2 Cell Culture & Maintenance

All cell cultures were maintained at 37°C in a humified incubator with 5% CO2. Routine testing for mycoplasma was carried out on all lines used in this project.

2.2.1 iPSC Culture

iPSCs were cultured in 6-well plate format, with wells precoated with Matrigel™ (Corning, 354230) at a concentration of 18.6μg/cm^2. iPSCs were maintained in mTeSR1™ (StemCell Technologies, 85850) supplemented with 1% Penicillin/Streptomycin (Pen/Strep) (Life Technologies, 15140122) with daily medium changes. Cells were regularly checked for spontaneous differentiation, which if present, was cleared away by mechanical scraping under an inverted microscope in sterile conditions. At 80% confluence, the cells were either passaged, cryogenically frozen, or dissociated to single cell for RO differentiation. Clump passaging was achieved using Versene (0.2% EDTA solution) (Life Technologies, 15040033). The treated cells were incubated at 37°C for 2-3 minutes before splitting at a ratio of 1:3 on freshly prepared Matrigel-coated plates. To freeze, the cells were spun down and pelleted at 300 x g for 3 minutes and reconstituted with a cryogenic freezing medium comprised of 90% foetal bovine serum (FBS) (Life Technologies, 10270106), 10% dimethyl sulfoxide (DMSO) (Sigma Aldrich, D2650) and 10μM Y-27632 (ROCK inhibitor (ROCKi)) (ChemDea, CD0141). ROCKi was also added to iPSCs upon initial thaw for the first 24 hours of culture for increased cell viability.

2.2.2 Differentiation of PT1 refractory iPSCs to mesenchymal-like cells

Uncontrollable spontaneous differentiation was observed in PT1 iPSCs upon initial culture. To counteract this, the cell line was subjected to an additional round of reprogramming. To achieve this, the cells were first cultured in a high-sera-containing medium comprised of DMEM/F12 with HEPES (Life Technologies, 31330038), 20% FBS, 1% Pen/Strep, 1% MEM-NEAAs (Life Technologies, 11140068) and 1% GlutaMAX (Life Technologies, 35050038) to direct their differentiation to mesenchymal-like cells. Cells were fed every other day. Once confluent, the cells were passaged using 0.05% Trypsin-EDTA solution (Life Technologies, 25300054) before plating for transduction by the Cytotune 2.0 (ThermoFisher, A16517) reprograming vectors.

2.2.3 Peripheral blood mononuclear cell (PBMC) expansion

Processed peripheral blood samples of PT2 were sent to our lab from our collaborators at RUMC, NL. We followed the CytoTune 2.0 manual (ThermoFisher, A16517) for the expansion of PBMCs for downstream cellular reprogramming. Briefly, PBMCs were plated at a density of $5x10^5$ cells/ml in a 24wp in Complete PBMC medium, comprised of StemPro™-34 medium (Life Technologies, 10639011) supplemented with 2mM L-Glutamine (Life Technologies, 25030081) and cytokines SCF (Life Technologies PHC2111)(100ng/ml), FLT-3 ligand (Life Technologies, PHC9414)(100ng/ml), IL-3 (Life Technologies, PHC0034)(20ng/ml) and IL-6 (Life Technologies, PHC0065)(20ng/ml) which were added fresh to media daily upon feeding. Cells were maintained for 4 days before plating for transduction by the Cytotune 2.0 reprogramming vectors.

2.2.4 Culture of primary mouse embryonic fibroblast cells (MEFs)

MEF cells were expanded and irradiated for use in the generation of conditioned medium (iMEF-CM). EmbryoMax® MEFs (Merck, PMEF-CFL) were thawed at P3 at a density of $2x10^5$ cells/cm^2 in T25 flasks precoated with 0.2% porcine gelatin (Sigma Aldrich, G1890). Upon reaching 90% confluence, cells were expanded to T75 flasks at a splitting ratio of 1:3 every 2-4 days, depending on passage number. At passage 4-5 upon reaching confluency, they were irradiated at a dose of 120kV, 4.0mA for 7 minutes using the Faxitron CP-160 irradiator. After a 1-hour recovery period, cells were trypsinised and pooled together in MEF medium, and counted via Trypan Blue (Sigma Aldrich, T8154) method to assess viability. Live cells were plated at a density of $5.6x10^4$cells/cm^2 in a T150 flask to prepare iMEF-CM. The remaining cells were frozen in freezing medium comprised of 90% FBS and 10% DMSO at a density of $1x10^6$ cells/ml. These iMEFs were later required for feeder plates during cellular reprogramming of PT1 and PT2.

For the iMEF-CM flasks, the medium was replaced 24 hours post-seeding with hESC medium consisting of Knockout DMEM (Life Technologies, 10829018), 20% Knockout Serum Replacement (KOSR) (Life Technologies, A3181502), 1% Pen/Strep, 1% GlutaMAX (Life Technologies, 35050087) and 1% MEM-NEAAs. The iMEF-CM was collected each day for a total of 10 consecutive days. It was filter sterilised using 0.2μm pore filter and stored at -20°C until use during reprogramming.

2.2.5 Cellular reprograming of PT1 and PT2 samples

Both samples were reprogrammed following the Cytotune 2.0 manual for fibroblasts (PT1) and PBMCs (PT2). Both protocols differ slightly in the initial stages as described below.

PT1 - *Mesenchymal-like cells (Fibroblasts)*

PT1 mesenchymal-like cells were plated at a density of $2.86x10^4$ cells/cm^2 in a 12-well plate precoated with 0.2% gelatin. 24-hours later, cells were transduced with Sendai viral (SeV) vectors containing reprogramming transgenes - at the recommended MOIs for fibroblast cells - *KOS* [MOI=5], *C-MYC* [MOI=5], *KLF4* [MOI=3]. 24 hours later, medium containing SeV reprogramming vectors was replaced with fresh MEF medium. Medium changes were conducted daily for 7-days post-transduction. At 6 days post-transduction iMEF feeder plates were prepared at a density of $1.57x10^4$ cells/cm^2 in a 6-well plate.

The next day, the transduced cells were trypsinised and plated on the iMEF feeder plates at 3 different densities – $1x10^4$ cells/well, $2.5x10^4$ cells/well and $5x10^4$ cells/well. Medium was switched to hESC medium 24 hours later and was replaced daily thereon. The remaining transduced cells were snap frozen as a positive control for downstream iPSC characterisation.

After 7 days of feeding with hESC medium, the medium was supplemented with iMEF-CM at a 1:1 ratio. This iMEF-CM was first supplemented with 1% insulin transferrin selenium-A (Life Technologies, 51300) and bFGF (Life Technologies, 13256029)(8ng/ml) to ensure transduced cells received continued growth factor supplementation from iMEF feeders.

Transduced cells were maintained in this manner for up to 28 days. Differentiated cell types were cleared from the emerging colonies each day to facilitate the expansion and growth of emerging iPSC colonies. Once large enough, each colony was mechanically passaged to a Matrigel-coated well of a 12 well plate. Each emergent iPSC colony was treated as a distinct clone and transferred to its own well.

PT2 – *Peripheral blood mononuclear cells (PBMCs)*

PBMC reprogramming followed a similar format to the mesenchymal-like cells. On the day of transduction, PBMCs were counted and $2.5x10^6$ cells were seeded in TC-treated 12-well plates in 1ml of expansion medium with growth factors as previously defined in **Section 2.2.3.** The same MOIs were used; *KOS* [MOI=5], *C-MYC* [MOI=5], *KLF4* [MOI=3]. Upon addition of SeV vectors, the plate was centrifuged at 300 x g for 60 minutes at 25°C. The vectors were then

diluted by the addition of an extra 1ml of expansion medium with no growth factors to reduce cytotoxicity. 24 hours later, medium was completely replaced by the pelleting of transduced cells and resuspension in expansion medium. The cells were allowed to rest for 48 hours before plating on iMEF feeder plates as described previously. The next steps were carried out in parallel and in the same manner as described for the reprogramming of mesenchymal-like cells.

2.2.6 RO differentiation

Two methods of differentiation were used for generating STGD1 ROs from all iPSC lines (PT1, PT2, WT2, WT3 and AC). These protocols are the BMP4-activated method **(Figure 2.1)** (Hallam *et al.*, 2018) and the IGF1-dependent refined method **(Figure 2.2)** (Zerti *et al.*, 2020). The wild-type control lines WT2 and WT3 are routinely used control iPSC lines that were derived from an earlier publication from our group (Buskin *et al.*, 2018).

BMP4-Activated method

iPSCs at 80% confluence were dissociated to single cells using Accutase (Life Technologies, A1110501) and resuspended in mTEsR1 medium containing 10µM ROCKi. iPSCs were plated at a density of 7,000 cells/well in Lipidure®-Coat Low Adhesion 96 well U-bottom plates (Amsbio, AMS.LCP-A-U96-6) and left to reaggregate for 48 hours (Day -2 → Day 0). Cultures were fed with differentiation medium between Day 0 and 18. This consisted of 45% Iscove's modified Dulbecco's medium (IMDM) (Life Technologies, 12440053), 45% Ham's F12 (Life Technologies, 31765029), 10% KOSR, GlutaMAX, 1% Chemically defined lipid concentrate (Life Technologies, 11905038), 1% Pen/Strep, 450µM 1-Thioglycerol (Sigma Aldrich, M6145), was added to the organoids. Half-medium changes of differentiation medium were conducted every other day until Day 6 when BMP4, at final concentration of 2.2nM was added to the culture medium. At Day 18, the culture medium was switched to maintenance medium which consisted of DMEM/F12 with HEPES, 10% FBS, 1% N2 Supplement (ThermoFisher, A1370701), 1% Pen/Strep, 0.1M Taurine (Sigma Aldrich, T8691), 0.25ug/ml Amphotericin B (Life Technologies, 15290018), with 0.5µM Retinoic Acid (Sigma Aldrich, R2625) added fresh each day until Day 120. Full outlined compositions are shown in **Table 2.2.** Organoids were maintained until Day 220 with feedings taking place 3 times per week.

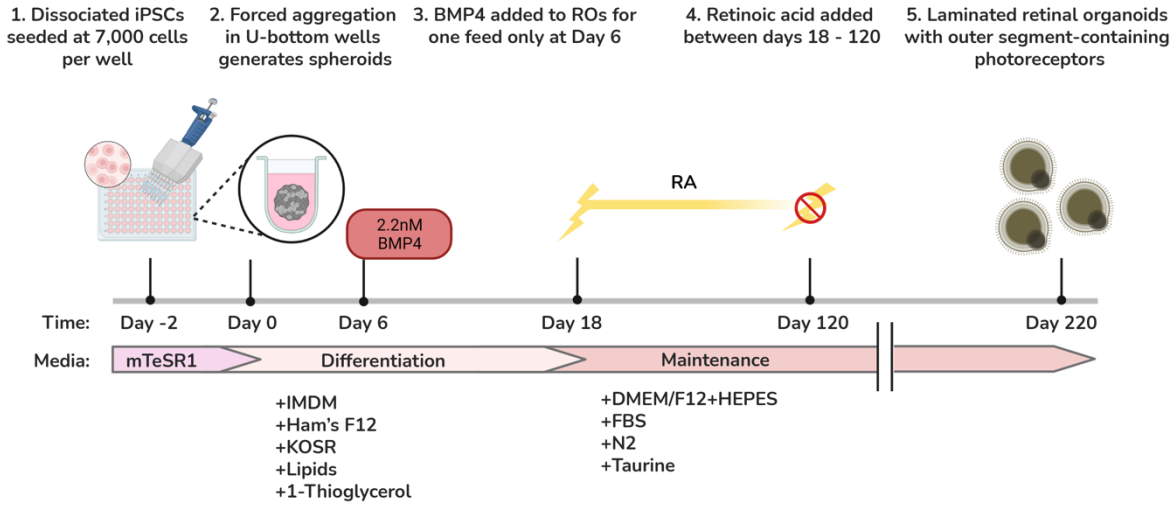

Figure 2.1 Schematic of BMP4-Activated protocol.

BMP4-Activated Protocol	Reagents	Concentration	Company:	Cat code:
	Differentiation Medium (Day 0-18)			
	IMDM	41%	Life Technologies	12440053
	HAMs F12	41%	Life Technologies	31765029
	KOSR	15%	Life Technologies	A3181502
	GlutaMAX	1%	Life Technologies	35050087
	Chemically-defined lipid concentrate	1%	Life Technologies	11905038
	Pen/Strep	1%	Life Technologies	15140122
	1-Thioglycerol	225µM	Sigma Aldrich	M6145
	Maintenance Medium (Day 18+)			
	DMEM/F12	86%	Life Technologies	31330038
	FBS	10%	Life Technologies	10270106
	N2	1%	Life Technologies	A1370701
	GlutaMAX	1%	Life Technologies	35050087
	Pen/Strep	1%	Life Technologies	15140122
	Taurine	1µM	Sigma Aldrich	T8691
	Amphotericin B	0.25µg/ml	Life Technologies	15290018
	Retinoic Acid (until D120)	0.5µM	Sigma Aldrich	R2625

Table 2.2 Media composition of BMP4-Activated protocol.

IGF1-dependent method

iPSCs were initially treated the same as in the BMP4-activated method until Day 0, when differentiation medium was added. This medium consisted of DMEM/F12, 20% KOSR, 2% B27 (Life Technologies, 17504001), 1% Pen/Strep, 1% MEM-NEAAs, 1% GlutaMAX and 5ng/ml IGF1 (Sigma, SRP3069). Medium was half-replaced every second day until Day 18. At Day 18, embryoid bodies (EBs) were transferred to pooled culture in ultra-low-attachment 6-well plates (Corning, 3741) and the medium was switched to Base I Medium consisting of DMEM/F12, 10% FBS, 2% B27, 1% Pen/Strep, 1% GlutaMAX, 1% MEM-NEAAs, 0.25µg/ml Amphotericin B, 0.1M Taurine and 5ng/ml IGF1. At Day 30, the medium was switched to Base II which has the same formulation of Base I with additions of 40ng/ml T3 (Sigma, T6397), 1% N2 Supplement, 1% Chemically defined lipid concentrate and an increase in IGF1 to 10ng/ml. From Day 30 until Day 120, 1µM Retinoic Acid was added to the culture medium fresh each day. The full composition of medium used for this method is outlined in **Table 2.3.**

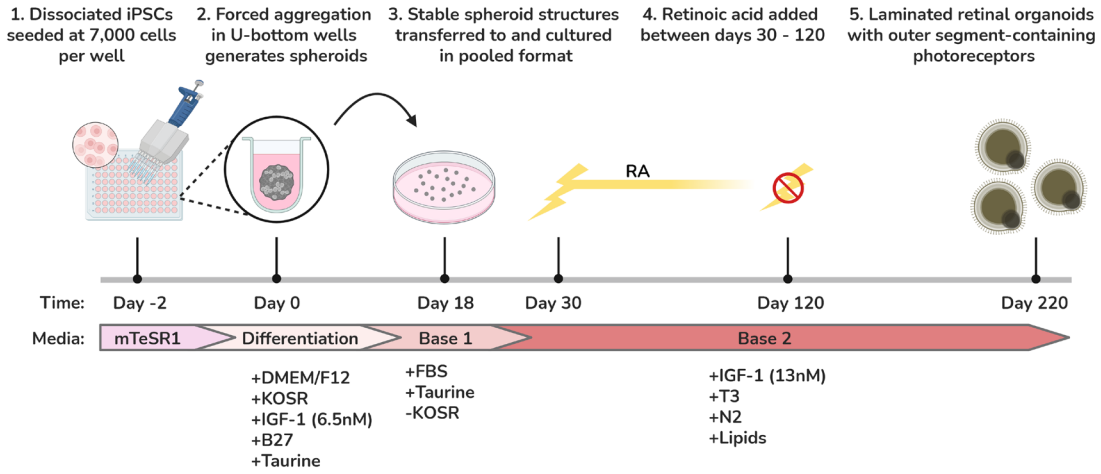

Figure 2.2 Schematic of IGF1-dependent method.

	Reagents	Concentration	Company:	Cat code:
IGF1-Dependent Protocol	**Differentiation Medium (Day 0-18)**			
	DMEM/F12	75%	Life Technologies	31330038
	KOSR	20%	Life Technologies	A3181502
	B27	2%	Life Technologies	17504001
	GlutaMAX	1%	Life Technologies	35050087
	Pen/Strep	1%	Life Technologies	15140122
	MEM-NEAAs	1%	Life Technologies	11140068
	IGF1	5ng/ml	Sigma Aldrich	SRP3069
	Base I (Day 18-30)			
	DMEM/F12	83%	Life Technologies	31330038
	FBS	10%	Life Technologies	10270106
	B27	2%	Life Technologies	17504001
	N2	1%	Life Technologies	A1370701
	GlutaMAX	1%	Life Technologies	35050087
	Pen/Strep	1%	Life Technologies	15140122
	MEM-NEAAs	1%	Life Technologies	11140068
	T3	400ng/ml	Sigma Aldrich	T6397
	Taurine	1µM	Sigma Aldrich	T8691
	Amphotericin B	0.25µg/ml	Life Technologies	15290018
	IGF1	5ng/ml	Sigma Aldrich	SRP3069
	Base II (Day 30+)			
	Base I with these modifications	99%		
	Chemically-defined lipid concentrate	1%	Life Technologies	11905038
	Increased IGF1	10ng/ml	Sigma Aldrich	SRP3069
	Retinoid Acid (until D120)	1µM	Sigma Aldrich	R2625

Table 2.3 Media composition for IGF1-dependent method.

2.3 iPSC Characterisation

2.3.1 RNA Isolation from iPSCs

iPSCs from both patients were cultured as mentioned above. Upon 80% confluency, $2x10^6$ cells per patient were harvested after an incubation with Versene for 3 minutes at 37°C. The cells were pelleted at 300 x g for 4-minutes, washed with PBS and pelleted one again. Samples were snap frozen and stored at -80°C until RNA isolation.

RNA isolation was carried out using the ReliaPrep™ RNA Miniprep System (Promega, Z6011) following manufacturer's specifications. All reagents used are included with the kit. Briefly, cells were lysed over ice with BL buffer and 1-Thioglycerol. Samples were frequently vortexed and pipetted to ensure complete cell lysis. Once lysis was achieved, 100% isopropanol was added to precipitate out the RNA. Cell lysates were then transferred to mini-columns and centrifuged at 14,000 for 30 seconds to facilitate the binding of RNA to the column. The filtrate was discarded, and the column washed once with RNA wash buffer, followed by centrifugation. DNase treatment was carried out for 15-minutes at room temperature to degrade any residual contaminating DNA. A series of washing steps with the RNA wash buffer was then carried out, with centrifugation steps between. Filtrate was discarded at each step. Finally, the RNA was eluted into 30µl of nuclease-free water (NFW) following a 3-minute incubation at room temperature. Concentration of eluted RNA was quantified using Qubit™ 3 Fluorometer (Thermofisher, Q33216).

2.3.2 cDNA Synthesis

Conversion of isolated RNA to cDNA was achieved using the Promega GoScript™ Reverse Transcription System (Promega, A5000). A total of 1µg of RNA was converted to cDNA to yield cDNA concentration 25ng/µl of cDNA. 2µl of random primers (Promega, C1181) were added to experimental RNA, and the full reaction brought up to 10µl with nuclease-free water (NFW). The RNA mixture was incubated at 70°C for 5 minutes, then at 4°C for an additional 5 minutes. The reverse transcription mixture was prepared according to **Table 2.4** for the appropriate number of samples. 30µl of then RT Mix was added to the Pre-RT mix (RNA + Random Primers) and placed in a SensoQuest Thermocycler with the following cycle:

1. 25°C for 5 minutes – Primer annealing
2. 42°C for 1 hour – Extension
3. 70°C for 15 minutes – Enzyme inactivation

cDNA was stored at -20°C until use for qPCR.

Reagents	Volume n=1
Pre-RT Mix	
Experimental RNA	x (1µg)
Random Primers	2µl
NFW	x to 10µl
RT Mix	
GoScript™ 5X Reaction buffer	8µl
25 mM MgCl2	6µl
dNTPs	2µl
Recombinant RNasin Ribonuclease Inhibitor	1µl
GoScript™ Reverse Transcriptase	2µl
NFW	11µl
Total Reaction Volume	40µl

Table 2.4 cDNA Synthesis Recipe.

2.3.3 PCR for Sendai Viral (SeV)Clearance and Pluripotency Gene Expression

Using primers specific for RNA from the Cytotune 2.0 Manual, in addition to primers designed in-house for pluripotency gene expression analysis **(Table 2.6),** PCR was carried out on the newly reprogrammed samples PT1 and PT2, in addition to non-template controls and a positive control for SeV clearance. The Promega GoTaq® DNA polymerase enzyme and buffer (Promega, M3001) were used in combination with dNTP Mix (Promega, C1141). RT-PCR mixture was prepared according to **Table 2.5** for the appropriate number of samples.

SeV Clearance PCR Cycle used as follows for a total of 35 cycles

1. 95°C for 30 seconds – Denaturation
2. 58-64°C for 30 seconds – Annealing (on gradient)
3. 70°C for 30 seconds – Elongation

Pluripotency Genes PCR Cycle used as follows for a total of 30 cycles

1. 95°C for 30 seconds – Denaturation
2. 60°C for 30 seconds – Annealing
3. 70°C for 30 seconds – Elongation

Products were run on a standard 2% Agarose Gel (Bioline, BIO-41026) alongside a 100bp DNA ladder (Thermofisher, SM0243). Products were visualised with the aid of GelRed® Nucleic Acid Stain (Biotium, SCT123) on the Gel Doc-II UV Transilluminator system (BioRad).

Reagents	Volume n=1
50µl Reaction	
GoTaq Reaction Buffer (Clear or Green)	10ul
dNTPs	1µl
Primer Mix (F+R 10µM)	10ul
G2 Polymerase	0.25µl
NFW	27.75µl
cDNA	1µl
Total Reaction Volume	50µl

Table 2.6 PCR Reaction Recipe.

Primer		Sequence		Product Size
SeV Clearance				
SeV_F	5'	GGATCACTAGGTGATATCGAGC	3'	181bp
SeV_R	5'	ACCAGACAAGAGTTTAAGAGATATGTATC	3'	
KOS_F	5'	ATGCACCGCTACGACGTGAGCGC	3'	528bp
KOS_R	5'	ACCTTGACAATCCTGATGTGG	3'	
c-Myc_F	5'	TAACTGACTAGCAGGCTTGTCG	3'	532bp
c-Myc_R	5'	TCCACATACAGTCCTGGATGATGATG	3'	
Pluripotency				
OCT4_F	5'	CTTGAATCCCGAATGGAAAGGG	3'	**164bp**
OCT4_R	5'	GTGTATATCCCAGGGTGATCCTC	3'	
SOX2_F	5'	GGCAGCTACAGCATGATGCAGGAGC	3'	**131bp**
SOX2_R	5'	CTGGTCATGGAGTTGTACTGCAGG	3'	
NANOG_F	5'	AGAAGGCCTCAGCACCTAC	3'	**206bp**
NANOG_R	5'	GGCCTGATTGTTCCAGGATT	3'	
Loading Control				
GAPDH_F	5'	TGCACCACCAACTGCTTAGC	3'	**86bp**
GAPDH_R	5'	GGCATGGACTGTGGTCATGAG	3'	

Table 2.5 Primer sequences for iPSC Characterisation.

2.3.4 PluriTest™ Assay

PluriTest™ assay (Thermofisher, A38154) was carried out externally by Thermofisher Scientific USA. This assay offers high-resolution global assessment of pluripotency. In summary, $1x10^6$ iPSCs were pelleted and shipped to the company on dry ice. RNA was isolated and purified from the provided cell pellet using the PureLink™ RNA Mini Kit (Thermofisher, 12183025) and quantified using the NanoDrop™. Resulting samples were then treated by DNase using the DNA-free™ Kit (AM1906) to remove potential contaminating genomic DNA. 100 ng total RNA was used to prepare the GeneChip® for the PluriTest™. Using the Applied Biosystems™ PrimeView™ Human Gene Expression Array in combination with the PluriTest bioinformatics tool, over 36,000 transcripts and variants are used as a reference to assess pluripotency in provided samples. Both pluripotent and non-pluripotent cells and tissues are features of the reference dataset, such that provided samples can yield pluripotency and novelty scores based on how similar sample transcriptomes are to the reference.

2.3.5 Karyostat™ Assay

Similarly, KaryoStat™ assay (Thermofisher Scientific, 905403) was carried out externally by Thermofisher Scientific USA. Cells were prepared in the same manner as for PluriTest™ assay. In summary, genomic DNA was isolated from provided cell pellets using the Genomic DNA Purification Kit (Thermofisher, K0512) and quantified using the Qubit™ dsDNA BR Assay Kit (Thermofisher, Q32850). 250ng of total genomic DNA was prepared and placed onto a GeneChip® microarray and placed in the KaryoStat™ to look for SNPs, CNVs and single nucleotide polymorphisms across the genome. This assay serves as a great alternative to the G-band karyotyping of stem cells, offering whole-genome coverage for accurate detection of chromosomal aberrations. The KaryoStat™array is optimised for balanced whole-genome coverage with a low-resolution DNA CN analysis, the assay covers all 36,000 RefSeq genes, including 14,000 OMIM® targets. The assay enables the detection of aneuploidies, submicroscopic aberrations, and mosaic events.

2.4 Retinal Organoid Characterisation

2.4.1 Fixation, embedding and cryosectioning of ROs

Samples were collected at Day 35, 60, 120, 180 and 220 for immunohistochemistry. A total of 8 ROs were taken for each iPSC line at each timepoint. ROs were transferred from culture plate to a 1.5ml tube containing PBS. Samples were fixed in 4% paraformaldehyde (PFA) (Thermofisher, 043368.9M) + 5% Sucrose (Sigma Aldrich, S0389) for 30 minutes at 4°C. ROs were then subjected to increased concentrations of sucrose at 6.25%, 12.5% for 1 hour before being left in 25% sucrose overnight at 4°C.

The next day, ROs were transferred to a small culture dish, one at a time, with a thin layer of optimum cutting temperature (OCT) compound (CellPath, KMA-0100-00A). The ROs were swirled around in the dish to remove residual sucrose. A thin layer of OCT was also added to cryomoulds (Tebu-bio UK, 18985-1) to prevent the destruction of POS when the RO was transferred into it. Once sufficient clearance of sucrose and the RO had sunk in the OCT, the ROs were transferred, using the viscosity of the OCT, and not touching the organoid, and positioned within the cryomould. Once all ROs were positioned correctly, the samples were snap frozen on dry ice and stored at -20°C. 10µm sections were taken using Leica cryostat (CM1850) and mounted onto Epredia™ SuperFrost Plus™ Adhesion slides (Thermofisher, 10149870).

2.4.2 Immunostaining of ROs

A panel of markers was used for each of the 5 development timepoints used in this study. A full list of antibodies used is presented in **Table 2.7.** Pre-processed post-mortem retinal tissue was also used for validation of ABCA4 antibodies and was stained in the same manner as ROs.

Slides were defrosted for an hour in a humidified staining chamber. 3x 10-minute PBS washes were conducted to rehydrate the sections and remove OCT surrounding the tissue. The samples were then blocked and permeabilised using 0.003% Triton-X-100 (Sigma Aldrich, 93443) and 10% normal goat serum (NGS) (Sigma Aldrich, S-26) in PBS for 1 hour at room temperature. In the meantime, primary antibodies were prepared according to their optimised dilutions in antibody diluent consisting of 0.001% Triton-X-100 and 1% NGS in PBS. Primary antibodies were then applied to the slides and left overnight at 4°C. The following day, sections were washed as previously with PBS as previously described and samples

incubated with secondary antibodies (1:1000 dilution) in PBS for 2 hours at RT. Slides were washed again with PBS before counterstaining with Hoechst in PBS (1:1,000) for 15 minutes. 3x 5-minute PBS washes were performed thereafter, and cover slips were mounted using Dako Mounting Medium (Agilent, S3023). Slides were stored at 4°C until imaging. Slides were imaged using the Zeiss AxioImagerZ2, equipped with an Apotome2 (Zeiss, Germany). A total of 5-10 images was taken per antibody combination, using several sections of the 8 different ROs. Final images are presented as a maximum intensity projection and adjusted for brightness and contrast in Adobe Photoshop (Adobe Creative Cloud).

Antibody:	Host:	Company:	Cat code:	Dilution:
Primary Antibodies				
AP2α	Mouse	Santa Cruz Biotechnology	SC-12726	1 in 200
PROX1	Rabbit	Millipore	AB5475	1 in 1500
CRX	Mouse	Abnova	H00001406-M02	1 in 200
VSX2	Rabbit	Sigma Aldrich	HPA003436	1 in 50
CRALBP	Mouse	Abnova	ab15051	1 in 200
PKCα	Mouse	BD Transduction Laboratories	610107	1 in 200
ABCA4	Mouse	Millipore	MABN2440	1 in 25
Recoverin	Rabbit	Millipore	AB5585	1 in 1000
SNCG	Mouse	Abnova	H00006623-M01A	1 in 500
Ki67	Mouse	BD Pharmingen	550609	1 in 50
CASP3	Rabbit	Cell Signalling	9661S	1 in 400
OPN1MW/LW	Rabbit	Millipore	AB5405	1 in 200
OPN1SW	Rabbit	Millipore	AB5407	1 in 200
RHOD	Mouse	Sigma Aldrich	O4886	1 in 200
GT335	Mouse	AdipoGen Life Sciences	AG-20B-0020	1 in 1000
ARR3	Rabbit	Novus Biological	NBP2-41249	1 in 100
ABCA4	Rabbit	Abcam	ab72955	1 in 100
Secondary Antibodies				
anti-Mouse A488	Goat	Jackson Immuno Research	115-545-146-JIR	1 in 1000
anti-Rabbit Cy3	Goat	Jackson Immuno Research	111-165-003-JIR	1 in 1000

Table 2.7 Primary and Secondary Antibodies used for Immunostaining.

2.4.3 Quantification of RO immunostaining

Quantification of positively stained cells was achieved using Zen® Blue Software (Zeiss, Germany) and MATLAB® (MathWorks®, MA) as described in Dorgau *et al.* (2019). Briefly, this script facilitates the cropping of neuroretinal regions from the RO images and subsequent identification of individual cell types using Hysteresis thresholding techniques to filter background noise. This facilitates the identification of each cell type within blue, green, and red fluorescent channels yielding information regarding cell size, average intensity values and length. Following this, the total size, and the percentage of the positive cells in red/green channel (retinal markers) that colocalise with cells of the blue channel (Hoechst nuclear marker) are exported to Excel and used for assessing composition of ROs and performing statistical analysis. A minimum of 5 images of ROs in each condition at each timepoint are used for quantification analysis. ABCA4 and CRALBP could not be quantified using this method, consequently, they were not measured.

2.4.4 Protein Isolation from ROs

16 ROs were collected per iPSC sample at Day 220 of differentiation to assess levels of ABCA4 protein expression. Cell lysates were prepared from pelleted ROs using ice-cold RIPA lysis buffer (Millipore, 20188) containing an EDTA-free protease inhibitor cocktail (Sigma Aldrich, 11873580001). Samples were incubated with the lysis buffer for 30 minutes on ice with frequent pipetting at 10-minute intervals to assist in the dissociation and lysis of the cells. Completely lysed samples were centrifuged at 1000 x g for 5 minutes at 4°C. Supernatants were collected and protein concentration quantified using the colorimetric Pierce BSA Protein Assay following manufacturer specifications.

2.4.5 Western blotting

30µg of protein from each RO sample were mixed with Novex Tris-Glycine SDS Sample Buffer (Thermofisher, LC2676) and NuPAGE Sample Reducing Agent (Thermofisher, NP0004), and subsequently incubated at 85°C before loading onto Novex™ Tris-Glycine Mini Protein Gels, 4–12%, 1.0 mm, WedgeWell™ format (Thermofisher, XP04125). Samples were separated in Novex Tris-Glycine SDS Running Buffer (Thermofisher, LC2675) alongside PageRuler Plus Prestained Protein Ladder (Thermofisher, 26619). Due to the large size of ABCA4 protein (~250kDa), the gel rig was run at 90V for 20 minutes, then increased to 120V for up to 2 hours. Proteins were transferred to PVDF membrane via wet transfer method. The membrane was

activated in 10% methanol and sandwich prepared in the order: 2 sponges, filter paper, gel, membrane, filter paper and 2 sponges. Transfer of samples was conducted at 30V for 90 minutes in Novex Tris-Glycine Transfer Buffer (Thermofisher, LC3675).

Primary antibodies were incubated with the membrane on a roller overnight at 4°C **(Table 2.8).** The following day, the membrane was incubated with secondary antibodies for 1 hour at room temperature. The signal was processed using SuperSignal™ West Pico PLUS Chemiluminescent Substrate (Thermofisher, 34580), visualised and analysed by Amersham Imager 600 (GE, USA) with ACTB as loading control.

Antibody:	Host:	Company:	Cat code:	Dilution:
Primary Antibodies				
ABCA4	Rabbit	Abcam	ab72955	1 in 100
ACTB	Mouse	Santa Cruz Biotechnology	sc-47778	1 in 500
Secondary Antibodies				
anti-Mouse IgG-HRP	Rabbit	Agilent Dako	P0260	1 in 2000
anti-Rabbit IgG-HRP	Swine	Agilent Dako	P0399	1 in 2000

Table 2.8 Primary and Secondary Antibodies used in Western Blotting.

2.5 Single Cell RNA Sequencing (scRNA-Seq)

2.5.1 Dissociation of ROs to single cells and sequencing library preparation

Originally due to sample availability and cost limitations, we performed scRNA-Seq on ROs from PT2, AC, WT2 and WT3 only and omitted PT1 ROs. A minimum 25 ROs per sample were harvested at Day 200 of differentiation and enzymatically dissociated to single cells using the Neurosphere Dissociation Kit (P) (Miltenyi Biotech, 130-095-943) following the manufacturer's protocol. Cell capture and sequencing libraries were generated using the Chromium Single Cell 3' Library and Gel Bead Kit v3.1 (10x Genomics, PN-1000121).

2.5.2 Data processing and quality control

Once libraries were generated for each sample, they were sequenced by the BSU at Newcastle University up to 50,000 reads per cell on the NovaSeq 6000 (Illumina). CellRanger mkfastq v3.1 was used to de-multiplex resulting BCL files into FASTQ files. Samples were then aligned to human reference genome GRCh38 for annotation and subsequent generation of gene

expression matrices for each sample. Quality control was carried out in R Studio (Posit) on the annotated reads with thresholds set to remove reads with ≤ 1000 reads or ≤ 500 genes. Cells with mitochondrial reads ≥ 10% were also removed from the dataset. Doublets were identified and removed using DoubletFinder v2.0.3 (McGinnis, Murrow and Gartner, 2019).

For each sample, individual normalisation was performed using Seurat (v3.1.3), an R toolkit designed for single-cell genomics analysis. Subsequently, the data were subjected to dimension reduction through PCA using the top 2000 highly variable genes. To alleviate batch effects within the datasets, we integrated the first 30 principal components of each sample using Harmony v0.1.1, resulting in the creation of a unified integrated dataset. Visualisation of the data involved the utilisation of Uniform Manifold Approximation and Projection (UMAP), which was based on the initial 10 batch-corrected coordinates and the clusters identified by Seurat. Differentially expressed markers between each cluster were identified using the Seurat FindMarkers function with the method Wilcoxon test. These genes were used to group cell types into population clusters on the UMAP at a resolution of 0.5.

Differential gene expression analysis was conducted using the Ingenuity Pathway Analysis (IPA) Software (Qiagen) to look for changes in ROs between PT2, affected control and wild-type ROs. IPA assisted in evaluating the functional aspects related to disease and the canonical pathways linked to the lists of differentially expressed genes (DEGs). Biostatistics were performed by the BSU in Newcastle University using R Studio.

2.5.3 Statistical Analysis

Statistical analyses on quantified fluorescence data from all ROs were conducted via GraphPad Prism v10 (GraphPad Software, LLC). One-way ANOVA (Šídák's multiple comparisons test) was primarily used to compare mean cell percentages ± SEM values of each retinal marker within distinct protocol subsets. Such that PT1 ROs were compared with AC and WT2 ROs in IGF1-dependent method, and PT2 ROs were compared with WT2 ROs in the BMP4-activated method. One-way ANOVA was also used in the same manner for assessing the relative expression of ABCA4 in Western blotting experiments across all samples at Day 220 of differentiation.

Statistics for scRNA-Seq experiments were conducted on R-Studio. The p-values associated with the plots in this dataset are from Fisher Exact test which was used to measure the differences in abundances between different phases of cell cycle and abundance of apoptotic transcripts within photoreceptors across samples.

Values of $p \leq 0.05$ were considered statistically significant (* = p-val ≤0.05, ** = p-val ≤ 0.01, *** = p-val ≤ 0.001, **** = p-val ≤ 0.0001).

2.6 Whole Genome Sequencing (WGS)

2.6.1 DNA Isolation

DNA was isolated from PT1, PT2, WT2 and AC iPSC lines for the purpose of WGS and mutation validation thereafter. iPSCs were pelleted and DNA was isolated using the QIAamp DNA Mini Kit (Qiagen, 56304) according to manufacturer specifications with extra optional steps to increase overall yield. Samples were eluted into 200µl of NFW. DNA concentrations were quantified by NanoDrop and samples were stored at -20°C until later use.

2.6.2 WGS of Samples

WGS on PT1 and PT2 iPSC-DNA was carried out by the Genomics Core Facility (GCF) at Newcastle University under the supervision of Dr. Jonathan Coxhead. Samples were sequenced on the NovaSeq 6000 Platform using a standardised SOP. Raw data was then processed by the BSU at Newcastle University – specifically Dr. Michael McCorkindale. FASTQ files resulting from the sequenced samples were subjected to quality control measures

including the removal of low-quality reads and adapter contamination using Cutadapt tool. Duplicates were marked and removed using Picard. Samples were aligned to GRCh38 human genome and annotated for variant calling where single nucleotide variants (SNVs), and small insertions/deletions (indels) were identified using the Genome Analysis Toolkit (Broad Institute). Called variants were filtered on resulting vcf files using a homemade Macular disease gene panel. Using Excel, variant prioritisation was carried out on the basis of pathogenicity scores (CADD, SIFT, PolyPhen-2, REVEL) and minor allele frequencies (MAF).

2.6.3 Validation of candidate variants from WGS

Variants identified in the .vcf files from WGS were validated using Sanger sequencing, performed by Dr. Bilal Alobaidi at Newcastle University. In preparation for this, mutation-specific primers were designed and desired products from PT1 and PT2 were amplified by PCR. Primers were generated using sequences obtained approximately 250bp upstream and downstream of the mutation of interest. These sequences were captured using the Integrated Genome Browser (IGV) genome browser and input into Primer 3 software (https://primer3.ut.ee/) to generate primers yielding products no more than 500bp in size. *In-silico* PCR tool (https://genome.ucsc.edu/cgi-bin/hgPcr) was used to ensure no unspecific binding of the primer and only the product of interest was amplified. DNA primers were synthesised by Sigma Aldrich and sent in liquid at 100µM concentration.

PCR was carried out as described for pluripotency assessment in **Section 2.3.3.** Mutation-specific primers used to validate candidate mutations is displayed in **Table 2.9.** PCR products were visualised via gel electrophoresis and imaging as described previously. Remaining PCR products were purified to remove residual primers using QIAquick PCR Purification Kit (Qiagen, 28104) and sent for Sanger sequencing. The sequence obtained from the Sanger traces was aligned with the reference DNA product using Clustal Omega (https://www.ebi.ac.uk/Tools/msa/clustalo/) to quickly detect mismatches and confirm mutation.

Primer		Sequence		Product Size
ABCA4				
c.5461-10T-C_F	5'	CGGTAACCCTCCCAGCTTT	3'	358bp
c.5461-10T-C_R	5'	AAACCCATGATGCTCTGCTG	3'	
c. 5603AT_F	5'	AAAACATTGTGGAGTGGGGC	3'	369bp
c. 5603AT_R	5'	CTTATGAGGCGGGTGTTTGG	3'	
c.4685T>C_F	5'	CAGCAGCAGTGGGAAAAGAG	3'	306bp
c.4685T>C_R	5'	TCCTACTCAAATCTCCAGTCTGT	3'	
PRPH2 EKG Haplotype				
EKG_F	5'	CAGCGATTCTCCCAGATTGC	3'	**374bp**
EKG_R	5'	TAAGATGGTGCCCTCCTTGG	3'	
ROM1				
ROM1_F	5'	GCAGCTCTATACCCTCCCTG	3'	**348bp**
ROM1_R	5'	aggaagggagACGCAAATCA	3'	

Table 2.9 Primer Sequences for Validating Candidate Variants from WGS.

2.7 Long-read RNA Sequencing (LRS)

2.7.1 Sample preparation

RNA was harvested from PT1, PT2 and WT2 ROs at Day 220 to ensure the full development of photoreceptor cells to secure mature *ABCA4* transcripts for LRS. ROs were cultured with a nonsense-mediated decay inhibitor – Puromycin (Sigma Aldrich, P7255) for 7 hours prior to harvest. RNA was isolated as described in **Section 2.3.1.** RNA-integrity number (RIN) was >9 for both samples.

2.7.2 Sequencing of Samples with PacBio LRS

LRS on the RNA samples prepared was carried out by the NU-OMICs facility, specifically Dr. Andrew Nelson at Northumbria University using the PacBio Sequel sequencer (Pacific Biosciences). RNA sequencing was carried out following the IsoSeq protocol to enable full-length transcriptome sequencing. Briefly, RNA is converted to cDNA and unique molecular barcodes (known as PacBio SMRTbell adaptors) are added to individual cDNA molecules to circularise cDNAs to encourage increased read depth via circularised consensus sequencing (CCS). The barcoded library pool is then subjected to real-time SMRT sequencing which produces long read lengths which can span entire transcripts, enabling its use in full-length transcriptome analysis, and in the identification of novel isoforms and alternative splicing events (Gonzalez-Garay, 2016).

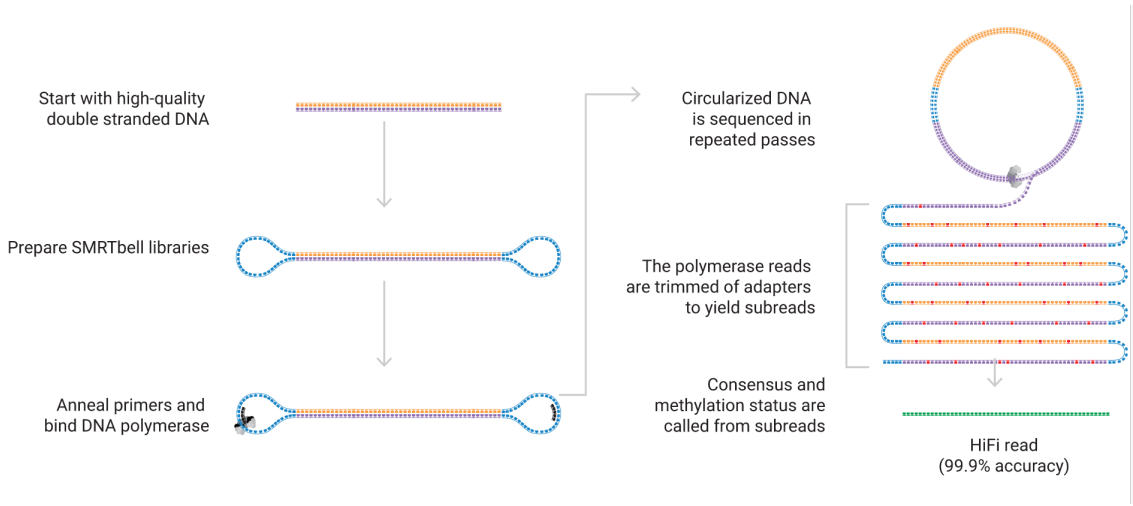

Figure 2.3 Library Preparation with PacBio System

Image source: https://www.pacb.com/technology/hifi-sequencing/

2.7.3 Analysis of Raw Data from LRS

Raw data was analysed by our collaborators Dr. Ana Conesa and Dr. Luìs Ferrandes at Valencia Polytechnic University in Spain. To calculate percent spliced-in (PSI) for *ABCA4* exons 39 and 40, we first aligned the Iso-Seq HiFi reads from the two patients and the control against hg19 assembly using minimap2 (v. 2.17-r941) with the following mapping parameters: -ax splice:hq -uf --MD -t 12 (Li, 2018). SAM files were converted into BAM and then indexed using Samtools (Li *et al.*, 2009). Spliced reads mapping to ABCA4 were quantified using ggsashimi (Garrido-Martín *et al.*, 2018) discarding any splice junctions with only one supportive read. PSI for exon skipping events was calculated considering exon inclusion and exclusion reads as in Saraiva-Agostinho and Barbosa-Morais (2019).

Transcript models were generated from HiFi reads following the official PacBio pipeline. Quality control of generated transcript models in the three samples was performed using SQANTI3 (Tardaguila *et al.*, 2018) which was also used to predict the open reading frames (ORFs) encoded in the RNA transcripts. The comparison between ABCA4 canonical protein (encoded in PB.390.3 transcript model from PT1) versus the truncated protein (encoded in PB.390.4 transcript model from PT1, which skips exon 39) was represented using tappAS (de la Fuente *et al.*, 2020). To include annotated protein features in the representation (e.g., protein domains or PTMs), transcript coordinates were first projected from hg19 to hg38 using UCSC LiftOver with default settings (Hinrichs *et al.*, 2006) and then IsoAnnotLite was used to annotate protein features in the predicted ORFs based on Ensembl v86 (hg38).

The three-dimensional representation of ABCA4 (P78363 from UniProt) was generated with iCn3D software (Wang *et al.*, 2020). 1,821-2,273 amino acid residues were highlighted to indicate the protein truncation resulting from exon 39 skipping. This protein region was selected based on a pairwise alignment (Madeira *et al.*, 2022) between the predicted coding sequences from PB.390.3 and PB.390.4 transcript models (PT1).

Chapter 3 Reprogramming and culture of monoallelic STGD1 patient iPSCs

3.1 Introduction

iPSC generation has had a profound impact on the research of human health and disease. The procedure of extracting somatic cells from human participants is relatively non-invasive and the overall process from start to finish can take as little as 1 month. Fibroblasts from skin (Takahashi *et al.*, 2007), PBMCs (Loh *et al.*, 2010) and erythroblasts (Yang *et al.*, 2008) from blood, renal tubular cells from urine (Zhou *et al.*, 2011) and keratinocytes from hair (Aasen *et al.*, 2008) have all been shown to be successful sources of cells for cellular reprogramming. From these PSCs, numerous terminally differentiated cells and tissues can be generated *in vitro*, supplying an abundant source of patient/disease-specific material to investigate amenably in the lab. This technology is particularly useful in the understanding of inherited retinopathies like STGD1, as iPSCs can be used to develop ROs and RPE, giving researchers access to tissue that otherwise would be inaccessible and unavailable.

The pluripotent capabilities of iPSCs enable indefinite culturing periods, allowing them to be genetically manipulated and edited with molecular tools such as Clustered Regularly Interspaced Short Palindromic Repeats (CRISPR) technology – as reviewed here (De Masi *et al.*, 2020). This is important for the generation of isogenic cell lines, knockout cell lines, corrected patient cell lines and many more. Particularly, isogenic iPSC lines are crucial for disease studies to negate the effects of genome variability between patient participants with the same genetic condition. With these strategies, researchers can gain greater scope over the function of genes in developing tissues, whilst also understanding the molecular pathogenesis of inherited diseases in tissue-specific contexts.

Despite their many applications in biological research, iPSCs do display limitations such as their efficiency in generation, retention of somatic cell epigenetic state and their tendency for genome instability over time. Numerous approaches now exist for the generation of iPSCs. However, the average efficiency of this process remains within the range of 0.1 – 4% for urine-derived somatic cells (Zhou *et al.*, 2011), and even lower for fibroblasts (Trevisan *et al.*, 2017) and blood-derived cells (Seki *et al.*, 2010). More recent approaches report the ability to reprogram at an efficiency of 800% using synergistic synthetic mRNAs encoding pluripotency factors alongside miRNA-367/302 (Kogut *et al.*, 2018). This high efficiency rate suggests multiple iPSC colonies can be derived from the same somatic cell.

It is believed that cellular reprogramming of somatic cells resets DNA methylation patterns. However, methylation signatures of somatic cells have been seen in low passage iPSCs. This has implications on the differentiation of such cells as it creates a tendency of the iPSCs to differentiate into the cell type from which they were derived (Kim *et al.*, 2011). Over time, iPSCs have also been shown to accumulate genomic aberrations, typically in the form of amplifications resulting from long-term culturing but also include sub-chromosomal CNVs and point mutations (Laurent *et al.*, 2011). These aberrations can cause the cells to behave differently, making it difficult to attribute experimental results to a disease-specific phenotype. It is also concerning in the context of clinical application as stem cell-derived therapeutics must be genomically stable to be safe for use in humans. Indeed, the continuation of the first stem-cell derived therapeutic for the treatment of AMD was halted following the identification of genomic instability in the cells used for developing the product (Garber, 2015). For the reasons outlined above, it is important to characterise newly generated iPSCs in the context of their morphology, clearance of reprogramming viral vectors, gene expression profiles, differentiation ability and genomic stability.

3.2 Aims

This chapter aims to explore the derivation and characterisation of iPSCs generated from the primary cells of two individuals diagnosed with monoallelic late-onset STGD1 by:

- Attempting to rescue previously reprogrammed patient iPSCs which display a refractory phenotype
- Differentiating refractory iPSCs to mesenchyme for supplemental cellular reprogramming
- Transducing two patient cell lines with SeV RNA-based reprogramming system (Cytotune 2.0) in the efforts to produce viable iPSC clones for later differentiation studies
- Confirming the removal of SeV vectors and expression of pluripotency genes in generated iPSC clones
- Investigating the pluripotent potential of resulting iPSC clones to form embryoid bodies (EBs)
- Assessing genome stability post-reprogramming

An overview of the experimental aims in this chapter is illustrated graphically in **Figure 3.1.**

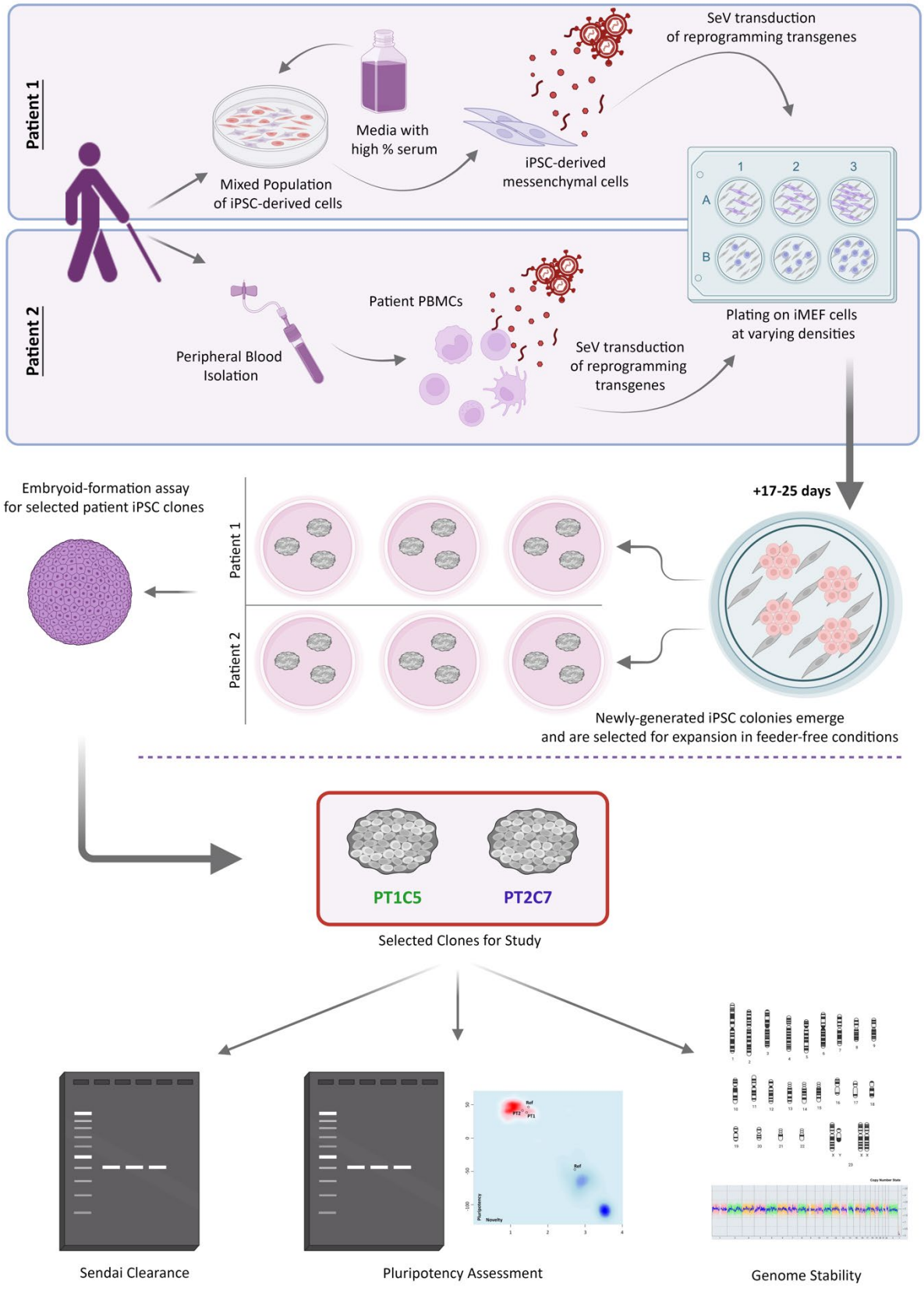

Figure 3.1 Graphical overview of chapter

3.3 Results

3.3.1 Patient 1 iPSCs display a non-rectifiable refractory phenotype

iPSCs from Patient 1 had previously been derived by our collaborators at Radboud University Medical Centre (RUMC), The Netherlands. This was achieved using a lentiviral vector delivery system to transduce patient fibroblasts with the necessary reprogramming factors. However, upon culture of the provided iPSC clone, we saw a persistent refractory phenotype with a high propensity for spontaneous differentiation combined with poor cell viability **(Figure 3.2 A).** The colonies did not display discrete borders, and individual cells within the colony were not tightly packed, as evidenced by the presence of gaps within the colonies. A large degree of differentiated cells persisted in the regions surrounding the colonies. Although these differentiated cells were non-uniform, the majority appeared to be of mesenchymal lineage with spindle-shaped cell bodies and large nuclei. Despite several rounds of mechanical and enzymatic cleaning regimes, it was not possible to eliminate the differentiated cell types. This atypical stem cell morphology and behaviour is reminiscent of partially reprogrammed clones.

Without access to the original primary cells of Patient 1, we opted for a secondary round of reprogramming on the defective iPSCs. To achieve this, feeding medium was replaced with fibroblast medium which consisted of a high serum concentration to direct any stem cell-like cells to differentiate into mesenchymal/fibroblastic-like cells as described in **Section 2.2.2 (Figure 3.2 B).** Following a 7-day feeding and maintenance schedule, a confluent well of fibroblastic mesenchymal-like cells was achieved approximately 20 days later **(Figure 3.2 C)** and was ready to undergo additional reprogramming

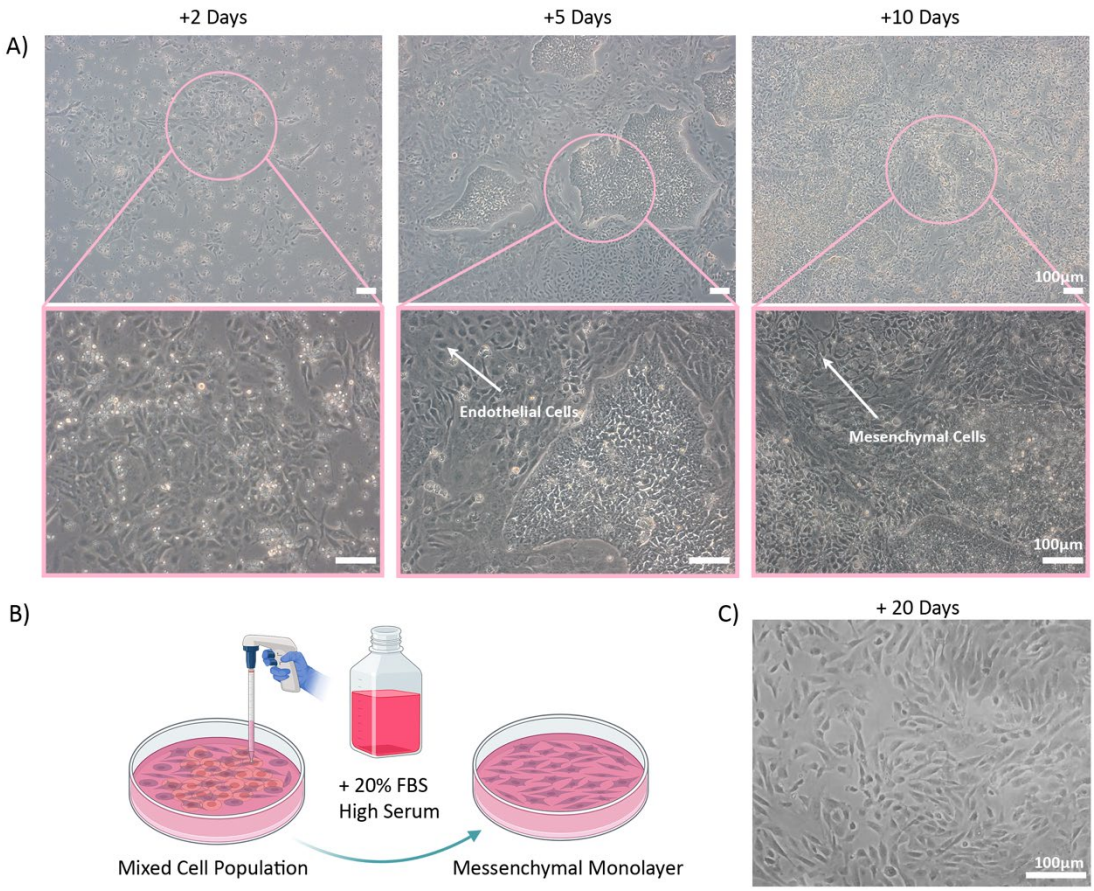

Figure 3.2 Refractory phenotype of Patient 1 iPSCs

A) Brightfield images of iPSC culture at 5x and 10x magnification at +2-, +5- and +10-days post-thaw. Non-uniform cell population is observed at each time point. iPSC colonies grow larger over a period of 10 days but continuously spontaneously differentiate as shown by presence differentiated cell types (fibroblastic and endothelial in morphology) surrounding the colonies. **B)** Mechanism for directed differentiation of refractory iPSCs to mesenchyme. **C)** +20 days post-thaw with high-sera medium, a monolayer of mesenchyme is achieved for the purpose of additional reprogramming. All scale bars are 100µm.

3.3.2 Patient 1 and Patient 2 produce many viable clones

Shortly following transduction of patient primary cells with transgene-expressing SeV from Cytotune 2.0 (an RNA-based cellular reprogramming system)**(Section 2.2.5),** we began to observe small, dome-shaped colonies with tightly packed cells at Day 11 **(Figure 3.3).**

Over the course of 17-25 days, with manual cleaning and careful monitoring, several of these colonies grew larger and flatter with discrete borders. Inside the colonies, cells were uniformly round and displayed a high nuclear-to-cytoplasmic ratio, comparable to iPSCs and therefore indicative of successful cellular reprogramming. In the remaining colonies, there was evidence of partial reprogramming with discontinuous colony borders and non-uniform cell morphology. This is likely a consequence of spontaneous differentiation. These clones were avoided when selecting clones to propagate further in feeder-free conditions with the Matrigel basement membrane matrix.

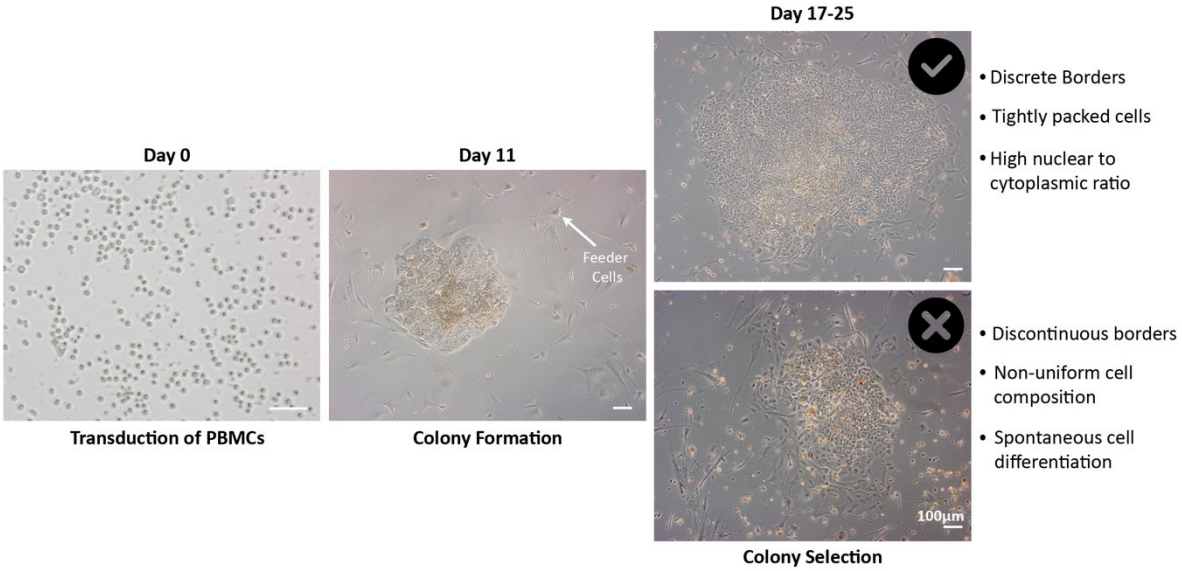

Figure 3.3 Reprogramming of PBMCs to iPSC

PBMCs were successful reprogrammed to iPSC following a 25-day transduction protocol using SeV transgene vectors. By Day 11, colony formation was evident. After an additional week of growth, colonies were morphologically assessed and selected for propagation to feeder-free conditions.

Many clones arose from this experiment on the reprogramming plates of both PT1 and PT2, however only clones that displayed key morphological features of successfully reprogrammed cells were selected for further propagation in feeder-free conditions. The propagation of selected iPSC clones was achieved via mechanical passaging **(Figure 3.4 A).** Feeder cells were cleared from the perimeter of the colony, followed by the sectioning of the colony into small

pieces using a p10 micropipette tip. The colony sections were transferred and seeded to a freshly prepared Matrigel coated well. All the sections of one clone were transferred to 1 well. Once 80% confluence was achieved, the clones were enzymatically dissociated and split at ratios of 1:3 into new Matrigel-coated wells.

Following propagation and expansion of these clones on Matrigel, we observed some evidence of partial reprogramming in both PT1 and PT2 clones, with characteristic spontaneous differentiation in culture. Disproportionately more colonies from PT1 failed adaptation to feeder-free culturing conditions, whilst the majority of PT2 clones adapted sufficiently. This resulted in 6 individual iPSC clones of PT1 and 20 clones from PT2 capable of culture on Matrigel-coated plates. Many of the successfully adapted clones were frozen as reserves, whilst 3 clones from each patient were maintained in continuous culture until Passage 16 **(Figure 3.4 B)** and then used for differentiation screening to embryoid bodies (EBs) using in-house protocols described in **Section 2.2.6**.

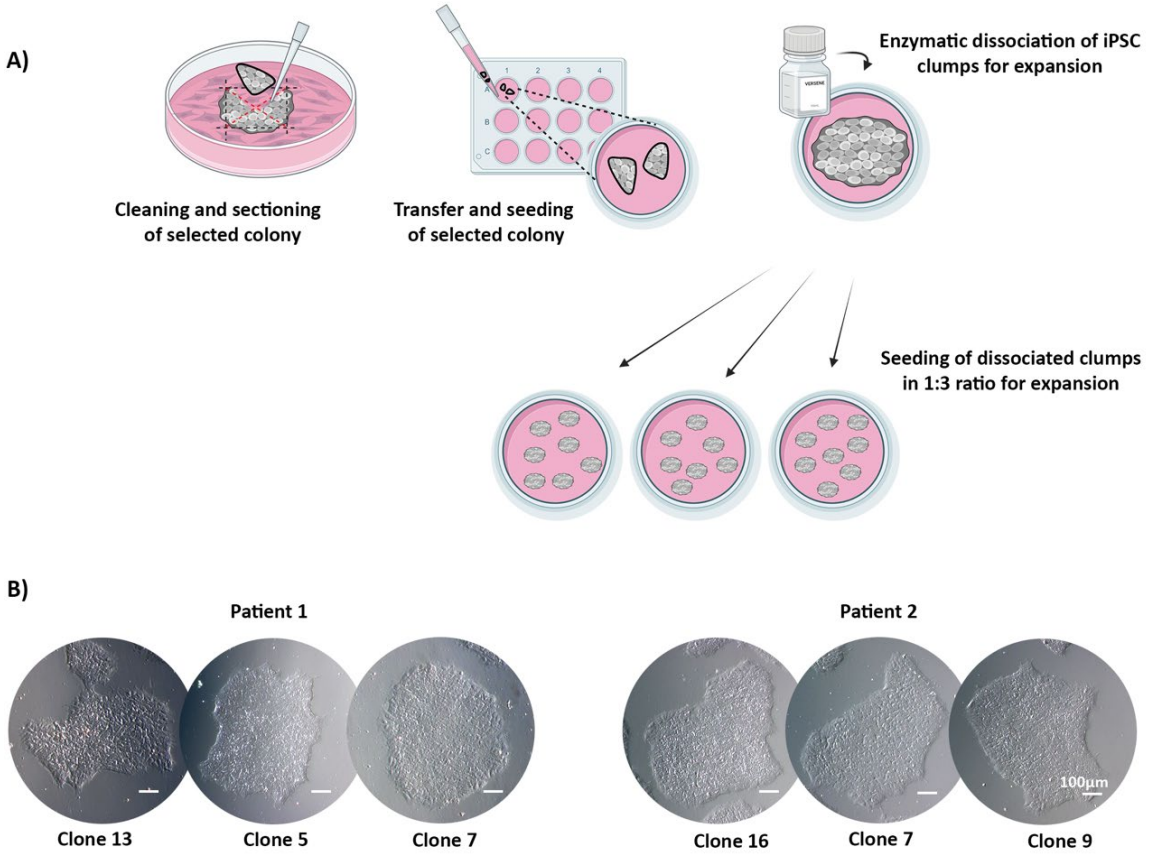

Figure 3.4 Adaption of selected clones to feeder-free conditions

A) Mechanism of colony selection and propagation in feeder free conditions. Under sterile conditions, the borders of the selected colony are cleared from feeder cells. The colony is then sectioned into smaller pieces and gently scraped up and transferred to one well of a 12-well plate in Matrigel. Once the well is confluent several days later, the iPSCs are enzymatically dissociated into clumps and passaged at a ratio of 1:3, enabling their expansion.
B) Three clones from both Patient 1 and Patient 2 adapted well to feeder-free conditions on Matrigel. Brightfield images of the colonies show discrete colony borders, tightly packed cells with no evidence of spontaneous differentiation. All scale bars are 100µm.

3.3.3 Pluripotency of clones is confirmed by their ability to differentiate to EBs

To select one clone from the three expanded to carry further into the study, we subjected each of the clones from both patients to an EB-forming assay at P16 using two RO differentiation protocols routinely used in our lab; BMP4-activated (Hallam *et al.*, 2018) and IGF1-dependent (Zerti *et al.*, 2020) methods. EBs were generated using a forced aggregation method in U-bottom wells for up to 15 days before assaying. At day 15, brightfield images were collected and the EBs were scored based on their colour (dark inner core, bright apical perimeter), size, presence of smooth round edge and presence/absence of cystic structures to give an overall EB-forming efficiency per plate of 96 EBs. A large degree of variability was observed in the ability of these clones to produce EBs and thus ROs, however the latter is discussed in greater detail in **Chapter 4.**

Of all the clones tested, it was apparent that Clone 5 of Patient 1 (PT1C5) in IGF1-dependent and Clone 7 of Patient 2 (PT2C7) in BMP4-activated protocols could produce morphologically consistent EBs with the highest efficiency – 50% + 80% respectively **(Figure 3.5).** The EBs of these clones were the only ones to later form a bright phase layer along the perimeter of the developing organoids, reminiscent of nascent neuroepithelium with an inner dark core. Other clones produced lobular bodies and cystic structures with little or none neuroepithelium. From this result, we proceeded with the clones PT1C5 and PT2C7, denoted **Patient 1 (PT1)** and **Patient 2 (PT2)** for the remainder of the study.

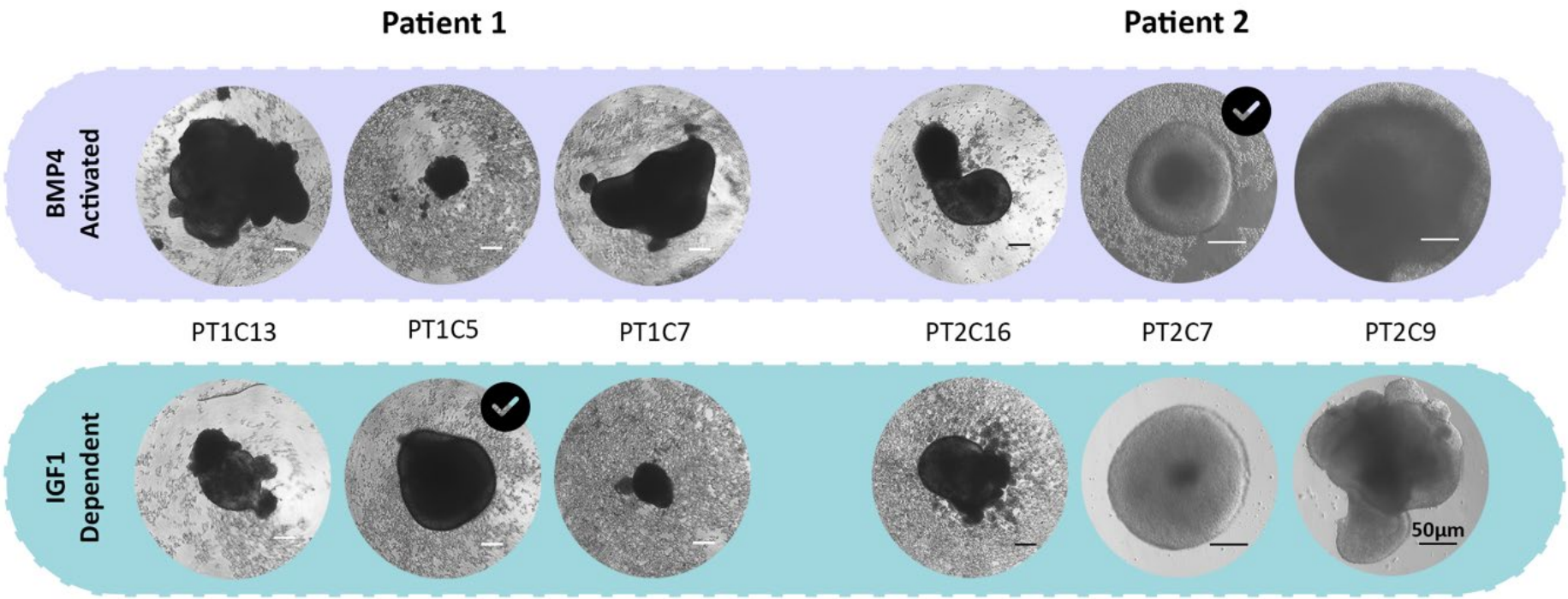

Figure 3.5 EB-forming assay of Patient 1 and Patient 2 clones

The ability of each clone of Patient 1 and Patient 2 to produce embryoid bodies was assessed via the directed differentiation of iPSCs towards retinal lineage. Two published protocols by our group (BMP4-activated & IGF1-dependent) were utilised in this experiment, which both involve a crucial EB-forming step within the first week of differentiation. Significant variability was observed in the clones with Patient 1 iPSCs forming viable EBs by Day 15 only in the IGF1-dependent protocol and Patient 2 in the BMP4-activated protocol. Brightfield images show how the EBs appeared at Day 15 in both protocols for all clones. Ideal candidate EBs should be rounded with a dark core and a bright-phase primitive neuroepithelium beginning to form on the apical edge. All scale bars are 50µm.

3.3.4 Patient iPSCs are clear from SeV vectors prior to differentiation

At the same time as the EB-forming assay, cell pellets were collected from each clone at P16 to test for the presence of SeV vectors and associated pluripotency factor transgenes. This was achieved via RT-PCR and gel electrophoresis (**Section 2.3.3)** with freshly transduced cells as a positive control and a routinely used iPSC line as negative control **(Figure 3.6).**

No bands, except for *GAPDH* (86bp), were observed in cDNA from PT1, PT2, or WT2 – serving as a negative iPSC control. In contrast, cDNA from a positive control (cells transduced for 24 hours and immediately frozen) displayed several bands corresponding to *GAPDH* (86bp*), SeV* (181bp), *c-MYC* (532bp) and *KOS* (528bp), as anticipated. The absence of these bands in cDNA from the patient iPSCs confirms their clearance of SeV vectors prior to their differentiation to EBs and subsequently, to ROs in **Chapter 4.**

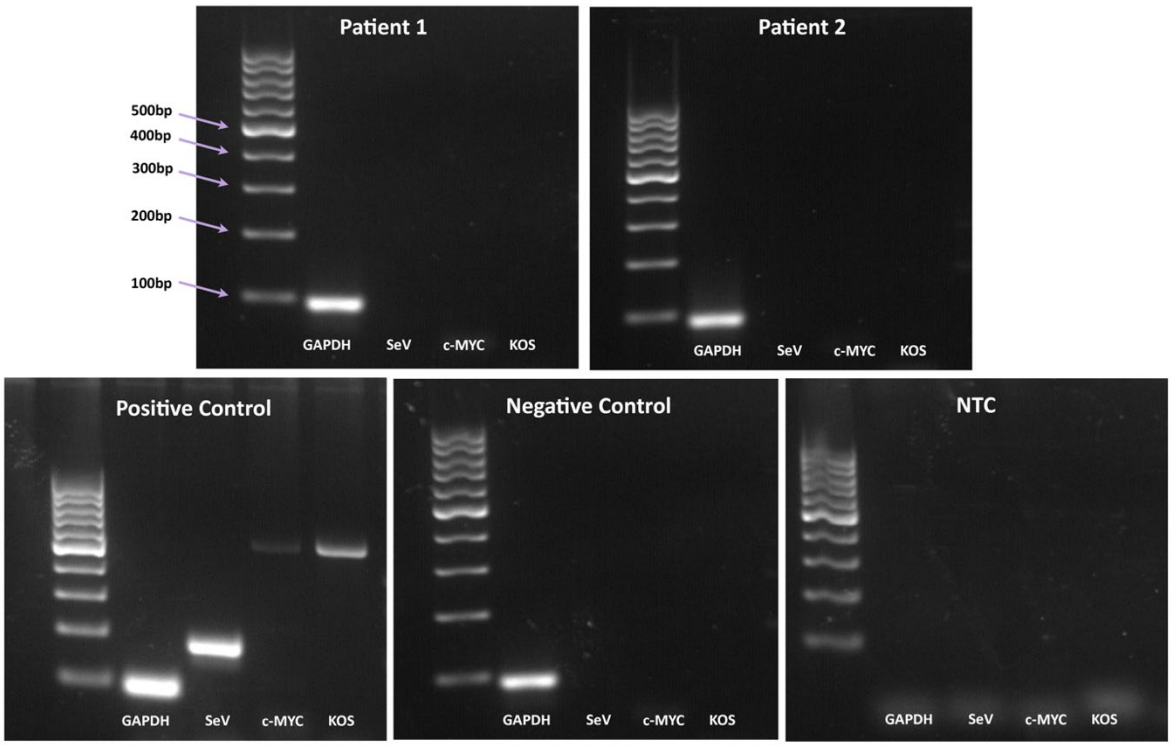

Figure 3.6 Patient iPSCs are clear from SeV vectors and associated transgenes

Clearance of SeV vectors following the generation of iPSCs and serial passaging was achieved by passage 16. RT-PCR for SeV and SeV-transgenes revealed no corresponding bands in either Patient 1 or Patient 2 iPSCs, similarly to negative iPSC control. In the positive control, bands corresponding to *SeV* (181bp), *c-MYC* (532bp) and *KOS* (528bp) were apparent. *GAPDH* (86bp) was utilised as a loading control and was apparent in each iPSC line tested. NTC serves as the non-template control for this experiment.

3.3.5 PT1 and PT2 express key transcription factors essential for pluripotency

PT1 and PT2 iPSCs were shown to be pluripotent in their ability to recapitulate features that are typical of iPSC derived ROs. This was observed from the continuation of the EB-forming assay to ROs and later differentiation studies spanning a time course of 220 days, as discussed in Chapter 4. However, to confirm that these iPSCs behave transcriptomically as PSCs, we first sought to confirm the expression of quintessential pluripotency factors – *OCT4, SOX2* and *NANOG* by RT-PCR and gel electrophoresis as described in **Section 2.3.3.**

Using *GAPDH* as a housekeeping gene, and a routinely used iPSC control line as positive control, we observed bands corresponding to these gene transcripts at the expected band size; *GAPDH* (86bp), *OCT4* (164bp), *SOX2* (131bp) and *NANOG* (206bp) in all conditions except the non-template control (NTC) **(Figure 3.7).**

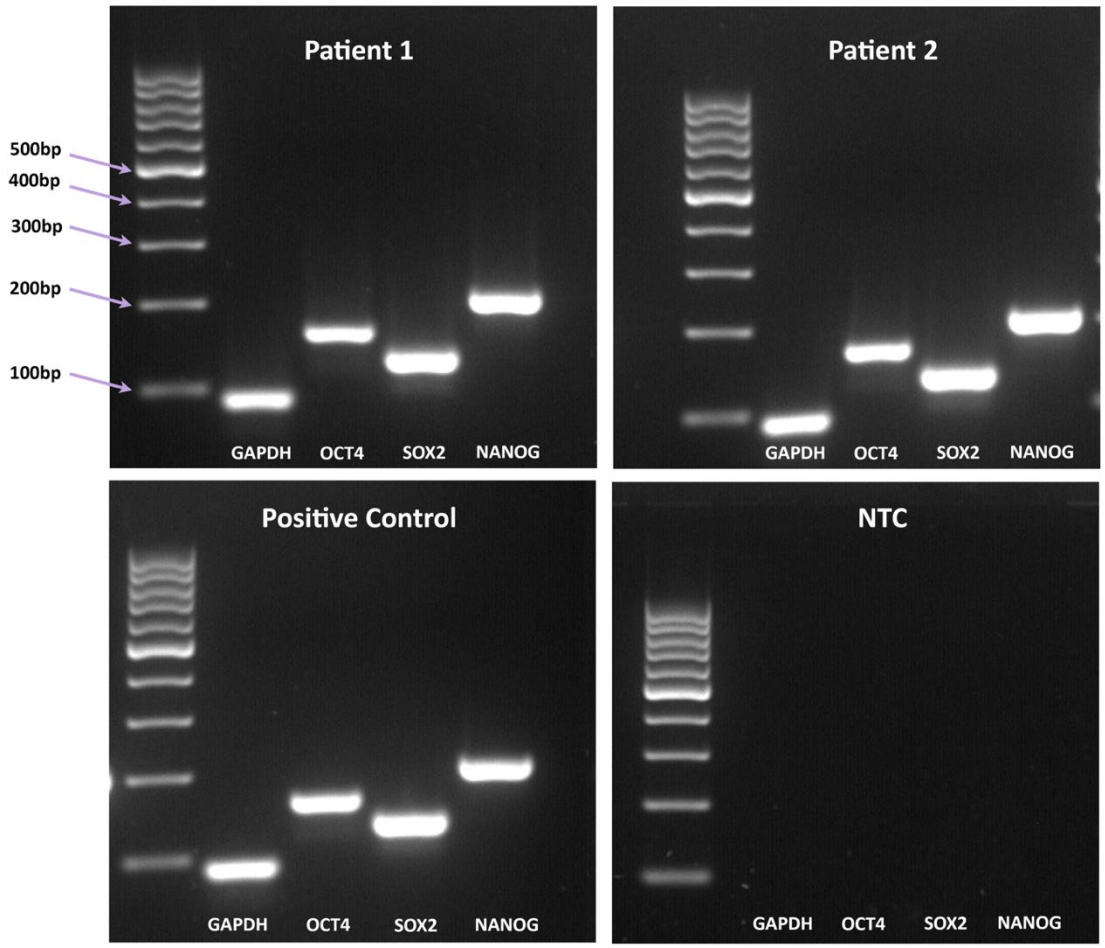

Figure 3.7 Patient iPSCs express transcriptional core of PSCs

Patient iPSCs are shown to express the key transcription factors essential for pluripotency in PSCs. Using RT-PCR, bands corresponding to *OCT4* (164bp), *SOX2* (131bp), and *NANOG* (206bp) were present in the patient iPSC lines and a routinely used positive iPSC control. *GAPDH* (86bp) was utilised as a loading control and was apparent in each iPSC line tested.

To further corroborate these results, we sent our samples to the PluriTest Characterisation Service provided by ThermoFisher Scientific (**Section 2.3.4**). This assay compares the gene expression profile of cells with an extensive and well-characterised reference dataset containing both pluripotent and non-pluripotent samples (cells and tissues). This test yields two results; the first being the PluriCor (pluripotency score) which is a grading of how similar the provided samples are to the pluripotent samples in the reference dataset. The second result is the novelty score which is assigned based on the recapitulation of gene expression signatures in the provided samples using the signatures of the pluripotent samples in the reference dataset only, indicating the general model fit for a given sample. PT1 scored 38.371 and PT2 scored 41.263 for pluripotency which is highly comparable to the iPSC control used which gave a score of 46.7892 **(Figure 3.8).**

In contrast, the non-iPSC control scored -44.717. Likewise, when testing for novelty, PT1 scored 1.393 and PT2 scored 1.321, which is akin to the iPSC control score of 1.480 and vastly dissimilar to the non-iPSC control score of 2.674. These scores are combined and graphed on a scatterplot, alongside an iPSC and non-iPSC control, to give a schematic representation of overall pluripotency in the provided samples. As seen on the scatterplot, PT1 and PT2 cluster with the iPSC reference in red, and not with the non-iPSC control in blue, as expected, confirming their pluripotency.

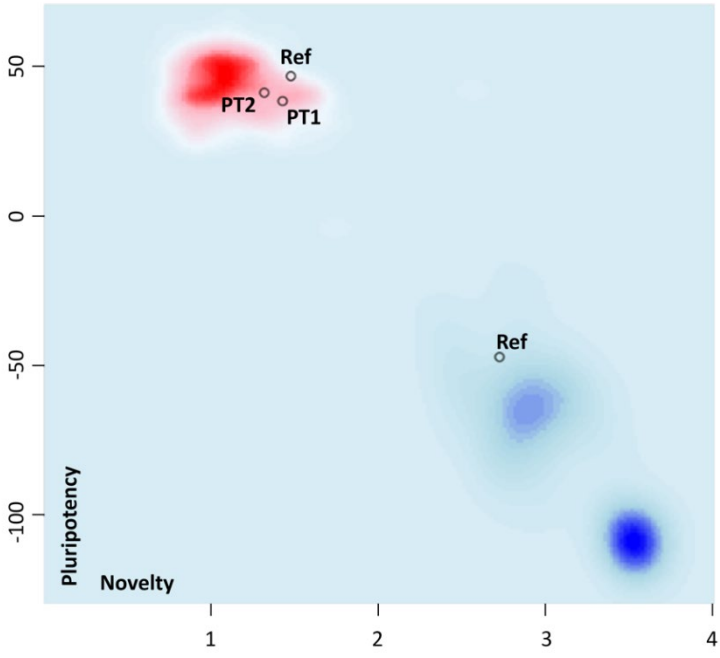

Sample	Result	PluriCor	NovelCor
Patient 1	Pass	38.3708	1.393234
Patient 2	Pass	41.2634	1.321097
iPSC CTRL	Pass	46.7892	1.480133
Non-iPSC CTRL	Fail	-44.7171	2.673582

Figure 3.8 Patient iPSCs display similar gene expression profiles to known pluripotent samples

Patient iPSCs were externally characterised using the PluriTest assay. This assay compares the transcriptomic profile of provided samples with both pluripotent and non-pluripotent cells and tissues in a reference dataset, yielding a PluriCor score. This score is an indication of how close transcriptomic profiles are between provided samples and the pluripotent samples in the reference data. A novelty score is also assigned which indicates a model fit for the provided sample with the reference database. The scores are graphed on a XY scatterplot alongside controls. The red and blue background hint to the empirical distribution to the pluripotent (red) and non-pluripotent (blue) samples in the reference dataset.

3.3.6 Karyotypic analysis displays chromosomal defects in PT1 genome

In the process of cellular reprogramming, it is not uncommon for iPSCs to acquire chromosomal aberrations. To assess the genome stability of our newly generated iPSC clones, PT1 and PT2 iPSCs were sent for a KaryoStat™ assay performed by ThermoFisher Scientific **(Section 2.3.5).** This assay assesses genome stability by recording any CNVs of known single-nucleotide polymorphisms (SNPs) across the whole genome. This allows for digital visualisation of chromosomal gains/losses with comparable resolution to the traditional method of g-banding enabling the detection of aneuploidies, submicroscopic aberrations, and mosaic events.

Each SNP is recorded on a plot and is then normalised to give a smooth signal plot. In a stable genome, the smooth signal should be within the boundaries of score 2, except for sex chromosomes in male genomes where they sit at score 1. As both patients were male, we observed a loss of X and gain of Y chromosomes (both at score 1) in the smooth signal plot, as expected **(Figure 3.9).**

The smooth signal plot of PT1 revealed chromosomal aberrations with a mosaic loss, and a gain at different SNPs in chr 20 **(Figure 3.9 B).** The copy number (CN) state of 1.55 highlights the mosaicism of loss at chr20p11.1 involving 152 genes found in the OMIM gene database. Whilst the score of 3 indicates complete gain at chr20q11.21 involving 232 OMIM genes (**Figure 3.9 A).** PT2 revealed a stable genome with no obvious chromosomal anomalies as shown in **Figure 3.9 B.**

.

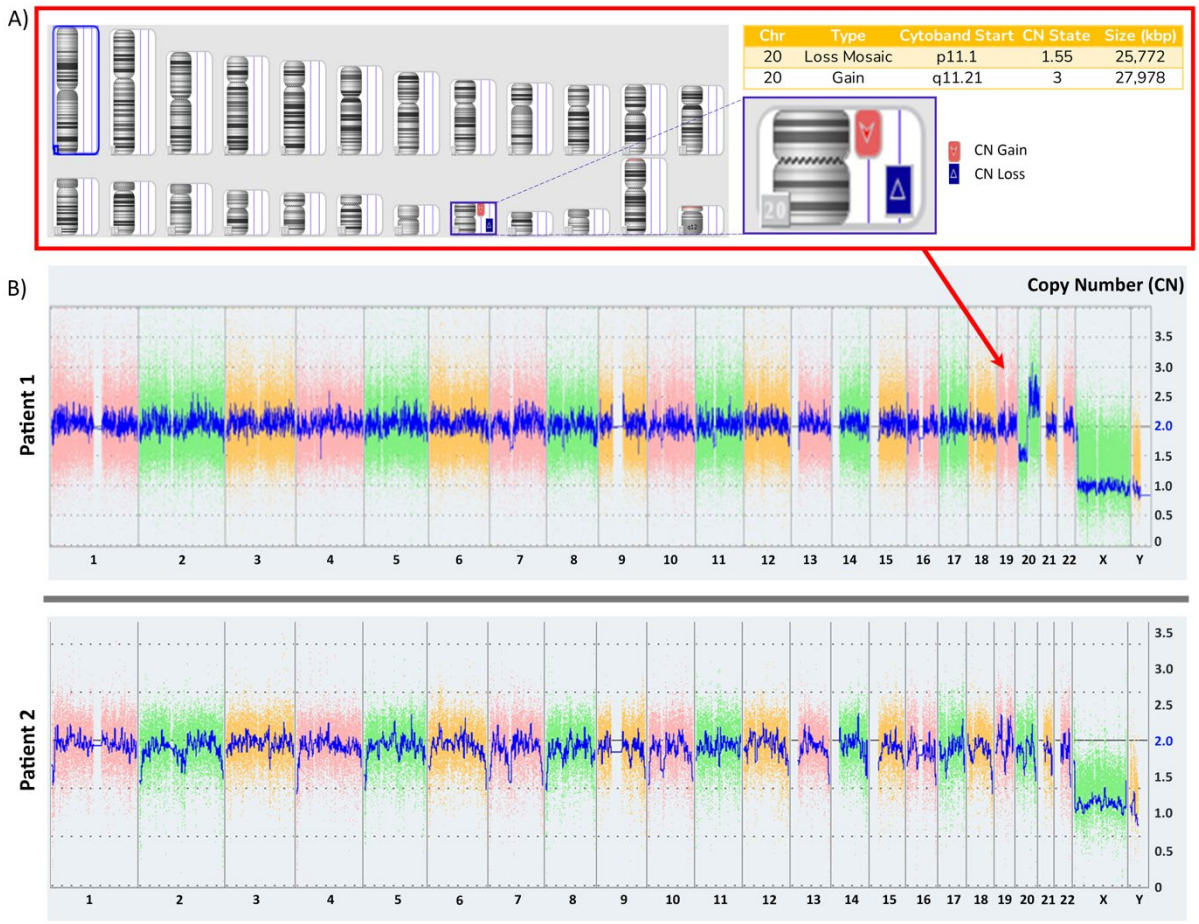

Figure 3.9 Karyotypic analysis reveals stable genome in Patient 2 iPSCs but genomic instability in present in Patient 1 iPSCs

Cells were characterised externally using the KaryoStat™ assay, which assesses the CNV of SNPs in each chromosome with a reference dataset to identify any genomic instability resulting from aneuploidies, submicroscopic aberrations, and mosaic events. The signal recorded for each SNP is normalised to give a smooth signal (blue line) which gives an indication of chromosomal gains (>2) or chromosomal losses (<2). **A)** Genomic instability was noted in PT1 iPSCs with gain at 20q11.2 and loss at 20p11.1. **B)** The smooth signal plot displays loss and gains at Chr 20 in PT1 iPSC whilst PT2 displays no evidence of genomic instability. Both patients are male as shown by one copy of X and Y chromosomes in both karyographs.

3.4 Discussion

Upon the initial thaw of PT1 iPSCs, we observed a clear refractory phenotype. The uncontrollable spontaneous differentiation observed is something that is frequently seen with partially reprogrammed iPSC clones that have been selected based on morphology alone. The first morphological change observed in the reprogramming process is the rapid increase in cellular proliferation and the reduction of overall cell size in the forming colony. Whilst some cells will express the genes expected for pluripotency, many cells will not undergo this morphological change and will remain fibroblastic (Plath and Lowry, 2011). Partial reprogramming is where the cell has acquired some stem-cell like characteristics such as gene expression or cell surface markers but has not made the full transition to true pluripotent state. These cells can remain 'pluripotent' in culture for up to 12 passages at times but will ultimately lose their pluripotent capabilities in culture and erroneously differentiate (Pfannkuche *et al.*, 2010).

PT1 iPSC culture contained a mixed population of cells characteristic of iPSCs and mesenchymal cells. Despite several manual cleaning approaches to remove the differentiated cells from the iPSCs, we could not rescue this iPSC line. Without access to additional clones or patient material, we proceeded to allow the cells to differentiate into a homogenous population of fibroblast/mesenchymal-like via the addition of high levels of serum. This facilitated additional cellular reprogramming using a non-integrative method of pluripotency factor delivery (Chichagova *et al.*, 2016; Ban *et al.*, 2011). This non-integrative method of reprogramming involves the delivery of pluripotency transgenes as RNA via SeV vectors. These vectors have an affinity for the cytoplasm of the cell and do not enter the nucleus of the cell, eliminating the chances of genomic integration. PT2 was reprogrammed alongside PT1 iPSC-derived mesenchymal cells, using a similar protocol with minor changes accounting for the difference in starting somatic cell. PT2 was reprogrammed using PBMCs isolated from whole blood. Both patients produced numerous iPSC-like clones. However, PT2 produced significantly more clones (20 clones vs 6 respectively). Three clones from each patient were propagated past passage 3 and used for an EB-forming assay to select the most suitable clone for the study. The rest of the clones were frozen.

For this assay, we used two different protocols (BMP4-activated & IGF1-dependent) that are routinely used in the Lako group for the formation of ROs (Zerti *et al.*, 2020; Hallam *et al.*, 2018). Despite differences in this protocol, both initially involve a step for EB formation within

the first 18 days of culture and are achieved via forced aggregation in U-bottom well plates. Again, we observed variable efficiency in the ability of clones to produce EBs within the first week of differentiation. However, one clone from each iPSC line – PT1 Clone 5 (PT1C5) and PT2 Clone 7 (PT2C7), were able to faithfully produce EBs across three 96-well plates. With this observation, we selected the successfully differentiated clones.

Cell pellets were taken at the time of EB-formation assay, and from these RNA was isolated. Using RT-PCR with primers designed for the detection of reprogramming transgenes and SeV vectors, we were able to confirm the cells had cleared Sendai virus and associated transgenes from the cells by passage 12. On average, it takes approximately two months and 10 passages to clear the cells from SeV and transgene expression (Choi, Lim and Lee, 2014), so this was an expected result.

Next, we wanted to ensure that the reprogrammed cells expressed the 3 key transcription factors that encompass the transcriptional core of PSCs. These include *OCT4, SOX2* and *NANOG*. Specifically*, OCT4* and *SOX2* sit on top of the regulatory network of transcription in PSCs. These two genes work in unison to activate downstream target genes that are involved in maintaining stem cell characteristics such as pluripotency and self-renewal (Chambers and Tomlinson, 2009). Amongst the many downstream targets of the OCT4/SOX2 protein complex, is *NANOG.* NANOG is essential for the maintenance of pluripotency in PSCs, such that its expression is seen only in undifferentiated cells (Rodda *et al.*, 2005). Using RT-PCR, we probed for the expression of these three genes in the newly reprogrammed iPSCs, alongside a positive control. In both PT1 and PT2 iPSCs, as well as positive control, we observed cDNA bands in the gel corresponding to *OCT4* (164bp), *SOX2* (131bp) and *NANOG* (206bp) confirming that the reprogramed cells express the transcriptional core in PSCs.

These results were further supported by the outcome of a PluriTest assay which compares the transcriptional profiles of provided cell samples with a database of cells and tissues from both pluripotent and non-pluripotent samples. The scores obtained from this assay were highly comparable with a positive pluripotent control used for the assay, indicating that PT1 and PT2 clones were indeed pluripotent. Novelty scores were low for the samples, which shows that the samples provided were homogenously reprogrammed and did not contain any differentiated or partially reprogrammed cells. This is deduced by the understanding that samples with low novelty scores can be reproduced transcriptomically using information derived only from the pluripotent samples in the reference dataset. In corollary to this,

samples with high novelty scores cannot be recapitulated transcriptomically using the data from the reference database. All this evidence indicates that PT1 and PT2 iPSCs are PSCs and are suitable for differentiation studies later in the project.

iPSCs are an invaluable tool in biological research due to their many applications in disease modelling, developmental studies, clinical applications and many more. However, there is always a concern of genomic instability that can arise during cellular reprogramming, directed differentiation or long-term continuous culture. To assess the genome stability of PT1 and PT2 clones, the cells were externally tested via the Karyostat™ service carried out by ThermoFisher Scientific. The karyotypical analysis revealed genomic instability in PT1 on both arms of chromosome 20 but a stable genome in PT2. Unfortunately, with the EB formation screen, we were unable to identify an alternative clone for PT1 suitable for the study and consequently, proceeded with this genomically unstable clone. However, *ABCA4* is the gene of interest for this project, which localises to chromosome 1, a region that shows no instability on the karyograph of PT1. This fact renders the iPSCs useable for the purpose of our overall objective in identifying the missing allele of *ABCA4* in this monoallelic STGD1 case.

In detail, 20q of PT1 displayed a CN gain with the amplification of 232 OMIM genes. 20q11.21 is a recurrent hot spot for mutation in ESC and iPSC lines. In a screening of 136 PSC lines gathered from around the globe, 20q11.21 amplifications were observed in more than 20% of lines (Amps et al., 2011). Other studies have also reported the acquisition of chromosomal duplications in 20q11.21 (Maitra *et al.*, 2005; Spits *et al.*, 2008; Wu *et al.*, 2008). Genome instability is a classic hallmark for the development of cancer. Interestingly, 20q11.21 duplications have been observed in several human cancers, including cervical (Scotto *et al.*, 2008), pancreatic (Mahlamäki *et al.*, 2002), gastric (Kimura *et al.*, 2004), ovarian and breast cancer, (Hodgson *et al.*, 2003) and many more. It is understood that genes located within this region have functions in cell proliferation and pluripotency and so duplications of such genes are likely to confer a selective advantage on those cells and favour their propagation. The association of 20q11.2 duplications in PSCs with long-term culturing, supports this finding (Laurent *et al.*, 2011).

Indeed, among the 232 genes amplified at 20q11.2 in PT1 iPSCs, there are genes with associations in growth and cell survival. From this list, we highlighted a few that may impact downstream RO generation and disease phenotypes from PT1 iPSCs. One example is the *BCL2L1* gene, of which one encoded isoform produces an anti-apoptotic protein known as

BCL-x_L. This isoform is expressed in undifferentiated PSCs and enhances cell survival, particularly of PSCs as single cells (Nguyen *et al.*, 2013). This increases the clonality of the affected cells, whilst also reportedly improving EB formation (Bai et al., 2012). Thereby, resistance to cell death gives the cell a significant advantage over wild-type cells. The anti-apoptotic protein encoded by BCL-x_L could potentially protect photoreceptors from stress-induced apoptosis as a secondary consequence of mutated ABCA4 protein. This could mask the true *in vitro* disease phenotype of PT1 when differentiated to ROs. This issue is further compounded by the duplication of other genes at 20q11.21 which have been reported to promote PSC qualities such as increased cell survival (*PDRG1*), cell growth (*ID1*) and cell proliferation (*TPX2, KIF3B*) (Lefort et al., 2008). In the retina, *ID1* encodes a transcription factor that is involved in RPC proliferation (Ghinia Tegla *et al.*, 2020), this could result in an overproliferation of certain retinal cell types, possibly leading to disruptions in the lamination of developing ROs. *TPX2* is an important mitotic regulator by regulating microtubule assembly and organisation. One study has observed defects in cell cycle progression through mitosis when overexpressed in immortalised RPE-1 cells. Abnormally high levels of TPX2 result in defects of microtubule cytoskeletal remodelling and G1 nuclei reformation between the transition of mitosis to interphase in the cell cycle (Naso *et al.*, 2020). In the context of PT1 ROs, this could result in the aberrant development of neurons expected in the neuroretina.

Whilst it has been conclusively shown that increased copies of the aforementioned genes in PSCs provide a selective advantage in culture allowing them to outcompete genomically stable cells (Peterson and Loring, 2014), the specific outcome of duplication on RO differentiation depends on the extent to which the gene dosage effect alters the balance of cellular pathways. In summary, this could manifest as changes in cell proliferation, differentiation, survival or function, which necessitates a meticulous analysis and clear delineation when assessing PT1's true STGD1 phenotype. As we have included another monoallelic STGD1 patient (PT2), and an affected control (AC), we will be able to compare phenotypes across the spectrum of mild to severe STGD1 disease which will help us to decipher the true phenotype in PT1 ROs.

We used the ability to form EBs as a benchmark for selecting a suitable clone that would likely differentiate to ROs in the next phase of the study. In hindsight, this might have selected for a more genomically unstable iPSC clone and would be an important consideration in the selection of clones for future experiments. In this case, only one clone could produce EBs and therefore we did not have alternative clones to choose from. However, other than genomic

instability, stem cells that acquire 20q11.2 CN gains are almost indistinguishable from genomically stable PSCs, sharing the same morphology, expression of pluripotency markers and rates of growth (Lefort et al., 2008). However, in a more recent study, overexpression of BCL-x_L in hESCs was correlated with reduced ability to differentiate into neurectoderm. This is due to an altered gene expression profile associated with the overexpression of BCL-x_L specifically. This results in a downregulation of genes involved in the TGF-β and SMAD-mediated signalling pathways that affect neuroectodermal lineage commitment in initial stages of differentiation. Meanwhile, mesodermal derivatives remain unaffected by the overexpression of BCL-x_L (Markouli *et al.*, 2019). Neural retina is derived from neuroectoderm during embryogenesis, so it is concerning that there is a reduced capability for neuroectodermal differentiation with PSCs harbouring 20q11.21 amplification. In a more recent study using single cell RNA-seq, a reduction in capabilities of neuroectodermal lineage commitment has also been observed (Jo *et al.*, 2020). Through teratoma formation, iPSCs with 20q11.21 amplification were shown to have reduced neuroectodermal cells corresponding to 8% of the cells assayed. This is compared with 11% of neuroectodermal cells in genomically stable iPSC-derived teratomas. Results from our RO differentiations confirm that ROs can be differentiated from iPSCs containing 20q11.2 and will be discussed in greater detail in Chapter 4.

A loss at 20p11.1 was also observed in PT1. There is little to no information regarding this chromosomal aberration in the literature and so one can deduce it is a less frequent occurrence in PSCs. The consequence of a reduced copy number of genes at 20p11.1 could also impact the disease phenotype of PT1 when differentiated to ROs. For example, Sulfiredoxin encoded by *SRXN1* is an important antioxidant protein in neuronal cells (Wu *et al.*, 2020). With reduced CN of this gene, cells of PT1 ROs could become more susceptible to oxidative-stress induced damage, which is already a common mechanism associated with retinal disease. Another gene, *RBCK1*, plays a key role in the formation of linear ubiquitin chain assembly complex (LUBAC), a critical component of the proteasome (Nitschke *et al.*, 2022). This could lead to downstream defects in protein degradation in PT1 ROs, leading to the formation of cellular aggregates, which could be falsely associated with ABCA4-mediated pathology. As mentioned previously, the addition of PT2 and AC iPSC-ROs will help uncover the true effects of ABCA4-mediated defects and those associated with the genomic instability of PT1 iPSCs.

Whilst chromosomal gains are more commonly associated with continued long-term culture of PSCs, chromosomal loss is more frequently associated with the reprogramming process (Laurent *et al.*, 2011). It is difficult to pinpoint whether the chromosomal loss arose in the first or second round of reprogramming in PT1 as we did not receive karyotypic data on this line, nor did we assess this ourselves prior to the second round of reprogramming. Evidence suggests that the cells could have been genomically unstable upon their arrival at our lab due to their refractory phenotype with uncontrollable spontaneous differentiation upon initial thaw. We know that the original reprogramming procedure utilised a lentiviral vector system for the delivery of reprogramming transgenes and one study has shown that in cells reprogrammed via lentiviral vectors, failure to silence transgenes following proviral insertion was associated with acquisition of genomic instability (Ramos-Mejia *et al.*, 2010).

In the second reprogramming event, we utilised a non-integrative reprogramming vector system (SeV vectors) to generate iPSCs. These viruses express reprogramming factors as RNA transcripts in the cytoplasm of the cell, and so they cannot integrate into the host genome. Our data also shows the clearance of Sendai viruses by RT-PCR following several sequential passages, suggesting that chromosomal deletion was already present in the iPSCs upon the second round of differentiation and likely occurred during the initial reprogramming event with lentiviral integrating vectors. It has also been shown in many studies that once the cell has acquired genomic instability, it tends to become more unstable over time. To speculate, if indeed the 20p11.1 deletion occurred at the initial reprogramming event, then the chromosomal gain at 20q11.2 would have occurred thereafter as is typically a consequence of long-term continued PSC culture.

It has been suggested that chromosomal aberrations in PSCs due to continuous long-term culture may be mitigated if enzymatic agents are discontinued in the passaging process (Laurent *et al.*, 2011; Bai *et al.*, 2015). To maintain genomic stability, mechanical picking and passaging of clones from one well to others is advised. However, this is a lengthy and laborious process, especially for individuals who are culturing many iPSC lines at once and therefore may not be physically feasible. To minimise the risks of losing an iPSC line altogether, it is recommended to freeze and bank early passage cells and routinely assess the karyotype of iPSCs in culture, particularly before big differentiation projects. In addition to this, caution should be taken regarding the reprogramming of a cell line that has already previously undergone a reprogramming event, especially via integrating lentiviral vectors. In our case,

we did not have primary material from PT1 to reprogram and utilised what material we had access to.

In summary, we developed iPSC lines for two monoallelic cases of STGD1 – denoted PT1 and PT2. Both iPSC lines are pluripotent, in their behaviour and their transcription, and can produce EBs in early differentiation studies. PT2 revealed a typical karyotype when assayed. However, PT1 displayed genomic instability affecting both arms of chromosome 20. This is a result that occurs frequently in pluripotent cell lines and should be taken into consideration for the interpretation of results in Chapter 4, when these iPSC lines are used to produce ROs. We will compare any results obtained from the PT1 iPSC line, with PT2 and both an unaffected control, and affected control with biallelic *ABCA4* mutations. The results of Chapter 5 will be largely unaffected as the gene of interest for STGD1 is *ABCA4* located on chromosome 1, where no genomic instability has been observed in either PT1 or PT2 iPSC line.

Chapter 4 Retinal organoid generation and characterisation from monoallelic STGD1 patient cases

4.1 Introduction

Despite STGD1 being one of the most prominent forms of inherited maculopathies affecting up to 1 in 8,000 individuals globally (Blacharski, 1988), there is currently no treatment or therapy for this debilitating disease. The generation of potential therapies is hindered somewhat by the lack of physiologically relevant disease models that accurately recapitulate the disease and mirror genotype-phenotype correlations.

Most of the research on STGD1 pathogenesis thus far has been conducted on *ABCA4*$^{+/-}$ and *ABCA4*$^{-/-}$ mouse models generated in the late 1990s (Weng *et al.*, 1999). These models have played a crucial role in uncovering the basic mechanisms that drive the disease's progression. One key discovery is the build-up of lipofuscin in the retina and RPE cells of these STGD1 models. Lipofuscin is characterised as an accumulation of undigested fats and lipids. These substances are photooxidative in nature, contributing to the generation of a stressful environment for the surrounding cells. In this study, the degree of lipofuscin accumulation was dependent on levels of residual ABCA4 protein and was exacerbated by exposure to blue light. Delayed dark adaptation of rod photoreceptors was an additional key observation from these mouse models (Mata *et al.*, 2001).

The observed phenotypes in the STGD1 mouse model correlate with human STGD1 phenotypes in the clinic (Tsang and Sharma, 2018) and are now known to arise due to the inefficient clearance of all-*trans*-retinal (vitamin A derivative) from POS post-phototransduction. This is a consequence of mutated ABCA4 protein, which plays a key role in the recycling of visual pigments, resulting in toxic bisretinoid precursor accumulation in the outer segment and subsequent lipofuscin accumulation in the RPE (Allikmets *et al.*, 1997a; Allikmets *et al.*, 1997b). The translation of these findings to human led to interventions for the management of this disease, such as the provision of blue light filtering sunglasses and diets low in vitamin A for those living with STGD1. Despite the capabilities of the murine models to recapitulate several features of STGD1 in humans, the model possesses a fundamental limitation: absence of photoreceptor degeneration. This is most likely due to a lack of macular region in the rodent retina, compounded by differing proportions of cone and rod photoreceptors present in the retina between the two species (Volland *et al.*, 2015).

As STGD1 is a disease of the macula in humans, this model displays substantial anatomical insufficiencies to accurately model the pathophysiology of ABCA4-mediated disease. For that reason, there is a requirement for more physiologically relevant STGD1 models that can faithfully recapitulate disease phenotypes. Whilst other groups have tried to generate a STGD1 model in animals that possess a macula or macula-like region of retina, such as pigs (Trapani *et al.*, 2019) or dogs (Le Bras, 2019), we chose an *in vitro* method to model human STGD1 with the use of iPSC and retinal organoid (RO) technology, reducing the need for animals in research in accordance with the 3Rs strategy (Würbel, 2017).

Since the introduction of cellular reprogramming via iPSC generation in Yamanaka's seminal study (Takahashi *et al.*, 2007), the field of disease modelling has been completely revolutionised. iPSC technology combined with recent advancements in gene editing strategies such as CRISPR (Jinek *et al.*, 2012) have made disease modelling more accessible. Many groups, including our own, have succeeded in differentiating these iPSCs to 3D laminated retinal tissue over the last decade (Meyer *et al.*, 2009; Eiraku *et al.*, 2011a; Nakano *et al.*, 2012; Phillips *et al.*, 2012; Gonzalez-Cordero *et al.*, 2013; Zhong *et al.*, 2014; Kuwahara *et al.*, 2015; Mellough *et al.*, 2015; Ohlemacher *et al.*, 2015; Hallam *et al.*, 2018; Capowski *et al.*, 2019; Dorgau *et al.*, 2019; Zerti *et al.*, 2020; Cowan *et al.*, 2020; West *et al.*, 2022).

ROs recapitulate the *in vivo* human retinal architecture, displaying apical-basal polarity across a stratified neuroepithelium. They contain all retinal neurons expected in the retina including rod and cone photoreceptors, bipolar cells, retinal ganglion cells (RGCs), ACs, HCs, and Müller glia. These cells are organised into distinct layers, creating a laminated structure as seen in *in vivo* human retina (Watson and Lako, 2023). The developmental timelines of RO differentiation from iPSCs closely follow the rates of retinogenesis *in utero* with the generation of retinal neurons corresponding to their birth order in the foetus (Collin *et al.*, 2019). Interestingly, transcriptomic profiles of ROs and foetal retina converge substantially demonstrating that iPSC-derived retinal tissue is highly reminiscent of nascent foetal retina (Cowan *et al.*, 2020). This innovative model provides an unparalleled opportunity to study retinogenesis in real-time, offering biological insights that are more akin to human physiology compared to existing *in vivo* animal models

Indeed iPSC-derived models have faithfully recapitulated elements of human retinal disease and in even some cases have even corrected the phenotypes observed by pharmacological intervention or gene therapy. Examples of such studies can be seen in the modelling of retinitis

pigmentosa (Buskin *et al.*, 2018; Gao *et al.*, 2020; Georgiou *et al.*, 2022), Lebers congenital amaurosis (LCA) (Parfitt *et al.*, 2016; Shimada *et al.*, 2017), X-linked juvenile retinoschisis (XLRS) (Huang *et al.*, 2019), Retinoblastoma (Rozanska *et al.*, 2022) and Usher syndrome (Leong *et al.*, 2022) to name a few. These studies demonstrate the suitability of ROs to model different retinal diseases in a patient-specific, gene-specific, and mutation-specific context enabling the in-depth study of various heterogenous inherited retinopathies. They also demonstrate that ROs are an excellent model for *in vitro* proof of concept disease studies to ameliorate or halt disease phenotypes. Further to this, the scalability of RO generation and maintenance makes them a fantastic model for *in vitro* toxicology studies (Hallam *et al.*, 2018; Dorgau *et al.*, 2022).

STGD1 research using stem cells thus far has been focussed on modelling the RPE. This stems from the unexpected discovery of ABCA4 protein expression in the RPE (Lenis *et al.*, 2018) and the drive to understand its function at that site. Previously, ABCA4 was thought to localise specifically to the rims of outer segment discs in rod and cone photoreceptor cells (Allikmets *et al.*, 1997b). A recent report demonstrated that iPSC-RPE from ABCA4$^{-/-}$ iPSCs accumulate intracellular lipid and ceramide deposits in a cell-autonomous manner (Farnoodian *et al.*, 2022). The model also displayed reduced capability of outer segment phagocytosis when challenged. These observations have been a bit of a conundrum in the STDG1 research field as it denies the classical mechanism of disease pathology, where A2PE-laden outer segment phagocytosis by RPE is understood to be the defining factor for development and progression of this disease.

As both photoreceptor cells and RPE cells express ABCA4 protein, and we know of the close relationship these tissues share with each other for overall retinal health and function (Yang, Zhou and Li, 2021) it is possible that there is complex interplay between the photoreceptors and RPE cells that amplify the pathology of STDG1 in humans. If RPE can demonstrate a cell-autonomous phenotype, this opens a gap in STGD1 research for the investigation of photoreceptors in isolation of functional RPE tissue and how that influences ABCA4 expression and function.

Some research groups have generated photoreceptor precursor cells (PPCs) from hESCs as a photoreceptor cell model *in vitro* (Zhou *et al.*, 2015). These cells show robust expression of CRX (a homeobox transcription factor responsible for photoreceptor cell differentiation and maintenance), along with cone photoreceptor markers S-opsin, cone transducin and cone

arrestin at both transcript and protein level in a relatively short differentiation period of 4-6 weeks. iPSC-derived PPCs can recapitulate retina-specific splicing patterns of the *ABCA4* gene (Sangermano *et al.*, 2016) and have been used as a means to assess the effects of putative splice altering variants on *ABCA4* expression following the identification of uncovered deep-intronic and splice altering variants in unresolved cases of STGD1 (Khan *et al.*, 2020b). They have also been used to assess therapeutic strategies such as CRISPR-mediated gene editing of causative mutations (De Angeli *et al.*, 2022) and antisense oligonucleotide (AON) application (Albert *et al.*, 2018) to restore functional transcript in the case of disease-causing splice variants.

Depending on the research question at hand, iPSC-derived PPCs can serve as a robust and high-throughput model for investigating photoreceptor-specific defects in an isolated culture system. However, this model does have its limitations. The retina is a complex tissue full of intricate neuronal networks that work in synchrony for the overall purpose of phototransduction. PPCs cannot recapitulate this level of complexity because of their immaturity and isolated culture. This is where iPSC-derived ROs introduce a notable advancement in vision research, offering a distinctive avenue for acquiring insightful biological knowledge that more closely emulates human physiology. This sets them apart from traditional *in vitro* 2D cell models and animal models, which may not fully capture the complexities of human retina function and development.

To this end, STGD1 ROs provide a more complex model that facilitates the maturation of photoreceptor cells enabling their development of POS where the ABCA4 protein is abundantly expressed. STGD1 ROs have been generated by other groups but published work so far does not focus on the characterisation of the model itself and instead focuses on their utility to modulate and restore *ABCA4* transcript and protein levels *in vitro* with the application of various therapeutics against splice-altering mutations (Kaltak *et al.*, 2023b).

This chapter of the thesis provides the first characterisation of STDG1 ROs over an extensive 220-day period, employing a diverse range of methodologies such as immunostaining, fluorescence imaging, scRNA-Seq, and Western blotting. We've incorporated samples from a range of patients including a notably severe biallelic STGD1 affected control (AC) with a verified genetic diagnosis, two late-onset monoallelic STGD1 cases (PT1 and PT2), and two unaffected controls (WT2 and WT3). This comprehensive selection spans the range of ABCA4-mediated disease manifestations, offering valuable insights into the genotype-phenotype

correlation theory of STGD1 pathology (Maugeri *et al.*, 1999b; van Driel *et al.*, 1998a). Such an in-depth exploration has been elusive in existing animal and cellular models. The initial observations from these ROs will be integral for further characterisation of ABCA4 function in the retina and for proof-of-concept disease rescue strategies for the treatment of STDG1. The ROs derived in this chapter will serve a purpose for studies in Chapter 5, where RNA harvested from mature photoreceptor cells will undergo long-read RNA sequencing in an effort to assess RNA defects in the monoallelic patient cases.

4.2 Aims

This chapter aims to describe the differentiation and characterisation of disease phenotype in ROs derived from newly generated iPSCs of the two individuals with late-onset STGD1 (PT1 and PT2), accompanied by a biallelic *ABCA4* affected control (AC). This was achieved by:

- Differentiating reprogrammed clones from Chapter 3 to ROs alongside unaffected and affected controls
- Maintaining ROs in culture for over 220 days to assess influence of protein defects on retinal development
- Performing immunostaining on ROs at critical development timepoints to ensure they correspond to retinal tissue
- Identifying any disease-specific phenotype as consequence of *ABCA4* mutation
- Performing scRNA-Seq on patient and control ROs to investigate cellular composition and gene expression signatures of STDG1 retinal cells
- Attempting to understand the pathophysiological mechanisms underpinning the disease-specific phenotypes observed in STGD1 ROs

An overview of the experimental aims in this chapter is illustrated graphically in **Figure 4.1.**

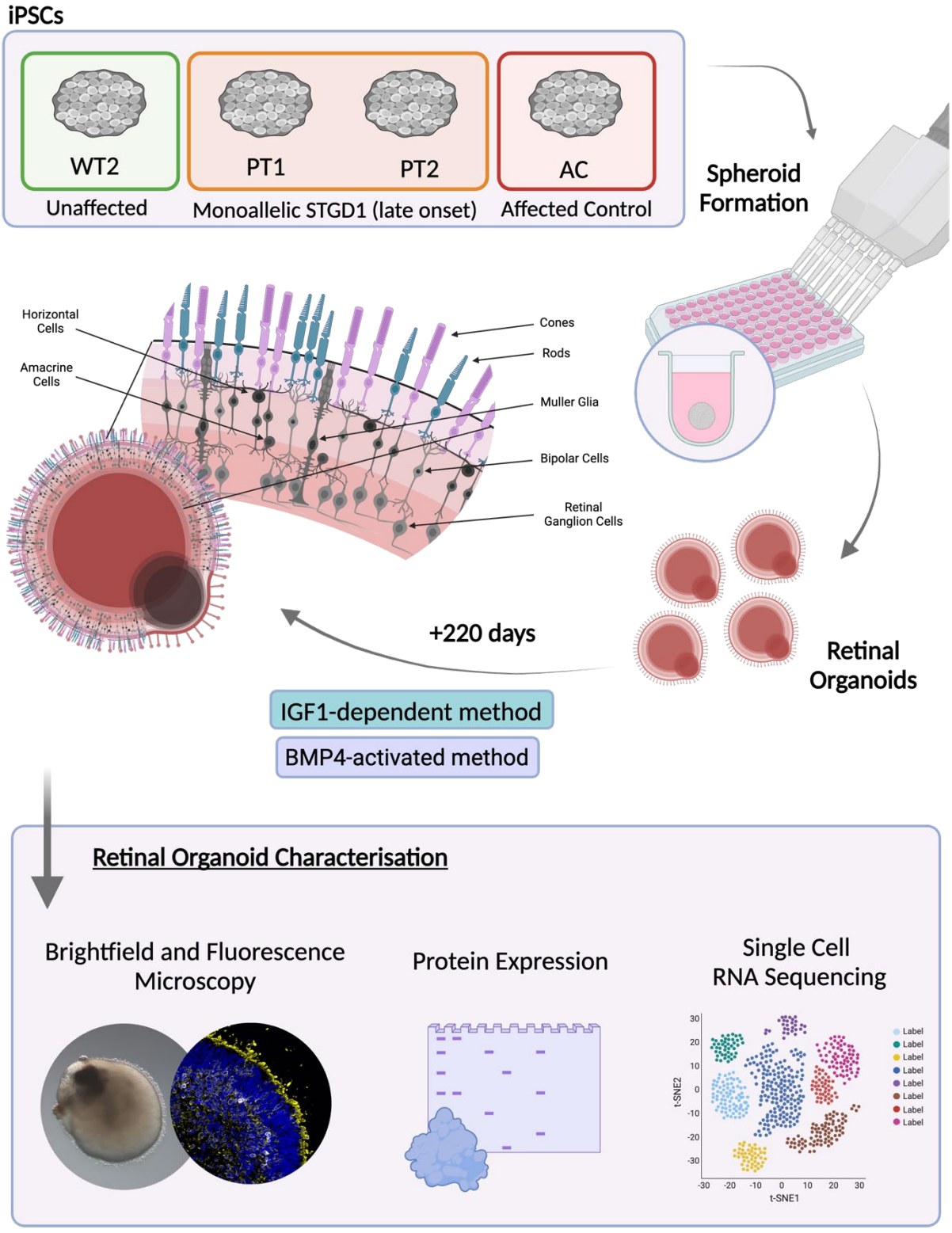

Figure 4.1 Graphical Overview of Chapter 4

4.3 Results

4.3.1 iPSCs display variable propensities for differentiation to ROs

In our original experimental outline, we aimed to utilise the optimised BMP4-activated method (Hallam *et al.*, 2018) for RO differentiation of all iPSC lines included in this study. However, from our initial differentiation studies with a routinely used iPSC line from the Lako Group (WT3) and a gifted biallelic STG1 iPSC line (AC) from a collaborator, it became apparent that the iPSC lines display different propensities to differentiate into ROs in the BMP4-activated method **(Figure 4.2).**

The WT3 iPSC line differentiated as expected in the BMP4-activated method (as described in **Section 2.2.6**) with EB formation within the first 7 days of seeding. By Day 30, the embryoids had developed into smooth spheroids with a dark core and bright edge around the perimeter of the spheroid **(Figure 4.2 A).** This bright perimeter is a characteristic feature observed in organoids of the central nervous system (CNS), including ROs. It corresponds to the primitive neuroepithelium from which the RPCs are derived. These RPCs continue to differentiate during development to give rise to the key neurons found in the retina: photoreceptors, RGCs, bipolar cells, ACs, HCs and Müller glia. By Day 90, the spheroids have transitioned to bona fide ROs. WT3 ROs generated using the BMP4-activated protocol display well defined structures with rounded edges becoming more prominent with the expansion of phase-bright neuroepithelium. The overall efficiency of WT3 with the BMP4-activated method, measured as number of viable EBs over total EBs seeded, was 76% (219/288 EBs).

When attempting to differentiate the AC iPSC line using the BMP4-activated method, we observed poor viability. A total of 3 separate differentiation attempts of the AC iPSC line using this method could not initiate transition of the EBs to spheroids. The initial EBs formed were also much smaller than expected and died before Day 60 **(Figure 4.2 A).** This resulted in a 0% efficiency (0/288 EBs) of differentiation.

The use of the AC iPSC line was essential for the purpose of this study to characterise genotype-phenotype correlations *in vitro*. Although the differentiation of this iPSC line with the BMP4-activated method was unsuccessful, the iPSCs themselves appeared morphologically intact and did not behave abnormally when in culture. Consequently, we decided to subject the AC line to further differentiation studies utilising the IGF1-dependent

protocol (Zerti *et al.*, 2020) devised by the Lako group **(Figure 4.2 B).** This protocol has had prior success in differentiating more 'difficult' iPSC lines.

Indeed, the AC line differentiated successfully using the IGF1-dependent protocol, generating 3D structures consistent with our expectations as outlined above, at each of the 3 recorded timepoints. Importantly, the ROs remained viable beyond the initial 90 days of differentiation with an overall efficiency of 60% (172/288 EBs) enabling their use in the study.

However, the WT3 iPSC control line did not respond favourably to the IGF1-dependent method and developed abnormally over the 90-day period demonstrated in **(Figure 4.2 B).** From as early as Day 30, the bright edge expected at the perimeter of the spheroid was barely discernible and difficult to differentiate from the dark inner core. By Day 60, the ROs appeared predominately dark with a thin, faint bright layer at the RO's periphery, indicating inadequate neuroretina formation. By Day 90, the darker core had expanded further outwards, engulfing the limited presumptive neuroretina that had developed. Consequently, the WT3 iPSC line could not be used alongside the AC iPSC line in the IGF1-dependent method.

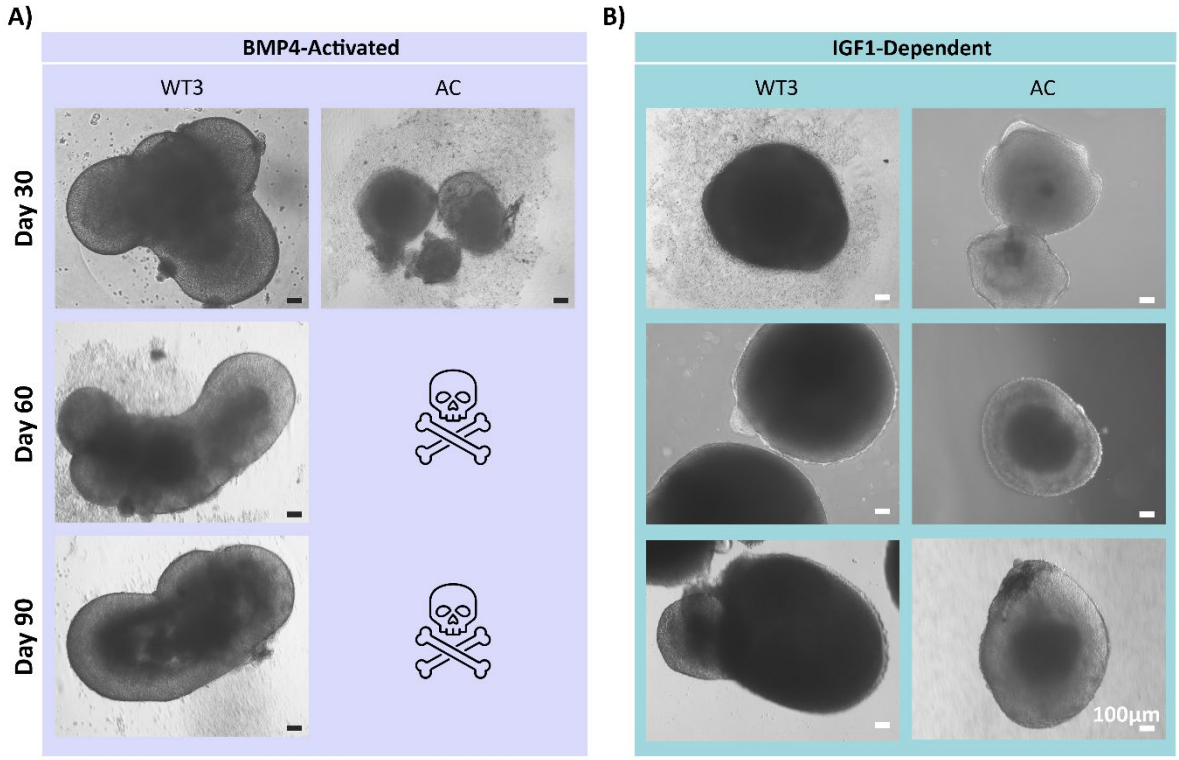

Figure 4.2 Variability in RO differentiation among control iPSC lines in response to distinct RO differentiation protocols

A) Brightfield images of unaffected control (WT3) and affected control (AC) iPSC-ROs derived from the BMP4-activated method of differentiation. WT3 iPSCs show consistent and expected RO development at each timepoint. The ROs exhibit uniform and well-defined structures with the appearance of primitive bright phase neuroepithelium as early as Day 30. This neuroepithelial organoid edge gradually becomes more distinct over time. ROs from WT3 remain viable post 90 days of differentiation. In contrast, AC iPSCs display multiple poorly defined 3D structures by Day 30, lacking apparent bright phase neuroepithelium. Additionally, excessive cellular debris surrounds these structures, leading to their failure to survive until Day 60 of differentiation. **B)** Differentiation of the same iPSC lines in the IGF1-dependent method revealed similar inconsistencies. Whilst WT3 formed uniform 3D structures, over the course of 90 days, no neuroepithelium formed. They grew larger than expected and did not share the same morphologies as observed in BMP4-activated method. In contrast, the AC line responded well to RO differentiation utilising the IGF1-dependent method. Bright phase neuroepithelium formed and became more defined over time as expected and although overall efficiency was lower at approx. 60% viability, ROs remained viable past 30 days of differentiation.

PT1 and PT2 iPSCs also responded variably to the BMP4-activated and IGF1-dependent protocols in **Figure 4.3**. The embryoid screening of newly generated patient iPSC clones (discussed in **Chapter 3**) occurred simultaneously with the differentiation of the control cell lines. Consequently, when screening, we utilised both protocols to assess the formation of EBs to ultimately select a suitable clone. As shown in **Figure 3.5** most EBs from the initial screening of PT1 and PT2 clones did not survive past Day 15. However, one clone from each patient (PT1C5 and PT2C7) successfully formed EBs in the IGF1-dependent protocol and BMP4-activated protocol respectively and was carried forward with later stage differentiations. We maintained PT1C5 and PT2C7 clones in **both** protocols up until Day 90 of differentiation and observed major differences in the long-term viability and structure of the ROs. In the BMP4-activated method - both PT1 and PT2 could produce ROs. Bright phase neuroepithelium appeared to form on the apical edge of the ROs (**Figure 4.3 A).** However, PT1 displayed low efficiency of differentiation - approximately 15% (44/288 EBs). By Day 90, the ROs of PT1 had large dark inner cores and thinning neuroepithelium, resulting in insufficient numbers of ROs surviving to Day 120. In contrast to this, PT2 displayed typical characteristics for ROs differentiated with the BMP4-activated protocol. Spheroids formed primitive neuroepithelium which became more defined in structure over time in the ROs. Efficiency rates for PT2 in the BMP4-activated protocol were favourable for the study at approximately 82% (236/288 EBs).

On the other hand, PT1 developed robust RO development in the IGF1-dependent protocol as demonstrated in **Figure 4.3 B.** Primitive neuroepithelium appeared as early as Day 30 and remained strongly defined throughout the differentiation period. Notably, retinal pigment

epithelium (RPE) spheres formed adjacent to the RO in PT1. This tends to occur in a cell-line specific and/or protocol-specific manner and can be attributed to the inherent self-organising capacity of iPSCs within this culture environment. The overall efficiency of PT1 in the IGF1-dependent protocol was approximately 50% (144/288 EBs). PT2 iPSCs did not respond to the IGF1-dependent protocol with poor spheroid formation by Day 30 with nothing to show for subsequent timepoints resulting in an overall yield of 0%.

As issues were observed when differentiating both patient and control iPSC lines to ROs with the two protocols, it was difficult to determine which protocol to carry forward in the study. Ultimately, it was deemed necessary to use both the BMP4-activated and IGF1-dependent protocols to generate ROs from all iPSC lines generated for this study. However, this introduces a confounding factor when attempting to assess the variability between control and patient iPSCs, as it becomes challenging to determine whether observed differences are due to protocol-specific effects or patient-specific effects. To mitigate these effects, we changed our unaffected control iPSC line from WT3 to another in-house iPSC line, WT2, generated from a different donor. WT2 has been previously shown to successfully differentiate using both the BMP4-activated and IGF1-dependent protocols. By utilising this new control line, we aimed to better discern the impact of the protocols themselves on the observed variability between patient and control iPSCs, independent of protocol-specific effects. For reader clarity going forward, all ROs generated from the BMP4-activated method will be displayed on a purple background and those from the IGF1-dependent method will be displayed on a blue background.

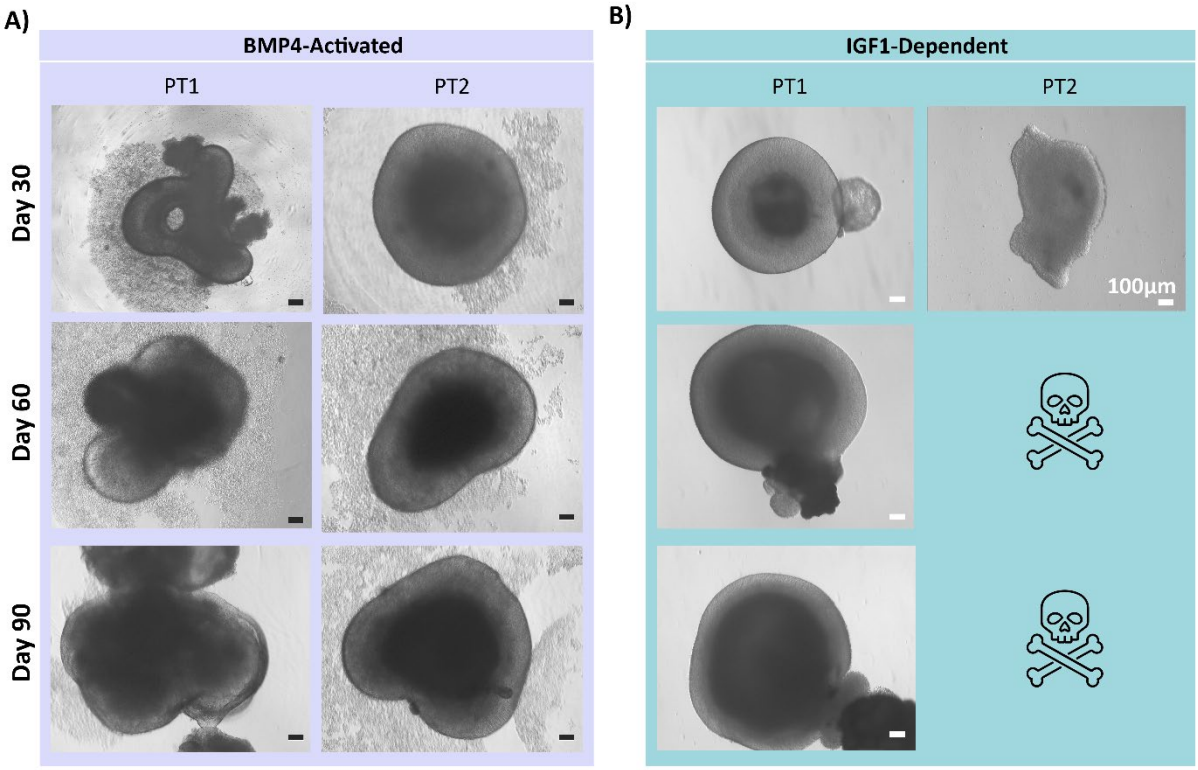

Figure 4.3 Variability in RO differentiation also apparent with reprogrammed STGD1 iPSC lines

A) PT1 iPSCs could produce RO structures using the BMP4-activated method but displayed limited neuroepithelium throughout the initial differentiation period, which continued to thin in later stages. Overall RO differentiation efficiency for PT1 in this method was 15%. In contrast, PT2 iPSCs produced consistent RO structures morphologically similar to the unaffected control in the BMP4-activated method, exhibiting an overall efficiency of 82%. **B)** PT1 responded more favourable to the IGF1-dependent method with clearly defined bright phase neuroepithelium from as early as Day 30. Structures remained viable in culture over 90 days and had an overall yield efficiency of 50%, which was a dramatic improvement to BMP4-actived method. PT2 on the other hand did not develop any viable RO structures with the IGF1-dependent method within the initial 30-day differentiation period.

A summary of the differentiation strategies and iPSC lines tested can be seen in **Figure 4.4.** The final iPSC lines used in the BMP4-activated method are WT2 and PT2, whilst in the IGF1-dependent method, there are WT2, AC and PT1, which are highlighted green. All failed differentiations are highlighted red.

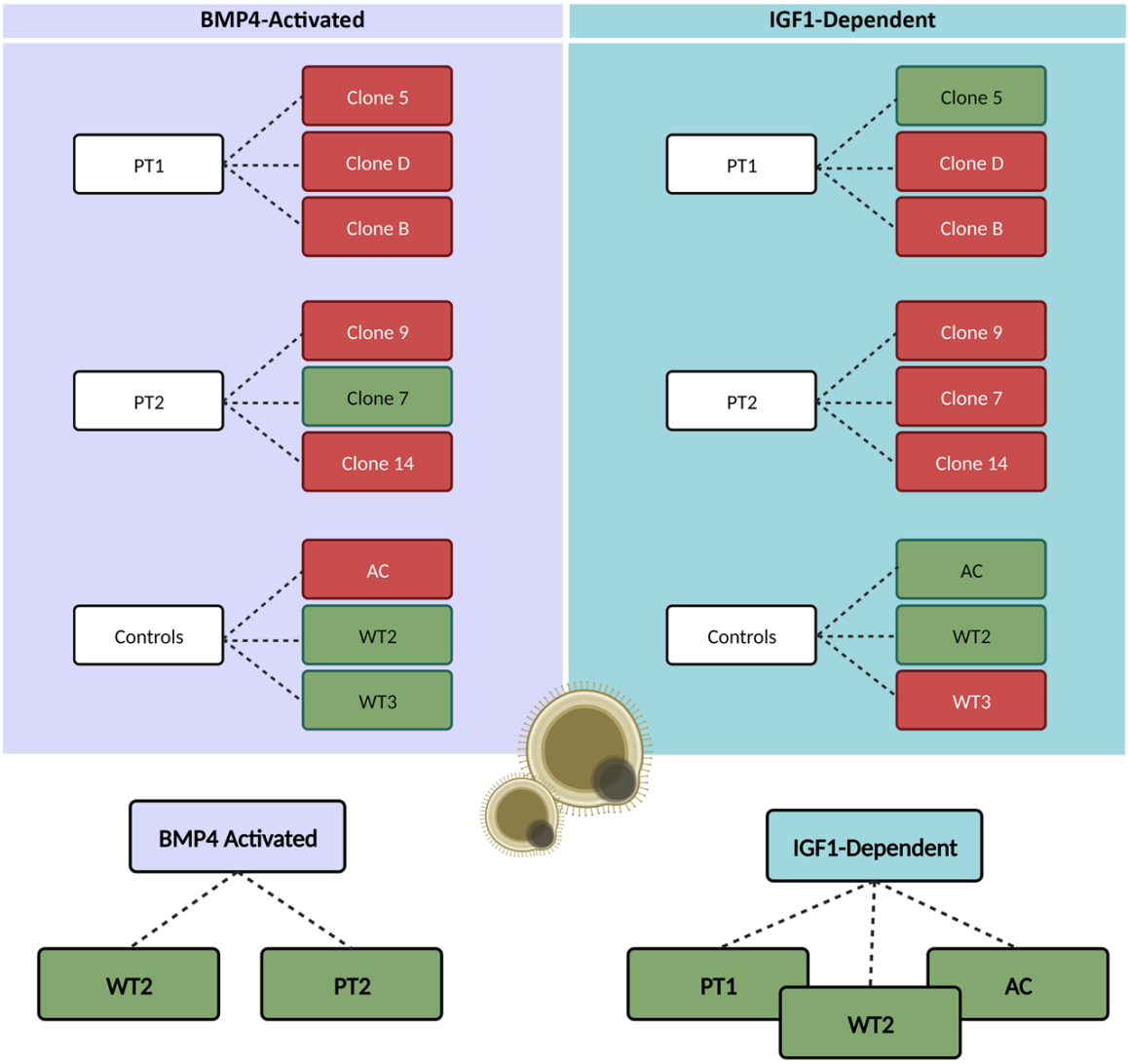

Figure 4.4 Summary of RO differentiations - Successes and Failures

An overall summary of all iPSC lines tested in both the BMP4-activated and IGF1-dependent protocols. Failed experiments are shown in red rectangles and successful differentiations are shown in green rectangles. Notably, WT2 produces successful RO structures consistently in both RO differentiation protocols as is used to mitigate any protocol-specific phenotypic effects.

The successful iPSC-RO lines used in the study are displayed clearly at the end of the figure in summarised format.

4.3.2 ROs from all iPSC lines continually develop until Day 220 and generate nascent POS

Following on from the 90 days of development displayed previously, ROs continue to develop over an additional period of 140 days to a total culture duration of 220 days **(Figure 4.5).** By Day 120, all ROs display a clearly defined retinal neuroepithelium, noticeable by the bright phase layer surrounding the organoid's perimeter. By Day 180, we begin to see thin, bristle-like structures extending from the organoid's apical edge, resembling photoreceptor inner and outer segment structures (referred to as IS and OS respectively). The formation of these structures occurred as early as Day 150, indicating correct photoreceptor cell maturation. By Day 220, the OS grew longer and were more abundant (indicated by red arrows in **Figure 4.5**). As ABCA4 is specifically expressed on the tips of POS, Day 220 was chosen as our endpoint for assessing phenotypic differences in the ROs along the spectrum of STGD1 cases and control cases included in our study. Although ROs can survive durations longer than 220 days in culture, doing so often compromises the integrity of inner retinal structures. Thus, the balance between photoreceptor maturation and maintenance of inner retinal architecture was a crucial consideration in the selection of this timepoint. It has also been noted that ROs do not mature any further past week 30 of differentiation (Cowan *et al.*, 2020).

There are some key morphological differences in the ROs resulting from the BMP4-activated method versus the IGF1-dependent method. Specifically, the neuroepithelium appears to be thinner in the BMP4-activated protocol. WT2 iPSC, which was differentiated in both of these protocols, confirmed the protocol-specific phenotype demonstrating its requirement in deciphering disease phenotype from protocol-specific phenotypes. Comparative analysis of WT2 organoids facilitates a better understanding of the variations across patient and control iPSC derived ROs and their significance in STGD1 pathogenesis.

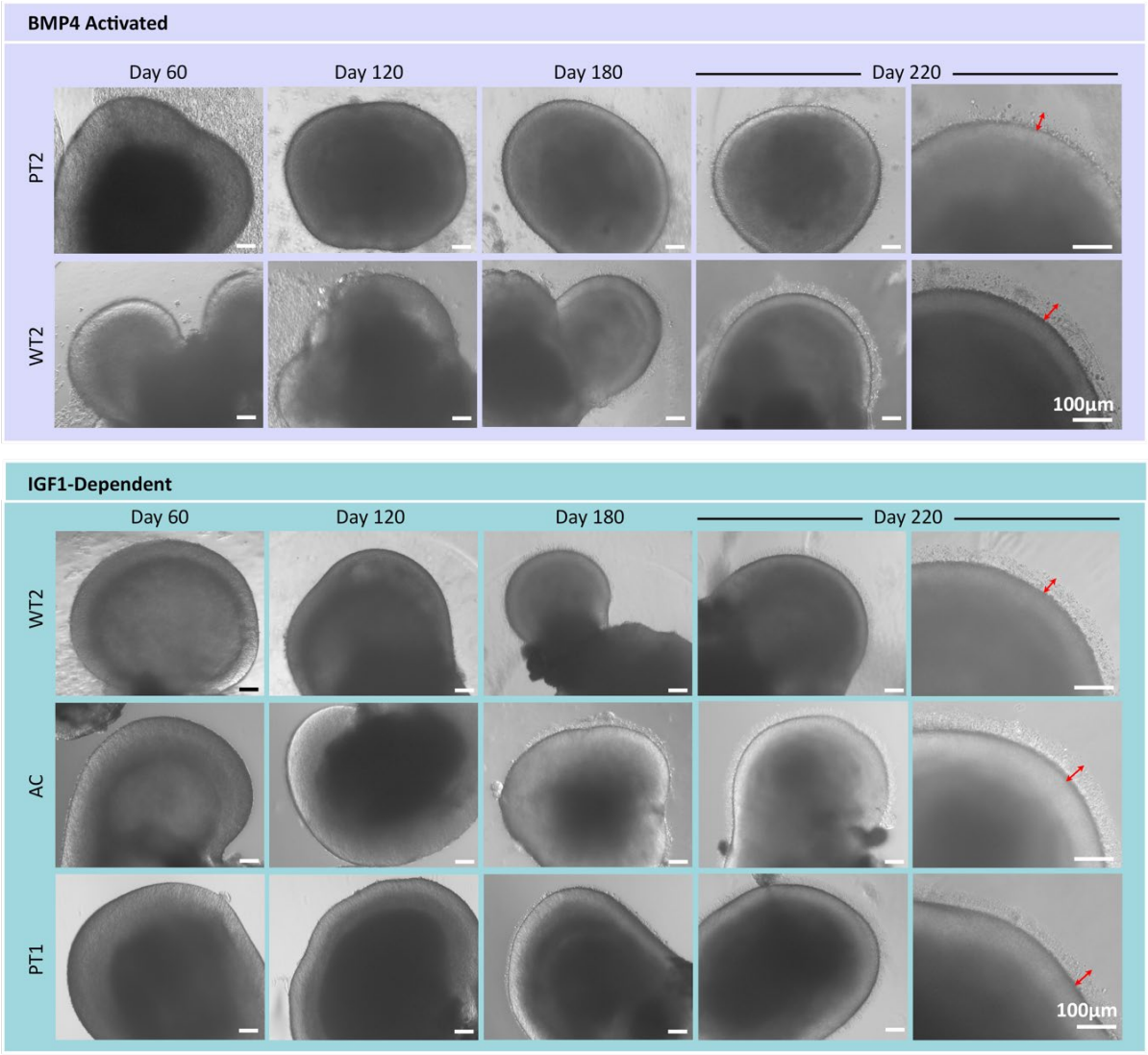

Figure 4.5 Brightfield images of full RO differentiation time course for patient and control iPSCs in respective protocols

Representative ROs derived using the BMP4-activated method of RO differentiation are displayed in the purple box. PT2 and WT2 are displayed at various timepoints of differentiation spanning Day 60 to Day 220. Similarly, representative ROs derived from the IGF1-dependent method of differentiation are displayed in the blue box. Across all lines and protocols, clearly defined RO structures are developed by Day 120 of differentiation. By Day 180, the characteristic inner and outer segment brush border is apparent on the organoid's apical edge and continues to develop longer structures by the final timepoint of Day 220 as evidence by the red arrows in the final column. Scale bars are 100µm.

4.3.3 Day 120 ROs positively express markers of early and late retinal neurogenesis

We utilised immunocytochemistry (as described in **Section 2.4.2**) as one of the main experimental outputs to track the progress of RO differentiation over a series of important timepoints throughout the 220-day differentiation period. Early differentiation of iPSCs to ROs is characterised by the presence of $VSX2^+$ RPCs and CRX^+ PPCs and. $Recoverin^+$ photoreceptors and $SNCG^+$ RGCs are also present in early retinogenesis, from approximately Day 35, but shown at Day 120 in **Figure 4.6.**

At Day 120, immunocytochemical data from all iPSC lines (WT2, AC, PT1 and PT2) subjected to the RO differentiation revealed the presence of early neurogenic markers aforementioned, alongside markers indicating the emergence of more specialised cell types such as $CRALBP^+$ Müller glia, $PROX1^+$ HCs and $AP2\alpha^+$ ACs **(Figure 4.6).** This indicated that the ROs were developing as expected and forming laminated structures characteristic of *in vivo* retinal tissue.

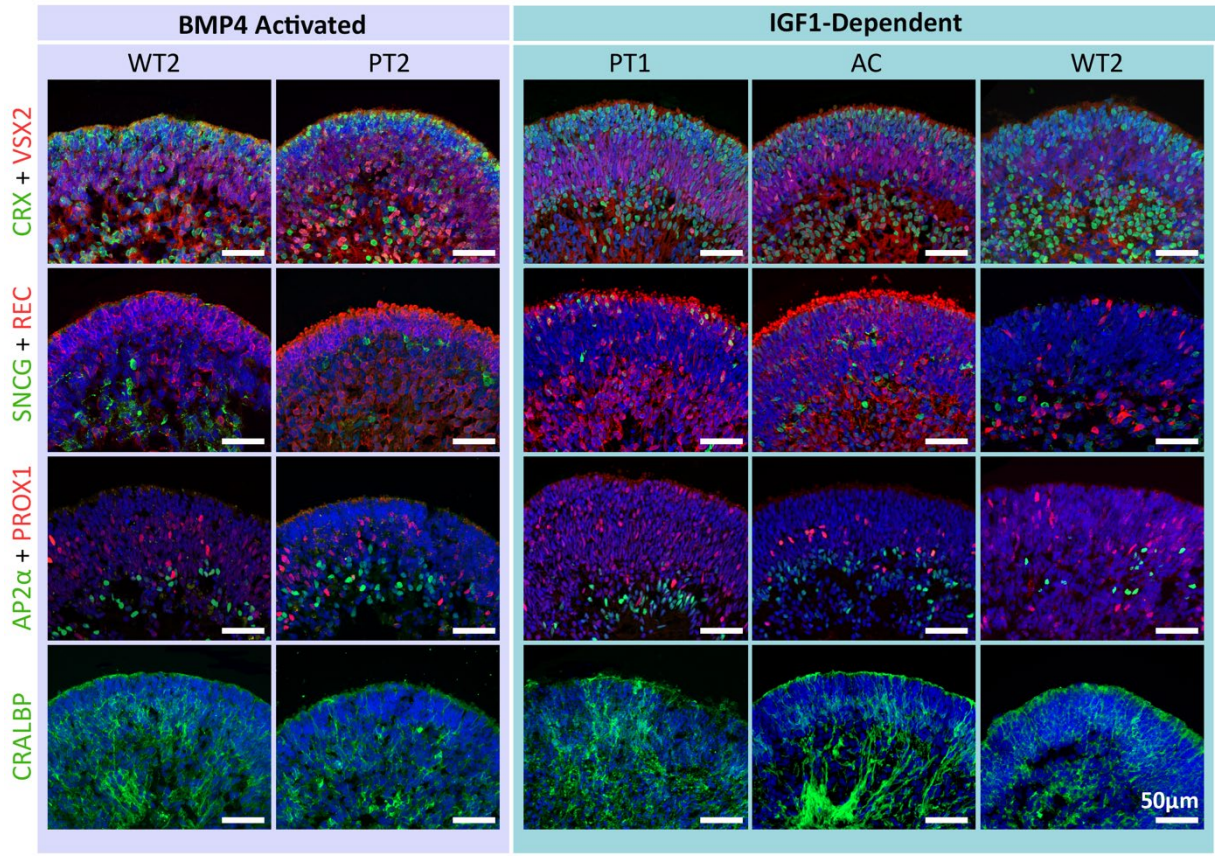

Figure 4.6 Patient and Control iPSC-ROs express both early neurogenic and specialised retinal neuron markers at Day 120 of differentiation

The purple panel represents ROs developed using the BMP4-activated protocol and the blue panel represents ROs derived from the IGF1-dependent protocol. Despite different protocols being used, all ROs stained positively for markers of early and late neurogenesis at this intermediary stage of retinogenesis. Positive markers included CRX (PPCs), VSX2 (RPCs), REC (photoreceptor cells), SNCG (RGCs), PROX1 (HCs), AP2α (ACs) and CRALBP (Müller glia). This suggests each iPSC-RO line is developing as expected and is suitable for use at later developmental timepoints. Notable observations include the increased incidence of CRX^{+} cells in ROs derived from the IGF1-dependent method. However, this is likely attributable to inherent differences in the developmental schedule of individual neurons between the BMP4-activated and IGF1-dependent method. Scale bars are 50µm.

4.3.4 Day 180 ROs express key markers of mature retinal neurons

By Day 180, the ROs of both protocols have developed structures characteristic of matured iPSC-derived retina, including the development of photoreceptor inner segments (IS) and OS from the apical edge of the RO body. In **Figure 4.7,** these structures are clearly observable in REC^+ photoreceptor cells in PT1 and AC iPSC-derived ROs. However, these are difficult to see in the staining from all other iPSC lines including the unaffected controls. This is due to processing issues with preserving the OS structures which was optimised during the later differentiations - hence the morphological differences in the immunocytochemistry. However, we know that they develop these structures from the brightfield images at the same timepoint in **Figure 4.5.**

In addition to the development of these structures, the ROs contain $PKC\alpha^+$ bipolar cells. These cells localise to the middle layers of the neuroepithelium between the photoreceptor cells and RGCs. In native retina, this would facilitate a chain of communication from the from the light-sensitive neurons to the visual centres of the brain through the optic nerve. This suggests that the differentiated cells in the ROs are capable of intrinsic lamination and potential functional circuitry.

In support of this, we observe a general trend of $AP2\alpha^+$ ACs overlying $PROX1^+$ HCs across all iPSC lines as seen in native retina. $CRALBP^+$ Müller glial cells are also present and expand their processes the whole way through the developed retina of the ROs at Day 180.

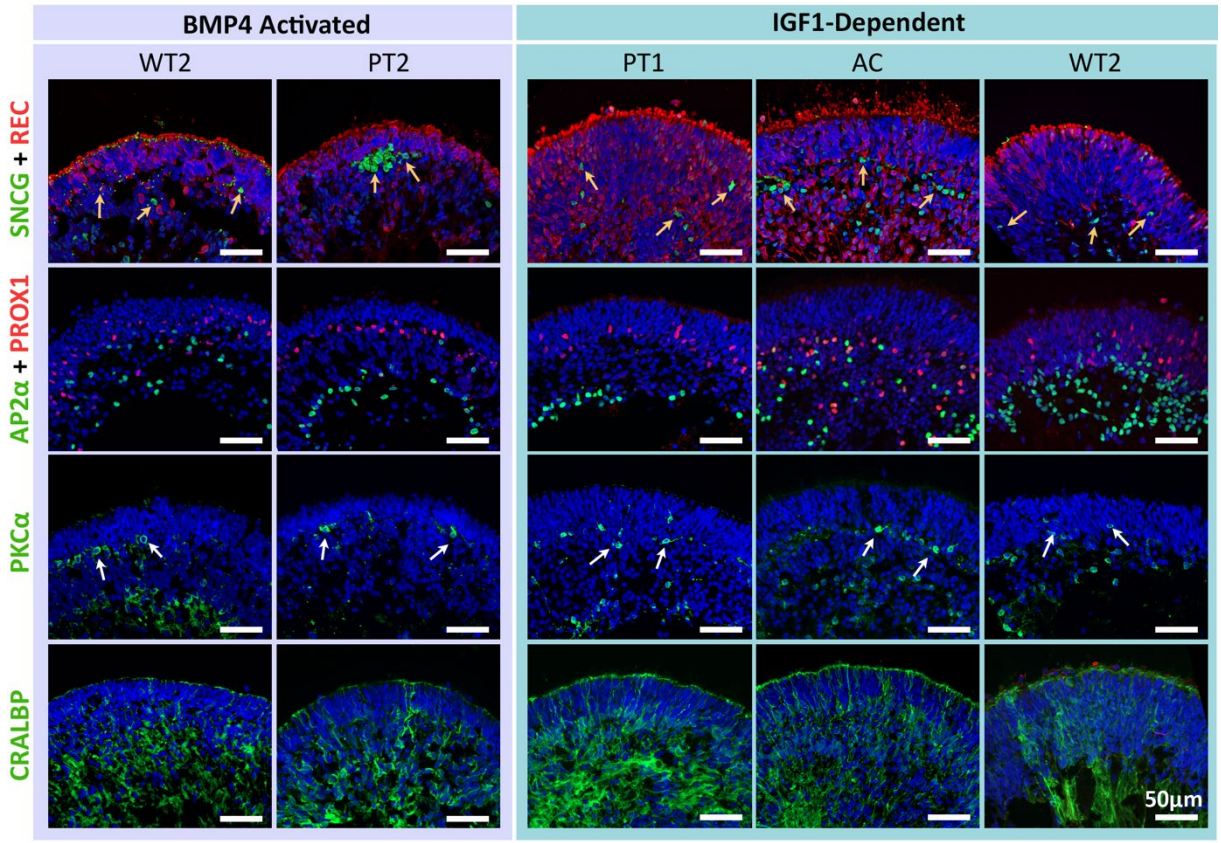

Figure 4.7 Patient and Control iPSC-ROs express mature markers of retinal neurons and display clear lamination patterns consistent with nascent retina at Day 180 of differentiation

The purple panel represents ROs developed using the BMP4-activated protocol and the blue panel represents ROs derived from the IGF1-dependent protocol. All iPSC-derived ROs possess markers for REC (photoreceptor cells), SNCG (RGCs, yellow arrows), PROX1 (HCs) AP2α (ACs), PKCα (bipolar cells, white arrows) and CRALBP (Müller glia). REC^+ photoreceptors are observed on the organoid's apical edge with $SNCG^+$ ganglion cells aligning in the lower central region of the organoid, defining the neural retina boundaries in the iPSC-ROs. $PKC\alpha^+$ cells are located centrally between the photoreceptor and RGCs, suggesting potential cell-cell connectivity. The interneurons: $PROX1^+$ HCs and $AP2\alpha^+$ ACs, are also found in the centre of the organoid with HCs overlying the ACs. Müller glial cells are present with their processes spanning the entire retinal structure. This resembles the nascent retina's correct lamination in both control and patient RO lines. One notable observation is the disruption to interneuron lamination in AC ROs where HCs and ACs are interspersed rather than forming distinct layers, suggesting possible tissue degeneration, and tissue remodelling. Scale bars are 50µm.

4.3.5 Quantification of retinal markers at Day 220 reveal few cell percentage variances across iPSC-lines.

Neurons continued to develop and mature until Day 220 of the differentiation protocol i.e., the endpoint of this study. At this point, it is expected that the ROs contain all differentiated retinal neurons with few developmental variances of cell numbers within the same protocol group, with the exception of any disease-specific phenotypic effects that arise. Evidence of neuronal staining at this timepoint is seen in **Figure 4.8 A**. Indeed, few developmental variances were observed across neuronal cell markers as shown by the quantification of neuronal cell percentages within a pooled RO cluster of 5 organoids **(Figure 4.8 B).** Quantification of cell percentages is described in **Section 2.4.3**. One-way ANOVA was performed to measure the significance in sample variability for each marker.

The percentage of Recoverin$^+$ photoreceptor cells remained static across all RO lines. Interestingly, we did however observe a mislocalisation of Recoverin$^+$ cells in the middle of ROs in a patient-specific manner, with AC and PT1 displaying the highest degree of retention. At such a late developmental timepoint, we expect photoreceptors to align on the apical edge. This phenotype is discussed more in detail later in **Section 4.3.8.**

A higher incidence of SNCG$^+$ RGCs was observed in the PT1, and AC ROs compared with their respective control WT2. AC also showed an increased incidence of interneurons HC (PROX1$^+$) and AC (AP2α$^+$). The only significant difference PT2 ROs displayed when compared to its respective unaffected control was a reduction in PROX1$^+$ cells. PKCα$^+$ cell numbers were similar across all lines. Whilst CRALBP$^+$ could not be quantified, the appearance of these Müller glial cells is as expected in all lines, with the cell processes stretching through the entire neural retina.

There is no one explanation for these variances in cell percentages across lines. They appear to occur in a patient-specific context with the most severe genotype correlating with the most affected phenotype in the STGD1 RO. This suggests that the ROs are capable of displaying disease severity. However, as ABCA4 protein is expressed exclusively in the photoreceptor cells of neural retina and should not govern the development of other retinal neurons directly, we hypothesize that ABCA4 mutations may increase the levels of stress and cause aberrant development or cellular degeneration of ROs in a patient-specific manner.

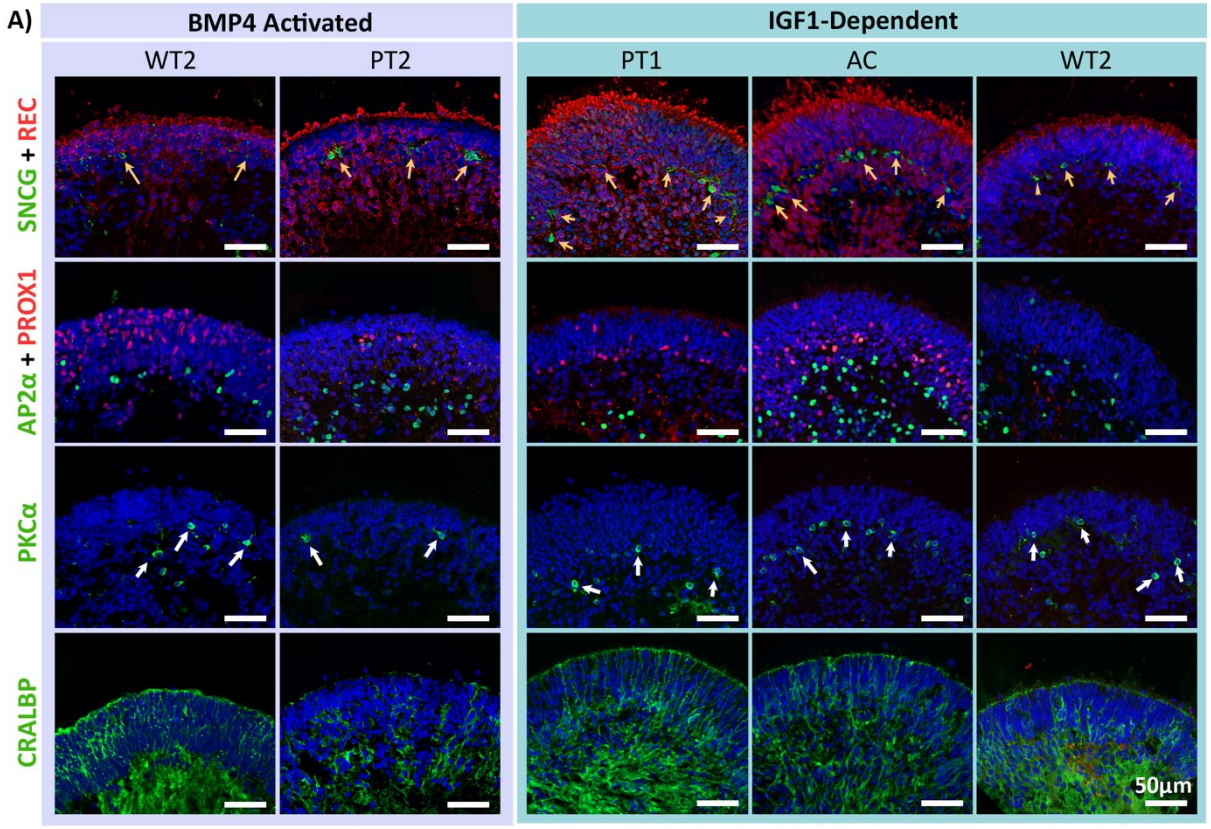
A)
BMP4 Activated
IGF1-Dependent
WT2
PT2
PT1
AC
WT2
SNCG + REC
AP2α + PROX1
PKCα
CRALBP
50µm

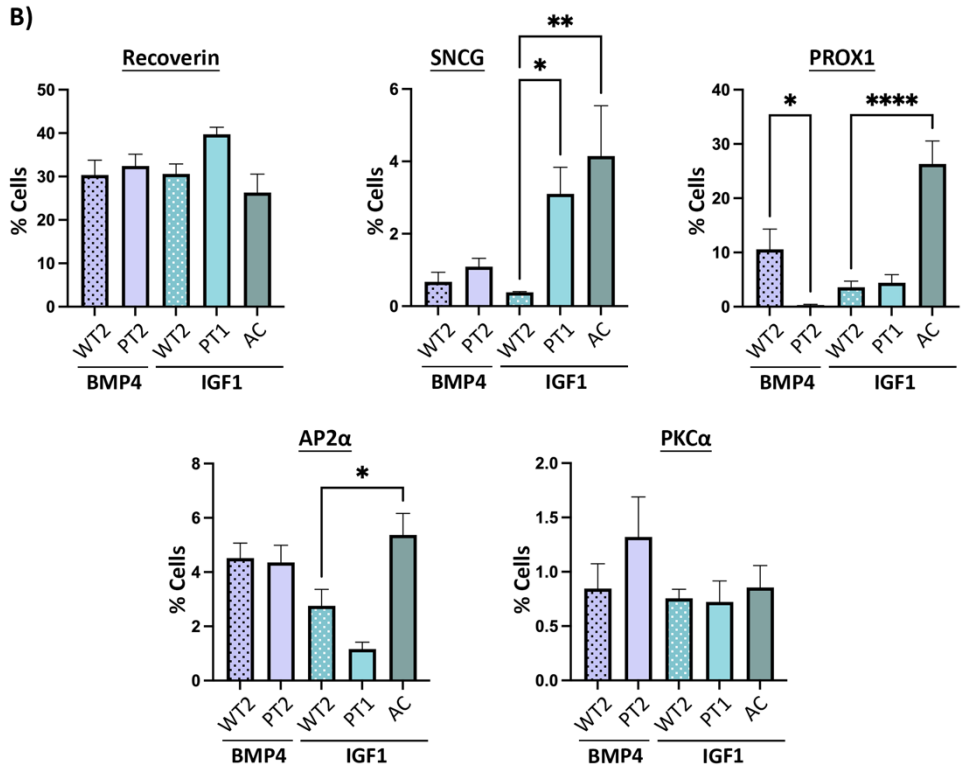
B)
Recoverin
SNCG
PROX1
AP2α
PKCα
% Cells
WT2
PT2
WT2
PT1
AC
BMP4
IGF1

Figure 4.8 Day 220 ROs display few neuron percentage variances between differentiated lines

A) The purple panel represents ROs developed using the BMP4-activated protocol and the blue panel represents ROs derived from the IGF1-dependent protocol. All iPSC-derived ROs possess markers for REC (photoreceptor cells), SNCG (RGCs, yellow arrows), PROX1 (HCs), AP2α (ACs), PKCα (bipolar cells, white arrows) and CRALBP (Müller glia). REC^{+} cells appear to mislocalise to the central part of the ROs in a patient-specific manner. There is evidence of interneuronal lamination disruption in the AC RO line. B) Few cell variances are observed from the quantification of cell percentages across all lines. A higher occurrence of $SNCG^{+}$ cells is apparent in PT1 and AC RO lines. $PROX1^{+}$ and $AP2α^{+}$ interneurons also occur at higher frequency in AC ROs. PT2 displays a reduction in $PROX1^{+}$ cells. One-way ANOVA analysis, n=5. * = p-val 0.05, ** = p-val 0.01, **** = p-val 0.0001. Scale bars are 50µm

4.3.6 ABCA4 is expressed in POS in both native and iPSC-derived retina

In the literature, ABCA4 is localised to the tips of OS of both rod and cone photoreceptors (Allikmets *et al.*, 1997b). To validate this expression pattern and ensure the reliability of a polyclonal ABCA4 antibody purchased for our studies, we conducted immunostaining on human post-mortem retinal tissue using ABCA4 in combination with the cone-specific outer segment marker GT335. Our findings indeed confirmed the highly specific localisation of ABCA4 to the tips of the POS, with colocalisation of GT335^{+} cone POS **(Figure 4.9 A).** We did not perform colocalisation experiments to assess for ABCA4 protein expression in rod photoreceptor cells as we could not identify a suitable antibody against the rhodopsin protein in a species other than mouse, which was the host species of our ABCA4 antibody. However, it is widely reported in the literature that ABCA4 is also expressed in rod photoreceptors (Illing, Molday and Molday, 1997; Sun and Nathans, 1997) and we also see *ABCA4* transcript expression in our scRNA-seq data that overlaps with both cone and rod photoreceptor cell clusters **(Figure 4.13).**

Subsequently, when employing identical immunocytochemical parameters for ABCA4 staining in ROs, we observed a diffused pattern of expression across the photoreceptor OS as shown in **Figure 4.9 B.** Unlike in native retina where the expression is limited to the tips of POS, the dotted expression pattern of ABCA4 was seen widespread throughout the POS. This deviation is likely attributed to the nascent properties of the POS which include incomplete disc formation and aberrant disc stacking, a characteristic of feature ROs.

Despite this, there was a marked difference in the visible levels of ABCA4 protein across the ROs, coinciding with the genotype severity of each iPSC-RO. The unaffected control (WT2) displayed the most abundant levels of ABCA4 protein. This was followed by PT2 which possesses the least severe pathogenic ABCA4 mutation, and then PT1 which carries a disease-causing ABCA4 allele of increased severity. AC displayed the lowest detectable level of ABCA4, consistent with a loss of function (LOF) mutation, combined with the moderately severe missense mutation it carries. This was interesting to observe, especially considering the AC and PT1 iPSC-ROs had the most preserved OS structures. These results provided support that the iPSC-ROs are capable of ABCA4 expression and serve their purpose in assessing genotype-phenotype correlations between STGD1 of varying severities.

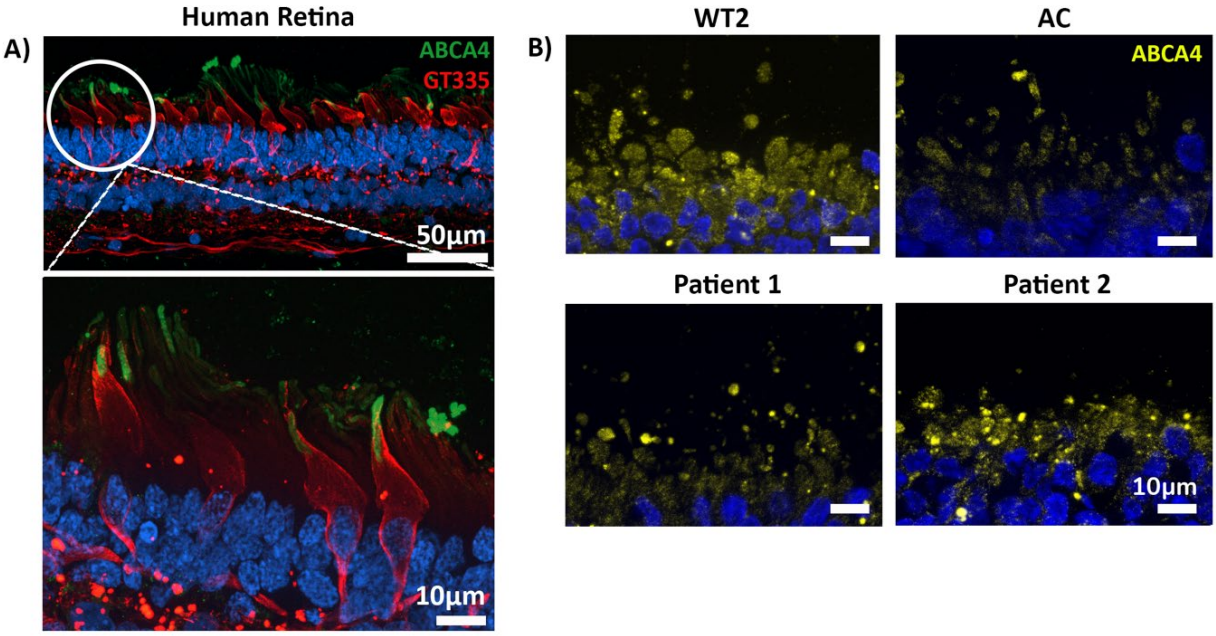

Figure 4.9 ABCA4 protein localises to POS in native retina and ROs

A) ABCA4 (green) and cone-specific GT335 (red) protein expression is depicted via immunohistochemistry staining in post-mortem retina tissue sample. The ABCA4 protein localises specifically to the POS tips of cone photoreceptor cells. **B)** ABCA4 (yellow) protein expression in nascent photoreceptor PIS and POS in Day 220 ROs. Staining patterns appear more diffuse throughout the IS and OS likely due to immature disc stacking in this developmental model. The degree of observable ABCA4 fluorescence appears to correlate with the estimated residual protein levels determined via the severity of patient line genotype. AC displays the lowest intensity of fluorescence, followed by PT1, PT2 and the unaffected control WT2. 20x magnification scale at 50µm and 63x magnification at 10µm.

4.3.7 Western blotting of lysates for ABCA4 reveal same genotype-phenotype correlations

As the expression pattern of ABCA4 in the immunostaining deviated from the expected pattern seen in native retina, we aimed to further validate the expression of ABCA4 in ROs via Western blotting (as described in **Section 2.4.5**). We utilised a monoclonal ABCA4 antibody with an epitope mapped to aa 2252 – 2262 of bovine ABCA4 that reacts with human tissue. From the lysates of each RO sample, we observed a band at approximately 250kDa **(Figure 4.10 A)** corresponding to the molecular weight of ABCA4. The samples varied in their levels of ABCA4 protein detected, consistent with immunocytochemical data and their respective ABCA4 genotypes.

When we quantified the relative protein levels against the levels of housekeeping gene ACTIN, we observed statistically significant variances between the samples **(Figure 4.10 B).** The AC and PT1 ROs deviated most significantly from the unaffected control (WT2), reflecting the severity of their individual genotypes. No significant variances were observed between the WT2 and PT2 ROs. Across all ROs, PT2 demonstrated the least significant ABCA4 phenotype. This coincides with the patient's clinical diagnosis of late-onset STDG1. Consequently, the ROs may not degenerate as much as is seen in more severe cases due to the mild severity of the *ABCA4* mutations these cells possess. Nonetheless, we can confirm that ABCA4 is expressed in the iPSC-ROs from individuals with STGD1 (both classical and late-onset presentation) and displays the levels of ABCA4 consistent with the genotype-phenotype correlation expectations.

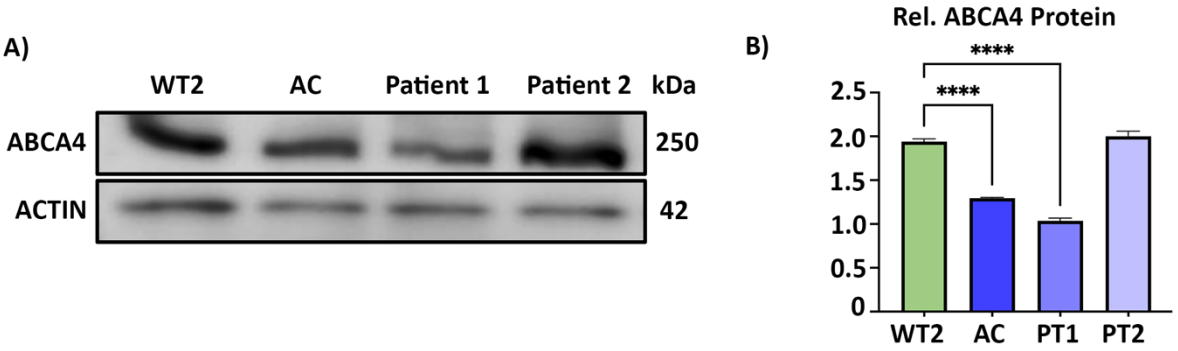

Figure 4.10 Western blotting confirms ABCA4 expression in iPSC-ROs

A) Western blotting revealed an abundance of protein at the expected size of ~250kDa. The intensity of the bands correlated with the severity of genotype possessed by each patient case. **B)** The intensity of the ABCA4 protein bands was normalised against a routinely used housekeeping protein: ACTIN and quantified. One-way ANOVA test revealed substantial significance in the reduction of protein in AC and PT1 samples. Whilst PT2 ABCA4 protein levels remained relatively close to WT2 samples. N=16 EBs per sample. **** = p-value < 0.0001

4.3.8 Photoreceptor mislocalisation occurs in later stages of differentiation and in a patient-specific manner

Throughout the differentiation time course, routine immunostaining was conducted to check for the development of the key retinal neurons. In addition to assessing the presence/absence of such neurons, it is also important to assess the localisation of these cells if present. Typically, we expect to observe them in a laminated manner, akin to native retina. Whilst all other retinal neurons aligned as expected in the ROs, we observed some disruption in the lamination in regard to the localisation of mature photoreceptor cells. We expect as the differentiation progresses to later stages, that photoreceptor cells align to the apical edge of the RO, with their developed ISs and OSs protruding outwards from the presumptive outer nuclear layer (ONL), generating the characteristic brush border seen in ROs.

Figure 4.11 A displays the observed photoreceptor mislocalisation during our differentiations, specifically in the patient iPSC-ROs. This phenotype first became evident at Day 180, with a higher occurrence of OPN1MW/LW^{+} cone cells concentrated in the central region of the organoids. Notably, the degree of cone mislocalisation appeared to correlate with the severity of *ABCA4* genotype in the samples. ROs from the AC displayed the most pronounced defect, characterised by the mislocalisation of numerous OPN1MW/LW^{+} cones in addition to RHO^{+} rods.

It is important to note that *ABCA4* has been implicated in other retinal degenerative conditions. These diseases exist along a spectrum of severity, which directly correlates with the levels of residual protein function in ABCA4. As aforementioned, the AC carries the most severe genotype in this study. When the case presented to the clinic, they were diagnosed with STGD1/borderline CRD based on their ocular phenotype. It is interesting to see that the organoids could recapitulate the severity of this case by involving both photoreceptor subtypes.

To quantify this effect across the patient lines at the final timepoint of Day 220, we gated the photoreceptors in the centre and on the apical edge (internal and external photoreceptors) of the ROs and counted the numbers of OPN1MW^{+} and RHO^{+} positive cells at both sites. Using a pre-designed MATLAB script developed in the Lako lab prior to the study, it was possible to quantify the number of positively stained cells without bias. We then conducted a one-way ANOVA on the resulting data compared with respective protocol controls to reveal statistically

significant differences between the patient and control RO samples for both internal and external OPN1MW$^+$ and RHO$^+$ cells.

OPN1MW$^+$ cells demonstrated the most pronounced mislocalisation among all tested photoreceptor markers. The quantified data reveals a remarkable reduction in external OPN1MW$^+$ cells across all patient ROs **(Figure 4.11 B).** Similarly, the internal OPN1MW$^+$ cells displayed a significant increase in numbers when compared with healthy controls, mirroring the observed trend of external OPN1MW$^+$ cells.

Based on immunocytochemistry results, RHO$^+$ cells also exhibited mislocalisation of rod photoreceptors. However, this phenomenon was exclusively observed in patient lines with the most severe genotypes – AC and PT1. The quantified data shows that external RHO$^+$ cells in the AC line displayed the highest reduction, followed by PT1 when compared to respective controls **(Figure 4.11 C).** Interestingly, PT2 showed an increase in external RHO$^+$ when compared with its corresponding control, indicating a potential cell line-specific effect rather than a genotypic effect. Regarding internal RHO$^+$ cells, a significant increase in positively stained cells was only observed in the AC ROs, while all other patient lines did not display significance when compared to their respective controls.

The observed mislocalisation of both cone and rod cells in the AC ROs adds an intriguing dimension to our findings, as it suggests a potential link between ABCA4-related disease severity and the extent of photoreceptor mislocalisation. However, no existing literature establishes a connection between *ABCA4* mutations and defective photoreceptor development during retinogenesis. To elucidate this further, we employed a single cell RNA-sequencing (scRNA-Seq) strategy in effort to gain insight into this photoreceptor anomaly.

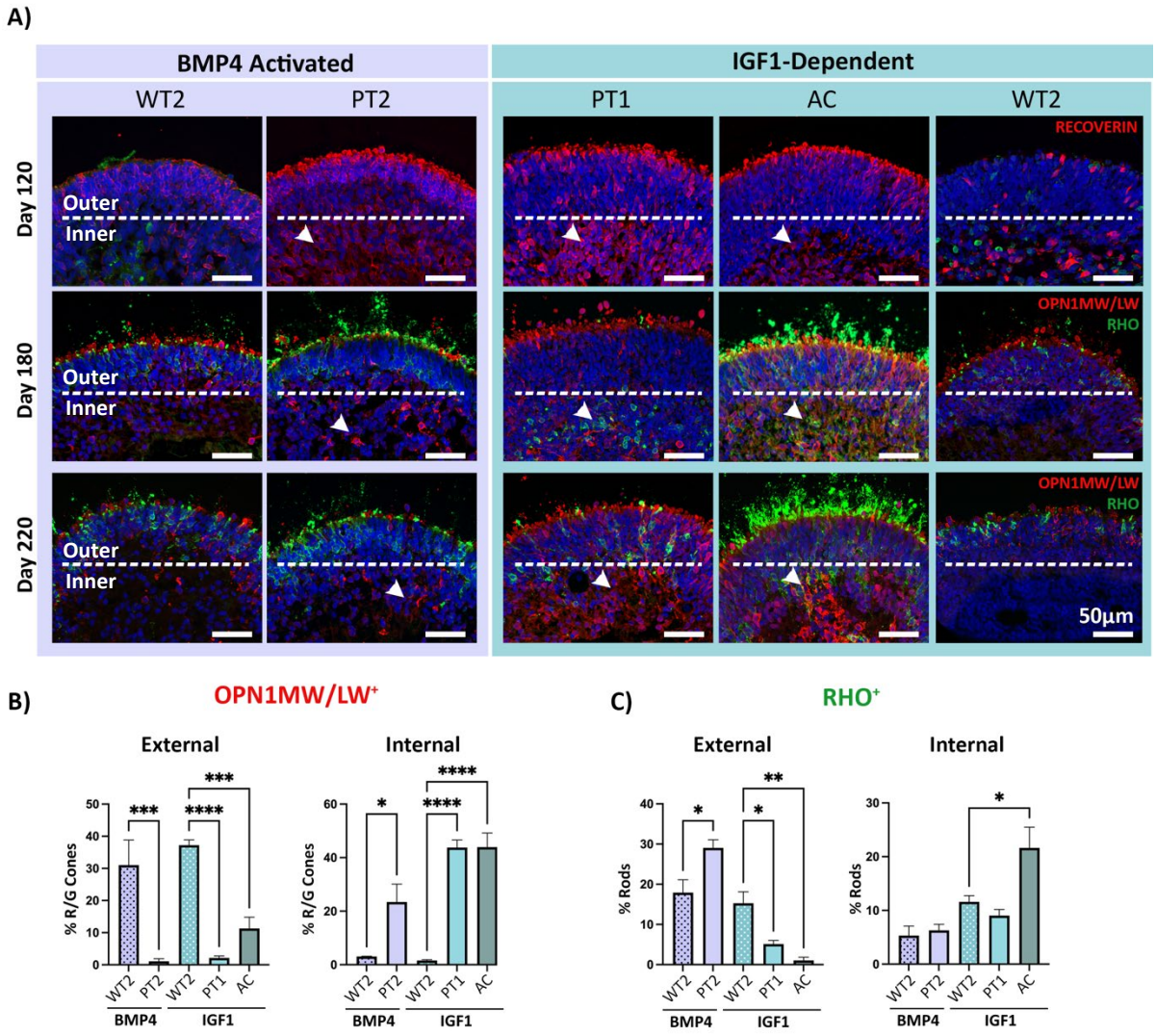

Figure 4.11 Photoreceptor cells are mislocalised in a patient-specific manner

The purple panel represents ROs developed using the BMP4-activated protocol and the blue panel represents ROs derived from the IGF1-dependent protocol. **A)** At Day 120, an abundance of REC^{+} photoreceptors mislocalise to the centre of the organoid when compared with WT2 controls as shown by white arrowheads. Some photoreceptor retention is expected as shown in WT2 controls. However, retention levels in PT2, PT1 and AC is abnormal. At Day 180 and Day 220, OPN1MW/LW^{+} cells confirm red/green cones to be the most affected cell by this phenomenon, also shown by white arrowheads. AC and PT1 ROs also display rod affection with the mislocalisation of RHO^{+} cells. There is evidence of correctly aligned photoreceptors on the RO's apical edge alongside positively stained OS in patient ROs (shown above dashed line) suggesting not all photoreceptors are affected. These results match the genotype-phenotype correlation matrix where the severity of phenotype directly correlates with residual protein function.

Mislocalised OPN1MW/LW^{+} and RHO^{+} photoreceptors were quantified at Day 220 by counting the number of externally and internally positioned photoreceptor cells. External/Internal boundaries are defined by the white line across the central region of the RO. **B)** A dramatic decrease in external OPN1MW/LW^{+} cones in PT2, PT1 and AC was observed when compared with their respective WT2 controls. In contrast, internal OPN1MW/LW^{+} cells displayed a significant increase in PT2, PT1 and AC internal cones. Significance was highest for the AC ROs which displayed the most enhanced phenotype. **C)** External RHO^{+} cells displayed a higher number of RHO^{+} cells in PT2 when compared with WT2. Whilst PT1 and AC ROs showed a substantial decrease in externally aligned RHO^{+} cells. When quantifying the internally mislocalised RHO^{+} cells, the only significant result observed was between the AC and WT2 ROs. Statistics: One-way ANOVA. N=5 ROs - comparing only within protocol groups (e.g., BMP4-activated PT2 vs WT2). * = p-val 0.05, ** = p-val 0.01, *** = p-val 0.001, **** = p-val 0.0001. Scale bars are 50µm.

4.3.9 iPSC-ROs possess expression signatures of key neuronal classes of the retina

ROs from AC and PT2 iPSCs were chosen along with two wild-type controls (WT2 and WT3) to partake in a scRNA-Seq experiment (as described in **Section 2.5**) and WT3 were differentiated using the BMP4-activated method, whilst AC and WT2 were differentiated with IGF1-dependent method. The disease-specific iPSC lines selected displayed the highest and lowest levels of photoreceptor retention, respectively, in the immunocytochemistry experiments at later timepoints. Following sample preparation and sequencing, the data were processed by Dr. Rachel Queen of the BSU at Newcastle University and we received gene expression data from the input samples. Where data was similar across WT2 and WT3 controls, averages were taken for statistical purposes.

In the UMAP of **Figure 4.12** individual cells are shown as dots on the plot. Cells cluster with other cells based on their gene expression signatures. Cells that significantly express distinct retinal neuron markers are easily identifiable and can be identified as a specific cell type cluster. The clustering for the integrated UMAP were manually assigned via this method, based on specific retinal cell types published in Sridhar *et al.* (2020). Among all 17 cell clusters identified in the integrated UMAP, we identified the key 7 cell types found in the neural retina: cone photoreceptors, rod photoreceptors, ACs, HCs, bipolar cells, retinal ganglion cells and Müller glia – (clusters 4, 13, 1, 6, 3, 12 and 9).

In addition to these key neuronal cells, we also identified several precursor/progenitor cell clusters including the T1, T2 and T3 populations which emerge transiently in developing retina - (clusters 7, 15, 16 and 17) (Sridhar *et al.*, 2020). Interestingly, we also identified cell clusters from extraretinal tissues aligning with markers of astrocytes, fibroblast/stromal cells, ocular surface epithelium (OSE) and lens - (clusters 2, 5, 8 and 10). An island of RPE (cluster 14) was also present in the UMAP.

The clustering of cells within the UMAP itself is arbitrary, but akin to how the cells develop clusters based on their shared gene expression signatures, the clusters will also associate with other clusters they derive from or are similar to. An example of this is the cone and rod photoreceptors (clusters 4 and 13) which appear to branch off from the T3 transient population (cluster 17) which are known progenitors of photoreceptors and bipolar cells. Similarly, the T2 transient population (cluster 16) is reported to give rise to HCs and ACs (clusters 6 and 1), both of which are in close proximity to each other on the UMAP. The other

transient population T1 (cluster 15) gives rise to RGCs (cluster 12) as displayed in the UMAP but interestingly, we can also see the association of T1 and T2 populations with the late RPCs cluster (cluster 7) as T1 emerges from late RPCs, and T2 from T1.

A cluster of proliferating cells (PCs) (cluster 11) was also identified in the integrated UMAP. A degree of proliferation is expected at Day 200 for the continued growth, maturation, and maintenance of the organoid, however we hypothesised that this could present answers to the mislocalised photoreceptor phenomena observed in our patient organoids and was later investigated.

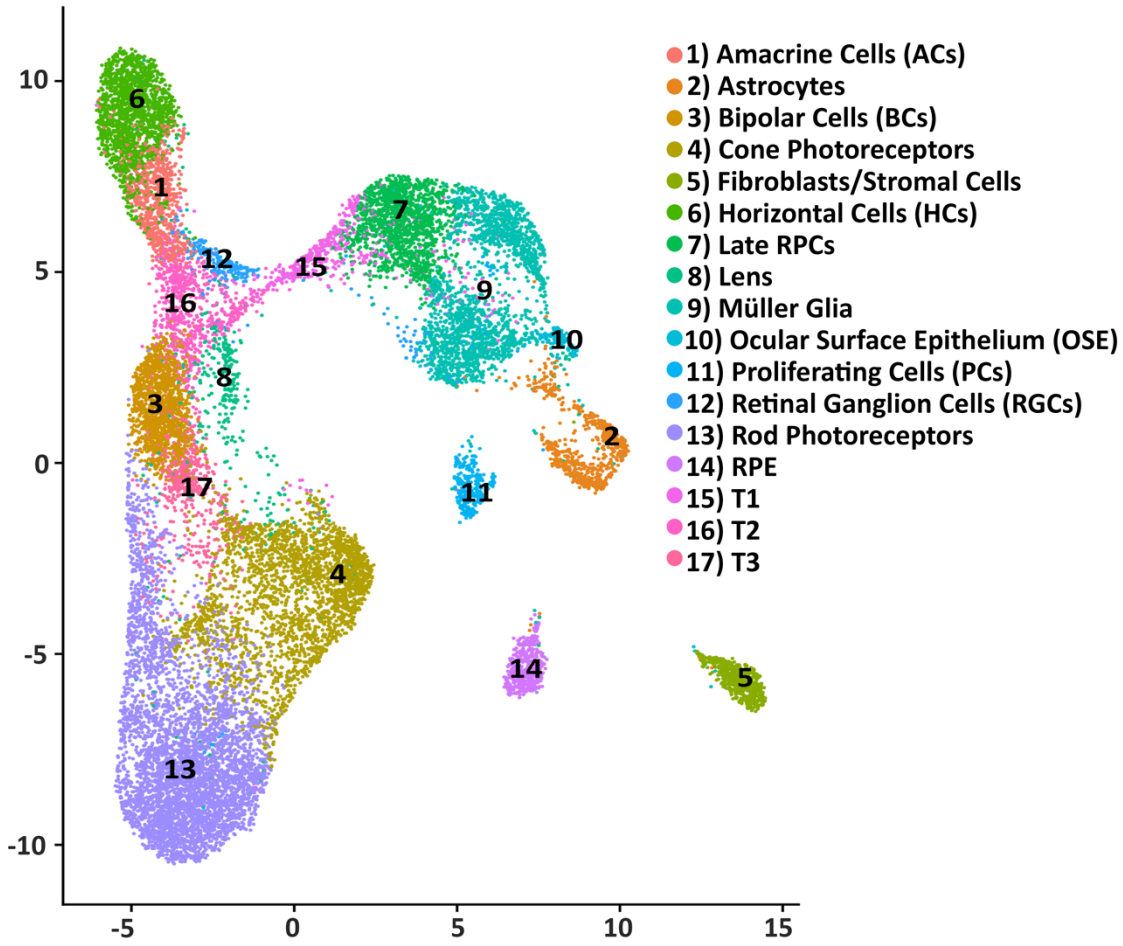

Figure 4.12 Integrated UMAP of single cell transcriptomes of AC, PT2 and WT ROs

Integrated UMAP of iPSC-ROs from combined single cells of AC, PT2, WT2 and WT3 ROs at Day 200 of differentiation. 17 distinct cell clusters were identified. Each dot on the UMAP represents a single cell, and cells that form clusters share overlapping gene expression signatures. Clusters sharing partial overlapping gene expression also arrange themselves in close proximity of each other on the UMAP.

Clustering analysis shows the presence of the key major neuronal cell types found in the retina – ACs (C1), Bipolar Cells (C3), Cones (C4), HCs (C6), Müller glia (C9), Retinal Ganglion Cells (C12) and Rods (C13). Extraretinal tissues also feature as clusters including Astrocytes (C2), Fibroblasts/Stromal Cells (C5), Lens (C8), Ocular Surface Epithelium (C10), RPE (C14). Precursor and Progenitor populations are also present with Later RPCs (C7), PCs (C11) and the transient progenitor populations T1, T2 and T3 (C15, C16, C17).

4.3.10 Rod and cone photoreceptors clusters express ABCA4 on transcriptomic level

There are a number of rod and cone-specific markers that can be used to differentiate photoreceptor clusters. We utilised *Rho* and *Arr3* gene expression to display rod and cone photoreceptors on the integrated UMAP **(Figure 4.13).** *Rho* encodes the rhodopsin protein, a rod-specific opsin protein with that enables visual perception in low levels of light. *Arr3* encodes arrestin-C, a cone-specific protein that localises to the IS and OS of cone photoreceptors.

The cells expressing *Rho* and *Arr3* transcripts localise to the annotated region of cone and rod photoreceptors in the UMAP as expected. The scRNA-Seq data reveals a colocalisation of cells expressing *ABCA4* transcripts with those expressing *Rho* and *Arr3* transcripts. Whilst there are a number of cells expressing *ABCA4* scattered throughout UMAP, the intensity of expression is highest in the rod and cone photoreceptor clusters confirming the expression of *ABCA4* in both rod and cone photoreceptor cells. Interestingly, we do not see significant enrichment of *ABCA4* transcript in cluster 14 which corresponds to RPE tissue where *ABCA4* expression has recently been observed (Lenis *et al.*, 2018).

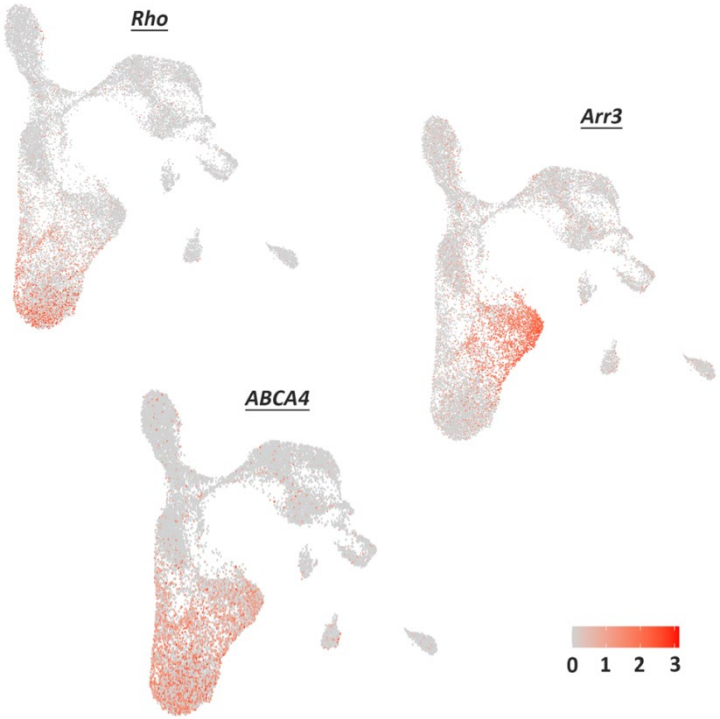

Figure 4.13 *ABCA4* expression enriched in cone and rod clusters

Individual UMAPs identifying rod and cone clusters by their expression of *Rho* and *Arr3* respectively. *ABCA4* expression is observed in overlapping positions of the rod and cone clusters confirming its expression in both of these photoreceptor subtypes.

4.3.11 The percentage composition of retinal neurons differs between STGD1 and WT ROs

Whilst we know that the ROs derived from AC, PT2 and WT2 each express the proteins associated with the major neuronal cell types of the retina as shown above in **Figure 4.7.** The scRNA-Seq data of the iPSC-ROs corroborated the development of these key neurons by generating cell clusters based on the unique transcriptomic signatures they possess.

The clustering analysis and annotation also enabled us to objectively quantify the number of individual retinal neuron classes in each sample, as a percentage of overall cells in the RO. This enabled us to understand the proportion of retinal neurons comprising each of the patient and control organoids. The percentages of these individual neuron clusters are represented independently for each RO sample and is proportional to the total cell count in that specific organoid line **(Figure 4.7 A).**

There are a number of key differences which can be clearly observed from the illustration of retinal neuron percentages in the RO samples. Importantly, the unaffected control lines (WT2 and WT3) look similar in overall percentage for each given neuron with the exception of rod photoreceptors, where WT2 appears to display a higher percentage of rod photoreceptor-associated transcripts. This is particularly important as WT2 and WT3 were generated using different protocols to control for protocol-specific phenotypes. WT2 was generated using the IGF1-dependent method and WT3 was generated using the BMP4-actived method.

Another potentially interesting result concerns the percentages of BCs versus rod photoreceptors in the AC sample, leading us to re-evaluate our hypothesis regarding cell cycle defects in ROs from STGD1 patients. The T3 population of cells acts as a transient progenitor cluster in retinal development and exhibits the remarkable ability to generate both bipolar and photoreceptor cells.

We observed a subtle but noteworthy increase in the number of T3 and bipolar cells within the AC sample in comparison to the PT2 (milder phenotype) and unaffected controls (WT2+WT3), and reduced cone and rod photoreceptors. This apparent bias towards bipolar cell generation over photoreceptor differentiation in the AC sample indicates potential challenges in determining the fate of photoreceptor cells from T3 progenitor cells. This hypothesis is further reinforced by the observation of a higher percentage of PCs in the AC sample, supporting the notion of altered cellular dynamics in STDG1 pathology.

Since these percentages are relative to the total number of cells present in a specific organoid sample, it is plausible that the higher proportion of BCs compared to photoreceptors is influenced by photoreceptor cell death. Given that this is an *in vitro* model of a degenerative retinal disease, such an outcome is highly likely. Apoptotic cells were assessed in **Section 4.3.14** through scRNA sequencing and later with CASP3 staining **(Figure 4.18).** A TUNEL assay would have been a useful addition to the study for the assessment of dying cells, however due to timing constraints and RO material, we were unable to carry out this experiment.

PT2 also exhibited a photoreceptor mislocalisation defect in **Figure 4.14 A**. With respect to the scRNA-Seq data, we don't see much of a photoreceptor effect on the transcript level. The T1 population, alongside late RPCs, appear to be expressed at higher rates in PT2 when compared with WT, suggesting potential defects in terminal differentiation to retinal neurons. Notably, there appears to be slightly elevated percentage of cone photoreceptors in PT2-ROs compared with WT-ROs, whereas the opposite was observed on protein level in immunocytochemistry experiments. However, transcriptomic data does not directly correlate with protein expression levels and the upregulation of genes associated with cone photoreceptors could be a compensatory mechanism due to photoreceptor degeneration or defects in the cell cycle.

In summary, the scRNA-Seq has given two potential causative factors for the mislocalisation of photoreceptor cells as seen in the immunocytochemistry experiments - 1) altered cell fate determination/cell cycle defects and 2) photoreceptor cell death. We looked at each hypothesis independently in **Sections 4.3.12, 4.3.13** and **4.3.14.**

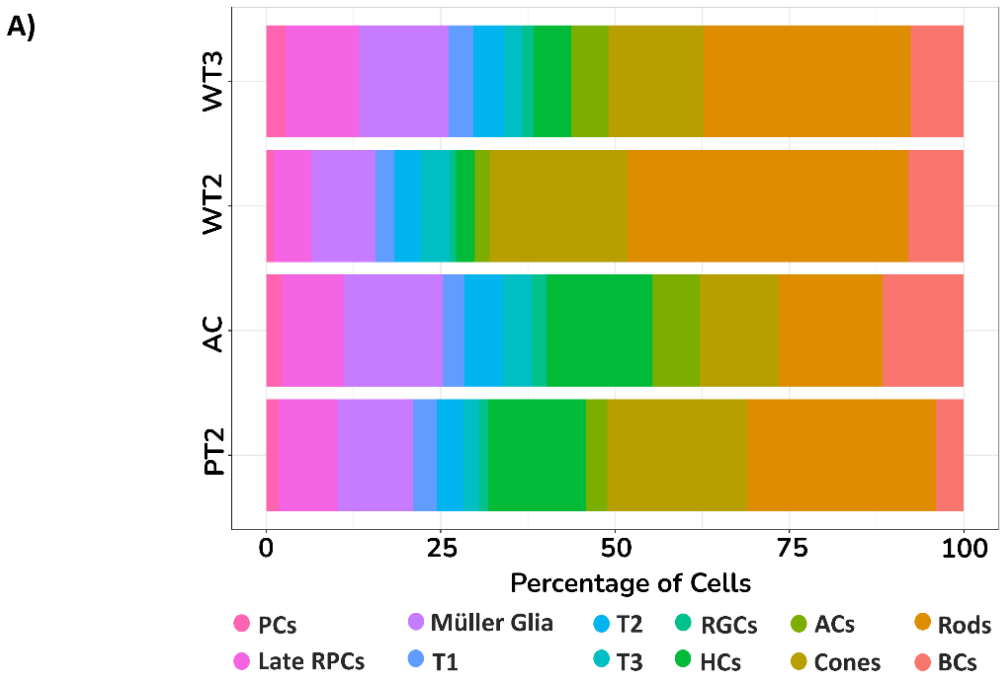
A)
WT3
WT2
AC
PT2
0
25
50
75
100
Percentage of Cells
PCs
Late RPCs
Müller Glia
T1
T2
T3
RGCs
HCs
ACs
Cones
Rods
BCs

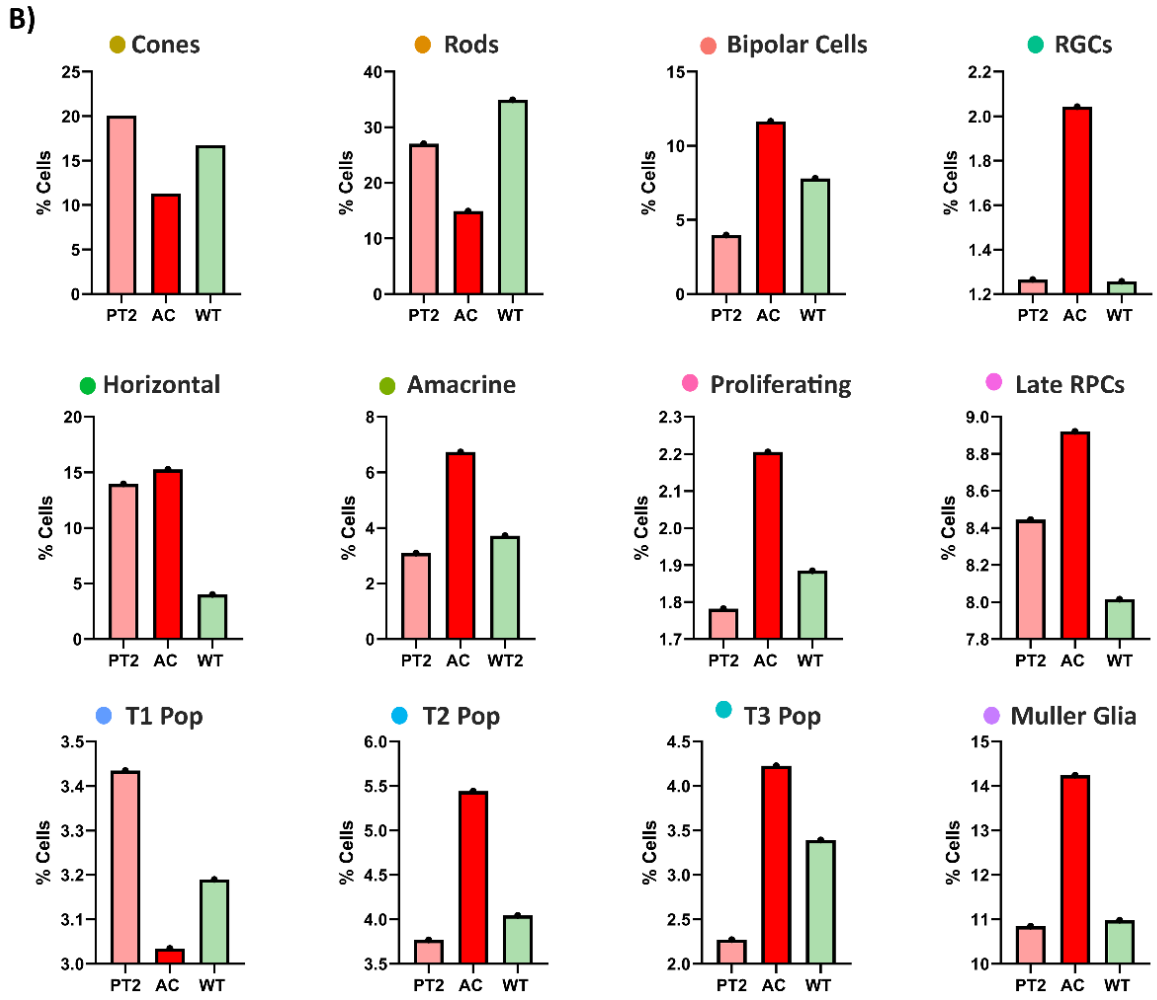
B)
Cones
Rods
Bipolar Cells
RGCs
Horizontal
Amacrine
Proliferating
Late RPCs
T1 Pop
T2 Pop
T3 Pop
Muller Glia
% Cells
PT2
AC
WT
WT2

Figure 4.14 Retinal Cell Percentages in iPSC-ROs for PT2, AC and WT

A) Stacked histogram representing the composition of each iPSC-RO line included in the scRNA-Seq study; WT3, WT2, AC and PT2. The cell clusters shown include those typically found in neural retina: proliferating cells (PCs), Müller glia, transient progenitors T1, T2 and T3, late RPCs, RGCs, ACs, HCs, rods, cones, and bipolar cells. The WT2 & WT3 lines represent WT organoids produced in IGF1-dependent protocol and BMP4-activated protocol respectively. The percentages of cells composing the WT2 and WT3 organoids were similar (with the exception of rods and were pooled for comparisons against patient lines. **B)** Displays comparisons of cell percentages within the PT2 and AC ROs versus the WT ROs. The most striking results correspond to the AC line which displays less cone and rod photoreceptors, but interestingly expresses higher levels of BCs alongside T2 and T3 transient clusters, suggesting defects in cell fate determination in this RO sample. The high presence of late RPCs and proliferating cells in AC supports this. Müller glia generation appears to also be favoured in AC ROs with a decrease of T1 transient cells and increase in Müller Glia. PT2 defects are minimal in comparison with a slight decrease in the percentage of rods and a slight increase in cones. T1 population is high in PT2, in addition to higher numbers of late RPCs when compared with WT also suggesting defects in terminal differentiation to retinal neurons.

4.3.12 Cell cycle progression is affected in photoreceptors from STGD1-ROs

We further investigated defects with the photoreceptor cells of STGD1-ROs using the scRNA-Seq data to determine which stages of the cell cycle they rest in. **Figure 4.15 A** displays the data in a stacked histogram alongside two negative controls. Notably, the proportion of photoreceptors in S and G2M phases of the cell cycle differs significantly from those in G1 phase in STGD1 ROs. Typically, terminally differentiated photoreceptors exist in the G1 phase.

To assess statistical significance of these differences, WT2+WT3 were pooled together and a Fisher exact test, to measure the differences in abundances between the different phases of the cell cycle – S phase, G2M phase and G1 phase, was performed **(Figure 4.15 B).** Rod and cone photoreceptor comparisons are displayed separately and each group is segregated based on the phase of cell cycle investigated - illustrated by matching background colours of the graphs with the stacked data in **part A** of the figure.

The most severe STGD1 case – AC, displayed a higher proportion of cone and rod photoreceptors in G2/M phase of the cell cycle. The G2/M phase is known as a cell cycle checkpoint, preventing cells with damaged DNA progressing to the next phase where mitosis is complete and G1 is initiated once again. In G2/M, the cells arrest and try to repair any damages incurred to the DNA of the cell. If this cannot be repaired, the cell undergoes apoptosis. In support of this, we observe significantly less cones and rods in G1 in the AC sample, which suggests that fewer cells are able to complete the cell cycle and succeed in their terminal differentiation to photoreceptor cells.

Similar trends are observed in the PT2 sample, where there are significantly more cone and rod photoreceptors in the S and G2/M phases of the cell cycle when compared with unaffected control ROs. The S phase is where the cell replicates its chromosomal content in preparation for mitosis. The higher occurrence of cells in S phases indicates that the photoreceptors in PT2 are less mature, suggesting challenges in their final differentiation into fully developed photoreceptors. Nevertheless, the disparities between PT2 and control ROs are not as substantial as those in the AC ROs (p-value * vs *** respectively), emphasizing a 'patient-specific' effect consistent with the genotype-phenotype correlation of ABCA4-mediated retinal disease.

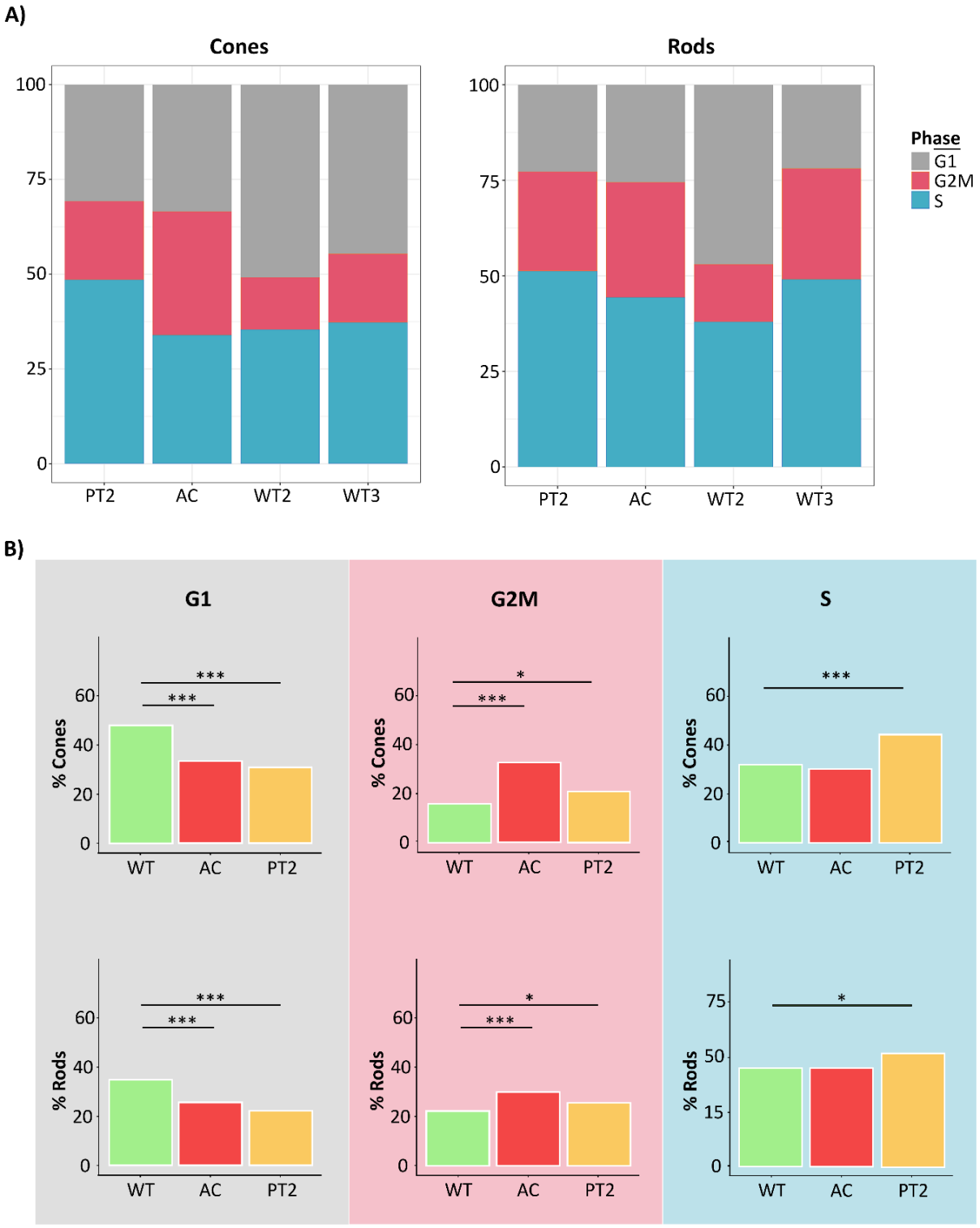

Figure 4.15 Photoreceptor cells in AC and PT2 organoids differ in the stage of cell cycle they reside when compared with WT photoreceptor cells

A) Stacked histograms display the 3 phases of the cell cycle (G1, G2M and S phase) in both cone and rod photoreceptors of PT2, AC and WT2&3 RO. Cone and rod photoreceptors in both PT2 and AC ROs show reduced numbers of cells in G1 phase of cell cycle, and instead show increased cell numbers in the intermediatory phases S and G2M checkpoints. **B)** With WT2+3 pooled together; Fisher exact test could be performed to measure the variance in abundance of cells in different phases of the cycle. This revealed a significant alteration

4.3.13 Patient ROs express proliferative markers on both protein and transcript level

With the presumption of photoreceptor immaturity, we hypothesised that mislocalised photoreceptors could still possess proliferative capabilities. To assess this, we performed immunocytochemistry with Ki67, a known marker of PCs. We co-stained all sample lines (with the exception of WT2 in IGF1-dependent protocol) with Recoverin, a marker of photoreceptor cells to see if co-localisation of markers was present **(Figure 4.16 A).** This would provide substantial evidence for our hypothesis of defects in cell cycle as the culprit in mislocalised photoreceptor cells.

Evidence of Ki67$^+$ cells were present in each of the cell lines, however, none colocalised with the Recoverin$^+$ cells in the centre of the ROs. It was visually apparent that a higher number of Ki67$^+$ cells were present in the patient ROs when compared with unaffected controls. This was statistically significant in patient-specific ROs when quantified (**Figure 4.16 A**), although percentage changes overall were low. The trend observed with increased Ki67$^+$ cells correlated with the severity of genotype possessed by the sample. Unspecific background staining was apparent in WT2 lines in the BMP4-activated protocol. The non-specificity of this staining was confirmed using secondary-only staining controls.

If the Ki67$^+$ cells were not the mislocalised photoreceptors, we were curious to investigate what cell types they were. From the scRNA-Seq data, we were able to visualise the clusters expressing markers of proliferation **(Figure 4.16 B)**. There was no evident enrichment of proliferation markers in the cone and rod photoreceptor clusters (clusters 4 and 13) as expected.

Interestingly, the most enriched cell cluster expressing proliferative markers was the fibroblast/stromal cell lineage. Müller glia (cluster 9) also show significant upregulation of proliferative markers which supports this hypothesis as these cells are known for their adaptive response to stress and injury. Cluster 11 corresponds to the proliferative cell cluster in the RO. In the gene list, the most significant DEGs within this cluster include *NEAT1, CXCL14* and *DKK1* which have all been implicated in stress response. *NEAT1* has been shown to be upregulated in response to oxidative stress (Luan *et al.*, 2021; Shao *et al.*, 2020). *CXCL14* is also enriched in AMD RPE cells as observed via scRNA-Seq (Collin *et al.*, 2023) and has been seen to correlate with the increased proliferation of Müller glial cell markers following photoreceptor injury (Krylov *et al.*, 2023). *DKK1* is an important mediator of Wnt signalling,

which promotes the proliferation of Müller glia-derived retinal progenitors after retinal injury (Osakada *et al.*, 2007).

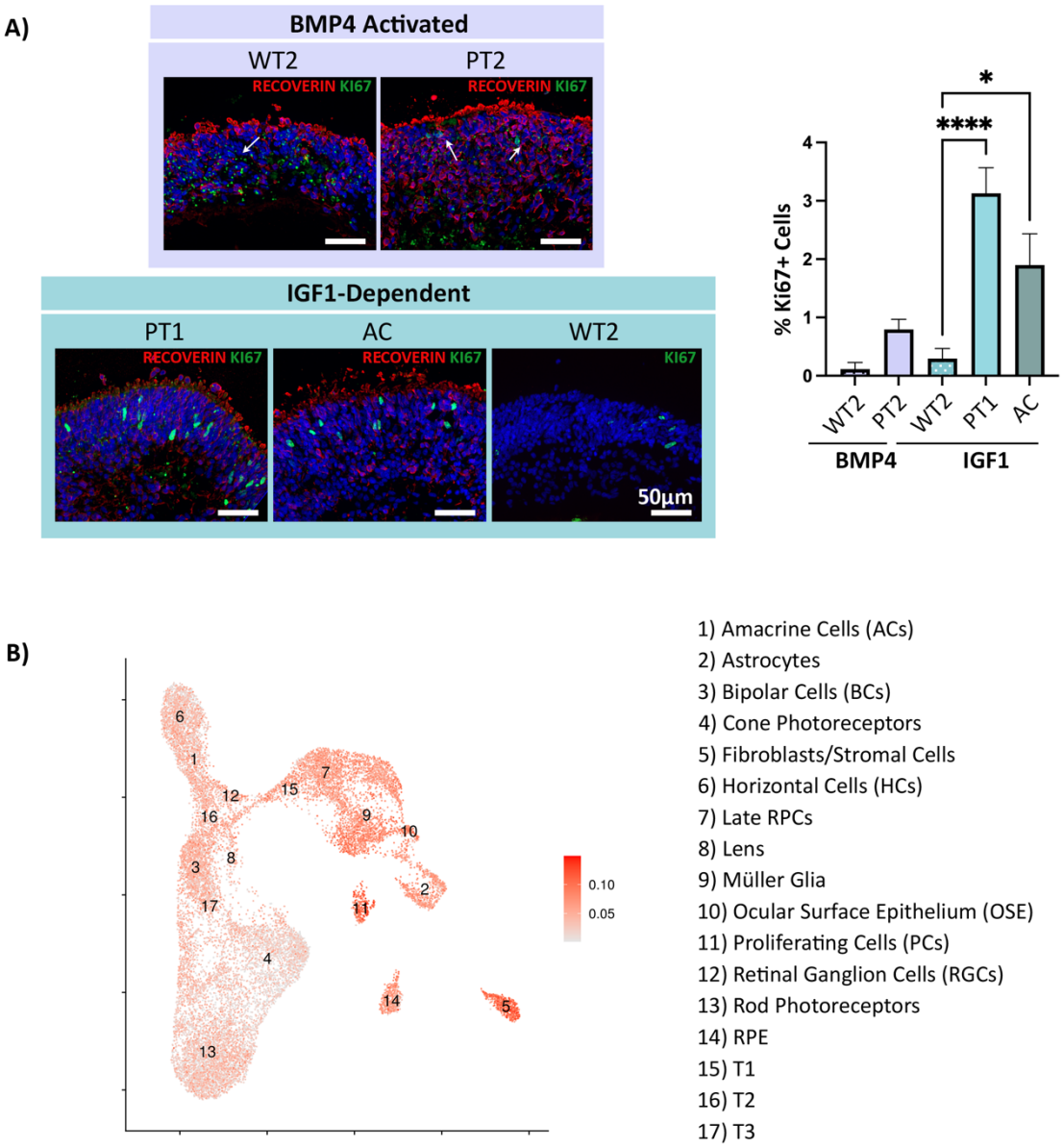

Figure 4.16 Evidence of proliferative gene expression but not enriched in photoreceptor cell populations.

A) Immunofluorescence of proliferative marker Ki67 shows evidence of proliferating cells across all organoid lines. However, when stained with photoreceptor marker Recoverin, there are no clear signs of colocalisation disproving theory of photoreceptor cells possessing proliferative capacity. The number of Ki67^{+} cells appear to correlate with the severity in genotype of STGD1-ROs. Background staining in green channel is apparent in WT2 (BMP4-activated protocol). This has been confirmed using secondary only staining controls. Quantified Ki67^{+} cells confirms this trend. shows White arrows indicate occluded Ki67^{+} cells. Scale bars are 50µm. **B)** On transcription level, scRNA-Seq UMAP shows the clusters enriched with proliferation markers are the fibroblasts/stomal cells (C5), proliferating cells (C11) clusters and Müller glia cells (C9). * = p-val 0.05, **** = p-val 0.0001.

4.3.14 Apoptosis-related gene expression in patient and control ROs

Another hypothesis for the patient-specific mislocalisation of photoreceptor cells is the eliciting of programmed cell death. To investigate this, the scRNA-Seq data were interrogated for the expression of apoptosis-related genes in the cone and rod photoreceptors. A list of genes included in this analysis is illustrated in **Figure 4.17 A**.

The data resulting from this analysis were graphed in **Figure 4.17 B** as a percentage of apoptotic cones and apoptotic rods in overall cones and rods present in the RO sample. Fisher's exact test was utilised once again to measure the abundance of apoptotic transcripts expressed in each photoreceptor subtype in each of the RO samples.

Although significance was achieved with slightly elevated apoptotic transcript abundance in PT2 cones when compared with WT2, the overall percentage difference was minimal and likely not an important result. For rod photoreceptors, there appeared to be significantly more apoptosis-related gene expression in the WT samples than in both AC and PT2 ROs. Whilst these results suggest that apoptosis-related gene expression is not causative of photoreceptor mislocalisation, it does not provide definitive answers as gene expression levels are not correlated with protein expression levels.

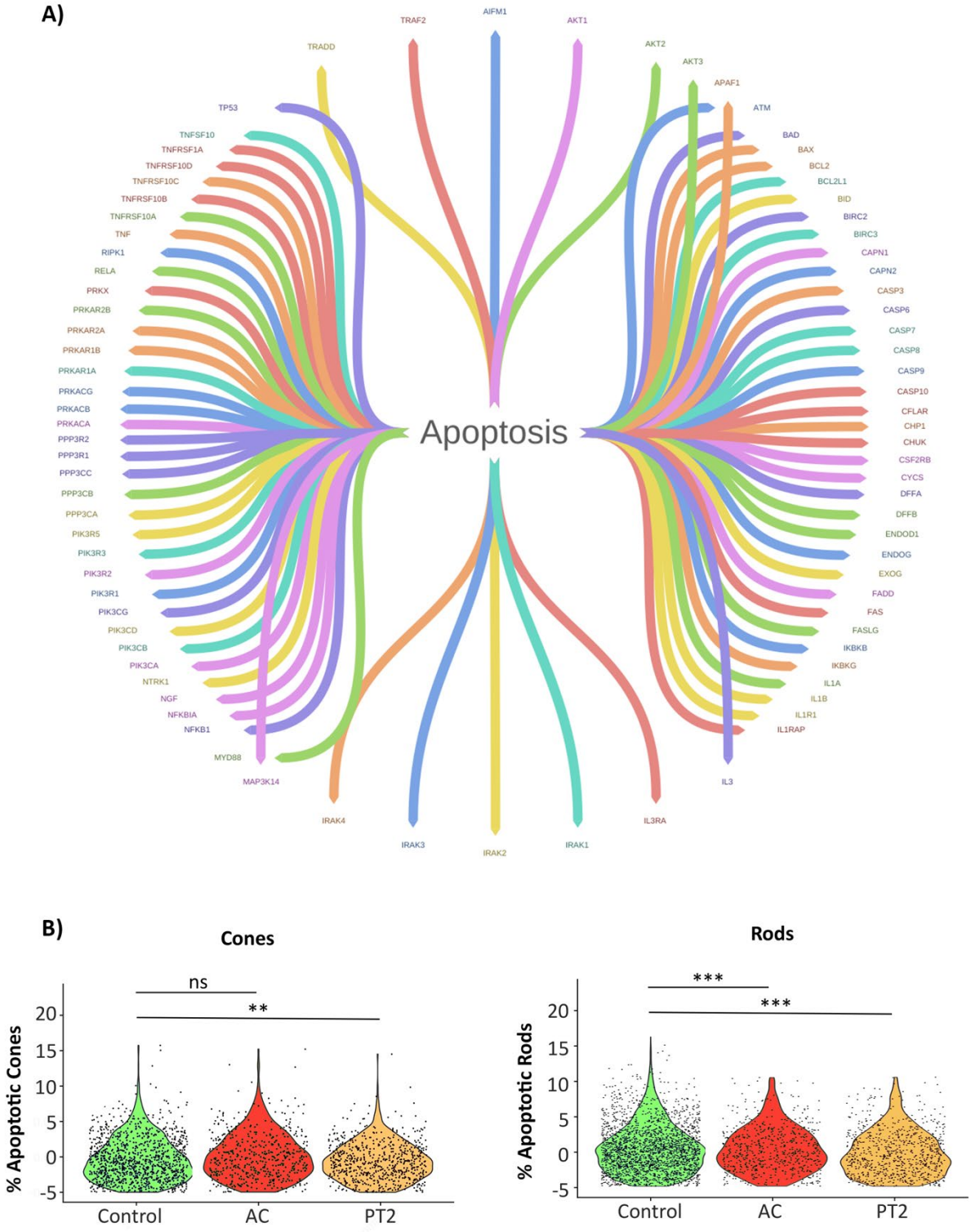

Figure 4.17 Expression of Apoptosis-related transcripts displays no obvious differences between STGD1 and WT ROs

A) Graph depicting all genes utilised in the transcriptomic analysis of apoptosis-related genes in rod and cone photoreceptors of STGD1 and WT ROs. Displayed in alphabetical order clockwise. B) In cones, there appears to be slightly elevated expression of apoptosis-related genes in PT2 ROs when compared with WT but the % change is minimal as likely not an important observation. No changes observed in AC vs. WT. In rods, there appears to significantly less expression of apoptosis related genes in both PT2 and AC ROs, but again the % differences is so minimal that it's likely irrelevant.

Due to the requirement of post-transcriptional modification to activate many apoptosis-related genes, we chose to investigate a ***single*** protein CASP3 which is commonly associated with apoptosis in the retina. We looked at *Casp3* on transcript level using the scRNA-Seq data and also on protein level using immunocytochemistry.

In **Figure 4.18 A**, we observed increased *Casp3* transcript expression in PT2 cone photoreceptor cells, while no significant expression was detected in rod photoreceptors. Conversely, in the AC ROs, *Casp3* transcript expression was higher in rod photoreceptors compared to cone photoreceptors.

On protein level in **Figure 4.18 B**, we observe a number of CASP3-expressing cells via immunocytochemistry staining predominantly in patient ROs. The severity of the genotype-phenotype correlation was evident, with the most severe line AC showing the highest number of cleaved $CASP3^+$ cells and PT2 exhibiting the lowest compared to WT2 samples. Quantification of $CASP3^+$ cells showed slight significance in comparisons using one-way ANOVA, between WT2 and AC (0.04% vs 0.27% ± 0.05%) in the IGF1-dependent protocol. However, the overall percentages of $CASP3^+$ cells in the whole of these ROs across all lines was very small, and likely negligible.

In addition to this, we attempted to quantify pro-CASP3 and cleaved-CASP3 using Western blotting; nevertheless, we were unable to detect CASP3 protein successfully on these blots (data not displayed). This observation aligns with our findings from immunocytochemistry, where only a small number of cells were detected.

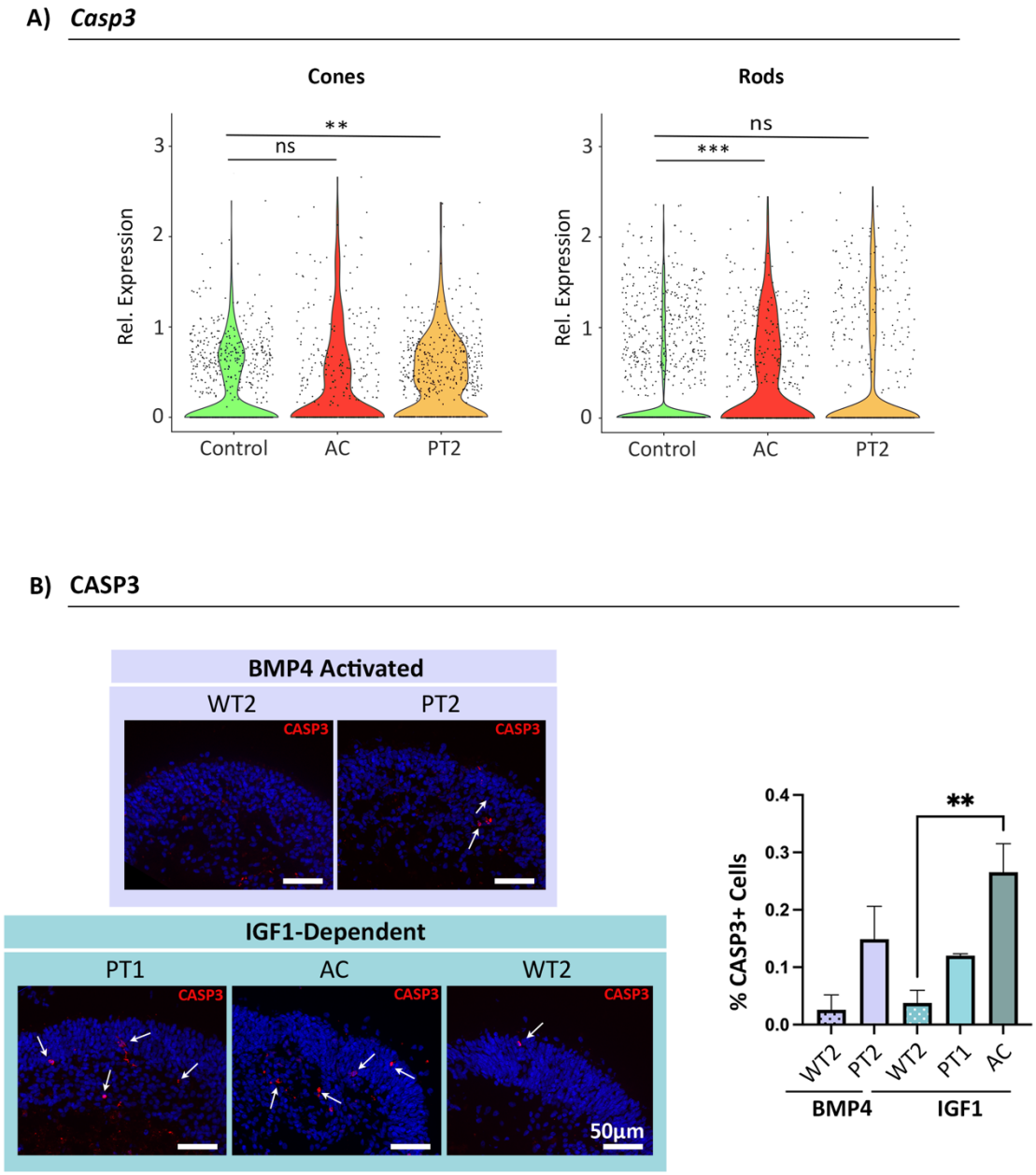

Figure 4.18 Activated Caspase-3 is present in a dose-specific effect in WT and STGD1 ROs

A) Comparisons of *Casp3* expression on transcript level in cone and rod photoreceptors of STGD1 and WT ROs. In cones, there is a significant elevation of *Casp3* expression whereas no changes are observed in the AC line. In rods, the opposite is true. There is significant upregulation of *Casp3* expression in AC whilst no significance is observed in PT2. **B)** On protein level, evidence of activated CASP3 expression is seen in most iPSC-ROs via immunofluorescence. When quantified, AC displays the highest quantity of CASP3 cells which is statistically significant, followed by PT1 and PT2 (but with no significance) when compared with the WT2 ROs derived in their respective protocols. ** = p-val 0.01.

4.3.15 Differential gene expression analysis on affected pathways reveals mass cellular dysfunction in patient ROs

Using the Ingenuity Pathway Analysis (IPA) software, we were able to group differential expression (DE) of genes in the patient versus control line photoreceptors into gene network pathways to underpin the most dysregulated pathways in the degenerating organoids.

A number of pathways were transcriptomically altered as shown in **Figure 4.19.** Significant DE was observed in 20% of the genes within the EIF2 signalling pathway across rods in both the AC and PT2 RO lines. In PT2 ROs specifically, both cone and rod photoreceptors displayed substantial expression change in 30% of genes in the oxidative phosphorylation pathway. This was further compounded by a DE of 10-20% of genes in the mitochondrial dysfunction pathway. Granzyme A signalling was also significantly altered across all patient lines for both cone and rod photoreceptors. These pathways intersect in their roles in cellular stress responses, energy metabolism, activation of cell death and cell fate determination, suggesting that the photoreceptor cells of STGD1 patient ROs are under substantial biological stress. In support of this, we observe over 30% of genes in the phototransduction pathway dysregulated between both cone and rod photoreceptors in patient and control ROs suggesting a potential functional impact on photoreceptor cells of STGD1 ROs.

The significant DE observed in these pathways suggests that STGD1 pathology is complex and multifaceted. The evident dysregulation in cellular stress responses, energy production, apoptotic pathways and visual transduction likely contribute towards an explanation for the photoreceptor dysfunction and degeneration in STGD1 patient ROs.

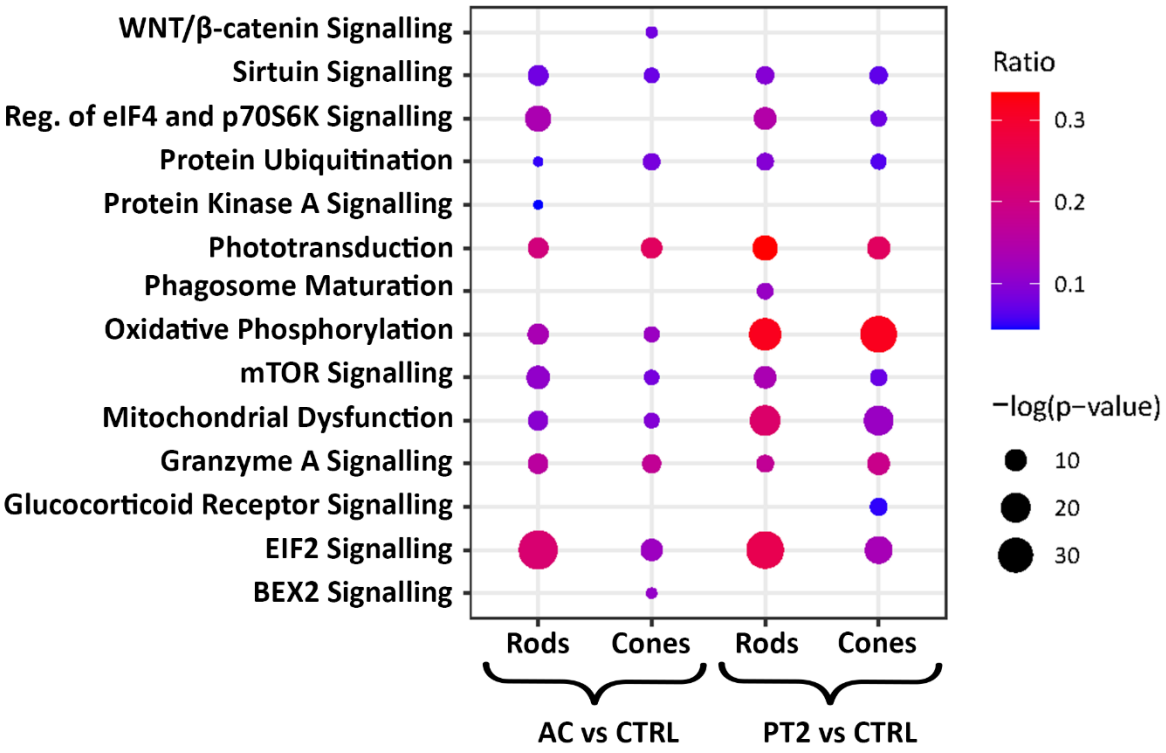

Figure 4.19 Dot plot of affected pathways in STGD1 RO Cone and Rod Photoreceptors

DE analysis revealed several affected disease pathways in STGD1 ROs. This dot plot represents the most significantly altered pathways ranging from 10-30% (blue to red gradient) of overall genes differentially expressed between patient and control cone and rod photoreceptors. The significance of affection is depicted as the overall size of the dot ranging from a -log p-value range of 10-30. Common pathways affected include EIF2 signalling, oxidative phosphorylation, mitochondrial dysfunction and granzyme A signalling which are all involved in stress response. Phototransduction was also significantly altered across all photoreceptors.

4.4 Discussion

In our study, we were able to demonstrate effective differentiation of patient and control iPSCs to ROs utilising two differentiation protocols routinely used in our lab – BMP4-activated method and the IGF1-dependent method (Hallam *et al.*, 2018; Zerti *et al.*, 2020). In preliminary studies, we tested the efficiency of AC and WT2 control iPSC lines to differentiate to ROs with the BMP4-activated method (Hallam *et al.*, 2018). This method is more frequently used in our lab due to its capability for high-throughput RO generation and ease of maintenance for over 200 days in culture - owing to its 96 well plate culturing format. WT3 is routinely differentiated with this method in our lab, and the results obtained were in line with our expectations from previous studies (Buskin *et al.*, 2018) – ROs with a dark inner core and bright phase neuroepithelium which became more defined throughout the period of 30-90 days of differentiation. In contrast to this, the AC line did not respond favourably to the BMP4-activated method of differentiation yielding poorly formed 3D spheroids by Day 30, which did not survive in culture until Day 60. The differentiation of AC iPSCs to ROs in the BMP4-activated method was attempted 3 times, but to of no avail.

The AC iPSC line is an essential control within our study, with its confirmed biallelic *ABCA4* genotype status and severe clinical phenotypic presentation. It would provide valuable insights in verifying genotype-phenotype correlation capabilities of the ROs in a STGD1 disease context and so we attempted to differentiate it using another method.

The IGF1-dependent method has been developed and refined in the Lako lab over the years (Mellough *et al.*, 2015; Collin *et al.*, 2019; Zerti *et al.*, 2020). The efficiency of WT3 and AC iPSCs lines were subsequently tested using this method – revealing interesting results. The AC iPSC differentiation was substantially improved with the generation of a bright phase neuroepithelium on the apical edge of the organoid as expected with ROs derived from this method. Survival of the resulting ROs past 90 days of differentiation was observed with approximately 60% efficiency. In contrast to this, the WT3 iPSC line did not develop ROs with neuroepithelium on the apical edge with this method. The resulting organoids remained dark throughout the structure while continually enlarging over the course of 90 days, rendering them unusable for the study.

Consequently, when screening the newly generated reprogrammed iPSC clones of PT1 and PT2 for their differentiation capability, we utilised both differentiation protocols in

anticipation for variance in the ability of these iPSCs to differentiate with a distinct protocol. Indeed, we observed clonal differences in their ability to generate EBs, but this also translated to later work when differentiating selected clones to ROs in this chapter. Whilst PT1 differentiated to atypically shaped organoids in the BMP4-activated method, there was evidence of neuroepithelium thinning and poor viability post-90 days. This was in contrast to the well-developed PT1 ROs derived from the IGF1-method of differentiation with a yield efficiency of 50% post 90 days. Whereas PT2 iPSCs developed ROs only in the BMP4-activated method of differentiation. A total of 3 differentiation attempts were carried out on each iPSC line with each protocol to ensure our observations were correct.

This phenomenon of iPSC variability with response to differentiation protocols has been observed a number of times in the literature (Hu *et al.*, 2010; Cooke *et al.*, 2023). The reasoning behind this is often distilled into three main areas of concern; genetic background (Kajiwara *et al.*, 2012; Kyttälä *et al.*, 2016; Kilpinen *et al.*, 2017), retention of donor somatic cell methylation signatures (Kim *et al.*, 2010; Bar-Nur *et al.*, 2011; Roost *et al.*, 2017; Wang *et al.*, 2018) and genetic stability (Nguyen *et al.*, 2013; Merkle *et al.*, 2017; D'Antonio *et al.*, 2018; Jo *et al.*, 2020). Even non-genetic factors such as cell passage number have been shown to influence overall differentiation variability of iPSCs (Cantor *et al.*, 2022).

In our own lab, we have observed variability in the differentiation of iPSCs to corneal tissue (Kamarudin *et al.*, 2018) and retinal tissue (Chichagova *et al.*, 2020). In the latter study, a comparative analysis of our in-house controls (WT1, WT2 and WT3) in their ability to differentiate to ROs using both the BMP4-activated and IGF1-dependent method was performed. Indeed, iPSC-line differences were observed in the propensity to differentiate to ROs under the same protocols used in this study, corroborating our results with WT3 iPSC line. The variances in differentiation ability were attributed to iPSC-line specific responses to BMP4 and IGF1 signalling factors which can display variable expression of receptors and ligands for each pathway, thereby making different iPSC lines more adaptable to specific protocols (Cooke *et al.*, 2023).

BMP4 is a member of the TGF-β superfamily and plays a crucial role in early retinogenesis with the specification and differentiation of RPCs during early neuroepithelial lineage commitment. BMP4 works synergistically with other developmental pathways such as Wnt, FGF and Hedgehog to regulate cell fate decisions during development and coordinate the dorsal/ventral patterning of the retina (Yang, 2004).

In the context of RO development, when added to the culture medium at Day 6, BMP4 triggers the development of optic vesicles, which are a developmental precursor structure to the optic cup. This increases the self-formation of neural retinal tissue, biasing the iPSCs to undertake development towards retinal lineage, likely by preventing early neuroepithelium from adopting telencephalic fate and instead directing it to retinal fate (Kuwahara *et al.*, 2015; Capowski *et al.*, 2019). Studies have shown that differences in the activity of key signalling pathways such as BMP and TGFβ signalling in early differentiation can greatly impact the response to differentiation protocols, especially since BMP4 activation is a time-sensitive approach to drive retinogenesis (Zhu *et al.*, 2016; Kamarudin *et al.*, 2018).

IGF1 has been demonstrated as a critical component of retinogenesis by specifically promoting RPC identity *in vitro*, supporting the differentiation of iPSCs into photoreceptors, bipolar cells, retinal ganglion cells and other retinal neurons (Lamba *et al.*, 2006). It has been implicated in early specification of eye fate in Xenopus embryos (Pera *et al.*, 2001). Our group have previously corroborated these results with the development of 3D optic cups in an IGF1-dependent manner (Mellough *et al.*, 2015). This study demonstrated rapid photoreceptor maturation, increased long-term culture viability and synapse formation of retinal neurons. Interestingly, ROs derived from the IGF1-dependent method can display cells with expression signatures of extraretinal tissues such as cornea and lens as evidenced in our own scRNA-Seq data and in early publications (Mellough *et al.*, 2012; Mellough *et al.*, 2015; Collin *et al.*, 2019).

Given this information and our preliminary findings from differentiation studies of control and patient iPSCs, it was apparent that we would need to use both the BMP4-activated and IGF1-dependent methods to derive ROs for the study. However, we were aware that this elicits a confounding factor of protocol variability in our study. To mitigate the impact of this, we chose an unaffected control – WT2, known to produce ROs when differentiated with either method as evidenced by our lab's earlier study (Chichagova *et al.*, 2020). By doing this, we are able to compare phenotypes arising in patient-specific ROs to the WT2 control in the respective protocol.

Further to this, as ABCA4 is a protein expressed in POS, most characterisation of resulting disease phenotypes were carried out at later timepoints (from Day 180 onwards) where the POS became most prominent. Despite differences in the initial stages of protocols for RO development, organoids typically follow the same transcriptional programmes leading to retinogenesis throughout the duration of the differentiation period which ultimately allows

them to become remarkedly similar by the endpoint of 200^{+} days. This has been demonstrated by an important study attempting to stage organoids at different timepoints across multiple different protocols (Capowski *et al.*, 2019). The assessment of RNA defects in monoallelic STGD1 cases also remains unaffected by the differentiation approach used to generate ROs as shown in Chapter 5.

A full table displaying the clones tested with both RO protocols is shown in **Figure 4.4** highlighting the vast variability of iPSC clones to differentiate to ROs. To summarise, we successfully differentiated WT2 and PT2 iPSCs to ROs using the BMP4-activated method, whilst PT1, AC and WT2 were differentiated with the IGF1-dependent method.

The ROs were kept in culture for 220 days. Brightfield imaging and immunostaining was conducted on Day 60, 120, 180 and 220 to ensure that the ROs were developing correctly throughout the course of differentiation. Immunostaining at Day 60 revealed positive expression of neurons undergoing early retinogenesis; CRX^{+} and VSX2^{+} cells mark photoreceptor precursor and retinal progenitor cells respectively, confirming that all iPSC-ROs had become fated to neural retina. Markers of RGCs (SNCG^{+}) and immature photoreceptors (RECOVERIN^{+}) cells were also observed at this timepoint. The presence of these cells lingered into the halfway point of differentiation at Day 120 but were also accompanied by retinal interneurons - ACs (AP2α^{+}) and HCs (PROX1^{+}). Müller glia (CRALBP^{+}) were also apparent and spread throughout the newly formed retinal tissue. Retinal lamination became apparent with photoreceptors aligning along the apical edge and RGCs at the innermost layer of the organoid in each cell line. This panel of markers was adopted for later timepoints – Day 180 and Day 220, showing increased lamination in control ROs. Photoreceptors were subcategorised into red/green cones (OPN1MW/LW^{+}) and rod photoreceptors (RHO^{+}) with evidence of POS on both brightfield and fluorescent images. These results corroborated findings on RO development from our groups' previous research with these protocols (Buskin *et al.*, 2018; Hallam *et al.*, 2018; Felemban *et al.*, 2018; Collin *et al.*, 2019; Zerti *et al.*, 2020).

Blue cones (OPN1SW^{+}) were not observed by immunostaining at any timepoint in ROs from the IGF1-dependent method. Blue cones appeared rarely in ROs from the BMP4-activated method (data not shown). Whilst the latter observation has been noted in (Hallam *et al.*, 2018), the lack of OPN1SW^{+} cones in the IGF1-dependent method is linked to the growth factors added to the culture medium.

In our organoids, the inclusion of T3 was initiated on Day 30 and continued until the end timepoint of 220 days. T3 has been associated with late-stage differentiation of cone photoreceptors into S- or M-opsin (blue or green) containing photoreceptors in murine retina (Roberts *et al.*, 2006). In the context of ROs, T3's role extends to influencing S- or M/L-opsin cone differentiation. Its impact depends on the concentration and duration of exposure, with studies indicating its positive effect on stabilising long-term RO cultures (Eldred *et al.*, 2018; Zerti *et al.*, 2020).

The sustained T3 exposure for 190 days in our IGF1-dependent protocol favours the M/L-opsin fate of cone photoreceptors over the S-opsin fate as observed in Zerti *et al.* (2020). We saw a similar result in the ROs differentiated in this study where IGF1-dependent ROs exhibited M/L-opsin cone enrichment, but we could not detect S-cones by immunocytochemistry. However, given the macular enrichment of M/L-opsin cones in native retina and the study's focus on STGD1, a macular disorder, administering T3 to the ROs to increase the presence of these cone subtypes align with a more physiologically relevant approach for modelling the disease.

The main disease-associated phenotypes observed in the patient ROs at later points of differentiation (between Day 180 – Day 220) relate the mislocalisation of photoreceptor cells and disruption to lamination. Interestingly, the severity of these phenotypes in the ROs coincided with the severity of *ABCA4* genotype possessed by the respective patient sample. The mislocalisation of Recoverin^{+} cells were first noted at Day 180 but had not resolved by Day 220 as shown in immunofluorescence **(Figure 4.6 and Figure 4.7).** As recoverin staining marks both rod and cone photoreceptors and ABCA4 is expressed by both, we were interested to see specifically whether cones or rods were more affected by this mislocalisation.

The AC ROs, which displayed the most severe levels of photoreceptor mislocalisation, showed that both rod (RHO^{+}) and red/green cones (OPN1MW/LW^{+}) cells were affected **(Figure 4.11).** Evidence of lamination disruption was also apparent with the HCs (PROX1^{+}) and ACs (AP2α^{+}). PT1 also displayed both cone and rod photoreceptor mislocalisation, and PT2 just cone photoreceptor affection, both with no obvious disruptions to retinal lamination. The decrease of severity in RO phenotype is supported by the age of onset of disease symptoms in these patients; AC with classic early onset STGD1, PT1 with later onset at 30 years and PT2 with the latest onset of symptoms at 44 years of age.

AC corresponds to the case (P1) reported in (Albert *et al.*, 2018) with the following biallelic variants; c.4539+2001G>A and c.4892T>C, corresponding to protein changes

p.Arg1514Leufs∗36 and p.Leu1631Pro, respectively. The study showed that the c.4539+2001G>A variant results in the incorporation of a pseudoexon (PE) due to aberrant splicing caused by enhancement of a splicing enhancer at the SF2 site, generating a new SRp55 motif. Consequently, the PE causes frameshifting at the *ABCA4* locus resulting in premature termination and complete LOF at that allele. It is now reported as a severe *ABCA4* variant. In combination with the missense allele c.4892T>C, this case fits the genotype-phenotype correlation for severe *ABCA4*-related disease (van Driel *et al.*, 1998a; Maugeri *et al.*, 1999b; Lee *et al.*, 2022b). This correlation matrix states that the disease severity is dependent on the residual functional protein remaining.

The appearance of disease-associated phenotypes occurring in a 'dose-specific' manner in the ROs was intriguing. In contrast to the severity of AC's condition, PT2's disease presented with symptoms on the milder end of the spectrum of ABCA4-mediated retinal disease with a later-onset of symptoms owing to preservation of central vision via foveal sparing. This later presentation of symptoms suggests that the uncovered variant in the PT2 case must be relatively mild to fit with the genotype-phenotype correlation matrix – and indeed, it was, as discussed in **Chapter 5.** This milder case of STGD1 presented a cone-specific phenotype when differentiated to RO, with no evidence of lamination disruption or rod photoreceptor cell involvement, suggesting a particular susceptibility of cone photoreceptors to defective ABCA4 protein. Despite both PT1 and PT2 harbouring the same complexed allele c.[5461-10T>C; 5603A>T], and both displaying a later onset of disease, the mislocalisation of photoreceptors was more severe in PT1 ROs involving both cone and rod photoreceptors, in a similar manner to AC ROs. As the other allele at the time of differentiation was unknown in both cases, we hypothesised that the influence of the unknown allele could be much greater in PT1 than in PT2. This is further explored in the next chapter.

At the time of writing, there are no published studies characterising ROs developed from STDG1 patients. From attending ISSCR 2022 and ISER 2023 we have become aware that, Dr. Anai Gonzalez-Cordero at the Children's Medical Research Institute in Australia is working on modelling STGD1 with ROs also. Whilst we have not seen published data, we have viewed immunocytochemical data at ISSCR 2022 on STGD1 ROs derived by this group and have observed a similar photoreceptor mislocalisation phenotype in both classical and late-onset STDG1. Interestingly, a paper published in 2020 reported the mislocalisation of rod photoreceptors in the modelling of late-onset retinitis pigmentosa (RP) due to mutations in

PDE6B with ROs, using a similar method of differentiation (Gao *et al.*, 2020). This study attributed the mislocalisation of rods to the accumulation of cyclic guanosine monophosphate (cGMP), a downstream target of PDE6B protein. We questioned whether misfolded ABCA4 protein, or a subsequent metabolite, in STGD1 ROs could accumulate in developing PRs and inhibit their translocation to the apical surface, resulting in the retention of these cells in the central region of the organoid.

Whilst ABCA4 protein is expressed in both cone and rod photoreceptors (Allikmets *et al.*, 1997a; Allikmets *et al.*, 1997b), the resulting phenotypes arising from STGD1 are restricted to the macular region, where the density of cone photoreceptor density peaks.

It is known that the recycling of visual pigments post-phototransduction relies on the interplay between the POS and the microvilli of RPE cells, which host a series of enzymes that catalyse the dissociation and regeneration of light-sensitive *11-cis*-retinal from *all-trans*-retinal (Rando, 2001). In the fovea, the cone:RPE density is 23:1, the highest ratio of photoreceptor cell to single RPE cell found in the retina (Snodderly *et al.*, 2002). Consequentially, the burden on RPE cells in this region to address waste and metabolic demands of cone photoreceptors is significantly higher than elsewhere in the retina.

The classic pathophysiological mechanism of STGD1 is distilled to the inability of defective ABCA4 protein in the outer segment to efficiently remove *all-trans*-retinal trapped within the disc segment to the cytoplasmic leaflet for degradation by cytosolic enzymes. The accumulation of these retinal molecules results in the generation of toxic bisretinoids which are metabolised to A2E when diurnally shed by photoreceptors and phagocytosed by RPE cells (Radu *et al.*, 2011; Tanna *et al.*, 2017). A2E is a frequent component of lipofuscin – an accumulation of residual lipids and proteins, leading to oxidative stress, inflammation, and impaired cellular processes that result in the degeneration and cell death of RPE cells, and consequently overlying photoreceptor cells in STGD1 (Sparrow *et al.*, 2003; Burke *et al.*, 2014).

Whilst this suggests a plausible explanation for why STGD1 phenotypes often do not extend to the peripheral retina, it was interesting to see a cone-specific effect in our organoid model of STGD1 as our model is devoid of a foveal/macular region and does not develop physiologically functioning RPE. This suggests a particular sensitivity of cone photoreceptors to genetic and environmental alterations exists.

Indeed, in a cone dominant $RHO^{-/-}ABCA4^{-/-}$ mouse model of STGD1, the biochemical differences between cone and rod photoreceptors to ABCA4 deficiency were assessed (Conley *et al.*, 2012). Some of the key results from this study showed that ABCA4-deficient cone photoreceptors generate substantially more A2E per mole of retinoid but in comparison with ABCA4-deficient rods, displayed fewer lipofuscin deposits in the RPE compared with ABCA4-deficient rods. This suggests that cone photoreceptors have a reduced ability to clear toxic bisretinoid precursors and likely retain them, enhancing their own cellular degeneration and causing potentially pathological phenotypes, even in the absence of RPE.

Cone sensitivity has been demonstrated in human under photopic and scotopic conditions (favouring cone and rod photoreceptors respectively) in central retina using chromatic pupil campimetry (CPC) as a measure of functional degeneration of photoreceptors. This showed no changes to rod function in the central retina in STGD1 patients, whereas cone function was significantly altered (Stingl *et al.*, 2022).

Few studies have demonstrated the potential of cone photoreceptor death preceding RPE death, challenging the overall classical view of molecular STGD1 pathophysiology. One such study observed preservation of RPE cells but loss of cone photoreceptors in foveal regions of STGD1 patients using adaptive optics scanning laser ophthalmoscopy (AOSLO) (Chen *et al.*, 2011). The authors note that their system is not capable of assessing the health of RPE in that region, but it is interesting to see cone loss precede RPE loss in STGD1 patients in the clinic using this methodology. Especially since our RO models from STGD1 show such stark cone photoreceptor mislocalisation, even in cases of milder genotypes.

The mislocalisation phenotype observed in the patient organoids was not consistent across all photoreceptor cells in the affected ROs, as evidenced by the immunostaining. It was clear that whilst a large proportion of photoreceptors were retained in the centre of the organoid, a proportion of photoreceptors did develop correctly and aligned on the apical edge of the RO with the appearance of outer segment brush border around the periphery. The topological positioning of the photoreceptors in the ROs is important for the development of POS and indeed for the purpose of this study involving ABCA4 protein as it is exclusively expressed in the POS of neural retina.

We validated the expression of ABCA4 in the tips of POS in native retina using immunohistochemistry. We also confirmed that the photoreceptors of iPSC-ROs express

ABCA4 in the same locality. However, as the staining pattern was not as discrete in ROs as is in native retina (likely due to underdeveloped outer segment discs), we decided to further confirm protein expression with Western blotting. Blotting for ABCA4 revealed its presence in all of the RO samples probed, with protein levels correlating with the expected output from genotypic predictions. Observing such a strong correlation with genotype, demonstrated the utility and suitability of RO modelling for STGD1 research. In support of this, ROs have been shown to express *ABCA4* transcripts with retina-specific isoforms and ABCA4 protein in a recently published manuscript, demonstrating a similar ABCA4 staining pattern and similar dose-specific effects in ROs (Cowan *et al.*, 2020; Kaltak *et al.*, 2023b). However, these studies do not provide a comprehensive characterisation of the STGD1 model throughout development. Any immunostaining displayed focused on the upper limits of the ONL in the organoid making it difficult to corroborate our mislocalisation phenotype.

As mentioned, there is currently very little published on the use of STGD1 for disease modelling. Most published articles discuss the utility of STGD1 ROs in the context of their ability to produce retina-specific *ABCA4* transcript isoforms and the ability to modulate and correct these deficiencies *in vitro* using antisense oligonucleotides (Khan *et al.*, 2020a; Kaltak *et al.*, 2023b). These studies highlight the suitability of ROs for accessing tissue-specific RNA and protein to assess the efficiencies of putative treatments for STGD1 caused by splicing defects in *ABCA4.* However, there is limited information about the development of these organoids over the time course of 220 days. Given that our study is the first to assess development in STGD1 organoids, and also report a visual photoreceptor defect by immunocytochemistry, we were interested to see if we could uncover a potential mechanism for how ABCA4 could influence the mislocalisation of cone and rod photoreceptor cells.

To this end, we employed scRNA-Seq technology to gain insight into the composition and transcriptomic signatures of cells in the STDG1 ROs. scRNA-Seq is a cutting-edge technique that gives the researcher access to the gene expression profiles of individual cells within a heterogeneous population. This provides insights into the diversity and functions of different cell types in complex tissues. We included ROs differentiated from the AC, PT2 and WT2 & WT3 iPSC lines. Due to limited time and resources, we excluded PT1 ROs from this experiment but the inclusion of PT2 and AC ROs cover the spectrum of STDG1 phenotypes ranging from mild to severe.

We first developed an integrated UMAP to visualise the cell clusters within the STGD1-RO cohort. This clustering works by grouping cells with similar gene expression patterns together, which can then be later annotated using knowledge of gene expression signatures of known cell types in that tissue from the literature. For example, cells that express rod-specific markers are often grouped in close proximity and will express key identifying genes of rod photoreceptors such as *Rho* or *Nrl.* Using this strategy, we were able to identify 17 transcriptomically distinct cell clusters in our ROs, including all key neuronal cell types expected in the retina (cone and rod photoreceptors, bipolar cells, RGCs, ACs, HCs, Müller glia and RPE). Extra-retinal tissues were also observed with clusters corresponding to OSE, fibroblasts, astrocytes, and lens. Progenitor cell clusters also existed in our RO samples corresponding to late RPCs and the transient progenitors known to give rise to RGCs (T1), HCs and ACs (T2) and bipolar cells or photoreceptor cells (T3) as previously identified and reported (Sridhar *et al.*, 2020). These results are consistent with the characterisation of ROs in a recent *in vitro* toxicology scRNA-Seq study from our own group (Dorgau *et al.*, 2022) - in addition to older scRNA-Seq studies on ROs from our group and others (Collin *et al.*, 2019; Sridhar *et al.*, 2020; Cowan *et al.*, 2020). *ABCA4* expression was also verified and shown to overlap in expression with the cone and rod photoreceptor clusters as anticipated. Notably, a cluster of proliferating cells (PCs) was also apparent in our integrated scRNA-Seq data, prompting our hypothesis that mislocalised photoreceptors in STGD1-ROs could be a consequence of cell cycling defects.

When investigating this, we noted the percentages of cells within each cluster remained relatively consistent between the milder STDG1 RO line (PT2) and control, with the exception of increased late RPCs and T1 progenitors. This is in contrast to decreased T2 populations and increased HCs cells in PT2. AC ROs displayed fewer cone and rod photoreceptors when compared with WT and PT2 ROs. Markers for all other cell types appear to be upregulated in AC ROs with the exception of T1 progenitor cells. There are two potential reasons for these observations: 1) The reduction in cone and rod photoreceptors could be a consequence of cell death and this reduction could boost the percentages of other cell types that comprise the AC RO sample. 2) The AC ROs display substantial cellular dysregulation and are preferentially upregulating markers of other retinal neurons over photoreceptor cells. Whilst these other retinal neurons are not themselves the primary target of ABCA4 mutations the disruption of photoreceptor cells caused by ABCA4 mutations can have downstream effects on the

signalling pathways involving retinal neurons as observed in other diseased RO models (Guo *et al.*, 2019; Völkner *et al.*, 2022; Diaz-Aguilar *et al.*, 2022).

In other models of retinal degeneration, including organotypic and *in vivo* models, lamination disruption and altered morphologies of cone and rod photoreceptors have been observed and have often been attributed to the activation of stress response and apoptotic cell pathways (Cuenca *et al.*, 2014). In an effort to explain the loss of photoreceptor planar polarity in the STGD1 ROs, we investigated the potential for cell cycle defects and also for evidence of cell death via using our scRNA-Seq data on the STGD1 ROs, and validating results using immunocytochemistry.

Cone and rod photoreceptors in the AC organoids expressed significantly more markers associated with the G2/M phase of the cell cycle compared with controls, whilst expressing significantly less markers associated with the G1 phase, where photoreceptors at Day 200^{+} are expected to arrest. Similarly, PT2 cone and rod photoreceptors expressed less markers associated with G1 phase but significantly more in the G2/M and S phases of cell cycle. Evidence has shown that cellular migration in developing stratified neuroepithelium is highly correlated with phases of the cell cycle, this process is known as interkinetic nuclear migration (IKNM) (Strzyz *et al.*, 2015). It has been understood that cells in S-phase occupy the basal positions of neuroepithelium. In G2/M-phase, the cells begin their ascent to the apical positions of the neuroepithelium (Leung *et al.*, 2011). In accordance with this study, it would suggest that a large proportion of rod and cone photoreceptors in PT2 are arrested in the S-phase of the cell cycle and cannot migrate to the apical surface, explaining their localisation to the basal position of the organoid. A relatively high percentage of rod and cone photoreceptors of AC ROs are in G2/M-phase suggesting they are still in the process of IKNM, although a significantly large proportion are retained at the basal position and impaired IKNM is likely not the only causative factor at play.

To this end, we investigated whether photoreceptors were undergoing apoptosis in the STGD1 ROs. In the transcriptomic data, we pooled a large number of genes involved in the induction and progression of apoptosis and checked DGE in diseased and control RO photoreceptors. The transcriptomic data was perplexing as both AC and PT2 displayed similar or lower percentages of apoptotic photoreceptor cells. However, as transcriptomic data does not always reflect the protein expression of proteins, especially in the context of cell death. We chose *Casp3* to investigate further on both transcriptomic and protein levels. Cones in PT2 and

rods in AC appeared to express more *Casp3* transcripts. In immunocytochemistry, pro- and cleaved- CASP3^{+} cells occurred more frequently in the AC and PT1 lines. When quantified, we observed a similar trend, however the total number of CASP3^{+} cells in the RO were minimal and consequently, this result is likely negligible. When performing Western blotting on all samples for cleaved CASP3, we could not detect any bands despite conducting two repeats. The experiment was conducted in the same manner as described in a recent study published by our group where levels of cleaved CASP3 were picked up in an iPSC-derived RO retinoblastoma model (Rozanska *et al.*, 2022). It is unknown whether experimental failure is due to technical error or if the STGD1 ROs are not expressing detectable levels of active CASP3.

Whilst a repeatable disease-specific phenotype was observed in our STDG1 ROs in a disease and dose-specific context, the underpinning mechanism of photoreceptor mislocalisation was not as clear cut. The molecular cause of this phenotype appears to be multifaceted and likely a result of degenerating tissue caused secondarily by the stress of harbouring mutated ABCA4. This hypothesis is supported by the vast degree of gene dysregulation observed when investigating the DEG networks in photoreceptors of STGD1 ROs versus control ROs. Affected pathways with abundant DEGs included mTOR signalling, mitochondrial dysfunction, oxidative phosphorylation, granzyme A signalling and EIF2 signalling. A number of these affected pathways are involved in stress responses such as unfolded protein response (UPR) (Starr and Gorbatyuk, 2019; McLaughlin *et al.*, 2022). Hyperactivation of mTOR signalling pathway has also been reported to disrupt retinal lamination in ROs (Lee *et al.*, 2022a). Importantly, expression of genes involved in the phototransduction pathway in photoreceptors of STGD1 ROs are substantially different to control, suggesting an impairment of function. ABCA4 is also expressed in RPE cells, but is less abundant than in photoreceptor cells (Lenis *et al.*, 2018). Interestingly, a recent study conducting scRNA-Seq of iPSC-RPE derived from STGD1 patients showed similar abnormal changes in mitochondrial structure and function, in addition to genes involved in UPR (Matynia *et al.*, 2022). This solidifies the idea that mutated ABCA4 is generating a stressful environment in the tissue, subsequently eliciting cellular degeneration in affected sites (i.e., photoreceptors and RPE cells).

In summary, despite initial difficulties with all iPSC lines displaying variable propensities to differentiate to ROs, we were able to generate robust ROs that survived in culture for over 220 days. We demonstrated that ROs develop normally with intrinsic retinal lamination in the 3D structure and the presence of all key neuronal cell types appearing at the correct time

points during development. Importantly, all RO samples generated inner and outer segment structures as evidenced from the appearance of a brush border around the perimeter of the organoid from Day 150 onwards, inferring their capabilities to express ABCA4 protein, which localises to the disc membranes of POS. Indeed, we validated ABCA4 expression in the model via transcriptomics and protein studies, demonstrating genotype-phenotype correlations with AC and PT1 expressing the least amount of ABCA4 protein when quantified against wild-type and PT2 RO samples. This finding alone highlights the utility of the model in studies attempting to rescue ABCA4 levels as shown in recent literature (Khan *et al.*, 2020a; Kaltak *et al.*, 2023b).

Our ROs further demonstrated a patient-specific phenotype of mislocalised photoreceptor cells, correlating with genotype severity. Our results argue against the classical disease pathomechanism of STGD1 which involves secondary photoreceptor degeneration consequentially from RPE death by demonstrating a particular vulnerability of cone photoreceptors in response to ABCA4 mutation. This cone defect was observed in our mildest STGD1 case with late-onset disease (PT2), and only involved rod photoreceptor cells in more severe genotypes (PT1 and AC), correlating with results shown previously in mouse models (Conley *et al.*, 2012).

scRNA-Seq data provided some insight into the composition of organoids in this study and provided potential insights into mechanisms behind photoreceptor mislocalisation. From the data presented thus far, we hypothesize that *ABCA4* mutation affects the development and survival of photoreceptor cells in ROs. In the absence of RPE, ABCA4 accumulates and burdens photoreceptor cells causing a global shift from gene expression patterns in healthy photoreceptors. DGE analysis shows an activated stress response caused by mutated ABCA4 - leading to altered gene expression in pathways related to mitochondrial dysfunction, altered photoreceptor metabolism and UPR, which could all contribute to the retention of photoreceptor cells as seen in previous RO models of retinal disease (Gao *et al.*, 2020). The finding of similar pathways activated in an iPSC-RPE model of STGD1 strengthens our results (Matynia *et al.*, 2022). In further experiments, it would be interesting to differentiate iPSC-RPE alongside iPSC-ROs of STGD1 patients using the same genetic backgrounds to see if results from the two models have a higher correlation.

The work thus far has provided some exciting insights into the pathology of STGD1 and generated further avenues of research to explore which will be discussed in the closing discussion in **Chapter 6**.

Chapter 5 Uncovering the missing inheritance of monoallelic STGD1 patients

5.1 Introduction

The *ABCA4* gene is located at chromosome 1p22.1 and spans a full 128kb. It contains 50 exons and encodes a large protein with a molecular mass of 250kDa (Tanna *et al.*, 2017). Over 1200 mutations have been identified in the gene thus far (as observed in the LOVD online repository - https://databases.lovd.nl/shared/genes/ABCA4), with even more being identified as recent as this year (Rodriguez-Hidalgo *et al.*, 2023). The spectrum of mutations observed in the *ABCA4* gene include structural variants, deep-intronic variants, protein-truncating variants, non-canonical splice site variants, missense variants, and complex variants (Cremers *et al.*, 2020).

With current NGS – including target-capture panels and WGS (Carss *et al.*, 2017; Sangermano *et al.*, 2019; Whelan *et al.*, 2023), smMIPs (Khan *et al.*, 2019; Khan *et al.*, 2020b) and Haloplex sequencing (Bauwens *et al.*, 2019a; Sangermano *et al.*, 2019) specific for the *ABCA4* locus, the genetic solve rate for STDG1 is approximately 80%. This includes cases where biallelic *ABCA4* variants are identified (65-70%), where just one variant is identified (15-20%) and where no *ABCA4* variants are identified - despite displaying strong clinical phenotypes associated with the disease (Zernant *et al.*, 2011). Most recent reports state <5% of cases are genetically unresolved in STGD1 research centres in New York and the Netherlands – but include monoallelic cases in this statistic where a strong clinical presentation of STGD1 is accompanied by one pathogenic allele in *ABCA4* (Cremers *et al.*, 2020).

One of the key questions asked in recent years relates to the apparent missing heritability in these monoallelic cases. The non-coding regions of the *ABCA4* gene were postulated to be a likely source of this. Over the years, many studies confirmed this hypothesis with the identification of RNA defects such as deep-intronic variants and non-canonical splice site variants which have been shown to alter the splicing and expression of *ABCA4* in a pathogenic manner (Braun *et al.*, 2013; Bauwens *et al.*, 2015; Sangermano *et al.*, 2019; Whelan *et al.*, 2023). These RNA defects represent a total of 9% of all mutations identified in *ABCA4* (Cremers *et al.*, 2020). Despite increased solve rates over the last decade, a proportion of individuals remain genetically unresolved following genomic sequencing and efforts are still being made

to uncover all genetic variation in the *ABCA4* gene. Nevertheless, accomplishing this task is more intricate than it seems.

The vast allelic heterogeneity evident in *ABCA4* is further compounded by a spectrum of potential phenotypes. STGD1 is characterised as a monogenic disease caused by mutations in the *ABCA4* gene but *ABCA4* itself is associated with other retinal degenerative disorders. According to RetNet (https://web.sph.uth.edu/RetNet/) - an online database that describes inherited retinal disorders and their causal genes, *ABCA4* is implicated in the development of autosomal recessive cone-rod dystrophy (arCRD) (Maugeri *et al.*, 2000), autosomal recessive retinitis pigmentosa (arRP) (Mullins *et al.*, 2012), STGD1 (Allikmets *et al.*, 1997b), and age-related macular degeneration (AMD) (Allikmets *et al.*, 1997a). The varying degrees of severity exhibited by these conditions is inversely related to its residual protein function following mutation. This is detailed in a genotype-phenotype correlation model which categorises known *ABCA4* variants as mild, moderate, or severe – suggesting that classic STGD1 is often a result of biallelic moderate variants or a combination of mild and severe variants *in trans* (van Driel *et al.*, 1998a). However, this model is oversimplified as demonstrated by a vast degree of heterogeneity in phenotypes within just the STGD1 cohort of ABCA4-mediated retinopathy.

This is particularly obvious when comparing classic STGD1 with late-onset STGD1 cases, which comprise a substantial proportion (33%) of all STGD1 cases (Runhart *et al.*, 2022). On average, classic STGD1 presents within the first two decades of life, whereas late-onset STGD1 presents within the fourth decade of life and is often misdiagnosed as AMD. In these patients, visual acuity is preserved in the central retina, mediated through a phenomenon known as foveal sparing. This characteristic appears to be mutation specific, often involving the c.5461-10T>C variant which is present in both participants (PT1 and PT2) of our own study (Westeneng-van Haaften *et al.*, 2012).

Until recently, a large proportion of late-onset STGD1 were monoallelic, often with just one moderate or severe variant identified with DNA sequencing. Over 50% of these cases were resolved with the identification of hypomorphic allele c.5603A>T (Zernant *et al.*, 2017). This variant had previously been categorised as a benign variant even though it segregated with disease in affected families. This is due to its high minor allele frequency (MAF) in the general population and also its incomplete penetrance in disease cohorts. The effects of this allele only become apparent when present *in trans* with a null allele. This poses a question as to whether other hypomorphic variants with high MAF scores exist in *ABCA4* and could they

constitute the missing heritability in the remaining STGD1 cases? A recent study has identified and reclassified several *ABCA4* variants that act hypomorphic. These variants contribute to STGD1 pathology in a distinct way, altering the disease course for patients who harbour them (Lee *et al.*, 2021). Following this, the genotype-phenotype correlation matrix has been updated to include 4 distinct phenotypes of ABCA4-mediated retinal pathology. These include cases defined by the common G1961E variant (Cella *et al.*, 2009), hypomorphic variants, moderate variants, and severe missense and predicted very severe (PVS1)/null variants correlating with a 4 potential prognostic outcomes (Prognosis 1-4), ranging from mild to severe (Lee *et al.*, 2022b). This updated model reflects the progress made in the understanding of *ABCA4* genetics over the last decade and provides a useful and much needed prognostic tool for genetic counselling of those affected by STGD1.

At present, STGD1 remains an incurable disease. This highlights the necessity of a confirmed genetic diagnoses for individuals with clinically diagnosed STGD1. This diagnosis not only gives individuals access to genetic counselling to plan for disease progression over their lifetime, but also gives individuals the autonomy to enlist in any clinical trials that may arise for STGD1, which often require a confirmed genetic diagnosis to be recruited.

The patients enlisted to our study are both monoallelic cases with the same complex allele c.[5461-10T>C, 5603A>T]. Both underwent HaloPlex sequencing at the *ABCA4* locus (Bauwens *et al.*, 2015) but did not reveal any additional variants likely causative of the disease phenotype. Both patients also presented with late-onset symptoms consistent with foveal sparing and a mean age of onset at ~40 years of age. With this clinical information and knowledge of the literature, we hypothesised that the missing inheritance in these patients is the consequence of either an RNA defect or a hypomorphic variant. To this end, we ensued WGS and LRS technologies to ensure a comprehensive screen of the *ABCA4* locus was carried out.

The effects of non-coding variants often need to be validated *in vitro* with midigene splicing assays to assess their contributions to disease pathology. To identify putative RNA defects in PT1 and PT2, we isolated RNA from mature ROs (Day 220) to capture *ABCA4* transcripts as they are expressed in native retina tissue (Cowan *et al.*, 2020). A similar approach was taken by the Pierce and Gamm groups in 2019 where they uncovered the missing heritability in a family group with cone dysfunction syndrome using an integrated short-read WGS and RNA-Seq method on transcripts derived from Day 160 ROs (Bronstein *et al.*, 2019). This facilitated

both the detection and functional assessment of non-coding variants in a small family with genetically unresolved retinal degeneration.

As mentioned, *ABCA4* is a large gene spanning 128kb. To facilitate the sequencing of such a large gene, we opted for a LRS approach using the PacBio IsoSeq platform (https://www.pacb.com/), instead of the standard short-read RNA-Seq approach. PacBio IsoSeq provides higher resolution of differentially spliced isoforms via the generation of sequence reads up to 20kb in length. This ensures that sequence reads cover several exons and introns and enables *de novo* genome assembly. This reduces the reliance on genome assembly prediction tools to stitch together sequenced reads, as is the case with the ~200bp reads from traditional RNA-Seq methods. The result of IsoSeq and downstream analyses is a list of full-length isoforms from the alternative splicing of target genes (Gonzalez-Garay, 2016). In one study, more than 10% of the transcripts obtained using the IsoSeq protocol represented previously unannotated intronic structures (Sharon *et al.*, 2013). This can give novel insights into the isoform diversity of any gene or tissue studied (Veiga *et al.*, 2022).

Moreover, the sequence reads from PacBio are extremely accurate due its CCS technology. This enables for higher read depth by resequencing the circularised DNA/cDNA, - thereby mitigating any potential sequence errors from single passes. Sequences from this system can be >99.999% accurate with up to 20 sequencing passes (Eid *et al.*, 2009; Larsen and Smith, 2012). This generates high fidelity sequence reads (HiFi reads) that we can exploit for the exploration of previously uncovered RNA defects and assess functionality of the *ABCA4* gene in PT1 and PT2 monoallelic cases.

5.2 Aims

This chapter aims to identify the missing inheritance of PT1 and PT2 - two monoallelic cases of late-onset STGD1 by:

- Isolating DNA from Patient iPSCs and performing WGS using the Illumina NovaSeq platform
- Ensuring sufficient quality of the data to identify candidate variants
- Filtering candidate variants by their involvement in macular and retinal degeneration
- Validating potentially causative variants with Sanger sequencing
- Isolating RNA from iPSC-derived ROs for PT1 and PT2 and performing LRS using the PacBio IsoSeq platform
- Checking for previously uncovered RNA defects in the LRS reads
- Investigating the impact of *ABCA4* mutations in PT1 and PT2 on transcript level utilising the sequence reads from the LRS data

An overview of the experimental aims in this chapter is illustrated graphically in **Figure 5.1.**

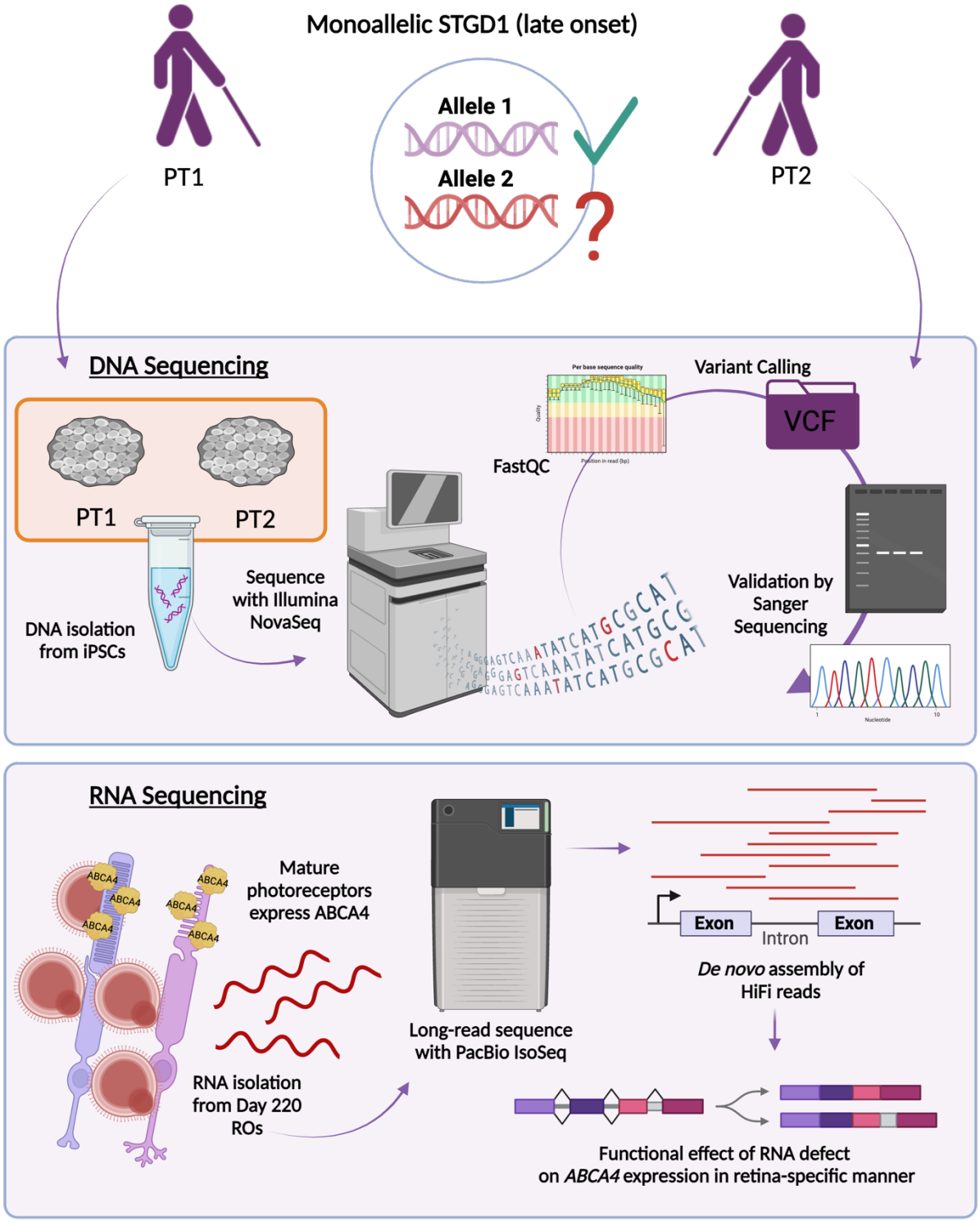

Figure 5.1 Graphical overview of chapter.

5.3 Results

5.3.1 Quality checks of WGS data from PT1 and PT2 monoallelic cases

Using DNA isolated from PT1 and PT2 iPSCs, WGS was carried out on the monoallelic cases using the Illumina NovaSeq platform as described in **Section 2.6**. Our aims were to ensure that PT1 and PT2 clinical phenotypes were indeed consequence of mutated *ABCA4* and not a result of genes that act as phenocopies to STGD1 - whilst also investigating candidate variants in *ABCA4* that could resolve the missing inheritance displayed in these cases.

Quality control of the resulting data was carried out by the Bioinformatics Support Unit (BSU) in Newcastle University using The Genome Analysis Toolkit (GATK). This software is the industry standard for identifying SNPs and indels in germline DNA and RNA-Seq data.

For PT1, the median read coverage was 22.0X with approximately 12% of transcripts reaching a coverage ≥ 33.0X with more than 500 million paired reads. PT2 displayed a mean read coverage of 42.0X with 85% of transcripts reaching a coverage ≥ 33.0X with also more than 500 million paired reads before filtering **(Figure 5.2).**

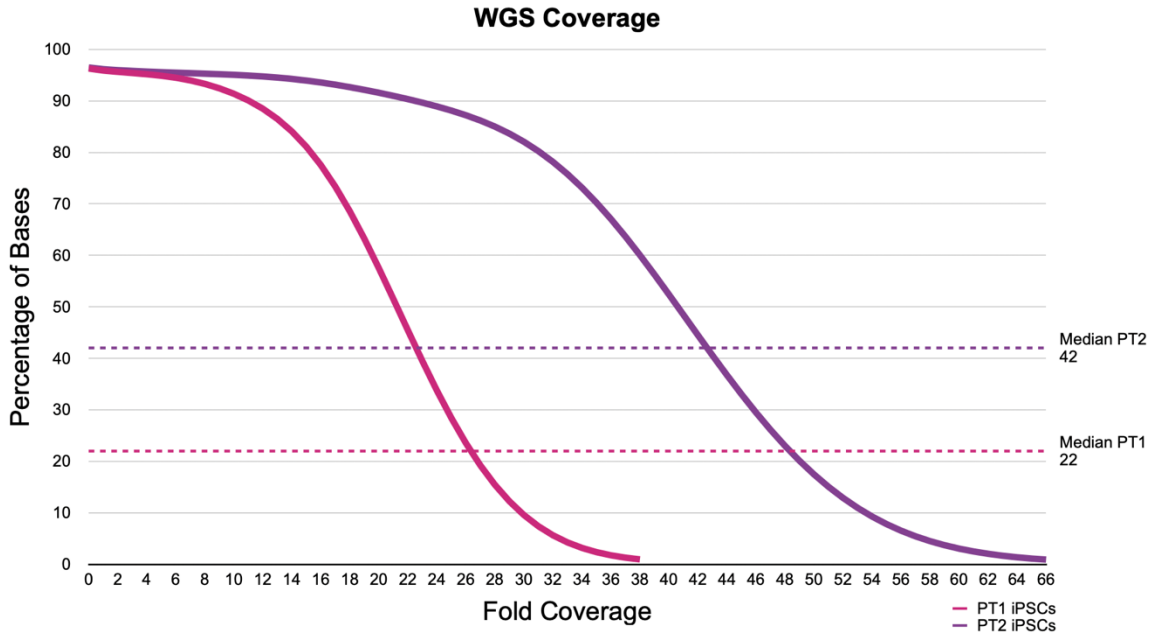

Figure 5.2 Read Depth of PT1 and PT2 WGS

The percentage drop off of bases in the genome territory of each sample: PT1 (pink) and PT2 (purple) for each fold coverage is shown via line plot. X-axis corresponds to fold coverage and y-axis corresponds to percentage of bases. The median values of sequence coverage are displayed by intersecting dotted lines corresponding to a value of 22.0X for PT1 and 42X for PT2. Note that 1% of the data is hidden to prevent very long tails in the distribution.

A FastQC report was generated for each of the samples - where poor-quality and duplicated reads were removed from the dataset. This resulted in more than 200 million unique reads for PT1 and just over 100 million unique reads for PT2 **(Figure 5.3).** Resulting read lengths in both samples averaged approximately 150bp **(Figure 5.4).**

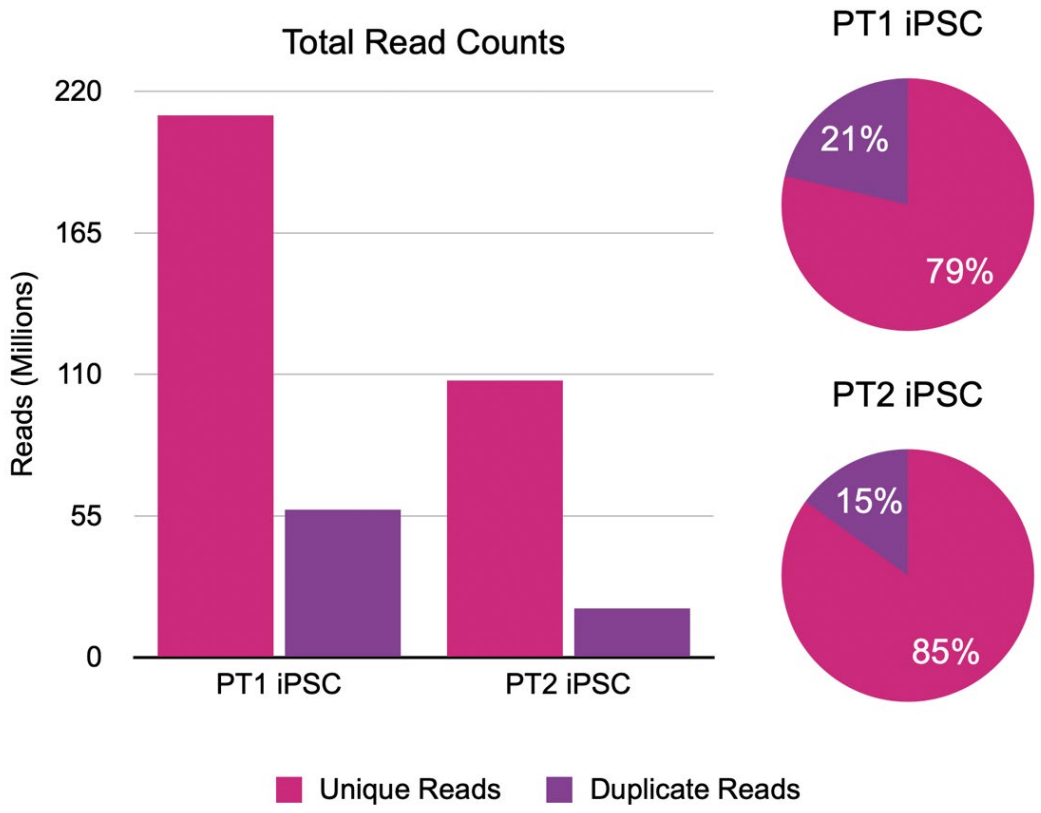

Figure 5.3 Total read counts following quality control filtering

Histogram displays the total number of reads (in millions) following the processing and filtering of raw data. More than 200 million reads were observed in PT1 and more than 100 million in PT2. X-axis shows samples analysed and the y-axis displays the read counts in millions. Duplicated reads were also apparent and shown as a percentage of the total reads in each sequenced patient (21% reads in PT1 and 15% reads in PT2) via pie chart analysis.

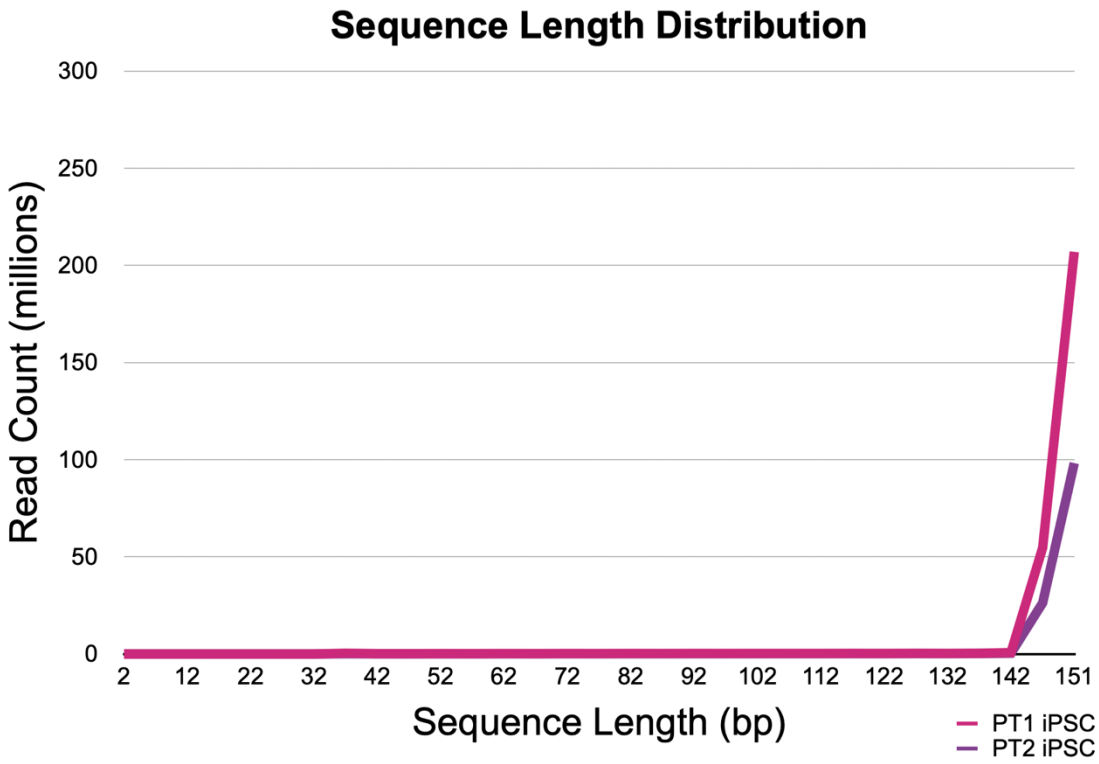

Figure 5.4 Sequence Length Distribution of Filtered Reads

Following the processing and filtering of sequenced reads, the average sequence length of PT1 and PT2 iPSCs corresponded to approximately 150bp. The x-axis displays the sequence length in base pairs (bp) and the read count is displayed on the y-axis in millions.

PHRED scores, which ascertain the quality or reliability of base calls in DNA sequencing data, were 35.1 for PT1 and 35.55 for PT2 **(Figure 5.5)**. For reference, PHRED scores typically range from 0 to 40, corresponding to a 100% to 99.99% base call accuracy, respectively. A PHRED score of 35 means that there is only a 1 in 10,000 chance that the base call is incorrect. This level of accuracy is often considered very reliable and is commonly used as a threshold for high-quality base calls in DNA sequencing analysis. Both samples passed the FastQC analysis with these PHRED scores and were suitable for downstream variant calling.

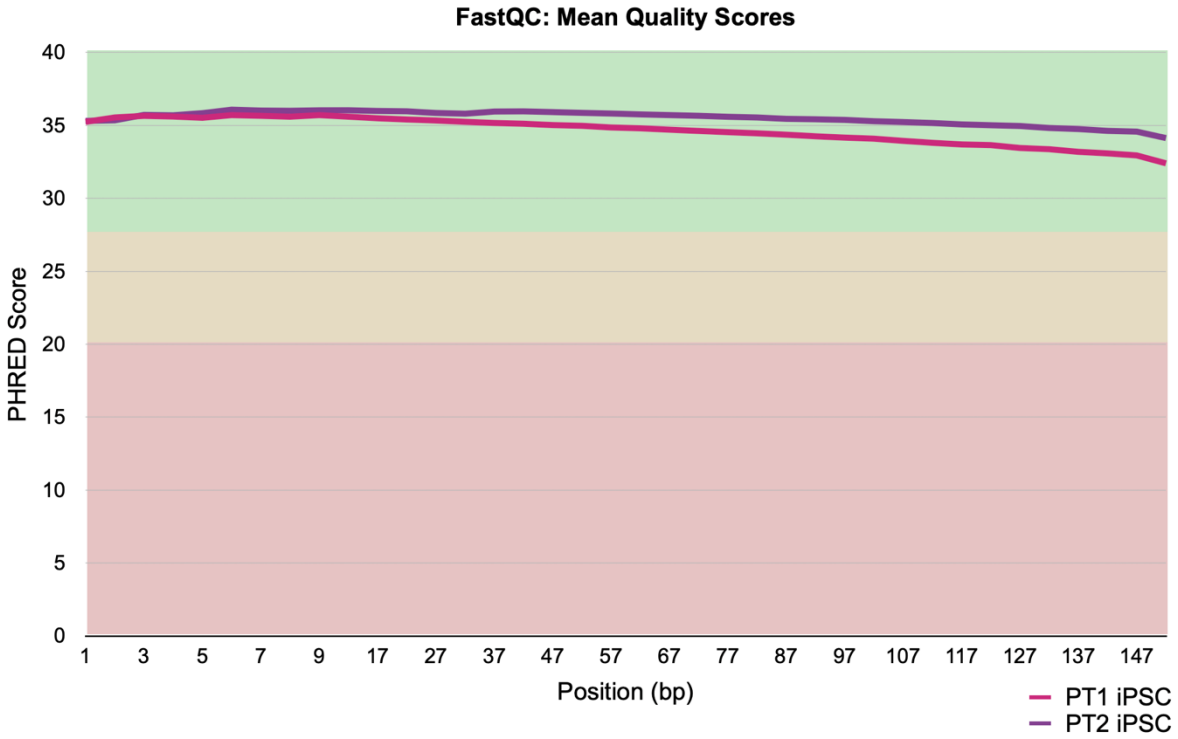

Figure 5.5 PT1 and PT2 sequenced reads pass quality control.

FastQC report shows a mean PHRED score of 35.1 and 35.55 for PT1 and PT2 sequenced samples following processing and filtering. This demonstrates high quality of data with base calling error rates of less than 1 in 10,000. Trend lines corresponding to PT1 and PT2 are shown in the green (pass rate) section of the chart. Orange and red sections of the graph correspond to poor quality data with little reliability.

5.3.2 Generation of macular disease gene panel for variant filtering

WGS generates an immense volume of raw data. In order to effectively manage this data in a structured and practical manner, we opted to assemble a gene panel targeting macular diseases. The logic behind this is that STGD1 is a macular disorder, so if the phenotypes presented by PT1 and PT2 are indeed phenocopies, genes involved in macular degeneration would be a probable source.

The generation of a macular disease gene panel was facilitated by accessing relevant literature on inherited macular diseases, online databases with known disease variants, in addition to readily available disease gene panels from companies providing sequencing services. The comprehensive list of genes incorporated for data filtration is visually depicted in **Figure 5.6.**

Within this gene panel, *ABCA4* is denoted in red as the primary contender for involvement in STGD1 pathology. Concurrently, *PROM1* and *PRPH2* are shaded in orange, reflecting their frequent occurrence as phenocopies of STGD1. *RP1L1, ELOVL4, CFH* and *CRX1*, in pale orange, have also demonstrated links to macular degeneration, albeit with less overlap in STGD1 phenotypes. In total, 33 genes are included in this disease panel. This colour-coded system signifies the potential of genes to trigger the clinical phenotypes witnessed in the monoallelic PT1 and PT2 STGD1 cases. The panel's creation served as an invaluable tool to streamline data to a more manageable scale and played a pivotal role in unveiling the missing inheritance in both PT1 and PT2.

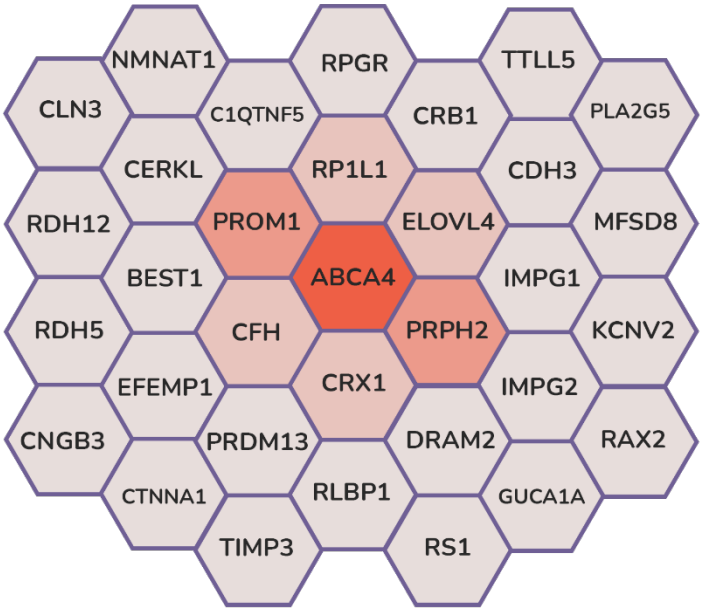

Figure 5.6 Macular disease gene panel

A panel of 33 genes used in the filtering of WGS to identify missing variants in the monoallelic STDG1 cases included in this study. Likely to least-likely genes causative of disease phenotype are arranged spatially from the centre to periphery and colour coded red to grey respectively.

5.3.3 Confirmation of known variants and identification of novel variants in ABCA4

Using this filtering strategy, we were unable to identify any relevant mutations in macular disease genes other than *ABCA4* - which could result in the distinct clinical phenotype observed by PT1 and PT2 probands. Consequently, we focused solely on the variants identified in *ABCA4*. This allowed us to confirm the presence of known variants in the resolved allele of PT1 and PT2. This allele is a complex of the variants: c.[5461-10T>C;5603A>T]. We only identified a previously uncovered variant in PT2.

Firstly, we checked for the intronic component - c.5461-10T>C, of this complex allele. We identified the variant in the variant calling file (vcf) and in the bam file via IGV software for both PT1 and PT2. This variant demonstrated a read depth of approximately 50%, suggesting the variant is present in a heterozygous state in both patients (**Figure 5.7).** To avoid confusion, it is important to note that the *ABCA4* gene in hg38 reference genome is in the 3' ← 5' orientation, so all called variants in *ABCA4* will be observed as the reverse complement in IGV figures.

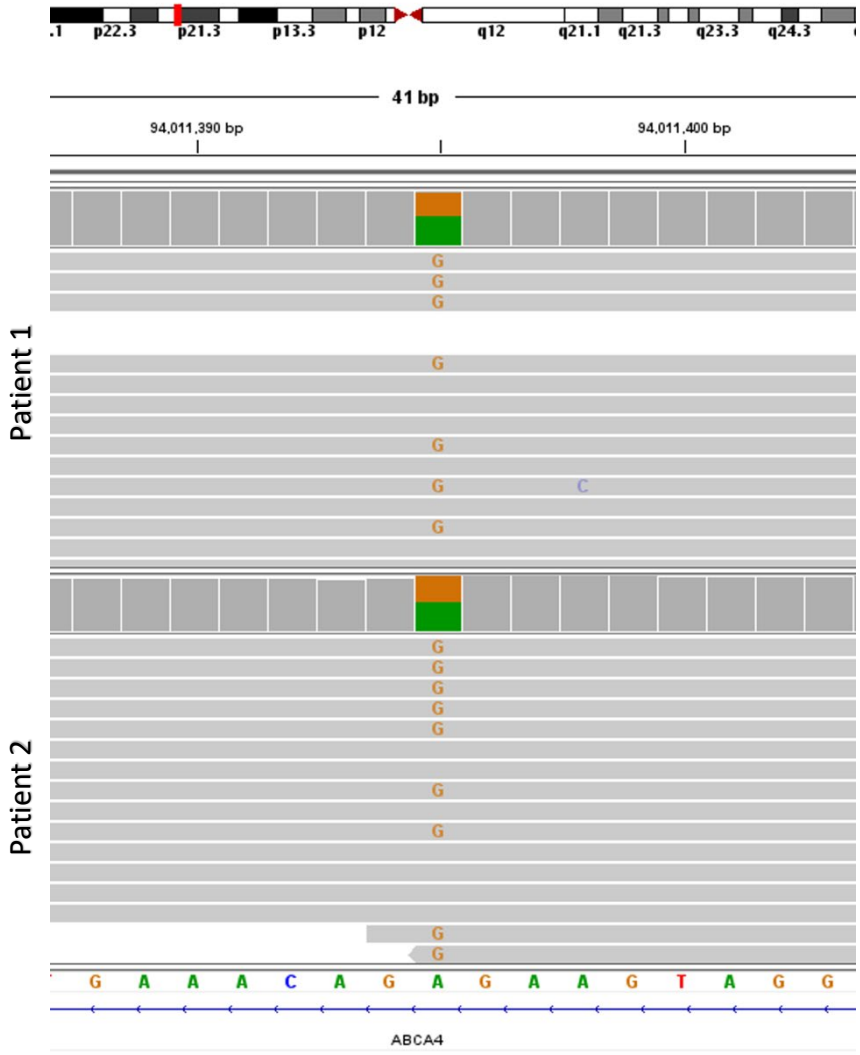

Figure 5.7 Detection and confirmation of c.5461-10T>C in *ABCA4* gene.

IGV view of the c.5461-10T>C variant in *ABCA4* with the base change from T→C (A→G in reverse complement). Read depth appears to be approx. 50% in both PT1 and PT2 indicating heterozygosity of this variant, validating previous reports with these patients. The approximate cytogenetic location of the mutation can be observed by a red line on the chromosome marker at the top of the screen.

We next looked at the other variant in the complexed allele: the missense variant c. 5603A>T. This has also been reported to be heterozygous in both PT1 and PT2. We observed this variant in the bam files of both patients and whilst we saw 50% read depth in PT2 as expected, we were surprised to see almost 100% read depth of the variant in PT1 **(Figure 5.8).** This suggests the variant in PT1 exists in a homozygous state, thereby providing biallelic variant resolution for PT1.

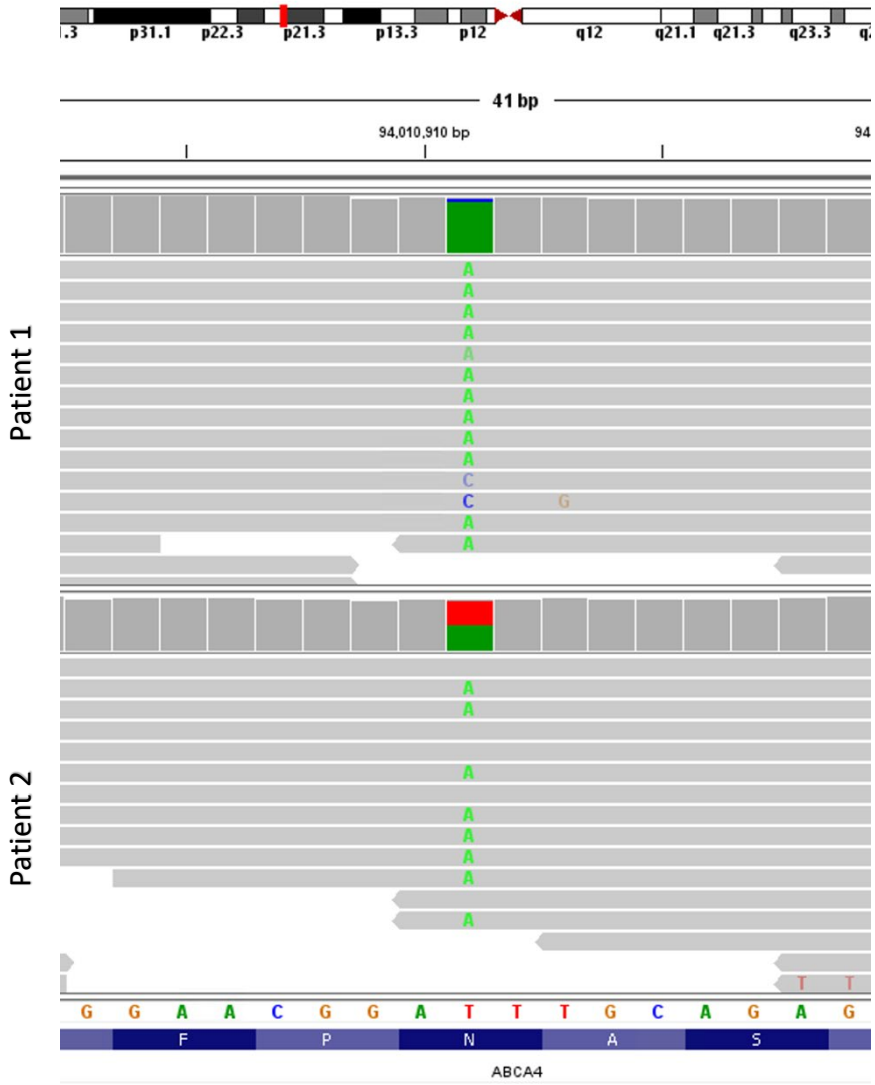

Figure 5.8 Detection and confirmation of c. 5603A>T in *ABCA4* – resolution of PT1 genotype.

IGV view of the c.5603A>T variant in *ABCA4* with the base change from A→T (T→A in reverse complement). Read depth appears to be approx. 50% in PT2 indicating heterozygosity of this variant validating previous reports. However, almost 100% read depth in PT1 suggests homozygosity of the variant thereby providing biallelic resolution for PT1.

In addition to confirming known variants in *ABCA4* for both PT1 and PT2, the vcf reported a previously undiagnosed missense variant (c.4685T>C) in *ABCA4* with uncertain significance in PT2. With a read depth of approximately 50%, it suggests this variant is in heterozygous state and could constitute the missing allele in PT2. This variant has been reported previously in ExAC databases with similar population frequencies in the general population. Despite this, we validated all alleles identified in the vcf by an additional sequencing method as is standard with diagnostic sequencing.

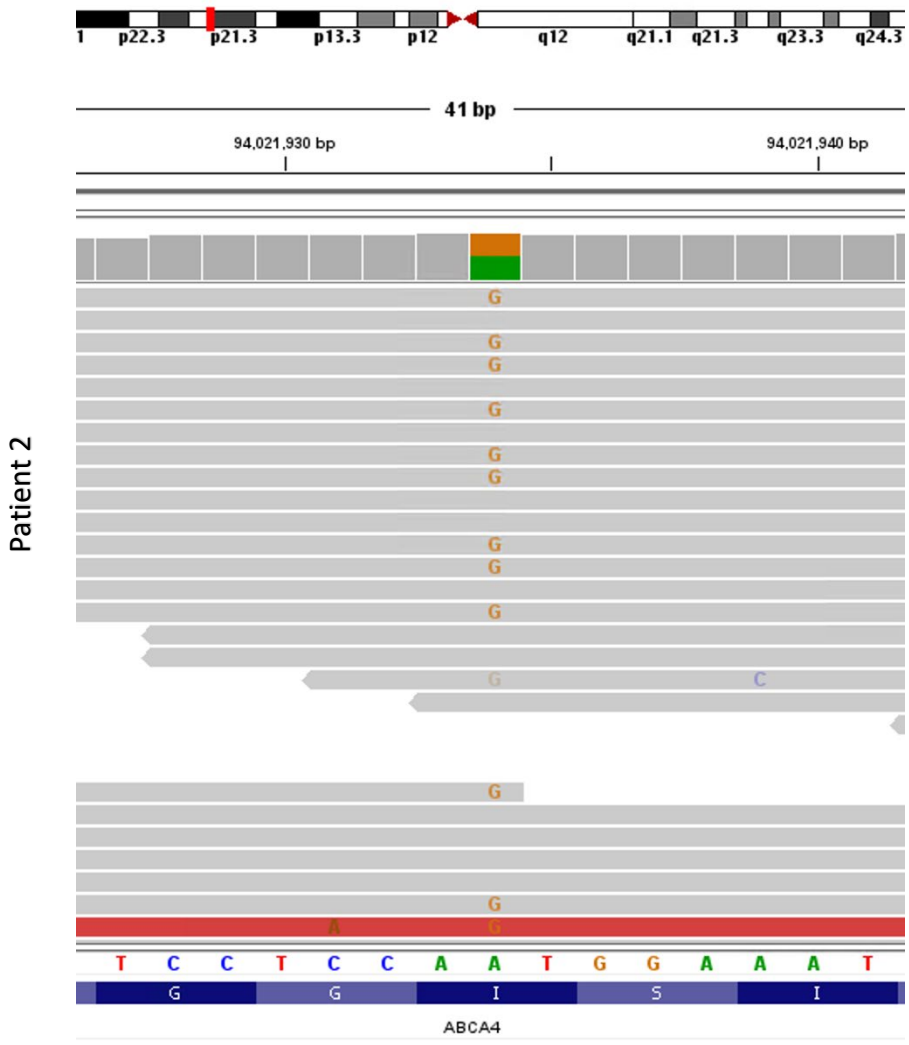

Figure 5.9 Identification of PT2-specific variant: c.4685T>C in *ABCA4*.

IGV view of the c.4685T>C variant in *ABCA4* the base change from T→C (A→G in reverse complement). Read depth appears to be approx. 50% in PT2 indicating heterozygosity of this variant, potentially resolving the missing allele in PT2 case.

5.3.4 Validation of ABCA4 mutations by Sanger sequencing

Mutations identified by WGS are typically validated by an additional sequencing method. Sanger sequencing tends to be the gold standard. To facilitate this, mutation-specific primers were designed for each of the *ABCA4* mutations identified in the vcf to amplify corresponding DNA for Sanger sequencing as described in **Section 2.6.3**. We ensured the PCR products corresponded with their expected band size via gel electrophoresis before sending for sequencing **(Figure 5.10 A).**

The traces derived from the Sanger sequencing confirmed the mutations identified in the WGS **(Figure 5.10 B).** Sequences were generated using both the forward and reverse primers to ensure that we captured the variant without background signal often seen at the beginning of Sanger sequences. By aligning the Sanger sequence (top row) with the reference sequence at that site (bottom row), we were able to detect mismatches (denoted by a loss of * which shows similarity to reference) and then map this back to the Sanger trace. The genetic orientation of the alignment (3'←5', or 5'→3') depends on whether the forward or reverse primer was used for the trace. Consequently, the alignments made for Mutation 1 and 2 are in reverse complement as the reverse primer was used for sequencing.

For Mutation 1 (c.5603A>T, p.Asn1868Ile), we observed full homozygosity of this variant in patient 1 as demonstrated on the Sanger trace by the dominant peak for nucleotide A. This is in contrast to the overlapping peaks of nucleotides A and T in PT2 confirming the heterozygosity of this variant. For Mutation 2 (c. 5461-10T>C, p.ThrValfs*13), we observed heterozygosity in both PT1 and PT2 denoted by overlapping peaks corresponding to the nucleotides A and G. The uncovered *ABCA4* variant (c.46855T>C, p.Ile1562Thr) in PT2 was also validated by Sanger sequencing and showed heterozygosity with overlapping peaks of T and C nucleotides. Confirmation of these results, suggest both monoallelic cases were genetically resolved following WGS.

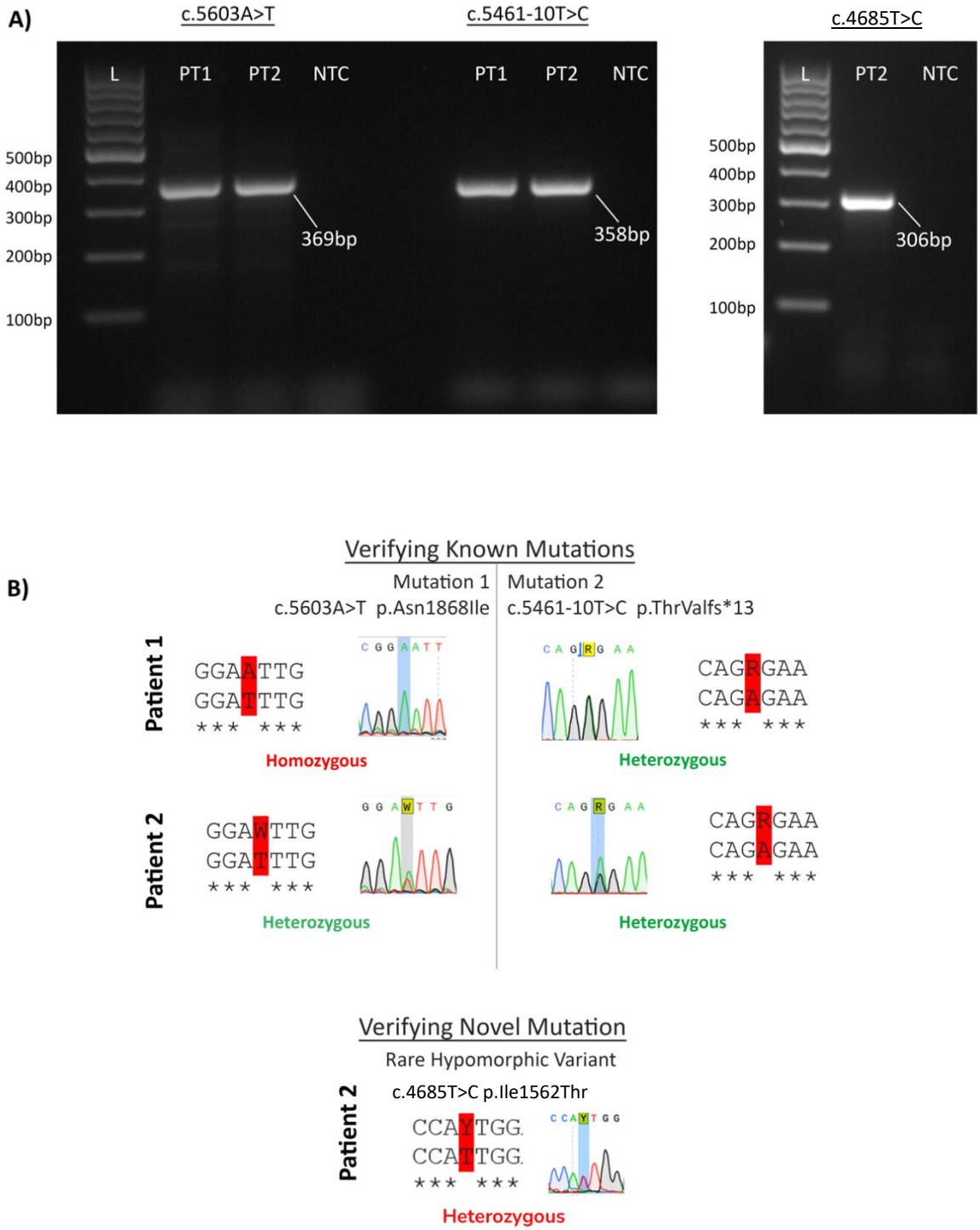

Figure 5.10 Validation of *ABCA4* mutations in PT1 and PT2 using Sanger Sequencing.

A) Agarose gels displaying PCR amplified products from DNA of both PT1 and PT2 alongside a 100bp ladder (L). Products corresponding to the expected band size for Mutation 1 (c.5603A>T) at 369bp and Mutation 2 (c.5461-10T>C) at 358bp were present in both PT1 and PT2 samples. For the PT2 specific variant, PCR products corresponding to the expected band size of 306bp were observed. Non-template controls (NTC) were included in both PCR reactions. **B)** Sanger results from the sequenced PCR products. DNA alignments between reference (bottom row) and Sanger sequences (top row) display mismatches, corresponding to the nucleotide peaks in the adjacent Sanger traces. Mutation 1 present in homozygous state in PT1 and heterozygous in PT2. Mutation 2 is heterozygous in both PT1 and PT2. Whilst the novel mutation is identified in heterozygous state in PT2.

5.3.5 Identification of EKG haplotype in PRPH2 and ROM1, frequently observed in STDG1 cases

Recent literature has reported associations of haplotype variants in *PRPH2* and *ROM1* as potentially *trans*-acting modifiers of STGD1 due to their overrepresentation in patients with STDG1. Our WGS data confirmed this observation with both patients demonstrating a triad of mutations that constitute the EKG haplotype in *PRPH2*. This EKG or otherwise known GAG haplotype is comprised of; Mutation 1 – c.1013A>G p.Asp338Gly, Mutation 2 – c.910C>G p.Gln304Glu, and Mutation 3 – c.929G>A p.Arg310Lys. IGV demonstrates the presence of these 3 mutations in both PT1 and PT2 genomes. PT1 shows 50% read depth for the variants in this haplotype compared with 100% read depth observed in PT2.

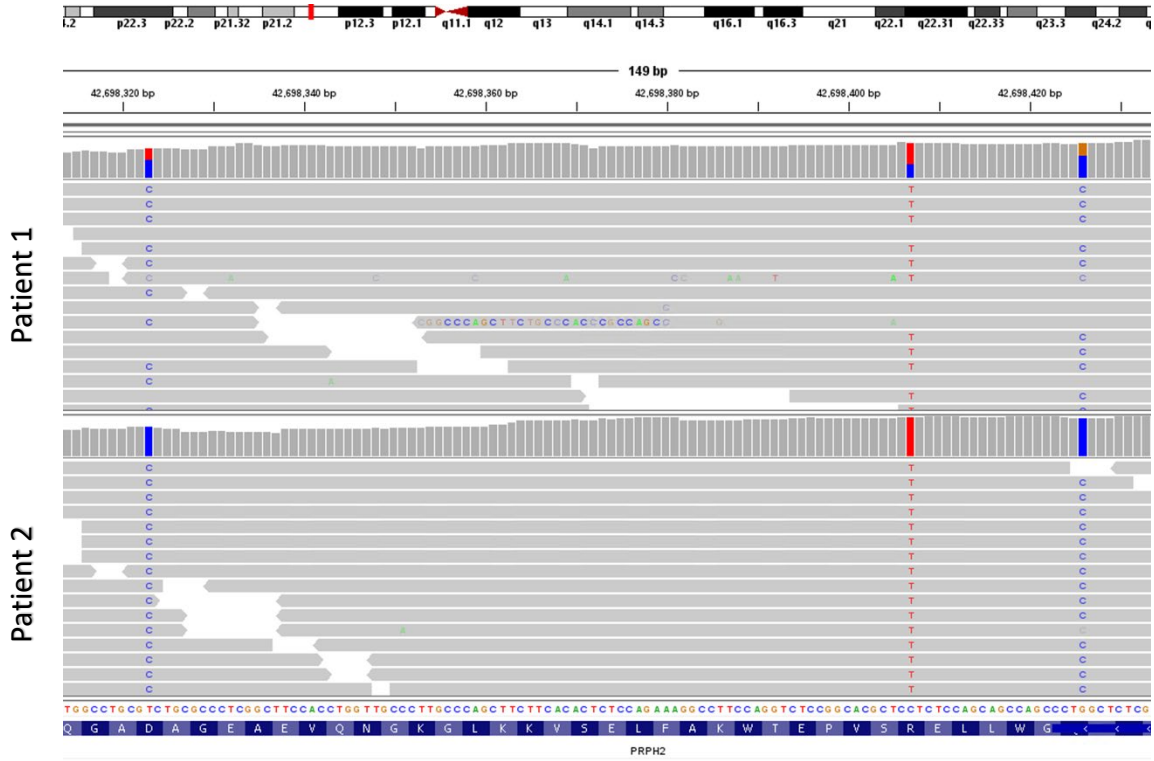

Figure 5.11 EKG (GAG) haplotype in *PRPH2* is present in both PT1 and PT2 genomes

IGV displays the presence of this *PRPH2* haplotype in both PT1 and PT2 samples. Patient 1 demonstrates 50% read depth of these variants.

The *ROM1* variant, c.353G>C, p.Gly118Ala, was also observed using IGV and was found present in both PT1 and PT2 samples with 100% read depth **(Figure 5.12).** Although the full influence of these variants is unknown, we validated them with Sanger sequencing.

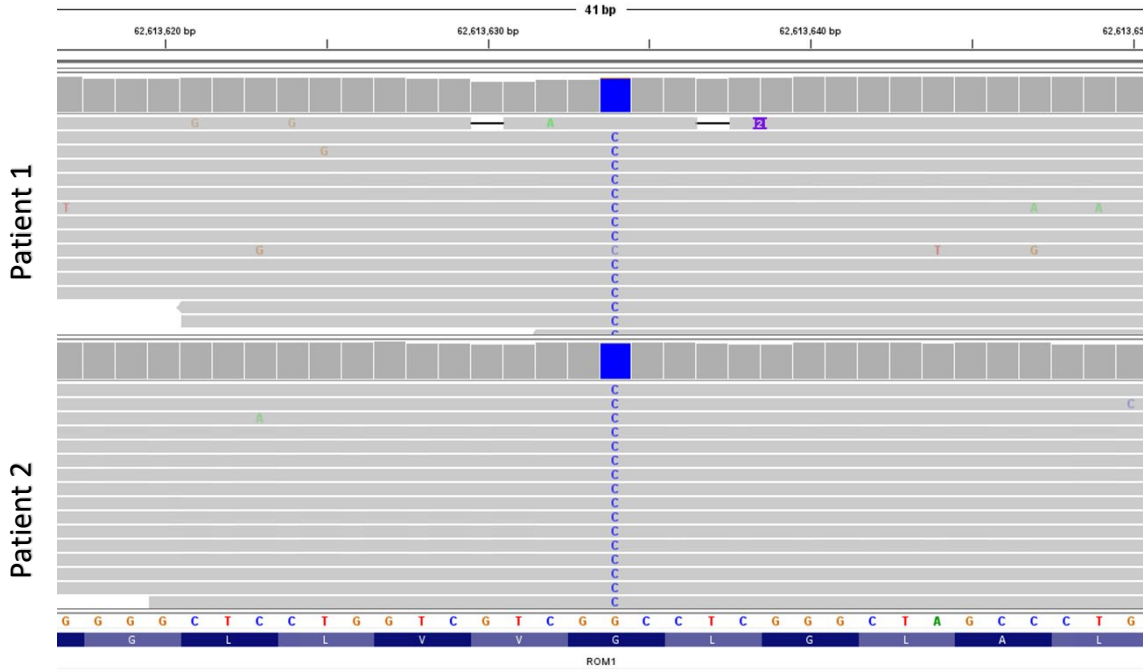

Figure 5.12 Potential *trans*-acting modifier variant in *ROM1* is present in both PT1 and PT2 genomes.

IGV displays the presence of this *ROM1* variant c.353G>C in both PT1 and PT2 samples. Both patients have a read depth of 100% for this variant.

5.3.6 Validation of PRPH2 Haplotype and ROM1 variant by Sanger sequencing

Mutation-specific primers were designed for each of the mutations constituting the EKG haplotype in the *PRPH2* gene and the rare variant in *ROM1* to amplify DNA for Sanger sequencing. We ensured the PCR products corresponded with their expected band size via gel electrophoresis before sending for sequencing **(Figure 5.13 A).**

The traces derived from the Sanger sequencing confirmed the mutations identified in the WGS as demonstrated by the mismatches in the DNA sequence alignments **(Figure 5.13 B).** Mutation 1 – c.1013A>G p.Asp338Gly, Mutation 2 – c.910C>G p.Gln304Glu and Mutation 3 – c.929G>A p.Arg310Lys were all confirmed to be in heterozygous state in PT1 and heterozygous state for PT2. The *ROM1* variant, c.353G>C p. Gly118Ala was present in homozygous state as shown in the Sanger traces.

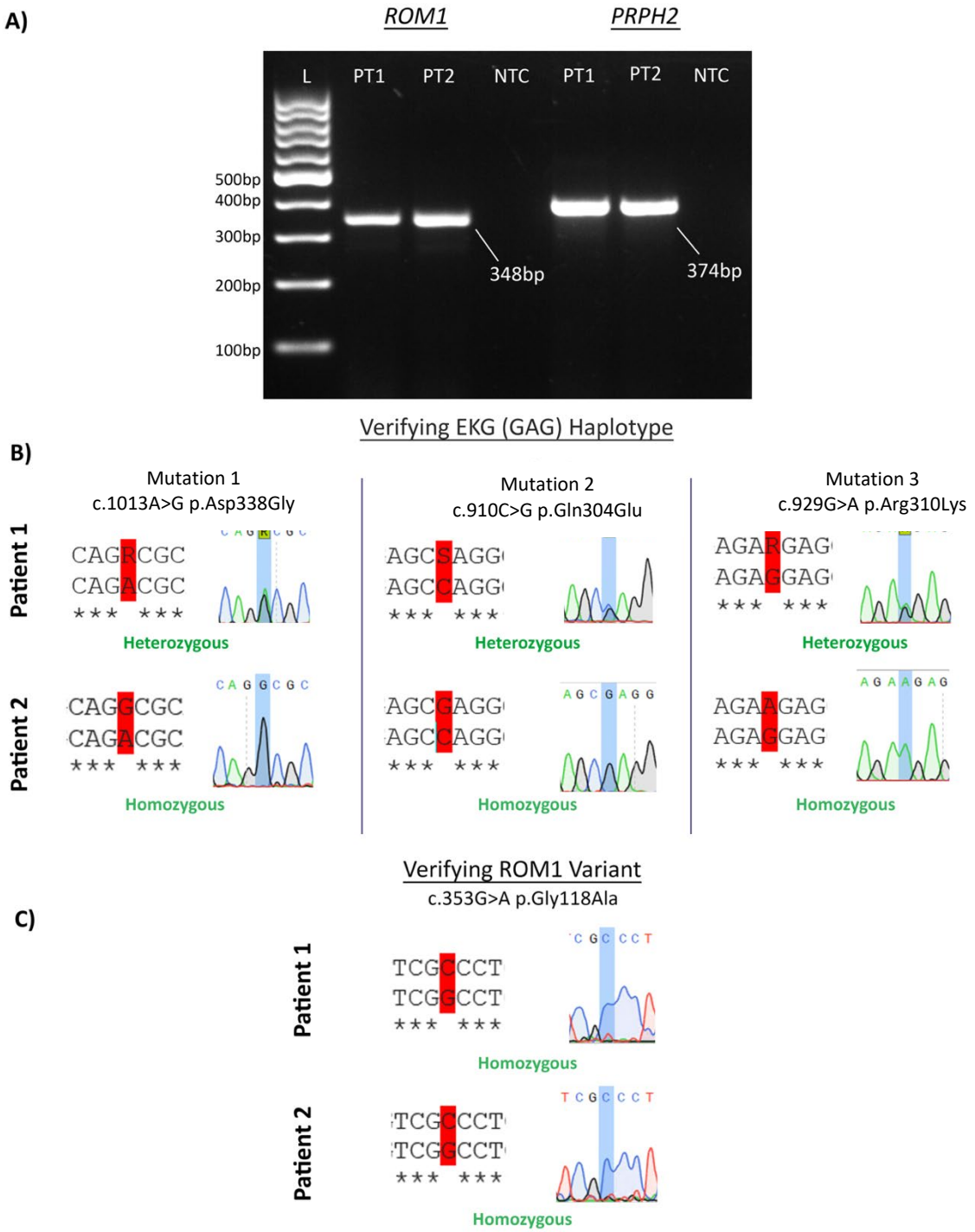

Figure 5.13 Validation of *PRPH2* EKG (GAG) haplotype and *ROM1* variant in PT1 and PT2 using Sanger Sequencing.

A) Agarose gels displaying PCR amplified products from DNA of both PT1 and PT2 alongside a 100bp ladder (L). Products corresponding to the expected band size for the EKG (GAG) haplotype in PRPH2 consisting of Mutation 1 (c.1013A>G), Mutation 2 (c.910C>G) and Mutation 3 (c.926G>A) were observed at 348bp. For the *ROM1* variant (c.353G>C), a band corresponding to 374bp was observed in both PT1 and PT2. Non-template controls (NTC) were included in both PCR reactions. **B,C)** Sanger results from the sequenced PCR products. DNA alignments between reference (bottom row) and Sanger sequences (top row) display mismatches, corresponding to the nucleotide peaks in the adjacent Sanger traces. **B)** Mutations in the EKG haplotype of *PRPH2* were present in heterozygous state in PT1 and homozygous state in PT2. **C)** The *ROM1* variant was present in homozygous state for both PT1 and PT2.

5.3.7 ABCA4 mutations are further validated in isoforms derived from LRS

We originally employed LRS in collaboration with Dr. Darren Smith and Dr. Andrew Nelson (Northumbria University) in an effort to uncover the missing alleles in the PT1 and PT2 monoallelic cases. To this end, we isolated RNA from Day 220 ROs to obtain tissue-specific *ABCA4* transcripts as described in **Section 2.7**. We originally hypothesised the presence of deep-intronic variants as the source of this missing inheritance, however we did not observe any novel RNA defect in either PT1 or PT2 with LRS. Instead, we utilised the data to further validate the known and novel *ABCA4* variants identified by WGS and gain more insight into their functional effects on the expression of *ABCA4*. The bioinformatic analysis including mapping and annotation of sequenced transcripts and isoform generation was done by our collaborators Dr. Luís Ferrández Perel and Dr Ana Conesa (University of Valencia).

c.5603A>T, p. Asn1868Ile was observed in IGV for both PT1 and PT2 **(Figure 5.14).** The green blocks correspond to nucleotide A, thus T in the negative strand. We know from DNA sequencing that PT1 is homozygous for c. 5603A>T, whilst PT2 is heterozygous. Despite this, all *ABCA4* isoforms from HiFi reads displayed by the bam file contained this mutation, with the exception of just one read, as indicated by the red box in **Figure 5.14.** This is an interesting observation that suggests allele-specific expression (ASE) is at play in PT2.

.

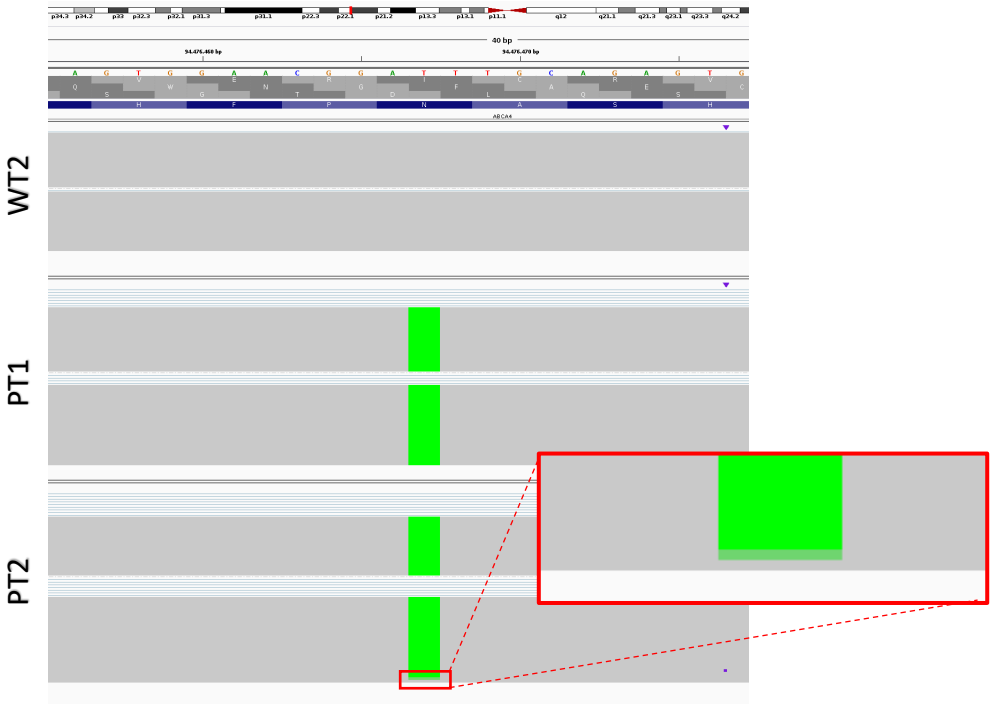

Figure 5.14 c.5603A>T mutation in *ABCA4* in PT1 and PT2 from LRS.

Bam files of HiFi sequence reads displayed in IGV browser for LRS data derived from Day 220 ROs. WT2 displays no defect, whereas PT1 and PT2 display the A>T variant change. The green boxes correspond to the nucleotide A, which on the reverse strand is T. The variant is homozygous in PT1 and appears to be dominantly expressed in PT2 despite its heterozygous status, with the exception of one read (red box) which is unaltered.

We were not expecting to see the 5461-10T>C, p.ThrValfs*13 variant in the HiFi sequence reads from any patient or control. However, in the IGV browser, we were able to observe one read in bam file of PT1 that had retained its introns and harboured the mutation as described **(Figure 5.15).** The brown read corresponds to the nucleotide G in that position, which is C on the reverse strand (i.e., T>C change).

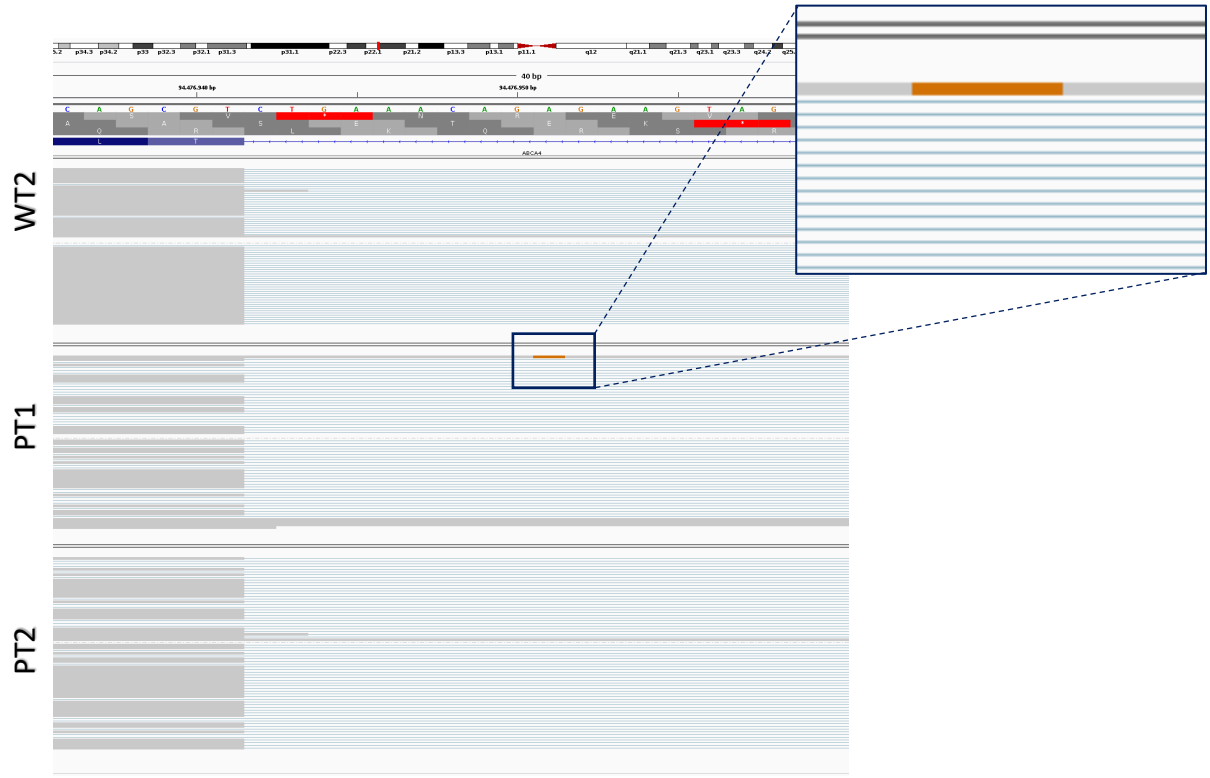

Figure 5.15 c.5461-10T>C mutation in *ABCA4* in PT1 and PT2 from LRS.

Bam files of HiFi sequence reads displayed in IGV browser for LRS data derived from Day 220 ROs. Intronic variants that involve exon skipping are not typically observed in sequenced reads, as evidenced in PT2 bam file. PT1 has evidence of one read (brown read in navy box) with retained introns containing the mutation in question. The brown read corresponds to the nucleotide G, which is C on the reverse strand.

We observed another interesting result when attempting to validate the newly uncovered variant c.4685T>C, p.Ile1562Thr in the HiFi reads from LRS. As shown in the IGV browser, we could not detect the mutation in resulting *ABCA4* transcripts. Whilst we were notified that

the sequences obtained from the RNA of PT2 ROs showed signs of degradation in the quality checks, sequenced isoforms from PT2 showed the c.5603A>T mutation faithfully. We hypothesised that the lack of variant seen in the bam file could be due to specific degradation of transcripts containing this mutation, due to issues with misfolding, or potential *cis*- or *trans*- acting modifiers that alter the expression of *ABCA4* alleles.

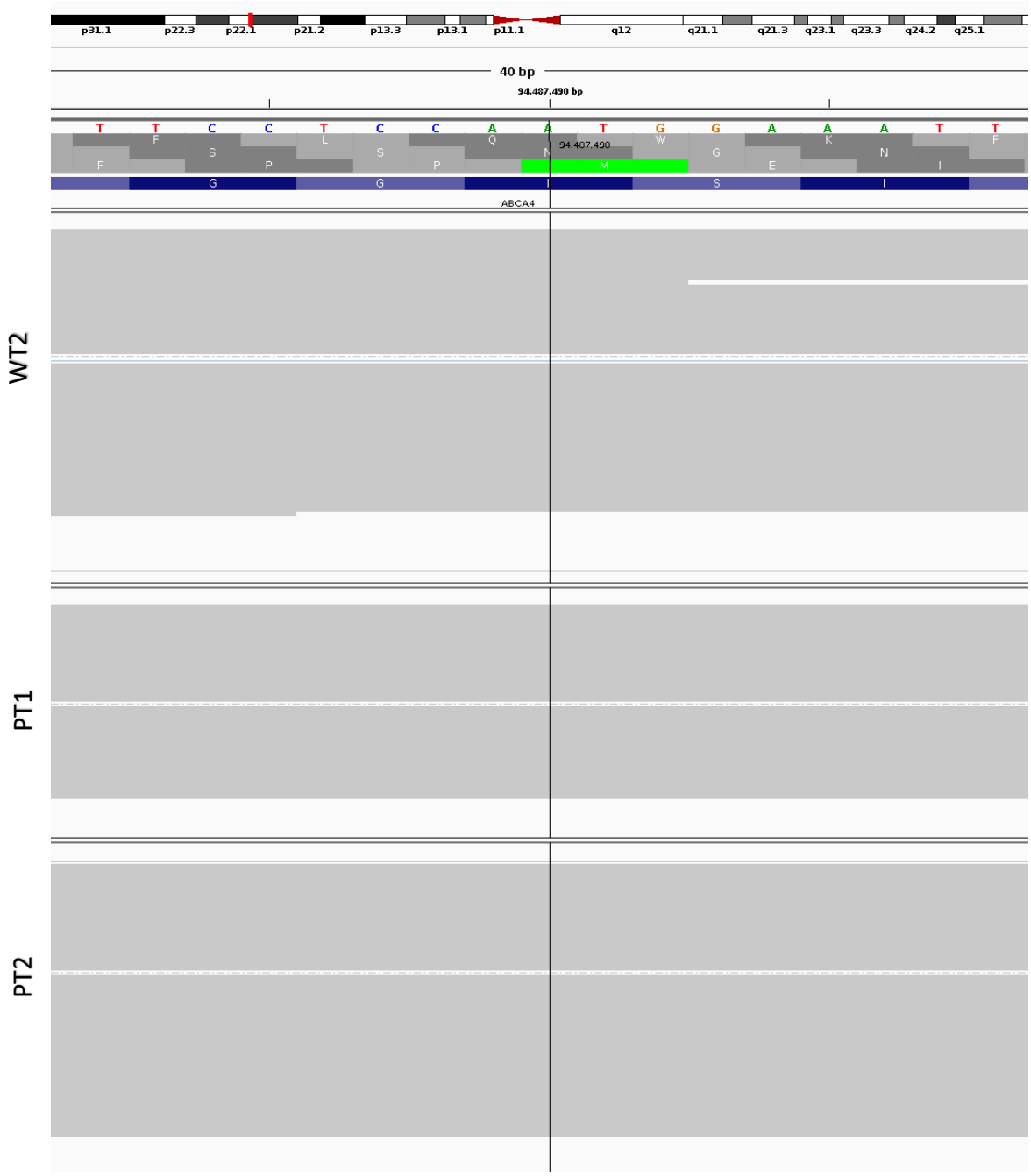

Figure 5.16 c.4685T>C mutation in *ABCA4* not seen in PT2 transcripts.

Bam files of HiFi sequence reads displayed in IGV browser for LRS data derived from Day 220 ROs. No variants were detected at the site expected in PT2 (black line).

5.3.8 c.5461-10T>C variant induces exon skipping in transcripts derived from PT1 and PT2 ROs

As LRS gives unique insights into isoforms with less reliance on *in silico* prediction for genome assembly (as is required with short-read traditional next generation sequencing), we used the technology to gain functional insights into the c.5461-10T>C variant in *ABCA4* to see if our ROs could recapitulate the splicing pattern reported in the literature (Sangermano *et al.*, 2016).

As shown in the sashimi plot (**Figure 5.17 A)** the c.5461-10T>C induces exon skipping of exon 39 and/or exon 40 in both PT1 and PT2. A reference *ABCA4* transcript is displayed at the bottom of the plot and the affected exons are within the shaded blue box. The numbers on the plot refer to the read depth of that exon in the sequenced data, which can be used to quantify the degree of exon skipping occurring. In **Figure 5.17 B,** the exon skipping data can be observed in a simplified manner with the affected exons shaded blue, and induced exon skipping shown as an arched line connecting unaffected exons. **Figure 5.17 C** demonstrates the percent-spliced-in (PSI) for exon 39 and 40 in all ROs. Transcripts from the WT2 ROs displayed a PSI value of 1 as expected. The patient organoids displayed lower values. For exon 39, PT1 exhibited a PSI value of 0.55, and PT2 0.71. For exon 40, PT1 exhibited a PSI value of 0.83 and PT2 a value of 0.71. This shows variability in the effect of the c.5461-10T>C on *ABCA4* transcripts, in accordance with the existing literature.

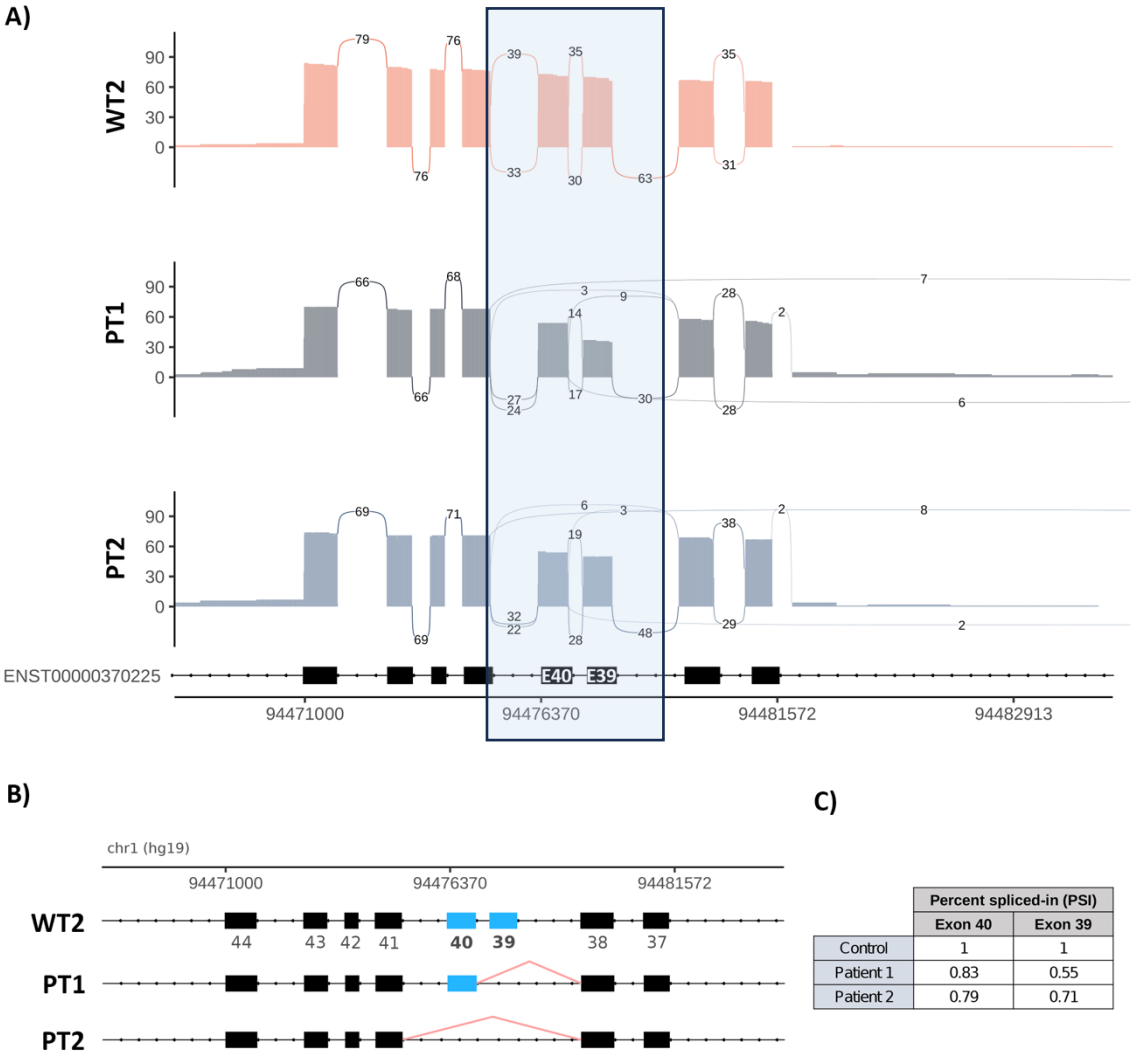

Figure 5.17 c. 5461-10T>C induces exon skipping in *ABCA4* transcripts from PT1 and PT2 ROs.

A) Sashimi plot derived from *ABCA4* transcripts of WT2, PT1 and PT2 displaying the exon skipping event associated with the c.5461-10T>C variant. The affected exons are shaded in blue and mapped to a reference *ABCA4* transcript. B) Displays the same results in a simplified manner with affected exons in blue and exon skipping shown by arched lines. C) The PSI values of exon 39 and exon 40 in all RO lines shows variable effects of the c.5461-10T>C mutation on the expression of *ABCA4* transcripts.

5.3.9 In depth view of the c.5461-10T>C variant in transcripts derived from PT1

To gain more insight into the functional effects of the c.5461-10T>C variant on *ABCA4* expression, we looked at how the mutation affects *ABCA4* on genomic, transcriptomic and protein levels. Due to the observed degradation in transcripts derived from PT2 ROs, we focused solely on PT1 for this analysis.

In **Figure 5.18 A,** the sequenced HiFi reads from PT1 are aligned to a hg19 reference at the *ABCA4* locus. In the genomic view, the red box shows the site of exon skipping induced by the c.5461-10T>C variant. There is a change to the untranslated regions (UTRs) following this exon skipping event as shown by the green lines in the PT1. In the transcript view, the red line indicates the region where the coding sequence (CDS) is significantly shortened due to exon 39 skipping in this case. On the protein level, this translates to the introduction of a premature stop codon, inducing premature termination of translation to protein as shown by the orange triangle on the protein view. This premature termination exists at a transmembrane domain site in the reference. The lost amino acids can be seen in the protein structure of ABCA4 in **Figure 5.18 B.** These transmembrane domains are a critical element of ABCA4 structure and function, such that the protein cannot function correctly without them. These results demonstrate why the c.5461-10T>C is extremely detrimental to ABCA4 function.

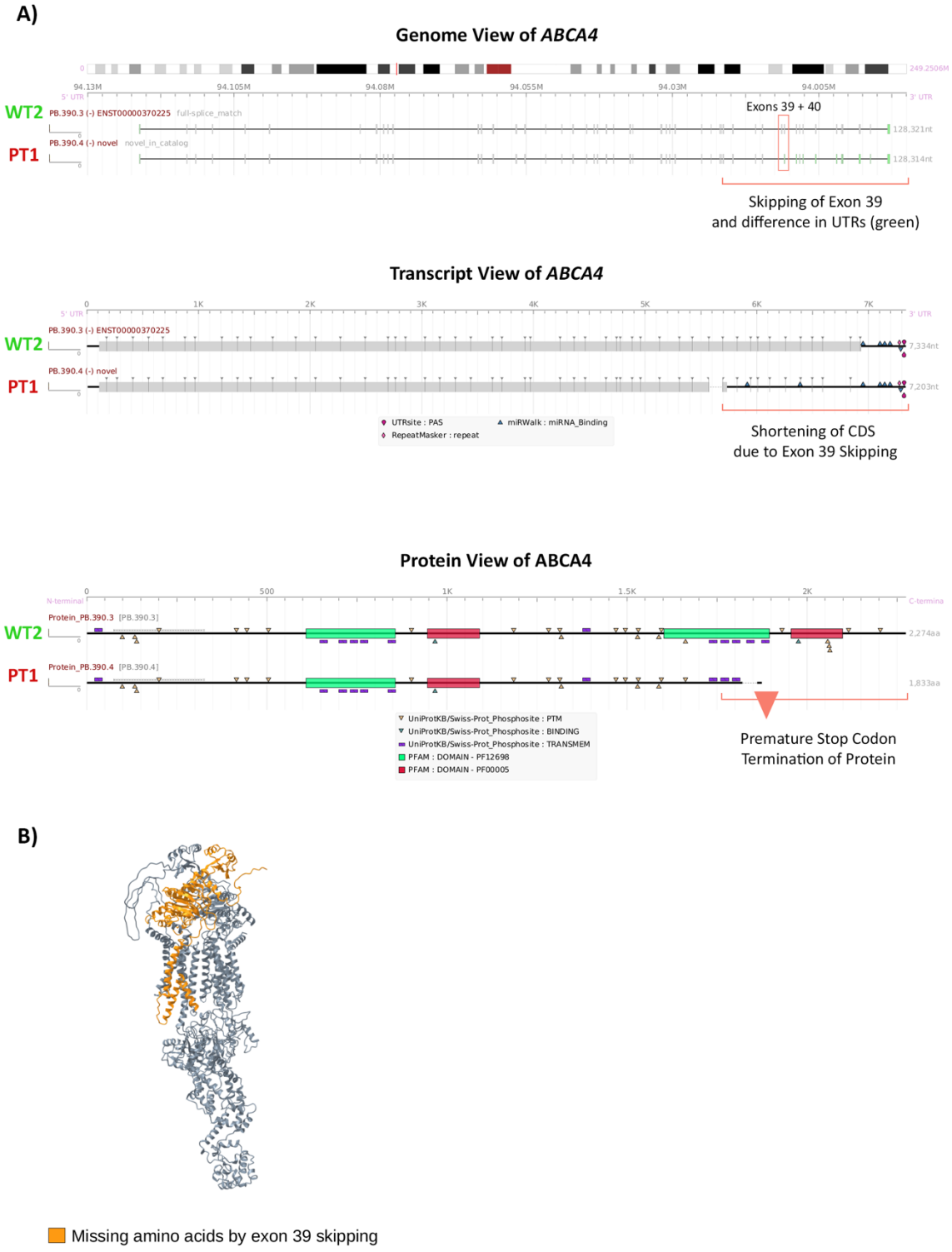

Figure 5.18 In-depth analysis of c.5461-10T>C in PT1 *ABCA4* transcripts.

A) Genomic, transcriptomic and protein view of the effects on *ABCA4* elicited by the c.5461-10T>C variant. On genome level, exon skipping generates more untranslated region (UTR) sites in the PT1 gene as observed in green. On transcript level, skipping of exon 39 causes significant shortening of the coding sequence (CDS) in PT1. In the protein alignments, the introduction of a premature stop codon induces premature termination of translation for the ABCA4 protein at a site containing important transmembrane domains. Reference used was derived from the hg19 genome. B) The amino acids affected by the mutation are observed in the 3D structure of ABCA4 protein.

5.4 Discussion

We achieved high quality sequence reads with sufficient read depth from DNA isolated from PT1 & PT2 iPSCs with the Illumina NovaSeq sequencer. The sequence read length averaged at approximately 150bp and genome assembly was facilitated through alignment with the hg38 reference genome. The sequence reads passed the FastQC report with high PHRED scores of 35.1 and 35.55 for PT1 and PT2 respectively. This enabled us to successfully identify the missing alleles in PT1 and PT2 monoallelic cases as well as confirming known *ABCA4* variants in those cases also.

The known variants observed in the WGS of both PT1 and PT2 constituted the c.5461-10T>C intronic variant and c.5603A>T hypomorphic variant in *ABCA4*. These variants were originally identified in these patients by our collaborators in RUMC using Haloplex sequencing. This is a high throughput, targeted sequencing approach at the gene of interest (*ABCA4)* that provides high read coverage and facilitates multiplexing of many patient samples to uncover variants causative in monogenic diseases (Bauwens *et al.*, 2015; Bauwens *et al.*, 2019b). The variants identified in the first sequencing event were shown to be complexed on one allele, resulting in monoallelicism of PT1 and PT2, which both showed strong clinical phenotypes of late-onset STGD1. PT1 and PT2 were thus recruited to our study for further investigation and resolution of their *ABCA4* genotype.

To appropriately filter the data to a more manageable and logical dataset, we filtered called variants on the vcf by their involvement in macular degeneration. As STGD1 is a macular degeneration, we wanted to rule out any potential phenocopies from other genes involved in maculopathies. We generated the macular disease gene panel for filtering the WGS data using a multitude of online resources including the macular dystrophy panel on Blueprint Genetics and Fulgent Genomics (https://blueprintgenetics.com/tests/panels/ophthalmology/macular-dystrophy-panel/) and (https://www.fulgentgenetics.com/Macular-Degeneration). In addition to several research articles investigating maculopathies with RNA-Seq data (Menon *et al.*, 2019; Cowan *et al.*, 2020). With this panel, we did not detect any promising causative variants in disease genes other than *ABCA4*. We also extended the panel to include genes involved in inherited retinopathies but this also did not reveal anything interesting. This

suggested that the patient phenotypes were indeed true STGD1 and due to mutations in the *ABCA4* gene.

With the WGS reads, we confirmed the presence of intronic variant c.5461-10T>C in both PT1 and PT2 in heterozygous state as previously reported. This was further validated in the Sanger sequencing traces which corresponded to overlapping peaks of the nucleotides T and C demonstrating heterozygosity at that allele. We also confirmed the presence of hypomorphic allele c.5603A>T in the same manner, which showed heterozygosity in PT2 as demonstrated by overlapping peaks of A and T nucleotides.

We were surprised to see that all reads on from the WGS contained the c.5603A>T mutation. This indicated homozygosity for this variant in PT1, instead of heterozygous state as previously reported. Sanger sequencing further confirmed this result with a single peak on the Sanger trace corresponding to the mutation change T>C. These results indicated resolution of the PT1 case with the full genotype as follows: **Allele 1**: c.[5461-10T>C, 5603A>T] and **Allele 2:** c.5603A>T.

In PT2, we identified an *ABCA4* variant that was not detected in the first round of DNA sequencing. The missense variant c.4685T>C was present in heterozygous state in both the WGS bam files and validated with Sanger sequencing. This variant has been reported previously on ClinVar with contradicting reports of pathogenicity, resulting in the reporting of this mutation as a variant of uncertain significance (VUS). This is likely due to the observation that c.4685T>C in homozygous state is not causative of disease and high MAF frequencies are observed in the general population with ExAC frequencies in European cohorts at 0.001305 versus allele frequencies in STGD1 cohorts as 0.00153 (Lee *et al.*, 2022b).

This recent publication from the Allikmets group in Columbia University has subsequently classified the c.4685T>C variant as a rare hypomorph, such that it its penetrance is only apparent when in combination with a null allele *in trans* (Lee *et al.*, 2022b). Following a discussion with Prof. Allikmets himself, he is in agreement that we have correctly resolved the *ABCA4* genotype of PT2 with compound heterozygote mutations: **Allele 1**: c.[5461-10T>C, 5603A>T] and **Allele 2:** c.4685T>C. However, we were unable to perform segregation analysis due to the inaccessibility of proband's familial DNA. We hoped to be able to phase the alleles using long-read RNA sequencing from PacBio but unfortunately the transcripts at that site

had low read depth for PT2, and we were unable to do so. Our collaborator has been able to inform the associated clinician of this outcome and segregation of the alleles will be performed locally in RUMC.

Hypomorphic variants are interesting and have only recently been identified as major contributors to *ABCA4*-mediated retinal disease. As observed in the c.4685T>C variant, hypomorphs are often classified as benign variants due to a high minor allele frequency (MAF) in the general population, masking any potential enrichment in STGD1 population. Their true pathogenic effect only becomes penetrant when they exist *in trans* with a null allele. When penetrant, these mutations often appear "clinically-dominant" irrespective of the mutation *in trans* such that the resulting phenotype is highly dependent on the hypomorph, more so than the other allele (Lee *et al.*, 2021).

One of the most frequently occurring hypomorphs in *ABCA4* is the c.5603A>T, p.Asn1868Ile mutation (Zernant *et al.*, 2017). Whilst *ABCA4* is known for its high degree of genetic polymorphism and harbours many missense variants with high MAF scores in the general population (Schmidt *et al.*, 2003), the c.5603A>T variant appears to be significantly enriched in STGD1 cohorts (20% STGD1 cohort vs 6.6% general population) (Maugeri *et al.*, 2002; Aguirre-Lamban *et al.*, 2011; Zernant *et al.*, 2017).

Slower disease progression is observed in individuals harbouring the c.5603A>T variant with resistance to autofluorescent lipofuscin fleck accumulation and a prevalence of foveal sparing (preservation of central retina structure and function). These so-called late-onset STGD1 cases typically present with visual defects within the fourth decade of life (Runhart *et al.*, 2018). This is in contrast to classical STGD1 cases which typically present within the first two decades (Tanna *et al.*, 2017).

The identification of c.5603A>T has resulted in the resolution of a large percentage of previously monoallelic cases (>50%) and ~80% of late-onset STGD1 in US populations (Zernant *et al.*, 2017). A similar study in Dutch populations confirm these findings but demonstrate that penetrance of the variant isn't just correlated on whether or not the mutation is present *in trans* to a deleterious allele. This is shown by the variable ages of onset even within familial cohorts with the same mutations, suggesting a potential for other genetic or environmental

modifiers such as gender in the penetrance of these alleles for ABCA4-mediated retinal disease (Runhart *et al.*, 2018).

Both PT1 and PT2 are cases of late onset STGD1 but are distinct from each other by the causality of c.5603A>T in disease pathogenesis. Despite carrying the same complex allele c.[5461-10T>C, 5603A>T] which is reported as a severe variant on its own (Green *et al.*, 2020), the true causality of c.5603A>T in STGD1 pathogenesis is observed only in PT1 where c.5603A>T was discovered in homozygous state. This fits with prognosis 1 of the updated genotype/phenotype correlation model (Lee *et al.*, 2022b). In contrast, the identifying accompanying allele of PT2 was a rare hypomorph which correlates more with Prognosis 2 in the updated model. This is interesting, as the iPSC-differentiated organoids displayed an enhanced degenerative phenotype in comparison with PT2.

During the analysis of WGS, a paper was published regarding the potential influence of *trans*-acting modifiers of ABCA4 disease (Zernant *et al.*, 2022). This paper found a link between individuals carrying the c.5603A>T p.Asn1868Ile variant and a common haplotype observed in *PRPH2*, a gene that frequently phenocopies STGD1. This EKG haplotype was increased by 12% in a genetically determined cohort where the c.5603A>T variant was causative of disease. It has been suggested that this haplotype further increases the penetrance of this allele, making consequential phenotypes more severe in patients. PT2 does not have true c.5603A>T penetrance as it is present only in complex with the c.5461-10T>C variant. The effects of *PRPH2* EKG haplotypes on resulting disease phenotypes could potentially explain why PT1 ROs have a stronger phenotype than that observed in PT2, despite the prognoses reported in updated genotype/phenotype correlations for genotypes of PT1 and PT2 suggesting otherwise. Whilst the connection between *PRPH2* and *ABCA4* is poorly understood, the authors of the study suggest the localisation of the proteins in the photoreceptor outer segment could have an indirect but additive effect in photoreceptor dysfunction, and that might underpin why mutations in both genes yield similar macular phenotypes in patients.

A rare variant in *ROM1* - c.353G>C, also appeared to be enriched in STGD1 patients (1.3% patients vs 0.3% controls) in their study. We observed the same variant in homozygous state in both PT1 and PT2 cases. No discernible differences were observed in cases with and without this variant in the study, however the rarity of the variant makes it difficult to truly

assess its impact on ACBA4 disease. Large cohorts are required to verify if any incremental additive effect consequence of *ROM1* variants exists in STGD1 pathology.

The resolution of PT1 and PT2 *ABCA4* genotypes was a key aim of this study. Whilst, we were satisfied by this outcome, we were surprised that the missing inheritance of both patients was resolved by missense variants in the coding regions of *ABCA4*. As mentioned, both patients underwent HaloPlex sequencing for the *ABCA4* locus by our collaborators and no additional causative variants were identified in *ABCA4*. This led us to believe that any potential variant in *ABCA4* must be in the non-coding regions of the gene, constituting a deep-intronic variant as previously described in the literature (Bauwens *et al.*, 2015; Sangermano *et al.*, 2019; Whelan *et al.*, 2023). Hence, we employed more advanced technologies such as WGS and LRS to increase our chances of capturing any RNA defect.

In hindsight, these sequencing strategies might have been 'overkill' for detecting missense *ABCA4* variants, regardless these experiments were not performed in vain. The WGS data was invaluable in the identification of *PRPH2* and *ROM1 trans*-acting modifiers in PT1 and PT2 samples and the LRS data was useful for exploring the functional effects of the c.5461-10T>C variant in RNA harvested from ROs of PT1 and PT2. This exploration further validated the STGD1 RO model for studying functional effects of *ABCA4* mutations.

The majority of STGD1 cases are resolved following genomic sequencing, with most causative mutations identified in the coding regions of the gene. However, a large proportion of cases (approximately 30%) remain genetically unsolved with either one or no mutations identified (Khan *et al.*, 2020b). A proportion of unsolved cases are likely due to mutations in the non-coding regions of the gene (Bauwens *et al.*, 2015; Bauwens *et al.*, 2019b; Khan *et al.*, 2020b; Whelan *et al.*, 2023). However, the investigation of these RNA defects is hampered by the restricted expression of *ABCA4* to photoreceptor cells in the retina. Retinal neurons have also been shown to demonstrate site-specific isoform expression (Murphy *et al.*, 2016), and so the requirement of physiologically relevant tissue is essential for studying the impact of RNA defects in STGD1 pathogenesis.

The common non-canonical splice site variant c.5461-10T>C illustrates this point perfectly. *In silico* analysis of this variant predicted a mild effect on the splicing efficiency of *ABCA4*. However, when investigated with RNA derived from iPSC-derived photoreceptor precursor

cells, a more pronounced effect with skipping of exon 39 and/or exon 40 was observed (Sangermano *et al.*, 2016). Whilst the LRS data did not identify any novel RNA defects in PT1 and PT2, we were able to investigate the detailed effects of this c.5461-10T>C variant in both cases with RNA resulting from matured ROs to validate the use of our model in the functional study of RNA defects in disease.

We were not expecting to observe transcripts containing the c.5461-10T>C variant but we did observe one read with the introns retained. The splicing events resulting from the mutation were visualised via Sashimi plot for PT1 and PT2, which displayed variable splicing effects with PSI scores for exon 39 - 0.55 for PT1 and 0.71 for PT2. Exon 40 was also impacted by the mutation with PSI scores 0.79 for PT1 and 0.71 for PT2.

We observed the c.5603A>T variant in all of the sequence reads from PT1. This is expected in PT1 as 50% of transcript is lost from the exon skipping induced by the c.5461-10T>C variant and the other 50% of the transcript contains the c.5603A>T variant. It was unexpected in PT2 however, as it carries the c.5603A>T variant in heterozygous state, and on the same allele as c.5461-10T>C variant. Exon 40 did appear to be retained in 79% of *ABCA4* transcripts in PT2 but this alone does not explain why the majority of reads contained the c.5603A>T variant. There is evidence to suggest that ASE is occurring in the PT2 case. High levels of ASE are observed in the CNS and in the retina (Aísa-Marín *et al.*, 2021). The degree of ASE could be influenced by the rare hypomorphic variant c.4685T>C in addition to the *trans*-acting *PRPH2* EKG haplotype and rare *ROM1* variants.

As the PT2 LRS sequences were degraded, we were unable to phase the alleles to confirm we have achieved biallelic resolution of this case. As aforementioned, segregation analysis on the proband's family members will be carried out locally to achieve this. Also due to this degradation, we could only investigate the effects on splicing from the c.5461-10T>C variant in PT1. We showed these alterations at gene, transcript and protein level by showing differences in UTRs shortening of the CDS and premature stop codon insertion. These results validated what was observed in the earlier studies using PPCs (Sangermano *et al.*, 2016) and demonstrate the reliability of ROs as a model for STGD1.

The necessity of a suitable model to study ABCA4-disease is exemplified by the limited therapeutic interventions available for this disease at present. To develop therapies, we first

need to understand the complete underlying pathomechanism and functional consequences of mutations in *ABCA4*. With regard to deep-intronic mutations, a relatively novel concept of AONs to silence splice-altering mutations via the generation and subsequent cleavage of double-stranded RNA molecules. The use of this technology has been demonstrated for several intronic *ABCA4* mutations so far (Albert *et al.*, 2018; Sangermano *et al.*, 2019) and most recently for the c.5461-10T>C variant where a 53% increase in correct *ABCA4* transcripts was achieved in ROs treated with a mutation-specific AON (Kaltak *et al.*, 2023b).

In summary, we identified the missing variants in PT1 and PT2 late-onset monoallelic cases. Resolution of PT1 was straight-forward with the identification of the c.5603A>T variant existing in homozygous and not heterozygous state. PT2 reveals a rare hypomorphic variant c.4685T>C which has been previously reported in ClinVar. We validated all mutations via Sanger sequencing and also some with LRS - facilitated through the PacBio IsoSeq platform. However, PT2's requires further confirmation by our collaborators in RUMC to ensure that c.4685T>C exists on the alternate allele. Both patients also carried the reported *trans*-acting modifier variants in *PRPH2* and *ROM1*, which could impact the severity of disease in both cases, but especially in PT1 where the *PRPH2* EKG haplotype is known to exert its affects mostly on the c.5603A>T hypomorphic variant. Whilst we are satisfied with the genetic outcomes for these STGD1 patients, a major limitation of the sequencing work is that all DNA and RNA was harvested from iPSC or iPSC-derived tissues. This was largely due to limited access to patient material at the time of the study. These results should be further validated in primary DNA from PT1 and PT2 probands. A segregation analysis with DNA from the proband's immediate family members will be carried out to ensure the variants are segregating with the disease and exist on separate alleles. These extra validation steps would significantly strengthen confidence in these results before providing a genetic diagnosis to the affected patients.

Chapter 6 General Discussion and Future Directions

STGD1 is the most common inherited maculopathy affecting up to 1 in 8,000 individuals globally. It is caused by mutations in the *ABCA4* gene – which encodes a protein crucial for the recycling of spent retinal molecules. Inefficient clearance of this waste results in a toxic build-up of bisretinoids and subsequent lipofuscin deposition in the retina, leading to degeneration of RPE cells and overlying photoreceptors in the macula (Tanna *et al.*, 2017). Individuals with STGD1 typically present with symptoms early in life, with deficits in high acuity central and chromatic vision, which progressively worsen over time. Despite this, there are currently no approved therapeutics to cure or alleviate this condition for those affected.

This is a common scenario across various IRDs. This group of blinding disorders stand as the primary cause of legal blindness in working-age individuals of the UK (Liew, Michaelides and Bunce, 2014). Characterised by the extensive allelic and phenotypic heterogeneity, each individual case of IRD has a relatively low occurrence rate. Such that, devising personalised therapeutics is near impossible, whilst universal therapeutic approaches to address all cases represents a significant challenge.

In 2017, a major breakthrough occurred when the first gene therapy for IRD received FDA approval for use in clinic. This momentous step forward offered much needed hope to patients and vision researchers alike. This therapy, Luxturna (voretigene neparvovec-rzyl), targets a cohort of patients with biallelic RPE65-mediated retinal disease (Smalley, 2017). In a gene supplementation strategy using adeno-associated viral (AAV) vectors, functional copies of *RPE65* are delivered to retinal cells to restore visual function. The first patient to receive this treatment in the UK was 23-year-old Jake Ternant. He received the life altering treatment in 2020 amidst the Covid-19 pandemic. In an interview with the BBC, he is reported saying - "Last year, for a lot of people was a dark and miserable year, but for me it was probably easily the best year of my life." (https://www.bbc.com/news/health-56906002). This emotive statement had undeniably inspired and reassured those living with inherited sight loss that advancements in medical science and technology has the potential to genuinely transform quality of life.

Regarding STGD1, gene supplementation strategies using AAVs similar to Luxturna are infeasible, largely due to the overall length of the *ABCA4* gene (128kb) and CDS (6.8kb). Phase

I/II clinical trials using lentiviral vectors instead (SAR422459 - EIAV-ABCA4)(ID: NCT01367444) have shown tolerance in treated patients but with variable results (Parker *et al.*, 2022). No significant improvement to vision were observed overall. A significant reduction in macular flecks was seen in one patient treated from the high-dose cohort. However, exacerbation of RPE atrophy was observed in 27% of treated eyes. The study has since been terminated.

Despite this, several other interventional clinical trials are active and ongoing on ClinicalTrials.gov for the treatment of STGD1. Ocugen is currently recruiting 42 participants for Phase I/II for its drug OCU410ST (ID: NCT05956626) which is an AAV serotype 5 capsid protein containing a gene construct encoding human retinoic acid receptor-related orphan receptor alpha (AAV5-h*RORA*). *RORA* encodes a nuclear hormone receptor that plays a pivotal role in various biological processes - such as photoreceptor development and maintenance, metabolism, phototransduction, inflammation and cell survival (Liu, Zou and Qin, 2017). This OCU410ST drug has been granted orphan drug approval by the FDA in April of this year (Press Release | Ocugen, 2023) on the basis of positive Phase I/II clinical results of their earlier product OCU400 for the treatment for RP and LCA, which has a similar strategy but instead encodes nuclear hormone receptor *NR2E3* (Li *et al.*, 2021). OCU400 was administered to 18 patients with RP via unilateral subretinal injection of AAV5-h*NR2E3* and 83% of patients demonstrated stabilisation or improvement of BCVA scores thereafter. Importantly, no OCU400-related serious adverse effects (SAE) were observed within low and medium dose cohorts (Hutton, 2023).

Phase I/II clinical trial for OCU410ST aims to assess safety and efficacy of subretinally delivered AAV5-h*RORA* in STGD1 patients. Primary outcome measures include changes in baseline BCVA, change in intraocular pressure (mmHg), safety and adverse events, ophthalmic safety screening using slit-lamp biomicroscopy, change of intensities in FAF and changes in ffERG responses. Pre-clinical animal models have shown the efficacy of this therapy in *ABCA4*$^{-/-}$ mice (Akula *et al.*, 2023) and so it will be exciting to see the results of these trials in human.

Nanoscope Therapeutics Inc. were also granted orphan drug approval for their proprietary gene-independent therapeutic strategy MCO-010 for the treatment of STGD1 (Press Release | NanoScope Therapeutics, 2023b). This follows from positive results from obtained from the Phase 2b RESTORE clinical trial of MCO-010 for the treatment of RP (ID: NCT04945772). MCO-

010 is an ambient-light activatable Multi-Characteristic Opsin (MCO) optogenetic therapy for vision restoration, irrespective of gene mutation. The objective is to re-sensitise retinal cells, improving vision for those affected by inherited retinopathies. The RESTORE trial treated 18 patients with advanced RP with unilateral intravitreal injection of MCO-010, in addition to 9 patients treated with sham control. All participants treated with MCO-010 demonstrated improvements to visual function compared with just 55.6% in placebo. MCO-010 was also well tolerated with no SAEs reported (Press Release | NanoScope Therapeutics, 2023a). Phase II STARLIGHT clinical trial (ID: NCT05417126) is currently underway for STGD1 having recruited 6 individuals. 6-month outcomes have recently been presented at the American Society of Retina Specialists in August (Press Release | NanoScope Therapeutics, 2023c) and demonstrate promising results including clinically meaningful improvements in BCVA, 3dB gain in mean visual field sensitivity, and importantly, no SAEs were observed.

The coming years hold great promise for individuals living with inherited sight loss. With a specific focus on addressing STGD1, patients can anticipate the availability of tailored therapeutic choices, enabling them to regain command over their vision. However, despite both of these therapeutic strategies being gene-independent approaches, a confirmed genetic diagnosis of STGD1 is still essential to enlist in these trials. This will most likely be the case for future therapeutics that are currently in development now.

This highlights the importance of obtaining a genetic diagnosis for inherited retinopathies, especially for conditions that do not yet have a cure. Over the last decade, research has been focused on uncovering all variation in the *ABCA4* gene. Generating better models that recapitulate features of human disease, whether *in vitro* or *in vivo,* has also been a key objective. Significant progress has been made in these endeavours, especially in genetic diagnoses, facilitated by the great advancements made in molecular genetic technology. Today, less than 5% of clinically diagnosed STGD1 patients remain genetically unresolved following *ABCA4* gene sequencing (Cremers *et al.*, 2020).

The identification of RNA defects and hypomorphs have drastically improved solve rates for STGD1 (Sangermano *et al.*, 2016; Zernant *et al.*, 2017; Albert *et al.*, 2018). However, the recent identification of gender imbalance for the penetrance of *ABCA4* hypomorphs (Runhart *et al.*, 2018), in addition to potentially *trans*-acting disease modifiers in *PRPH2* and *ROM1* (Zernant *et al.*, 2022) further complicates and challenges current views on STGD1 pathology

as a Mendelian monogenic disease. The missing inheritance in the remaining 5% of STGD1 diagnosed individuals, along with those constituting the resolved 95% of cases with a single pathogenic allele in *ABCA4* identified, are likely candidates for RNA defects and elusive hypomorphic alleles.

RNA defects and hypomorphic alleles alter gene expression patterns, complicating their detection and interpretation using DNA sequencing alone. A comprehensive approach, involving functional analysis at the DNA and RNA level, is required to elucidate their contribution to disease. As hypomorphic alleles tend to reduce gene activity, rather than cause complete loss of function - they are often miscategorised as benign polymorphisms. Their penetrance in disease is often conditional, such as existing in *trans* with a null allele (Zernant *et al.*, 2017) which is why RNA analysis is required to assess their impact on gene expression.

Similarly, it is difficult to identify RNA defects utilising DNA sequencing alone. Whilst splice prediction tools, such as Alumut or SpliceAI, can predict the putative effects of RNA defects, their accuracy varies (Sangermano *et al.*, 2016) – especially in the case of *ABCA4*, which is expressed specifically in the retina, a site that undergoes unique splicing programmes (Murphy *et al.*, 2016). This demonstrates the importance of utilising physiologically relevant RNA for validation and functional assessment of candidate RNA defects. This is challenging due to limited access to patient retinal tissue. Consequently, the creation of appropriate models capable of mimicking the observed splicing patterns in the human retina must be generated to study the effects of these variants in STDG1 pathology.

iPSC-derived ROs can be used to model STGD1 *in vitro*. ROs recapitulate the human retinal architecture *in vitro* with the presence of all key retinal neurons (Collin *et al.*, 2019). They have been shown to develop at similar rates to foetal retina and overlap in gene expression profiles (Cowan *et al.*, 2020) making them an excellent model to functionally assess RNA defects and hypomorphic alleles *in vitro*. In our study, PT1 and PT2 monoallelic cases were resolved following WGS. LRS of RNA isolated from matured STGD1-RO photoreceptors added value to the diagnosis by giving us unique insights into the expression patterns of *ABCA4* in both patients. An example can be seen with PT2 *ABCA4* transcripts which only displayed the c.5603A>T variant and not the rare hypomorph c.4685T>C - indicating the occurrence of ASE at this site. We were also able to validate the STGD1-ROs in their ability to recapitulate splicing

defects in PT1 consequential of the c.5461-10T>C deep intronic variant, as previously observed by 2D iPSC-PPC culture (Sangermano *et al.*, 2016).

Future directives to confirm this diagnosis of both PT1 and PT2 would encompass Sanger sequencing validation using primary cells from the patient, rather than DNA from iPSCs. Segregation analysis on the proband's family members would also add confidence to these genetic diagnoses by enabling the phasing of alleles to confirm compound heterozygosity, particularly in PT2, in addition to ensuring the pathogenic alleles segregate with disease. Only then, should the patients be informed of their genetic diagnosis and receive appropriate genetic counselling.

ROs have been used to model a myriad of retinal diseases. Our own group have demonstrated the utility of ROs in published works in the study of pre-mRNA processing factor (PRPF)-mediated RP (Buskin *et al.*, 2018; Georgiou *et al.*, 2022) and Retinoblastoma (Rozanska *et al.*, 2022). We also have ongoing projects involving the use of iPSC-ROs for DRAM2 and PROM1 – mediated maculopathies. In the last 5 years, we have demonstrated the high-throughput capabilities of this technology for *in vitro* toxicology and pharmacological intervention of disease - with an optimised 96 well plate culturing system (Hallam *et al.*, 2018) and the generation of defined protocols for specific photoreceptor subtype generation (Zerti *et al.*, 2020). A proof-of-principle toxicological study was recently published by our group demonstrating the fidelity of the model to reproduce and predict *in vivo* responses to different drugs known to be retinotoxic (Dorgau *et al.*, 2022).

This thesis describes the generation and characterisation of a STGD1-RO model that spans the phenotypic spectrum of ABCA4-disease – from late-onset STDG1 to more classic presentation. From our knowledge, this is the first study to characterise STGD1-ROs throughout their development and to identify a patient-specific defect correlating with ABCA4 disease severity. The implications of this model are significant, offering a platform to elucidate fundamental disease mechanisms, conduct drug screening and development, expedite pre-clinical studies with reduction to use of animal models, as well as understanding early transcriptomic signatures of disease to enable development of early intervention strategies for families with a genetic predisposition to STDG1.

In our model, cone photoreceptors were impacted in all cases ranging from mild to severe disease. Whilst rods were also affected in more severe genotypes, the consistent cone phenotype suggests a particular vulnerability of these cells to mutated *ABCA4*. A similar observation was reported in the literature over a decade ago in ABCA4-deficient mice (Conley *et al.*, 2012). This challenges the current view of STGD1 pathology, which hypothesises that photoreceptor degeneration is secondary to RPE loss in the macula – where RPE cell death is mediated through excessive lipofuscin accumulation from the inefficient clearance of toxic bisretinoid precursors from diurnally shed and phagocytosed photoreceptor outer segments. In STGD1 patients, death of cone photoreceptors has been postulated to precede RPE atrophy based on the observations made through AOSLO imaging, where regions devoid of cone photoreceptors still harbour visible RPE cells (Chen *et al.*, 2011; Song *et al.*, 2015). Given these findings, it would be interesting to test the functional output of cone photoreceptors in STGD1 ROs using multi-electrode arrays (MEAs) such as described in Dorgau *et al.* (2022) to see if cones are impacted on a functional level in a disease-specific manner.

It was affirming to observe a similar pattern of degeneration in our *in vitro* model. However, it was difficult to decipher the exact pathological mechanism underpinning photoreceptor retention in the ROs. There are several other factors that may have influenced this phenotype. One major factor to consider is the innate immaturity of photoreceptors in RO cultures, which are most comparable to photoreceptors at foetal day 110 (Sridhar *et al.*, 2020). The lack of apposing and functional RPE tissue could also influence the development of disease phenotype, considering that cell-autonomous defects have been observed with *in vitro* cultures of STGD1 RPE tissue (Farnoodian *et al.*, 2022). However, this is difficult to assess due to culturing limitations with the RO model. scRNAseq experiments have provided insights into altered transcriptional networks in STGD1-ROs with significant DEGs in pathways such as those involved in stress response. Similar transcriptomic effects have been published for other late-onset RO models of retinal disease (Gao *et al.*, 2020). The observed defects are likely outcomes of the increased stress of mutated genes commonly associated with retinal diseases, rather than being solely attributed to *ABCA4* mutation itself. With timing constraints following the Covid-19 pandemic, and consequential delays in the handing and processing of scRNA-Seq data, we could only perform limited validation of results. In our study, we focused primarily on transcriptomic data from photoreceptor clusters, however, we demonstrated

increased expression of proliferative markers in other clusters from the scRNAseq. Once such cluster includes Müller glia which play a key role in degenerative processes through the act of gliosis. Recent publications have shown that other cell types in diseased ROs such as Müller glia show early transcriptomic signals indicative of early activation of cell death (Leong *et al.*, 2022). Future experiments should focus on interrogating the influence of other cell types in the ROs on the overall STGD1 disease phenotype as the phenotype may not be restricted to just photoreceptor cells. Cell cycle defects and apoptotic gene expression signatures were of particular interest for this study. Future experiments would involve performing BD CycleTest on live STGD1-ROs to investigate differences in cell cycle stages. TUNEL assays, in addition to analysis of other cell death proteins, would be critical experiments to conduct in the endeavour to fully understand photoreceptor degeneration in STGD1. A recent paper reports the ability to test ABCA4 function using an ATPase-based assay (Kaltak *et al.*, 2023a). It would have been interesting to use a similar approach to see if we could determine the functional consequences of the mutations on ABCA4 activity, coupled with photoreceptor responses using electrophysiology to gain better insights into the impact of STGD1 on human retina.

In recent years, ABCA4 was found to also be expressed in endo-lysosomal membranes RPE cells in mice, although at a much lower abundance than in photoreceptor cells (Lenis *et al.*, 2018). Despite this, genetically modified mice that express mutant ABCA4 in photoreceptors but wild-type ABCA4 in RPE display partial rescue of disease. This suggests a significant proportion of STGD1 pathology comes from deficits in RPE tissue. It is unknown whether this would translate to the human *in vivo* scenario where the distribution and density of cone and rod photoreceptors differ significantly. However, this finding has spurred investigations using iPSC technology to derive human STGD1-RPE cells *in vitro* (Matynia *et al.*, 2022; Farnoodian *et al.*, 2022). In these models, reduced recycling of retinaldehydes following challenge with outer segments was observed (Ng *et al.*, 2022). Further to this, higher levels of levels of lipofuscin were detected in STGD1-RPE upon the addition of bovine retinal extracts. Such accumulation was shown to trigger the activity of complement C3 activity leading to membrane attack complex (MAC) deposition and subsequent RPE cell death implicating complement dysregulation in STGD1 pathology. Similar results were observed in the Farnoodian study, with reduced photoreceptor outer segment phagocytosis by iPSC-RPE, in addition to lipid handling defects (Farnoodian *et al.*, 2022). In both of these studies, these

defects occurred autonomously to photoreceptor cells, indicating that ABCA4-deficient RPE is capable of recapitulating features of human STGD1 autonomously.

The probable *in vivo* situation encompasses the presence of both ABCA4-deficient photoreceptors and RPE cells. Nevertheless, evaluating this scenario *in vitro* presents challenges due to the absence of functional RPE in STGD1-RO differentiations. A significant contributing factor to this is the distinct culturing formats of these tissues. While ROs adopt a spheroidal shape and are cultured in suspension, RPE cells form a 2D monolayer. Co-grafts of hESC-derived ROs and RPE have been developed for the purpose of complete retinal replacement in mice with retinal degeneration. Transplanted tissue survived long-term in the subretinal space of transplanted mice demonstrating successful integration into host retina followed by the generation of new photoreceptors and neuronal processes (Thomas *et al.*, 2021). One promising direction for advancing our understanding of STGD1 pathology and improving *in vitro* disease modelling of macular diseases in general, is to generate co-cultures of iPSC-derived RO and RPE similar to the aforementioned approach to gain valuable insights into the interplay between photoreceptors and RPE in the context of ABCA4-disease.

Our own group has adopted the strategy of differentiating disease-specific iPSCs to RO and RPE in tandem to assess how the disease manifests in both tissues autonomously (Buskin *et al.*, 2018; Georgiou *et al.*, 2022; Rozanska *et al.*, 2022; Cerna-Chavez *et al.*, 2023). Whilst there are publications characterising iPSC-derived STGD1-RPE (Ng *et al.*, 2022; Farnoodian *et al.*, 2022), none of them explore genotypic/phenotypic correlations as such in our study with iPSC-ROs. A major future directive of this study would be to address this gap in knowledge utilising the same cohort of patients in this study. Ideally with both RO and RPE differentiations occurring in parallel to fully assess genotype/phenotype correlations in both tissues. Further to this, it would be important to include more patient cases that span the full updated spectrum of the genotype/phenotype correlation by the Allikmets group (Lee *et al.*, 2022b) to confidently demonstrate these correlations *in vitro* with iPSC-derived ROs and RPE.

Recent modifications to RO differentiation protocols have shown that supplementation with antioxidants and BSA-bound fatty acids supports the development of photoreceptor outer segments (West *et al.*, 2022). This allows for improved outer segment formation with organised stacks. ROs from this protocol also appear to express outer segments in higher abundance than those in our study. Supplementation to our own protocols with these factors

could facilitate outer segment collection from STGD1-ROs for subsequent feeding to iPSC-RPE, aiming to mimic the visual cycle *in vitro*. It would be interesting to see if this would exacerbate disease in the iPSC-RPE model.

Overall, the results generated through this research provide invaluable insights into the intricate pathology of STGD1. Our study has provided genetic resolution to previously monoallelic cases of STGD1, which enables those individuals to enlist in clinical trials for treatments in development. We have developed a model with a quantifiable phenotypic defect in photoreceptors in a culture of neurosensory retina only. An emphasis on cone photoreceptor vulnerability was observed and no previous reports of such defect have been made. We show that genotype-phenotype correlations are possible *in vitro*, with mutation-induced molecular pathology, making this model incredibly important for drug development, *in vitro* toxicology and further disease modelling. The development and characterisation of the STGD1-RO model offer a significant leap forward in our understanding of this condition, enabling us to better dissect its underlying mechanisms in greater detail. As we continue to unravel the complexities of STGD1 through this innovative model, we not only advance the scientific understanding of the disease but also pave the way for facilitating the development of more targeted and effective therapeutic interventions. Ultimately, this research holds great promise for the future of STGD1 patients, offering them renewed hope for improved diagnosis, treatment and most importantly, a better quality of life.

Bibliography

1) Aasen, T., et al. (2008) 'Efficient and rapid generation of induced pluripotent stem cells from human keratinocytes', *Nature Biotechnology,* 26(11), pp. 1276-1284.
2) Achberger, K., et al. (2019) 'Merging organoid and organ-on-a-chip technology to generate complex multi-layer tissue models in a human retina-on-a-chip platform', *eLife,* 8, pp. e46188.
3) Aguirre-Lamban, J., et al. (2011) 'Further associations between mutations and polymorphisms in the ABCA4 gene: clinical implication of allelic variants and their role as protector/risk factors', *Invest Ophthalmol Vis Sci,* 52(9), pp. 6206-12.
4) Aísa-Marín, I., García-Arroyo, R., Mirra, S. and Marfany, G. (2021) 'The Alter Retina: Alternative Splicing of Retinal Genes in Health and Disease', *Int J Mol Sci,* 22(4).
5) Akula, M., McNamee, S., Chan, N. P. M., DeAngelis, M. M. and Haider, N. B. (2023) 'RORA Modifier Gene Therapy Rescues Retinal Degeneration in a Juvenile AMD Mouse Model of Stargardt Disease', *Investigative Ophthalmology & Visual Science,* 64(8), pp. 3842-3842.
6) Al Gwairi, O., Thach, L., Zheng, W., Osman, N. and Little, P. J. (2016) 'Cellular and Molecular Pathology of Age-Related Macular Degeneration: Potential Role for Proteoglycans', *J Ophthalmol,* 2016, pp. 2913612.
7) Albert, S., et al. (2018) 'Identification and Rescue of Splice Defects Caused by Two Neighboring Deep-Intronic ABCA4 Mutations Underlying Stargardt Disease', *The American Journal of Human Genetics,* 102(4), pp. 517-527.
8) Allikmets, R., et al. (1997a) 'Mutation of the Stargardt disease gene (ABCR) in age-related macular degeneration', *Science,* 277(5333), pp. 1805-7.
9) Allikmets, R., et al. (1997b) 'A photoreceptor cell-specific ATP-binding transporter gene (ABCR) is mutated in recessive Stargardt macular dystrophy', *Nat Genet,* 15(3), pp. 236-46.
10) Amps, K., et al. (2011) 'Screening ethnically diverse human embryonic stem cells identifies a chromosome 20 minimal amplicon conferring growth advantage', *Nat Biotechnol,* 29(12), pp. 1132-44.
11) Anokye-Danso, F., et al. (2011) 'Highly efficient miRNA-mediated reprogramming of mouse and human somatic cells to pluripotency', *Cell Stem Cell,* 8(4), pp. 376-88.
12) Arık, Y. B., et al. (2021) 'Microfluidic organ-on-a-chip model of the outer blood-retinal barrier with clinically relevant read-outs for tissue permeability and vascular structure', *Lab Chip,* 21(2), pp. 272-283.
13) Bai, H., Chen, K., Gao, Y.-X., Arzigian, M., Xie, Y.-L., Malcosky, C., Yang, Y.-G., Wu, W.-S. and Wang, Z. Z. (2012) 'Bcl-xL enhances single-cell survival and expansion of human embryonic stem cells without affecting self-renewal', *Stem Cell Research,* 8(1), pp. 26-37.
14) Bai, Q., Ramirez, J. M., Becker, F., Pantesco, V., Lavabre-Bertrand, T., Hovatta, O., Lemaître, J. M., Pellestor, F. and De Vos, J. (2015) 'Temporal analysis of genome alterations induced by single-cell passaging in human embryonic stem cells', *Stem Cells Dev,* 24(5), pp. 653-62.
15) Ban, H., et al. (2011) 'Efficient generation of transgene-free human induced pluripotent stem cells (iPSCs) by temperature-sensitive Sendai virus vectors', *Proceedings of the National Academy of Sciences,* 108(34), pp. 14234-14239.
16) Bar-Nur, O., Russ, Holger A., Efrat, S. and Benvenisty, N. (2011) 'Epigenetic Memory and Preferential Lineage-Specific Differentiation in Induced Pluripotent Stem Cells Derived from Human Pancreatic Islet Beta Cells', *Cell Stem Cell,* 9(1), pp. 17-23.

17) Bassett, A. R. (2017) 'Editing the genome of hiPSC with CRISPR/Cas9: disease models', *Mammalian Genome,* 28(7), pp. 348-364.
18) Bauwens, M., et al. (2015) 'An augmented ABCA4 screen targeting noncoding regions reveals a deep intronic founder variant in Belgian Stargardt patients', *Hum Mutat,* 36(1), pp. 39-42.
19) Bauwens, M., et al. (2019a) 'ABCA4-associated disease as a model for missing heritability in autosomal recessive disorders: novel noncoding splice, cis-regulatory, structural, and recurrent hypomorphic variants', *Genet Med,* 21(8), pp. 1761-1771.
20) Bauwens, M., et al. (2019b) 'ABCA4-associated disease as a model for missing heritability in autosomal recessive disorders: novel noncoding splice, cis-regulatory, structural, and recurrent hypomorphic variants', *Genetics in Medicine,* 21(8), pp. 1761-1771.
21) Ben-Yosef, T. (2022) 'Inherited Retinal Diseases', *Int J Mol Sci,* 23(21).
22) Blacharski (1988) 'Fundus flavimaculatus', *Retinal dystrophies and degenerations*, pp. 135-159.
23) Bohrer, L. R., et al. (2023) 'Automating iPSC generation to enable autologous photoreceptor cell replacement therapy', *Journal of Translational Medicine,* 21(1), pp. 161.
24) Boughman, J. A., Vernon, M. and Shaver, K. A. (1983) 'Usher syndrome: definition and estimate of prevalence from two high-risk populations', *J Chronic Dis,* 36(8), pp. 595-603.
25) Boulton, M. and Dayhaw-Barker, P. (2001) 'The role of the retinal pigment epithelium: Topographical variation and ageing changes', *Eye,* 15(3), pp. 384-389.
26) Braun, T. A., et al. (2013) 'Non-exomic and synonymous variants in ABCA4 are an important cause of Stargardt disease', *Hum Mol Genet,* 22(25), pp. 5136-45.
27) Bronstein, R., et al. (2019) 'A combined RNA-seq and whole genome sequencing approach for identification of non-coding pathogenic variants in single families', *bioRxiv*, pp. 766717.
28) Buck, T. M., et al. (2023) 'CRB1 is required for recycling by RAB11A+ vesicles in human retinal organoids', *Stem Cell Reports,* 18(9), pp. 1793-1810.
29) Burke, T. R., et al. (2014) 'Quantitative fundus autofluorescence in recessive Stargardt disease', *Investigative ophthalmology & visual science,* 55(5), pp. 2841-2852.
30) Burke, T. R., Tsang, S. H., Zernant, J., Smith, R. T. and Allikmets, R. (2012) 'Familial discordance in Stargardt disease', *Molecular vision,* 18, pp. 227-233.
31) Burke, T. R., Yzer, S., Zernant, J., Smith, R. T., Tsang, S. H. and Allikmets, R. (2013) 'Abnormality in the external limiting membrane in early Stargardt Disease', *Ophthalmic Genetics,* 34(1-2), pp. 75-77.
32) Buskin, A., et al. (2018) 'Disrupted alternative splicing for genes implicated in splicing and ciliogenesis causes PRPF31 retinitis pigmentosa', *Nature Communications,* 9(1), pp. 4234.
33) Cantor, E. L., Shen, F., Jiang, G., Tan, Z., Cunningham, G. M., Wu, X., Philips, S. and Schneider, B. P. (2022) 'Passage number affects differentiation of sensory neurons from human induced pluripotent stem cells', *Scientific Reports,* 12(1), pp. 15869.
34) Capowski, E. E., et al. (2019) 'Reproducibility and staging of 3D human retinal organoids across multiple pluripotent stem cell lines', *Development,* 146(1).
35) Carss, K. J., et al. (2017) 'Comprehensive rare variant analysis via whole-genome sequencing to determine the molecular pathology of inherited retinal disease', *The American Journal of Human Genetics,* 100(1), pp. 75-90.

36) Cella, W., Greenstein, V. C., Zernant-Rajang, J., Smith, T. R., Barile, G., Allikmets, R. and Tsang, S. H. (2009) 'G1961E mutant allele in the Stargardt disease gene ABCA4 causes bull's eye maculopathy', *Exp Eye Res,* 89(1), pp. 16-24.
37) Cerna-Chavez, R., Rozanska, A., Poretti, G. L., Benvenisty, N., Parulekar, M. and Lako, M. (2023) 'Retinal pigment epithelium exhibits gene expression and phagocytic activity alterations when exposed to retinoblastoma chemotherapeutics', *Experimental Eye Research,* 233, pp. 109542.
38) Chahine Karam, F., et al. (2022) 'Human iPSC-Derived Retinal Organoids and Retinal Pigment Epithelium for Novel Intronic RPGR Variant Assessment for Therapy Suitability', *J Pers Med,* 12(3).
39) Chambers, I. and Tomlinson, S. R. (2009) 'The transcriptional foundation of pluripotency', *Development,* 136(14), pp. 2311-22.
40) Chan, E. M., et al. (2009) 'Live cell imaging distinguishes bona fide human iPS cells from partially reprogrammed cells', *Nat Biotechnol,* 27(11), pp. 1033-7.
41) Chapot, C. A., Euler, T. and Schubert, T. (2017) 'How do horizontal cells 'talk' to cone photoreceptors? Different levels of complexity at the cone-horizontal cell synapse', *J Physiol,* 595(16), pp. 5495-5506.
42) Charbel Issa, P., Barnard, A. R., Singh, M. S., Carter, E., Jiang, Z., Radu, R. A., Schraermeyer, U. and MacLaren, R. E. (2013) 'Fundus Autofluorescence in the Abca4−/− Mouse Model of Stargardt Disease—Correlation With Accumulation of A2E, Retinal Function, and Histology', *Investigative Ophthalmology & Visual Science,* 54(8), pp. 5602-5612.
43) Chaya, T., Matsumoto, A., Sugita, Y., Watanabe, S., Kuwahara, R., Tachibana, M. and Furukawa, T. (2017) 'Versatile functional roles of horizontal cells in the retinal circuit', *Scientific Reports,* 7(1), pp. 5540.
44) Chen, L., Lee, W., de Carvalho, J. R. L., Jr., Chang, S., Tsang, S. H., Allikmets, R. and Sparrow, J. R. (2019) 'Multi-platform imaging in ABCA4-Associated Disease', *Sci Rep,* 9(1), pp. 6436.
45) Chen, Y., Ratnam, K., Sundquist, S. M., Lujan, B., Ayyagari, R., Gudiseva, V. H., Roorda, A. and Duncan, J. L. (2011) 'Cone Photoreceptor Abnormalities Correlate with Vision Loss in Patients with Stargardt Disease', *Investigative Ophthalmology & Visual Science,* 52(6), pp. 3281-3292.
46) Chichagova, V., et al. (2023) 'Incorporating microglia-like cells in human induced pluripotent stem cell-derived retinal organoids', *J Cell Mol Med,* 27(3), pp. 435-445.
47) Chichagova, V., Hilgen, G., Ghareeb, A., Georgiou, M., Carter, M., Sernagor, E., Lako, M. and Armstrong, L. (2020) 'Human iPSC differentiation to retinal organoids in response to IGF1 and BMP4 activation is line- and method-dependent', *Stem Cells,* 38(2), pp. 195-201.
48) Chichagova, V., Sanchez-Vera, I., Armstrong, L., Steel, D. and Lako, M. (2016) 'Generation of Human Induced Pluripotent Stem Cells Using RNA-Based Sendai Virus System and Pluripotency Validation of the Resulting Cell Population', in Nagy, A. and Turksen, K. (eds.) *Patient-Specific Induced Pluripotent Stem Cell Models: Generation and Characterization*. New York, NY: Springer New York, pp. 285-307.
49) Cho, H.-J., et al. (2010) 'Induction of pluripotent stem cells from adult somatic cells by protein-based reprogramming without genetic manipulation', *Blood,* 116(3), pp. 386-395.
50) Choi, I. Y., Lim, H. and Lee, G. (2014) 'Efficient generation human induced pluripotent stem cells from human somatic cells with Sendai-virus', *J Vis Exp,* (86).
51) Cideciyan, A. V., Swider, M., Schwartz, S. B., Stone, E. M. and Jacobson, S. G. (2015) 'Predicting Progression of ABCA4-Associated Retinal Degenerations Based on Longitudinal

Measurements of the Leading Disease Front', *Invest Ophthalmol Vis Sci,* 56(10), pp. 5946-55.

52) Collin, J., et al. (2023) 'Single-cell RNA sequencing reveals transcriptional changes of human choroidal and retinal pigment epithelium cells during fetal development, in healthy adult and intermediate age-related macular degeneration', *Human Molecular Genetics,* 32(10), pp. 1698-1710.
53) Collin, J., Queen, R., Zerti, D., Dorgau, B., Hussain, R., Coxhead, J., Cockell, S. and Lako, M. (2019) 'Deconstructing Retinal Organoids: Single Cell RNA-Seq Reveals the Cellular Components of Human Pluripotent Stem Cell-Derived Retina', *STEM CELLS,* 37(5), pp. 593-598.
54) Conley, S. M., Cai, X., Makkia, R., Wu, Y., Sparrow, J. R. and Naash, M. I. (2012) 'Increased cone sensitivity to ABCA4 deficiency provides insight into macular vision loss in Stargardt's dystrophy', *Biochim Biophys Acta,* 1822(7), pp. 1169-79.
55) Cooke, J. A., et al. (2023) 'Propensity of Patient-Derived iPSCs for Retinal Differentiation: Implications for Autologous Cell Replacement', *Stem Cells Translational Medicine,* 12(6), pp. 365-378.
56) Cornelis, S. S., Bax, N. M., Zernant, J., Allikmets, R., Fritsche, L. G., den Dunnen, J. T., Ajmal, M., Hoyng, C. B. and Cremers, F. P. (2017) 'In Silico Functional Meta-Analysis of 5,962 ABCA4 Variants in 3,928 Retinal Dystrophy Cases', *Hum Mutat,* 38(4), pp. 400-408.
57) Cowan, C. S., et al. (2020) 'Cell Types of the Human Retina and Its Organoids at Single-Cell Resolution', *Cell,* 182(6), pp. 1623-1640.e34.
58) Cremers, F. P. M., Lee, W., Collin, R. W. J. and Allikmets, R. (2020) 'Clinical spectrum, genetic complexity and therapeutic approaches for retinal disease caused by ABCA4 mutations', *Progress in Retinal and Eye Research,* 79, pp. 100861.
59) Cremers, F. P. M., et al. (1998) 'Autosomal Recessive Retinitis Pigmentosa and Cone-rod Dystrophy Caused by Splice Site Mutations in the Stargardt's Disease Gene ABCR', *Human Molecular Genetics,* 7(3), pp. 355-362.
60) Cuenca, N., Fernández-Sánchez, L., Campello, L., Maneu, V., De la Villa, P., Lax, P. and Pinilla, I. (2014) 'Cellular responses following retinal injuries and therapeutic approaches for neurodegenerative diseases', *Progress in Retinal and Eye Research,* 43, pp. 17-75.
61) Cukras, C. A., Wong, W. T., Caruso, R., Cunningham, D., Zein, W. and Sieving, P. A. (2012) 'Centrifugal Expansion of Fundus Autofluorescence Patterns in Stargardt Disease Over Time', *Archives of Ophthalmology,* 130(2), pp. 171-179.
62) Curcio, C. A., Sloan, K. R., Kalina, R. E. and Hendrickson, A. E. (1990) 'Human photoreceptor topography', *J Comp Neurol,* 292(4), pp. 497-523.
63) D'Antonio, M., et al. (2018) 'Insights into the Mutational Burden of Human Induced Pluripotent Stem Cells from an Integrative Multi-Omics Approach', *Cell Reports,* 24(4), pp. 883-894.
64) Damjanov, I. and Solter, D. (1974) 'Experimental teratoma', *Curr Top Pathol,* 59, pp. 69-130.
65) De Angeli, P., Reuter, P., Hauser, S., Schöls, L., Stingl, K., Wissinger, B. and Kohl, S. (2022) 'Effective splicing restoration of a deep-intronic ABCA4 variant in cone photoreceptor precursor cells by CRISPR/SpCas9 approaches', *Molecular Therapy - Nucleic Acids,* 29, pp. 511-524.
66) de la Fuente, L., et al. (2020) 'tappAS: a comprehensive computational framework for the analysis of the functional impact of differential splicing', *Genome Biology,* 21(1), pp. 119.

67) De Masi, C., Spitalieri, P., Murdocca, M., Novelli, G. and Sangiuolo, F. (2020) 'Application of CRISPR/Cas9 to human-induced pluripotent stem cells: from gene editing to drug discovery', *Human Genomics,* 14(1), pp. 25.
68) Del Pozo-Valero, M., et al. (2022) 'Impact of next generation sequencing in unraveling the genetics of 1036 Spanish families with inherited macular dystrophies', *Investigative Ophthalmology & Visual Science,* 63(2), pp. 11-11.
69) Dewing, J. M., Lotery, A. J. and Ratnayaka, J. A. (2023) 'The disparity between funding for eye research vs. the high cost of sight-loss in the UK', *Eye,* 37(4), pp. 584-586.
70) Diaz-Aguilar, M., Choi, J., Min, H., Lee, E.-J., Grandjean, J. M. D., Kroeger, H., Wiseman, R. L. and Lin, J. (2022) 'Achromatopsia Retinal Organoid Transcriptomes Reveal Increased Gliosis and Dysregulation of Unfolded Protein Response', *Investigative Ophthalmology & Visual Science,* 63(7), pp. 1471-1471.
71) Dockery, A., Stephenson, K., Keegan, D., Wynne, N., Silvestri, G., Humphries, P., Kenna, P. F., Carrigan, M. and Farrar, G. J. (2017) 'Target 5000: Target Capture Sequencing for Inherited Retinal Degenerations', *Genes (Basel),* 8(11).
72) Dorgau, B., et al. (2023) 'Deciphering the spatio-temporal transcriptional and chromatin accessibility of human retinal organoid development at the single cell level', *bioRxiv*, pp. 2023.07.19.549507.
73) Dorgau, B., et al. (2019) 'Decellularised extracellular matrix-derived peptides from neural retina and retinal pigment epithelium enhance the expression of synaptic markers and light responsiveness of human pluripotent stem cell derived retinal organoids', *Biomaterials,* 199, pp. 63-75.
74) Dorgau, B., et al. (2022) 'Human Retinal Organoids Provide a Suitable Tool for Toxicological Investigations: A Comprehensive Validation Using Drugs and Compounds Affecting the Retina', *Stem Cells Translational Medicine,* 11(2), pp. 159-177.
75) Eid, J., et al. (2009) 'Real-time DNA sequencing from single polymerase molecules', *Science,* 323(5910), pp. 133-8.
76) Eiraku, M., Takata, N., Ishibashi, H., Kawada, M., Sakakura, E., Okuda, S., Sekiguchi, K., Adachi, T. and Sasai, Y. (2011a) 'Self-organizing optic-cup morphogenesis in three-dimensional culture', *Nature,* 472(7341), pp. 51-56.
77) Eiraku, M., Takata, N., Ishibashi, H., Kawada, M., Sakakura, E., Okuda, S., Sekiguchi, K., Adachi, T. and Sasai, Y. (2011b) 'Self-organizing optic-cup morphogenesis in three-dimensional culture', *Nature,* 472(7341), pp. 51-6.
78) Eldred, K. C., et al. (2018) 'Thyroid hormone signalling specifies cone subtypes in human retinal organoids', *Science,* 362(6411), pp. eaau6348.
79) Ergun, E., et al. (2005) 'Assessment of central visual function in Stargardt's disease/fundus flavimaculatus with ultrahigh-resolution optical coherence tomography', *Invest Ophthalmol Vis Sci,* 46(1), pp. 310-6.
80) Euler, T., Haverkamp, S., Schubert, T. and Baden, T. (2014) 'Retinal bipolar cells: elementary building blocks of vision', *Nature Reviews Neuroscience,* 15(8), pp. 507-519.
81) Evans, M. J. and Kaufman, M. H. (1981) 'Establishment in culture of pluripotential cells from mouse embryos', *Nature,* 292(5819), pp. 154-156.
82) Fan, J., et al. (2020) 'A simplified system for the effective expression and delivery of functional mature microRNAs in mammalian cells', *Cancer Gene Therapy,* 27(6), pp. 424-437.
83) Farkas, M. H., Lew, D. S., Sousa, M. E., Bujakowska, K., Chatagnon, J., Bhattacharya, S. S., Pierce, E. A. and Nandrot, E. F. (2014) 'Mutations in pre-mRNA processing factors 3, 8, and

31 cause dysfunction of the retinal pigment epithelium', *Am J Pathol,* 184(10), pp. 2641-52.
84) Farnoodian, M., et al. (2022) 'Cell-autonomous lipid-handling defects in Stargardt iPSC-derived retinal pigment epithelium cells', *Stem Cell Reports,* 17(11), pp. 2438-2450.
85) Felemban, M., et al. (2018) 'Extracellular matrix component expression in human pluripotent stem cell-derived retinal organoids recapitulates retinogenesis in vivo and reveals an important role for IMPG1 and CD44 in the development of photoreceptors and interphotoreceptor matrix', *Acta Biomaterialia,* 74, pp. 207-221.
86) Flamier, A., Barabino, A. and Bernier, G. (2016) 'Differentiation of human embryonic stem cells into cone photoreceptors', *Bio-protocol,* 6(14), pp. e1870-e1870.
87) Forrester, J. V., Dick, A. D., McMenamin, P. G., Roberts, F. and Pearlman, E. (2016) 'Chapter 1 - Anatomy of the eye and orbit', in Forrester, J.V., Dick, A.D., McMenamin, P.G., Roberts, F. and Pearlman, E. (eds.) *The Eye (Fourth Edition)*: W.B. Saunders, pp. 1-102.e2.
88) Gao, M. L., Lei, X. L., Han, F., He, K. W., Jin, S. Q., Zhang, Y. Y. and Jin, Z. B. (2020) 'Patient-Specific Retinal Organoids Recapitulate Disease Features of Late-Onset Retinitis Pigmentosa', *Front Cell Dev Biol,* 8, pp. 128.
89) Garber, K. (2015) 'RIKEN suspends first clinical trial involving induced pluripotent stem cells', *Nature Biotechnology,* 33(9), pp. 890-891.
90) Garrido-Martín, D., Palumbo, E., Guigó, R. and Breschi, A. (2018) 'ggsashimi: Sashimi plot revised for browser- and annotation-independent splicing visualization', *PLoS Comput Biol,* 14(8), pp. e1006360.
91) Georgiou, M., et al. (2022) 'Activation of autophagy reverses progressive and deleterious protein aggregation in PRPF31 patient-induced pluripotent stem cell-derived retinal pigment epithelium cells', *Clinical and Translational Medicine,* 12(3), pp. e759.
92) Ghinia Tegla, M. G., Buenaventura, D. F., Kim, D. Y., Thakurdin, C., Gonzalez, K. C. and Emerson, M. M. (2020) 'OTX2 represses sister cell fate choices in the developing retina to promote photoreceptor specification', *Elife,* 9.
93) Ghosh, Z., Wilson, K. D., Wu, Y., Hu, S., Quertermous, T. and Wu, J. C. (2010) 'Persistent Donor Cell Gene Expression among Human Induced Pluripotent Stem Cells Contributes to Differences with Human Embryonic Stem Cells', *PLOS ONE,* 5(2), pp. e8975.
94) Giacomelli, E., et al. (2020) 'Human-iPSC-derived cardiac stromal cells enhance maturation in 3D cardiac microtissues and reveal non-cardiomyocyte contributions to heart disease', *Cell stem cell,* 26(6), pp. 862-879. e11.
95) Gonzalez-Cordero, A., et al. (2017) 'Recapitulation of Human Retinal Development from Human Pluripotent Stem Cells Generates Transplantable Populations of Cone Photoreceptors', *Stem Cell Reports,* 9(3), pp. 820-837.
96) Gonzalez-Cordero, A., et al. (2013) 'Photoreceptor precursors derived from three-dimensional embryonic stem cell cultures integrate and mature within adult degenerate retina', *Nature biotechnology,* 31(8), pp. 741-747.
97) Gonzalez-Garay, M. L. (2016) 'Introduction to Isoform Sequencing Using Pacific Biosciences Technology (Iso-Seq)', in Wu, J. (ed.) *Transcriptomics and Gene Regulation*. Dordrecht: Springer Netherlands, pp. 141-160.
98) Gozlan, S., et al. (2023) 'Bankable human iPSC-derived retinal progenitors represent a valuable source of multipotent cells', *Communications Biology,* 6(1), pp. 762.
99) Green, J. S., et al. (2020) 'The genetic architecture of Stargardt macular dystrophy (STGD1): a longitudinal 40-year study in a genetic isolate', *Eur J Hum Genet,* 28(7), pp. 925-937.

100) Guo, Y., et al. (2019) 'Modeling Retinitis Pigmentosa: Retinal Organoids Generated From the iPSCs of a Patient With the USH2A Mutation Show Early Developmental Abnormalities', *Frontiers in Cellular Neuroscience,* 13.
101) Haeseleer, F., Huang, J., Lebioda, L., Saari, J. C. and Palczewski, K. (1998) 'Molecular characterization of a novel short-chain dehydrogenase/reductase that reduces all-trans-retinal', *J Biol Chem,* 273(34), pp. 21790-9.
102) Hallam, D., et al. (2018) 'Human-Induced Pluripotent Stem Cells Generate Light Responsive Retinal Organoids with Variable and Nutrient-Dependent Efficiency', *Stem Cells,* 36(10), pp. 1535-1551.
103) Hartong, D. T., Berson, E. L. and Dryja, T. P. (2006) 'Retinitis pigmentosa', *Lancet,* 368(9549), pp. 1795-809.
104) Heavner, W. and Pevny, L. (2012) 'Eye development and retinogenesis', *Cold Spring Harb Perspect Biol,* 4(12).
105) Henly, C. (2021) *Foundations of Neuroscience.* Michigan, USA: Michigan State University Libraries.
106) Hinrichs, A. S., et al. (2006) 'The UCSC Genome Browser Database: update 2006', *Nucleic Acids Res,* 34(Database issue), pp. D590-8.
107) Hodgson, J. G., Chin, K., Collins, C. and Gray, J. W. (2003) 'Genome amplification of chromosome 20 in breast cancer', *Breast cancer research and treatment,* 78, pp. 337-345.
108) Hu, B.-Y., Weick, J. P., Yu, J., Ma, L.-X., Zhang, X.-Q., Thomson, J. A. and Zhang, S.-C. (2010) 'Neural differentiation of human induced pluripotent stem cells follows developmental principles but with variable potency', *Proceedings of the National Academy of Sciences,* 107(9), pp. 4335-4340.
109) Huang, K.-C., et al. (2019) 'Morphological and molecular defects in human three-dimensional retinal organoid model of X-linked juvenile retinoschisis', *Stem Cell Reports,* 13(5), pp. 906-923.
110) Hussein, S. M., et al. (2011) 'Copy number variation and selection during reprogramming to pluripotency', *Nature,* 471(7336), pp. 58-62.
111) Hutton, D. 2023. Ocugen announces positive clinical study update from the phase 1/2 trial of OCU400. *Ophthalmology Times.*
112) Illing, M., Molday, L. L. and Molday, R. S. (1997) 'The 220-kDa rim protein of retinal rod outer segments is a member of the ABC transporter superfamily', *J Biol Chem,* 272(15), pp. 10303-10.
113) Jaakson, K., et al. (2003) 'Genotyping microarray (gene chip) for the ABCR (ABCA4) gene', *Hum Mutat,* 22(5), pp. 395-403.
114) Jia, F., et al. (2010) 'A nonviral minicircle vector for deriving human iPS cells', *Nat Methods,* 7(3), pp. 197-9.
115) Jinek, M., Chylinski, K., Fonfara, I., Hauer, M., Doudna, J. A. and Charpentier, E. (2012) 'A Programmable Dual-RNA–Guided DNA Endonuclease in Adaptive Bacterial Immunity', *Science,* 337(6096), pp. 816-821.
116) Jo, H. Y., et al. (2020) 'Functional in vivo and in vitro effects of 20q11.21 genetic aberrations on hPSC differentiation', *Sci Rep,* 10(1), pp. 18582.
117) Kajiwara, M., et al. (2012) 'Donor-dependent variations in hepatic differentiation from human-induced pluripotent stem cells', *Proceedings of the National Academy of Sciences,* 109(31), pp. 12538-12543.
118) Kaltak, M., Blanco-Garavito, R., Molday, L. L., Dhaenens, C.-M., Souied, E. E., Platenburg, G., Swildens, J., Molday, R. S. and Cremers, F. P. M. (2023a) 'Stargardt disease-

associated in-frame ABCA4 exon 17 skipping results in significant ABCA4 function', *Journal of Translational Medicine,* 21(1), pp. 546.

119) Kaltak, M., et al. (2023b) 'Antisense oligonucleotide therapy corrects splicing in the common Stargardt disease type 1-causing variant ABCA4 c.5461-10T>C', *Mol Ther Nucleic Acids,* 31, pp. 674-688.

120) Kamarudin, T. A., et al. (2018) 'Differences in the Activity of Endogenous Bone Morphogenetic Protein Signaling Impact on the Ability of Induced Pluripotent Stem Cells to Differentiate to Corneal Epithelial-Like Cells', *Stem Cells,* 36(3), pp. 337-348.

121) Kandel, E. R., Schwartz, J. H., Jessell, T. M., Siegelbaum, S., Hudspeth, A. J. and Mack, S. (2000) *Principles of neural science.* McGraw-hill New York.

122) Kandoi, S., Martinez, C., Chen, K., Mehine, M., Mansfield, B., Duncan, J. L. and Lamba, D. A. (2023) 'Disease modelling and pharmacological rescue of autosomal dominant Retinitis Pigmentosa associated with RHO copy number variation', *medRxiv*.

123) Khan, M., et al. (2020a) 'Detailed Phenotyping and Therapeutic Strategies for Intronic ABCA4 Variants in Stargardt Disease', *Mol Ther Nucleic Acids,* 21, pp. 412-427.

124) Khan, M., et al. (2020b) 'Resolving the dark matter of ABCA4 for 1054 Stargardt disease probands through integrated genomics and transcriptomics', *Genetics in Medicine,* 22(7), pp. 1235-1246.

125) Khan, M., et al. (2019) 'Cost-effective molecular inversion probe-based ABCA4 sequencing reveals deep-intronic variants in Stargardt disease', *Hum Mutat,* 40(10), pp. 1749-1759.

126) Kilpinen, H., et al. (2017) 'Common genetic variation drives molecular heterogeneity in human iPSCs', *Nature,* 546(7658), pp. 370-375.

127) Kim, K., et al. (2010) 'Epigenetic memory in induced pluripotent stem cells', *Nature,* 467(7313), pp. 285-290.

128) Kim, K., et al. (2011) 'Donor cell type can influence the epigenome and differentiation potential of human induced pluripotent stem cells', *Nat Biotechnol,* 29(12), pp. 1117-9.

129) Kim, T. W., Che, J. H. and Yun, J. W. (2019) 'Use of stem cells as alternative methods to animal experimentation in predictive toxicology', *Regul Toxicol Pharmacol,* 105, pp. 15-29.

130) Kimberling, W. J., et al. (2010) 'Frequency of Usher syndrome in two pediatric populations: Implications for genetic screening of deaf and hard of hearing children', *Genet Med,* 12(8), pp. 512-6.

131) Kimura, Y., Noguchi, T., Kawahara, K., Kashima, K., Daa, T. and Yokoyama, S. (2004) 'Genetic alterations in 102 primary gastric cancers by comparative genomic hybridization: gain of 20q and loss of 18q are associated with tumour progression', *Modern pathology,* 17(11), pp. 1328-1337.

132) Klapper, S., Swiersy, A., Bamberg, E. and Busskamp, V. (2016) 'Biophysical Properties of Optogenetic Tools and Their Application for Vision Restoration Approaches', *Frontiers in Systems Neuroscience,* 10, pp. 74.

133) Kogut, I., et al. (2018) 'High-efficiency RNA-based reprogramming of human primary fibroblasts', *Nature Communications,* 9(1), pp. 745.

134) Kolb, H., Fernandez, E. and Nelson, R. (1995) *Webvision: the organization of the retina and visual system [Internet]*. Available at: https://pubmed.ncbi.nlm.nih.gov/21413389/.

135) Kong, J., et al. (2008) 'Correction of the disease phenotype in the mouse model of Stargardt disease by lentiviral gene therapy', *Gene Ther,* 15(19), pp. 1311-20.

136) Kruczek, K. and Swaroop, A. (2020) 'Pluripotent stem cell-derived retinal organoids for disease modeling and development of therapies', *Stem Cells,* 38(10), pp. 1206-1215.
137) Krylov, A., Yu, S., Veen, K., Newton, A., Ye, A., Qin, H., He, J. and Jusuf, P. R. (2023) 'Heterogeneity in quiescent Müller glia in the uninjured zebrafish retina drive differential responses following photoreceptor ablation', *Frontiers in Molecular Neuroscience,* 16.
138) Kuwahara, A., Ozone, C., Nakano, T., Saito, K., Eiraku, M. and Sasai, Y. (2015) 'Generation of a ciliary margin-like stem cell niche from self-organizing human retinal tissue', *Nature Communications,* 6(1), pp. 6286.
139) Kyttälä, A., et al. (2016) 'Genetic Variability Overrides the Impact of Parental Cell Type and Determines iPSC Differentiation Potential', *Stem Cell Reports,* 6(2), pp. 200-12.
140) Lamb, T. D. and Pugh, E. N., Jr (2006) 'Phototransduction, Dark Adaptation, and Rhodopsin Regeneration The Proctor Lecture', *Investigative Ophthalmology & Visual Science,* 47(12), pp. 5138-5152.
141) Lamb, T. D. and Pugh, E. N., Jr. (2004) 'Dark adaptation and the retinoid cycle of vision', *Prog Retin Eye Res,* 23(3), pp. 307-80.
142) Lamba, D. A., Karl, M. O., Ware, C. B. and Reh, T. A. (2006) 'Efficient generation of retinal progenitor cells from human embryonic stem cells', *Proceedings of the National Academy of Sciences,* 103(34), pp. 12769-12774.
143) Lambertus, S., van Huet, R. A. C., Bax, N. M., Hoefsloot, L. H., Cremers, F. P. M., Boon, C. J. F., Klevering, B. J. and Hoyng, C. B. (2015) 'Early-Onset Stargardt Disease: Phenotypic and Genotypic Characteristics', *Ophthalmology,* 122(2), pp. 335-344.
144) Lancaster, M. A. and Knoblich, J. A. (2014) 'Generation of cerebral organoids from human pluripotent stem cells', *Nature Protocols,* 9(10), pp. 2329-2340.
145) Lancaster, M. A., et al. (2013) 'Cerebral organoids model human brain development and microcephaly', *Nature,* 501(7467), pp. 373-379.
146) Lane, A., et al. (2020) 'Modeling and Rescue of RP2 Retinitis Pigmentosa Using iPSC-Derived Retinal Organoids', *Stem Cell Reports,* 15(1), pp. 67-79.
147) Larsen, P. A. and Smith, T. P. (2012) 'Application of circular consensus sequencing and network analysis to characterize the bovine IgG repertoire', *BMC Immunol,* 13, pp. 52.
148) Laurent, L. C., et al. (2011) 'Dynamic Changes in the Copy Number of Pluripotency and Cell Proliferation Genes in Human ESCs and iPSCs during Reprogramming and Time in Culture', *Cell Stem Cell,* 8(1), pp. 106-118.
149) Le Bras, A. (2019) 'A new model for Stargardt disease?', *Lab Animal,* 48(5), pp. 138-138.
150) Lee, S. H., et al. (2022a) 'Role of mTORC1 activity during early retinal development and lamination in human-induced pluripotent stem cell-derived retinal organoids', *Cell Death Discovery,* 8(1), pp. 56.
151) Lee, W., et al. (2014) 'The external limiting membrane in early-onset Stargardt disease', *Invest Ophthalmol Vis Sci,* 55(10), pp. 6139-49.
152) Lee, W., Zernant, J., Nagasaki, T., Fishman, G. A., Tsang, S. H. and Allikmets, R. (2021) 'Clinical and Genetics Characterization of Hypomorphic Variants in Stargardt disease', *Investigative Ophthalmology & Visual Science,* 62(8), pp. 2171-2171.
153) Lee, W., Zernant, J., Su, P.-Y., Nagasaki, T., Tsang, S. H. and Allikmets, R. (2022b) 'A genotype-phenotype correlation matrix for ABCA4 disease based on long-term prognostic outcomes', *JCI Insight,* 7(2).

154) Lefort, N., Feyeux, M., Bas, C., Féraud, O., Bennaceur-Griscelli, A., Tachdjian, G., Peschanski, M. and Perrier, A. L. (2008) 'Human embryonic stem cells reveal recurrent genomic instability at 20q11.21', *Nat Biotechnol,* 26(12), pp. 1364-6.

155) Lenis, T. L., et al. (2018) 'Expression of ABCA4 in the retinal pigment epithelium and its implications for Stargardt macular degeneration', *Proceedings of the National Academy of Sciences,* 115(47), pp. E11120-E11127.

156) Leong, Y. C., Di Foggia, V., Pramod, H., Bitner-Glindzicz, M., Patel, A. and Sowden, J. C. (2022) 'Molecular pathology of Usher 1B patient-derived retinal organoids at single cell resolution', *Stem Cell Reports,* 17(11), pp. 2421-2437.

157) Leung, L., Klopper, A. V., Grill, S. W., Harris, W. A. and Norden, C. (2011) 'Apical migration of nuclei during G2 is a prerequisite for all nuclear motion in zebrafish neuroepithelia', *Development,* 138(22), pp. 5003-5013.

158) Li, H. (2018) 'Minimap2: pairwise alignment for nucleotide sequences', *Bioinformatics,* 34(18), pp. 3094-3100.

159) Li, H., Handsaker, B., Wysoker, A., Fennell, T., Ruan, J., Homer, N., Marth, G., Abecasis, G. and Durbin, R. (2009) 'The Sequence Alignment/Map format and SAMtools', *Bioinformatics,* 25(16), pp. 2078-9.

160) Li, S., et al. (2021) 'Nr2e3 is a genetic modifier that rescues retinal degeneration and promotes homeostasis in multiple models of retinitis pigmentosa', *Gene Ther,* 28(5), pp. 223-241.

161) Liew, G., Michaelides, M. and Bunce, C. (2014) 'A comparison of the causes of blindness certifications in England and Wales in working age adults (16–64 years), 1999–2000 with 2009–2010', *BMJ Open,* 4(2), pp. e004015.

162) Liu, K., Zou, C. and Qin, B. (2017) 'The association between nuclear receptors and ocular diseases', *Oncotarget,* 8(16), pp. 27603-27615.

163) Loh, Y.-H., et al. (2010) 'Reprogramming of T cells from human peripheral blood', *Cell stem cell,* 7(1), pp. 15-19.

164) Lois, N., Halfyard, A. S., Bird, A. C., Holder, G. E. and Fitzke, F. W. (2004) 'Fundus autofluorescence in Stargardt macular dystrophy-fundus flavimaculatus', *Am J Ophthalmol,* 138(1), pp. 55-63.

165) Luan, L., Hu, Q., Wang, Y., Lu, L. and Ling, J. (2021) 'Knockdown of lncRNA NEAT1 expression inhibits cell migration, invasion and EMT by regulating the miR-24-3p/LRG1 axis in retinoblastoma cells', *Exp Ther Med,* 21(4), pp. 367.

166) Ludwig, T. E., Bergendahl, V., Levenstein, M. E., Yu, J., Probasco, M. D. and Thomson, J. A. (2006) 'Feeder-independent culture of human embryonic stem cells', *Nature Methods,* 3(8), pp. 637-646.

167) MacDonald, I. M. and Sieving, P. A. (2018) 'Investigation of the effect of dietary docosahexaenoic acid (DHA) supplementation on macular function in subjects with autosomal recessive Stargardt macular dystrophy', *Ophthalmic Genetics,* 39(4), pp. 477-486.

168) Madeira, F., Pearce, M., Tivey, A. R. N., Basutkar, P., Lee, J., Edbali, O., Madhusoodanan, N., Kolesnikov, A. and Lopez, R. (2022) 'Search and sequence analysis tools services from EMBL-EBI in 2022', *Nucleic Acids Res,* 50(W1), pp. W276-w279.

169) Mahlamäki, E. H., Bärlund, M., Tanner, M., Gorunova, L., Höglund, M., Karhu, R. and Kallioniemi, A. (2002) 'Frequent amplification of 8q24, 11q, 17q, and 20q-specific genes in pancreatic cancer', *Genes Chromosomes Cancer,* 35(4), pp. 353-8.

170) Maitra, A., et al. (2005) 'Genomic alterations in cultured human embryonic stem cells', *Nature Genetics,* 37(10), pp. 1099-1103.
171) Mäkeläinen, S., et al. (2019) 'An ABCA4 loss-of-function mutation causes a canine form of Stargardt disease', *PLOS Genetics,* 15(3), pp. e1007873.
172) Marchetto, M. C., Yeo, G. W., Kainohana, O., Marsala, M., Gage, F. H. and Muotri, A. R. (2009) 'Transcriptional signature and memory retention of human-induced pluripotent stem cells', *PLoS One,* 4(9), pp. e7076.
173) Markouli, C., et al. (2019) 'Gain of 20q11.21 in Human Pluripotent Stem Cells Impairs TGF-β-Dependent Neuroectodermal Commitment', *Stem Cell Reports,* 13(1), pp. 163-176.
174) Martin, G. R. (1981) 'Isolation of a pluripotent cell line from early mouse embryos cultured in medium conditioned by teratocarcinoma stem cells', *Proc Natl Acad Sci U S A,* 78(12), pp. 7634-8.
175) Martínez-Mir, A., Paloma, E., Allikmets, R., Ayuso, C., del Rio, T., Dean, M., Vilageliu, L., Gonzàlez-Duarte, R. and Balcells, S. (1998) 'Retinitis pigmentosa caused by a homozygous mutation in the Stargardt disease gene ABCR', *Nat Genet,* 18(1), pp. 11-2.
176) Martins-Taylor, K., Nisler, B. S., Taapken, S. M., Compton, T., Crandall, L., Montgomery, K. D., Lalande, M. and Xu, R. H. (2011) 'Recurrent copy number variations in human induced pluripotent stem cells', *Nat Biotechnol,* 29(6), pp. 488-91.
177) Masland, R. H. (2001) 'Neuronal diversity in the retina', *Current Opinion in Neurobiology,* 11(4), pp. 431-436.
178) Mata, N. L., Tzekov, R. T., Liu, X., Weng, J., Birch, D. G. and Travis, G. H. (2001) 'Delayed Dark-Adaptation and Lipofuscin Accumulation in abcr+/− Mice: Implications for Involvement of ABCR in Age-Related Macular Degeneration', *Investigative Ophthalmology & Visual Science,* 42(8), pp. 1685-1690.
179) Matynia, A., et al. (2022) 'Assessing Variant Causality and Severity Using Retinal Pigment Epithelial Cells Derived from Stargardt Disease Patients', *Transl Vis Sci Technol,* 11(3), pp. 33.
180) Maugeri, A., et al. (2002) 'The ABCA4 2588G>C Stargardt mutation: single origin and increasing frequency from South-West to North-East Europe', *European Journal of Human Genetics,* 10(3), pp. 197-203.
181) Maugeri, A., Klevering, B. J., Rohrschneider, K., Blankenagel, A., Brunner, H. G., Deutman, A. F., Hoyng, C. B. and Cremers, F. P. (2000) 'Mutations in the ABCA4 (ABCR) gene are the major cause of autosomal recessive cone-rod dystrophy', *Am J Hum Genet,* 67(4), pp. 960-6.
182) Maugeri, A., et al. (1999a) 'The 2588G→ C mutation in the ABCR gene is a mild frequent founder mutation in the Western European population and allows the classification of ABCR mutations in patients with Stargardt disease', *The American Journal of Human Genetics,* 64(4), pp. 1024-1035.
183) Maugeri, A., et al. (1999b) 'The 2588G-->C mutation in the ABCR gene is a mild frequent founder mutation in the Western European population and allows the classification of ABCR mutations in patients with Stargardt disease', *Am J Hum Genet,* 64(4), pp. 1024-35.
184) Mayerl, S. J., et al. (2022) 'Human retinal organoids harboring IMPG2 mutations exhibit a photoreceptor outer segment phenotype that models advanced retinitis pigmentosa', *Stem Cell Reports,* 17(11), pp. 2409-2420.

185) McGinnis, C. S., Murrow, L. M. and Gartner, Z. J. (2019) 'DoubletFinder: Doublet Detection in Single-Cell RNA Sequencing Data Using Artificial Nearest Neighbors', *Cell Syst,* 8(4), pp. 329-337.e4.
186) McLaughlin, T., Medina, A., Perkins, J., Yera, M., Wang, J. J. and Zhang, S. X. (2022) 'Cellular stress signaling and the unfolded protein response in retinal degeneration: mechanisms and therapeutic implications', *Molecular Neurodegeneration,* 17(1), pp. 25.
187) Mellough, C. B., Collin, J., Khazim, M., White, K., Sernagor, E., Steel, D. H. W. and Lako, M. (2015) 'IGF-1 Signaling Plays an Important Role in the Formation of Three-Dimensional Laminated Neural Retina and Other Ocular Structures From Human Embryonic Stem Cells', *Stem Cells,* 33(8), pp. 2416-2430.
188) Mellough, C. B., Sernagor, E., Moreno-Gimeno, I., Steel, D. H. and Lako, M. (2012) 'Efficient stage-specific differentiation of human pluripotent stem cells toward retinal photoreceptor cells', *Stem Cells,* 30(4), pp. 673-86.
189) Menon, M., et al. (2019) 'Single-cell transcriptomic atlas of the human retina identifies cell types associated with age-related macular degeneration', *Nature Communications,* 10(1), pp. 4902.
190) Merkle, F. T., et al. (2017) 'Human pluripotent stem cells recurrently acquire and expand dominant negative P53 mutations', *Nature,* 545(7653), pp. 229-233.
191) Meyer, J. S., Shearer, R. L., Capowski, E. E., Wright, L. S., Wallace, K. A., McMillan, E. L., Zhang, S. C. and Gamm, D. M. (2009) 'Modeling early retinal development with human embryonic and induced pluripotent stem cells', *Proc Natl Acad Sci U S A,* 106(39), pp. 16698-703.
192) Michaelides, M., et al. (2007) 'ABCA4 mutations and discordant ABCA4 alleles in patients and siblings with bull's-eye maculopathy', *Br J Ophthalmol,* 91(12), pp. 1650-5.
193) Mischler, A., Karakis, V., Mahinthakumar, J., Carberry, C. K., San Miguel, A., Rager, J. E., Fry, R. C. and Rao, B. M. (2021) 'Two distinct trophectoderm lineage stem cells from human pluripotent stem cells', *J Biol Chem,* 296, pp. 100386.
194) Moiseyev, G., Chen, Y., Takahashi, Y., Wu, B. X. and Ma, J. X. (2005) 'RPE65 is the isomerohydrolase in the retinoid visual cycle', *Proc Natl Acad Sci U S A,* 102(35), pp. 12413-8.
195) Molday, L. L., Rabin, A. R. and Molday, R. S. (2000) 'ABCR expression in foveal cone photoreceptors and its role in Stargardt macular dystrophy', *Nat Genet,* 25(3), pp. 257-8.
196) Molday, R. S. (2007) 'ATP-binding cassette transporter ABCA4: molecular properties and role in vision and macular degeneration', *J Bioenerg Biomembr,* 39(5-6), pp. 507-17.
197) Molday, R. S., Zhong, M. and Quazi, F. (2009) 'The role of the photoreceptor ABC transporter ABCA4 in lipid transport and Stargardt macular degeneration', *Biochimica et Biophysica Acta (BBA) - Molecular and Cell Biology of Lipids,* 1791(7), pp. 573-583.
198) Mullins, R. F., Kuehn, M. H., Radu, R. A., Enriquez, G. S., East, J. S., Schindler, E. I., Travis, G. H. and Stone, E. M. (2012) 'Autosomal recessive retinitis pigmentosa due to ABCA4 mutations: clinical, pathologic, and molecular characterization', *Invest Ophthalmol Vis Sci,* 53(4), pp. 1883-94.
199) Murphy, D., Cieply, B., Carstens, R., Ramamurthy, V. and Stoilov, P. (2016) 'The Musashi 1 Controls the Splicing of Photoreceptor-Specific Exons in the Vertebrate Retina', *PLOS Genetics,* 12(8), pp. e1006256.
200) Nakano, T., et al. (2012) 'Self-formation of optic cups and storable stratified neural retina from human ESCs', *Cell Stem Cell,* 10(6), pp. 771-785.

201) Naso, F. D., et al. (2020) 'Excess TPX2 Interferes with Microtubule Disassembly and Nuclei Reformation at Mitotic Exit', *Cells,* 9(2), pp. 374.
202) Nelson, R. and Connaughton, V. (2012) 'Bipolar Cell Pathways in the Vertebrate Retina', *Webvision: The Organization of the Retina and Visual System [Internet]*: University of Utah Health Sciences Center.
203) Ng, E. S. Y., Kady, N., Hu, J., Dave, A., Jiang, Z., Pei, J., Gorin, M. B., Matynia, A. and Radu, R. A. (2022) 'Membrane Attack Complex Mediates Retinal Pigment Epithelium Cell Death in Stargardt Macular Degeneration', *Cells,* 11(21), pp. 3462.
204) Nguyen, H. T., Geens, M., Mertzanidou, A., Jacobs, K., Heirman, C., Breckpot, K. and Spits, C. (2013) 'Gain of 20q11.21 in human embryonic stem cells improves cell survival by increased expression of Bcl-xL', *Molecular Human Reproduction,* 20(2), pp. 168-177.
205) Nitschke, S., et al. (2022) 'Glycogen synthase downregulation rescues the amylopectinosis of murine RBCK1 deficiency', *Brain,* 145(7), pp. 2361-2377.
206) O'Connor, M. D. (2013) 'The 3R principle: advancing clinical application of human pluripotent stem cells', *Stem Cell Research & Therapy,* 4(2), pp. 21.
207) O'Hara-Wright, M. and Gonzalez-Cordero, A. (2020) 'Retinal organoids: a window into human retinal development', *Development,* 147(24).
208) Ohlemacher, S. K., Iglesias, C. L., Sridhar, A., Gamm, D. M. and Meyer, J. S. (2015) 'Generation of highly enriched populations of optic vesicle− like retinal cells from human pluripotent stem cells', *Current protocols in stem cell biology,* 32(1), pp. 1H. 8.1-1H. 8.20.
209) Okita, K., et al. (2011) 'A more efficient method to generate integration-free human iPS cells', *Nat Methods,* 8(5), pp. 409-12.
210) Osafune, K., Caron, L., Borowiak, M., Martinez, R. J., Fitz-Gerald, C. S., Sato, Y., Cowan, C. A., Chien, K. R. and Melton, D. A. (2008) 'Marked differences in differentiation propensity among human embryonic stem cell lines', *Nat Biotechnol,* 26(3), pp. 313-5.
211) Osakada, F., Ooto, S., Akagi, T., Mandai, M., Akaike, A. and Takahashi, M. (2007) 'Wnt Signaling Promotes Regeneration in the Retina of Adult Mammals', *The Journal of Neuroscience,* 27(15), pp. 4210-4219.
212) Pagon, R. A. (1988) 'Retinitis pigmentosa', *Surv Ophthalmol,* 33(3), pp. 137-77.
213) Palczewski, K. (2006) 'G Protein–Coupled Receptor Rhodopsin', *Annual Review of Biochemistry,* 75(1), pp. 743-767.
214) Parfitt, D. A., et al. (2016) 'Identification and correction of mechanisms underlying inherited blindness in human iPSC-derived optic cups', *Cell stem cell,* 18(6), pp. 769-781.
215) Parker, M. A., et al. (2022) 'Three-Year Safety Results of SAR422459 (EIAV-ABCA4) Gene Therapy in Patients With ABCA4-Associated Stargardt Disease: An Open-Label Dose-Escalation Phase I/IIa Clinical Trial, Cohorts 1-5', *Am J Ophthalmol,* 240, pp. 285-301.
216) Pera, E. M., Wessely, O., Li, S. Y. and De Robertis, E. M. (2001) 'Neural and head induction by insulin-like growth factor signals', *Dev Cell,* 1(5), pp. 655-65.
217) Peterson, S. E. and Loring, J. F. (2014) 'Genomic instability in pluripotent stem cells: implications for clinical applications', *J Biol Chem,* 289(8), pp. 4578-84.
218) Pfannkuche, K., Fatima, A., Gupta, M. K., Dieterich, R. and Hescheler, J. (2010) 'Initial Colony Morphology-Based Selection for iPS Cells Derived from Adult Fibroblasts Is Substantially Improved by Temporary UTF1-Based Selection', *PLOS ONE,* 5(3), pp. e9580.
219) Phillips, M. J., et al. (2012) 'Blood-derived human iPS cells generate optic vesicle–like structures with the capacity to form retinal laminae and develop synapses', *Investigative ophthalmology & visual science,* 53(4), pp. 2007-2019.

220) Piccardi, M., et al. (2019) 'Antioxidant saffron and central retinal function in ABCA4-related stargardt macular dystrophy', *Nutrients,* 11(10), pp. 2461.
221) Pierce, G. B. and Dixon, F. J., Jr. (1959) 'Testicular teratomas. I. Demonstration of teratogenesis by metamorphosis of multipotential cells', *Cancer,* 12(3), pp. 573-83.
222) Plath, K. and Lowry, W. E. (2011) 'Progress in understanding reprogramming to the induced pluripotent state', *Nat Rev Genet,* 12(4), pp. 253-65.
223) Popova, E. (2014) 'ON-OFF Interactions in the Retina: Role of Glycine and GABA', *Curr Neuropharmacol,* 12(6), pp. 509-26.
224) Press Release | Alkeus Pharmaceuticals Inc (2023) *Alkeus Announces $150 Million Series B Financing, Supporting Rapid Registration Path for gildeuretinol (ALK-001) in the Treatment of Stargardt Disease*. Available at: https://alkeuspharma.com/press-release.
225) Press Release | FDA (2018) *FDA approves novel gene therapy to treat patients with a rare form of inherited vision loss*. Available at: https://www.fda.gov/news-events/press-announcements/fda-approves-novel-gene-therapy-treat-patients-rare-form-inherited-vision-loss.
226) Press Release | NanoScope Therapeutics (2023a) *Nanoscope Therapeutics Announces Presentation of Key Results from Phase 2b RESTORE Trial of MCO-010 for the Treatment of Retinitis Pigmentosa at the ARVO Annual Meeting - Nanoscope Therapeutics*. Nanoscope Therapeutics -. Available at: https://nanostherapeutics.com/2023/04/27/nanoscope-therapeutics-announces-presentation-of-key-results-from-phase-2b-restore-trial-of-mco-010-for-the-treatment-of-retinitis-pigmentosa-at-the-arvo-annual-meeting.
227) Press Release | NanoScope Therapeutics (2023b) *Nanoscope Therapeutics Receives Fast Track Designation by the FDA for MCO-010 for the Treatment of Stargardt Disease - Nanoscope Therapeutics*. Nanoscope Therapeutics -. Available at: https://nanostherapeutics.com/2023/01/30/nanoscope-therapeutics-receives-fast-track-designation-by-the-fda-for-mco-010-for-the-treatment-of-stargardt-disease.
228) Press Release | NanoScope Therapeutics (2023c) *Nanoscope Therapeutics Unveils Clinical Trial Results for MCO-010 in Treating Stargardt Disease - Nanoscope Therapeutics*. Nanoscope Therapeutics -. Available at: https://nanostherapeutics.com/2023/08/09/nanoscope-therapeutics-unveils-clinical-trial-results-for-mco-010-in-treating-stargardt-disease.
229) Press Release | Ocugen (2023) *Ocugen Announces OCU410ST Receives Orphan Drug Designation for Treatment of ABCA4-Associated Retinopathies | Ocugen, Inc*. Available at: https://ir.ocugen.com/news-releases/news-release-details/ocugen-announces-ocu410st-receives-orphan-drug-designation.
230) Puri, M. C. and Nagy, A. (2012) 'Concise Review: Embryonic Stem Cells Versus Induced Pluripotent Stem Cells: The Game Is On', *STEM CELLS,* 30(1), pp. 10-14.
231) Purves D, A. G., Fitzpatrick D, et al., editors. (2001) *Neuroscience. - 2nd edition.* Sunderland (MA): : Sinauer Associates.
232) Quazi, F., Lenevich, S. and Molday, R. S. (2012) 'ABCA4 is an N-retinylidene-phosphatidylethanolamine and phosphatidylethanolamine importer', *Nat Commun,* 3, pp. 925.
233) Quinn, P. M. J. and Wijnholds, J. (2019) 'Retinogenesis of the Human Fetal Retina: An Apical Polarity Perspective', *Genes,* 10(12), pp. 987.
234) Radu, R. A., Hu, J., Yuan, Q., Welch, D. L., Makshanoff, J., Lloyd, M., McMullen, S., Travis, G. H. and Bok, D. (2011) 'Complement System Dysregulation and Inflammation in

the Retinal Pigment Epithelium of a Mouse Model for Stargardt Macular Degeneration*', *Journal of Biological Chemistry,* 286(21), pp. 18593-18601.

235) Radu, R. A., Yuan, Q., Hu, J., Peng, J. H., Lloyd, M., Nusinowitz, S., Bok, D. and Travis, G. H. (2008) 'Accelerated accumulation of lipofuscin pigments in the RPE of a mouse model for ABCA4-mediated retinal dystrophies following Vitamin A supplementation', *Investigative ophthalmology & visual science,* 49(9), pp. 3821-3829.

236) Ramos-Mejia, V., Muñoz-Lopez, M., Garcia-Perez, J. L. and Menendez, P. (2010) 'iPSC lines that do not silence the expression of the ectopic reprogramming factors may display enhanced propensity to genomic instability', *Cell Research,* 20(10), pp. 1092-1095.

237) Rando, R. R. (2001) 'The Biochemistry of the Visual Cycle', *Chemical Reviews,* 101(7), pp. 1881-1896.

238) Rao, M. S. and Malik, N. (2012) 'Assessing iPSC reprogramming methods for their suitability in translational medicine', *Journal of Cellular Biochemistry,* 113(10), pp. 3061-3068.

239) Roberts, M. R., Srinivas, M., Forrest, D., Morreale de Escobar, G. and Reh, T. A. (2006) 'Making the gradient: Thyroid hormone regulates cone opsin expression in the developing mouse retina', *Proceedings of the National Academy of Sciences,* 103(16), pp. 6218-6223.

240) Rodda, D. J., Chew, J.-L., Lim, L.-H., Loh, Y.-H., Wang, B., Ng, H.-H. and Robson, P. (2005) 'Transcriptional Regulation of Nanog by OCT4 and SOX2 *', *Journal of Biological Chemistry,* 280(26), pp. 24731-24737.

241) Rodrigues, A., et al. (2022) 'Modeling PRPF31 retinitis pigmentosa using retinal pigment epithelium and organoids combined with gene augmentation rescue', *NPJ Regen Med,* 7(1), pp. 39.

242) Rodriguez-Hidalgo, M., et al. (2023) 'ABCA4 c.6480-35A>G, a novel branchpoint variant associated with cone-rod dystrophy and macular dystrophy', *Investigative Ophthalmology & Visual Science,* 64(8), pp. 4509-4509.

243) Roost, M. S., et al. (2017) 'DNA methylation and transcriptional trajectories during human development and reprogramming of isogenic pluripotent stem cells', *Nature Communications,* 8(1), pp. 908.

244) Roska, B., Nemeth, E. and Werblin, F. S. (1998) 'Response to change is facilitated by a three-neuron disinhibitory pathway in the tiger salamander retina', *J Neurosci,* 18(9), pp. 3451-9.

245) Rotenstreich, Y., Fishman, G. A. and Anderson, R. J. (2003) 'Visual acuity loss and clinical observations in a large series of patients with Stargardt disease', *Ophthalmology,* 110(6), pp. 1151-8.

246) Rozanska, A., et al. (2022) 'pRB-Depleted Pluripotent Stem Cell Retinal Organoids Recapitulate Cell State Transitions of Retinoblastoma Development and Suggest an Important Role for pRB in Retinal Cell Differentiation', *Stem Cells Transl Med,* 11(4), pp. 415-433.

247) Runhart, E. H., et al. (2022) 'Stargardt disease: monitoring incidence and diagnostic trends in the Netherlands using a nationwide disease registry', *Acta Ophthalmol,* 100(4), pp. 395-402.

248) Runhart, E. H., et al. (2018) 'The Common ABCA4 Variant p.Asn1868Ile Shows Nonpenetrance and Variable Expression of Stargardt Disease When Present in trans With Severe Variants', *Investigative Ophthalmology & Visual Science,* 59(8), pp. 3220-3231.

249) Runhart, E. H., et al. (2019) 'Late-Onset Stargardt Disease Due to Mild, Deep-Intronic ABCA4 Alleles', *Invest Ophthalmol Vis Sci,* 60(13), pp. 4249-4256.

250) Sangermano, R., et al. (2016) 'Photoreceptor Progenitor mRNA Analysis Reveals Exon Skipping Resulting from the ABCA4 c.5461-10T→C Mutation in Stargardt Disease', *Ophthalmology,* 123(6), pp. 1375-85.
251) Sangermano, R., et al. (2019) 'Deep-intronic ABCA4 variants explain missing heritability in Stargardt disease and allow correction of splice defects by antisense oligonucleotides', *Genetics in Medicine,* 21(8), pp. 1751-1760.
252) Sanjurjo-Soriano, C., et al. (2023) 'USH2A variants causing retinitis pigmentosa or Usher syndrome provoke differential retinal phenotypes in disease-specific organoids', *HGG Adv,* 4(4), pp. 100229.
253) Saraiva-Agostinho, N. and Barbosa-Morais, N. L. (2019) 'psichomics: graphical application for alternative splicing quantification and analysis', *Nucleic Acids Res,* 47(2), pp. e7.
254) Schlaeger, T. M., et al. (2015) 'A comparison of non-integrating reprogramming methods', *Nature Biotechnology,* 33(1), pp. 58-63.
255) Schmidt, S., et al. (2003) 'Detailed Analysis of Allelic Variation in the ABCA4 Gene in Age-Related Maculopathy', *Investigative Ophthalmology & Visual Science,* 44(7), pp. 2868-2875.
256) Schmitz-Valckenberg, S., Holz, F. G., Bird, A. C. and Spaide, R. F. (2008) 'Fundus autofluorescence imaging: review and perspectives', *Retina,* 28(3), pp. 385-409.
257) Schmitz-Valckenberg, S., et al. (2021) 'Fundus autofluorescence imaging', *Prog Retin Eye Res,* 81, pp. 100893.
258) Scholl, H. P., DeBartolomeo, G., Washington, I. and Saad, L. (2022) 'ALK-001 (C20-D3-Vitamin A) slows the growth of atrophic lesions in ABCA4-related Stargardt Disease: Results of a Phase 2 placebo-controlled clinical trial (TEASE study)', *Investigative Ophthalmology & Visual Science,* 63(7), pp. 38-38.
259) Schwartz, S. D., et al. (2012) 'Embryonic stem cell trials for macular degeneration: a preliminary report', *The Lancet,* 379(9817), pp. 713-720.
260) Schwartz, S. D., et al. (2015) 'Human embryonic stem cell-derived retinal pigment epithelium in patients with age-related macular degeneration and Stargardt's macular dystrophy: follow-up of two open-label phase 1/2 studies', *The Lancet,* 385(9967), pp. 509-516.
261) Scotto, L., et al. (2008) 'Identification of copy number gain and overexpressed genes on chromosome arm 20q by an integrative genomic approach in cervical cancer: potential role in progression', *Genes, Chromosomes and Cancer,* 47(9), pp. 755-765.
262) Seki, T., et al. (2010) 'Generation of Induced Pluripotent Stem Cells from Human Terminally Differentiated Circulating T Cells', *Cell Stem Cell,* 7(1), pp. 11-14.
263) Sequiera, G. L., et al. (2022) 'Development of iPSC-based clinical trial selection platform for patients with ultrarare diseases', *Science Advances,* 8(14), pp. eabl4370.
264) Shao, K., Xi, L., Cang, Z., Chen, C. and Huang, S. (2020) 'Knockdown of NEAT1 exerts suppressive effects on diabetic retinopathy progression via inactivating TGF-β1 and VEGF signaling pathways', *J Cell Physiol,* 235(12), pp. 9361-9369.
265) Sharon, D., Tilgner, H., Grubert, F. and Snyder, M. (2013) 'A single-molecule long-read survey of the human transcriptome', *Nature Biotechnology,* 31(11), pp. 1009-1014.
266) Shimada, H., et al. (2017) 'In Vitro Modeling Using Ciliopathy-Patient-Derived Cells Reveals Distinct Cilia Dysfunctions Caused by CEP290 Mutations', *Cell Rep,* 20(2), pp. 384-396.

267) Smalley, E. (2017) 'First AAV gene therapy poised for landmark approval', *Nature biotechnology,* 35(11), pp. 998-1000.
268) Snodderly, D. M., Sandstrom, M. M., Leung, I. Y.-F., Zucker, C. L. and Neuringer, M. (2002) 'Retinal Pigment Epithelial Cell Distribution in Central Retina of Rhesus Monkeys', *Investigative Ophthalmology & Visual Science,* 43(9), pp. 2815-2818.
269) Sommer, C. A., Stadtfeld, M., Murphy, G. J., Hochedlinger, K., Kotton, D. N. and Mostoslavsky, G. (2009) 'Induced pluripotent stem cell generation using a single lentiviral stem cell cassette', *Stem Cells,* 27(3), pp. 543-9.
270) Song, H., Rossi, E. A., Latchney, L., Bessette, A., Stone, E., Hunter, J. J., Williams, D. R. and Chung, M. (2015) 'Cone and rod loss in Stargardt disease revealed by adaptive optics scanning light ophthalmoscopy', *JAMA ophthalmology,* 133(10), pp. 1198-1203.
271) Sparrow, J. R., Fishkin, N., Zhou, J., Cai, B., Jang, Y. P., Krane, S., Itagaki, Y. and Nakanishi, K. (2003) 'A2E, a byproduct of the visual cycle', *Vision Research,* 43(28), pp. 2983-2990.
272) Sparrow, J. R., Gregory-Roberts, E., Yamamoto, K., Blonska, A., Ghosh, S. K., Ueda, K. and Zhou, J. (2012) 'The bisretinoids of retinal pigment epithelium', *Prog Retin Eye Res,* 31(2), pp. 121-35.
273) Sparrow, J. R., Wu, Y., Kim, C. Y. and Zhou, J. (2010) 'Phospholipid meets all-trans-retinal: the making of RPE bisretinoids', *J Lipid Res,* 51(2), pp. 247-61.
274) Spits, C., Mateizel, I., Geens, M., Mertzanidou, A., Staessen, C., Vandeskelde, Y., Van der Elst, J., Liebaers, I. and Sermon, K. (2008) 'Recurrent chromosomal abnormalities in human embryonic stem cells', *Nature Biotechnology,* 26(12), pp. 1361-1363.
275) Sridhar, A., et al. (2020) 'Single-Cell Transcriptomic Comparison of Human Fetal Retina, hPSC-Derived Retinal Organoids, and Long-Term Retinal Cultures', *Cell Rep,* 30(5), pp. 1644-1659.e4.
276) Stargardt, K. (1909) 'Über familiäre, progressive Degeneration in der Maculagegend des Auges', *Albrecht von Graefes Archiv für Ophthalmologie,* 71, pp. 534-550.
277) Starr, C. R. and Gorbatyuk, M. S. (2019) 'Delineating the role of eIF2α in retinal degeneration', *Cell Death Dis,* 10(6), pp. 409.
278) Stevens, L. C. and Little, C. C. (1954) 'Spontaneous Testicular Teratomas in an Inbred Strain of Mice', *Proc Natl Acad Sci U S A,* 40(11), pp. 1080-7.
279) Stingl, K., et al. (2022) 'Evaluation of Local Rod and Cone Function in Stargardt Disease', *Investigative Ophthalmology & Visual Science,* 63(3), pp. 6-6.
280) Stone, E. M., et al. (2017) 'Clinically Focused Molecular Investigation of 1000 Consecutive Families with Inherited Retinal Disease', *Ophthalmology,* 124(9), pp. 1314-1331.
281) Strzyz, P. J., Lee, H. O., Sidhaye, J., Weber, I. P., Leung, L. C. and Norden, C. (2015) 'Interkinetic nuclear migration is centrosome independent and ensures apical cell division to maintain tissue integrity', *Dev Cell,* 32(2), pp. 203-19.
282) Sullivan, S. R., Egli, D., Akutsu, H., Melton, D. A., Eggan, K. C. and Cowan, C. A. 'Derivation of human embryonic stem cell lines'.
283) Sun, H., Molday, R. S. and Nathans, J. (1999) 'Retinal stimulates ATP hydrolysis by purified and reconstituted ABCR, the photoreceptor-specific ATP-binding cassette transporter responsible for Stargardt disease', *J Biol Chem,* 274(12), pp. 8269-81.
284) Sun, H. and Nathans, J. (1997) 'Stargardt's ABCR is localized to the disc membrane of retinal rod outer segments', *Nat Genet,* 17(1), pp. 15-6.

285) Taapken, S. M., Nisler, B. S., Newton, M. A., Sampsell-Barron, T. L., Leonhard, K. A., McIntire, E. M. and Montgomery, K. D. (2011) 'Karyotypic abnormalities in human induced pluripotent stem cells and embryonic stem cells', *Nature Biotechnology,* 29(4), pp. 313-314.

286) Takahashi, K., Tanabe, K., Ohnuki, M., Narita, M., Ichisaka, T., Tomoda, K. and Yamanaka, S. (2007) 'Induction of pluripotent stem cells from adult human fibroblasts by defined factors', *cell,* 131(5), pp. 861-872.

287) Takahashi, K. and Yamanaka, S. (2006) 'Induction of pluripotent stem cells from mouse embryonic and adult fibroblast cultures by defined factors', *Cell,* 126(4), pp. 663-76.

288) Takebe, T., Zhang, R.-R., Koike, H., Kimura, M., Yoshizawa, E., Enomura, M., Koike, N., Sekine, K. and Taniguchi, H. (2014) 'Generation of a vascularized and functional human liver from an iPSC-derived organ bud transplant', *Nature Protocols,* 9(2), pp. 396-409.

289) Tanna, P., Strauss, R. W., Fujinami, K. and Michaelides, M. (2017) 'Stargardt disease: clinical features, molecular genetics, animal models and therapeutic options', *Br J Ophthalmol,* 101(1), pp. 25-30.

290) Tardaguila, M., et al. (2018) 'SQANTI: extensive characterization of long-read transcript sequences for quality control in full-length transcriptome identification and quantification', *Genome Res,* 28(3), pp. 396-411.

291) The Nobel Assembly at Karolinska Institutet 2012. The Nobel Prize in Physiology or Medicine 2012 jointly to John B. Gurdon and Shinya Yamanaka for the discovery that mature cells can be reprogrammed

292) to become pluripotent.

293) Thomas, B. B., Lin, B., Martinez-Camarillo, J. C., Zhu, D., McLelland, B. T., Nistor, G., Keirstead, H. S., Humayun, M. S. and Seiler, M. J. (2021) 'Co-grafts of Human Embryonic Stem Cell Derived Retina Organoids and Retinal Pigment Epithelium for Retinal Reconstruction in Immunodeficient Retinal Degenerate Royal College of Surgeons Rats', *Frontiers in Neuroscience,* 15.

294) Thomson, J. A., Itskovitz-Eldor, J., Shapiro, S. S., Waknitz, M. A., Swiergiel, J. J., Marshall, V. S. and Jones, J. M. (1998) 'Embryonic stem cell lines derived from human blastocysts', *Science,* 282(5391), pp. 1145-7.

295) Toms, M., Pagarkar, W. and Moosajee, M. (2020) 'Usher syndrome: clinical features, molecular genetics and advancing therapeutics', *Ther Adv Ophthalmol,* 12, pp. 2515841420952194.

296) Trachsel-Moncho, L., Benlloch-Navarro, S., Fernández-Carbonell, Á., Ramírez-Lamelas, D. T., Olivar, T., Silvestre, D., Poch, E. and Miranda, M. (2018) 'Oxidative stress and autophagy-related changes during retinal degeneration and development', *Cell Death & Disease,* 9(8), pp. 812.

297) Trapani, I., et al. (2019) 'Somatic or germline ABCA4 editing to generate a pig model of Stargardt disease type 1', *Investigative Ophthalmology & Visual Science,* 60(9), pp. 4230-4230.

298) Trevisan, M., Desole, G., Costanzi, G., Lavezzo, E., Palù, G. and Barzon, L. (2017) 'Reprogramming Methods Do Not Affect Gene Expression Profile of Human Induced Pluripotent Stem Cells', *Int J Mol Sci,* 18(1).

299) Tsang, S. H. and Sharma, T. (2018) 'Stargardt Disease', in Tsang, S.H. and Sharma, T. (eds.) *Atlas of Inherited Retinal Diseases*. Cham: Springer International Publishing, pp. 139-151.

300) van Driel, M. A., Maugeri, A., Klevering, B. J., Hoyng, C. B. and Cremers, F. P. (1998a) 'ABCR unites what ophthalmologists divide(s)', *Ophthalmic Genet,* 19(3), pp. 117-22.
301) van Driel, M. A., Maugeri, A., Klevering, B. J., Hoyng, C. B. and Cremers, F. P. M. (1998b) 'ABCR unites what ophthalmologists divide(s)', *Ophthalmic Genetics,* 19(3), pp. 117-122.
302) Veiga, D. F. T., et al. (2022) 'A comprehensive long-read isoform analysis platform and sequencing resource for breast cancer', *Science Advances,* 8(3), pp. eabg6711.
303) Völkner, M., et al. (2022) 'HBEGF-TNF induce a complex outer retinal pathology with photoreceptor cell extrusion in human organoids', *Nature Communications,* 13(1), pp. 6183.
304) Volland, S., Esteve-Rudd, J., Hoo, J., Yee, C. and Williams, D. S. (2015) 'A comparison of some organizational characteristics of the mouse central retina and the human macula', *PLoS One,* 10(4), pp. e0125631.
305) Wang, J., et al. (2020) 'iCn3D, a web-based 3D viewer for sharing 1D/2D/3D representations of biomolecular structures', *Bioinformatics,* 36(1), pp. 131-135.
306) Wang, J. S. and Kefalov, V. J. (2011) 'The cone-specific visual cycle', *Prog Retin Eye Res,* 30(2), pp. 115-28.
307) Wang, L., et al. (2018) 'Retinal Cell Type DNA Methylation and Histone Modifications Predict Reprogramming Efficiency and Retinogenesis in 3D Organoid Cultures', *Cell Rep,* 22(10), pp. 2601-2614.
308) Warren, L., et al. (2010) 'Highly efficient reprogramming to pluripotency and directed differentiation of human cells with synthetic modified mRNA', *Cell Stem Cell,* 7(5), pp. 618-30.
309) Watson, A. and Lako, M. (2023) 'Retinal organoids provide unique insights into molecular signatures of inherited retinal disease throughout retinogenesis', *Journal of Anatomy,* 243(2), pp. 186-203.
310) Webster, A. R., et al. (2001) 'An Analysis of Allelic Variation in the ABCA4 Gene', *Investigative Ophthalmology & Visual Science,* 42(6), pp. 1179-1189.
311) Weng, J., Mata, N. L., Azarian, S. M., Tzekov, R. T., Birch, D. G. and Travis, G. H. (1999) 'Insights into the Function of Rim Protein in Photoreceptors and Etiology of Stargardt's Disease from the Phenotype in abcr Knockout Mice', *Cell,* 98(1), pp. 13-23.
312) West, E. L., et al. (2022) 'Antioxidant and lipid supplementation improve the development of photoreceptor outer segments in pluripotent stem cell-derived retinal organoids', *Stem cell reports,* 17(4), pp. 775-788.
313) Westeneng-van Haaften, S. C., Boon, C. J., Cremers, F. P., Hoefsloot, L. H., den Hollander, A. I. and Hoyng, C. B. (2012) 'Clinical and genetic characteristics of late-onset Stargardt's disease', *Ophthalmology,* 119(6), pp. 1199-210.
314) Whelan, L., et al. (2023) 'Detailed analysis of an enriched deep intronic ABCA4 variant in Irish Stargardt disease patients', *Sci Rep,* 13(1), pp. 9380.
315) Whelan, L., et al. (2020) 'Findings from a Genotyping Study of over 1000 People with Inherited Retinal Disorders in Ireland', *Genes,* 11(1), pp. 105.
316) Woltjen, K., et al. (2009) 'piggyBac transposition reprograms fibroblasts to induced pluripotent stem cells', *Nature,* 458(7239), pp. 766-770.
317) Wu, H., et al. (2008) 'Copy number variant analysis of human embryonic stem cells', *Stem Cells,* 26(6), pp. 1484-9.
318) Wu, Z., Lu, Z., Ou, J., Su, X. and Liu, J. (2020) 'Inflammatory response and oxidative stress attenuated by sulfiredoxin-1 in neuron-like cells depends on nuclear factor erythroid-2-related factor 2', *Mol Med Rep,* 22(6), pp. 4734-4742.

319) Würbel, H. (2017) 'More than 3Rs: the importance of scientific validity for harm-benefit analysis of animal research', *Lab Animal,* 46(4), pp. 164-166.
320) Yang, S., Zhou, J. and Li, D. (2021) 'Functions and Diseases of the Retinal Pigment Epithelium', *Frontiers in Pharmacology,* 12.
321) Yang, W., Mills, J. A., Sullivan, S., Liu, Y., French, D. L. and Gadue, P. (2008) 'iPSC reprogramming from human peripheral blood using Sendai virus mediated gene transfer'.
322) Yang, X.-J. (2004) 'Roles of cell-extrinsic growth factors in vertebrate eye pattern formation and retinogenesis', *Seminars in Cell & Developmental Biology,* 15(1), pp. 91-103.
323) Yaqoob, Z., Wu, J. and Yang, C. (2005) 'Spectral domain optical coherence tomography: a better OCT imaging strategy', *BioTechniques,* 39(6S), pp. S6-S13.
324) Yokobayashi, S., Okita, K., Nakagawa, M., Nakamura, T., Yabuta, Y., Yamamoto, T. and Saitou, M. (2017) 'Clonal variation of human induced pluripotent stem cells for induction into the germ cell fate†', *Biology of Reproduction,* 96(6), pp. 1154-1166.
325) Yoshihara, M., Hayashizaki, Y. and Murakawa, Y. (2017) 'Genomic Instability of iPSCs: Challenges Towards Their Clinical Applications', *Stem Cell Rev Rep,* 13(1), pp. 7-16.
326) Zakrzewski, W., Dobrzyński, M., Szymonowicz, M. and Rybak, Z. (2019) 'Stem cells: past, present, and future', *Stem Cell Research & Therapy,* 10(1), pp. 68.
327) Zernant, J., Lee, W., Collison, F. T., Fishman, G. A., Sergeev, Y. V., Schuerch, K., Sparrow, J. R., Tsang, S. H. and Allikmets, R. (2017) 'Frequent hypomorphic alleles account for a significant fraction of ABCA4 disease and distinguish it from age-related macular degeneration', *J Med Genet,* 54(6), pp. 404-412.
328) Zernant, J., et al. (2022) 'Rare and common variants in ROM1 and PRPH2 genes trans-modify Stargardt/ABCA4 disease', *PLoS Genet,* 18(3), pp. e1010129.
329) Zernant, J., et al. (2011) 'Analysis of the ABCA4 gene by next-generation sequencing', *Invest Ophthalmol Vis Sci,* 52(11), pp. 8479-87.
330) Zerti, D., Dorgau, B., Felemban, M., Ghareeb, A. E., Yu, M., Ding, Y., Krasnogor, N. and Lako, M. (2020) 'Developing a simple method to enhance the generation of cone and rod photoreceptors in pluripotent stem cell-derived retinal organoids', *Stem Cells,* 38(1), pp. 45-51.
331) Zhong, X., et al. (2014) 'Generation of three-dimensional retinal tissue with functional photoreceptors from human iPSCs', *Nature Communications,* 5(1), pp. 4047.
332) Zhou, D., Yang, Q., Li, J., Zeng, S., Li, Z., Liu, X., Li, J., Zhou, W. and Chai, Y. (2023) 'Retinal organoid models show heterozygous rhodopsin mutation favors endoplasmic reticulum stress-induced apoptosis in rods', *Stem Cells Dev*.
333) Zhou, S., Flamier, A., Abdouh, M., Tétreault, N., Barabino, A., Wadhwa, S. and Bernier, G. (2015) 'Differentiation of human embryonic stem cells into cone photoreceptors through simultaneous inhibition of BMP, TGFβ and Wnt signaling', *Development,* 142(19), pp. 3294-306.
334) Zhou, T., et al. (2011) 'Generation of induced pluripotent stem cells from urine', *J Am Soc Nephrol,* 22(7), pp. 1221-8.
335) Zhou, W. and Freed, C. R. (2009) 'Adenoviral Gene Delivery Can Reprogram Human Fibroblasts to Induced Pluripotent Stem Cells', *STEM CELLS,* 27(11), pp. 2667-2674.
336) Zhu, L., et al. (2016) 'The mitochondrial protein CHCHD2 primes the differentiation potential of human induced pluripotent stem cells to neuroectodermal lineages', *Journal of Cell Biology,* 215(2), pp. 187-202.

Appendices

Appendix A: List of publications

1. **Watson, A.** & Lako, M. (2023) Retinal organoids provide unique insights into molecular signatures of inherited retinal disease throughout retinogenesis. Journal of Anatomy, 243, 186–203. Available from: https://doi.org/10.1111/joa.13768

Appendix B: Duplicated and deleted genes in PT1 iPSC Sample

Chr20q11.21 duplication		
DEFB118	VSTM2L	SLC2A10
DEFB119	TTI1	EYA2
DEFB121	RPRD1B	MIR3616
DEFB122	TGM2	ZMYND8
DEFB123	KIAA1755	LOC100131496
DEFB124	LOC149684	LOC101927377
REM1	BPI	LINC01754
LINC00028	LBP	NCOA3
HM13	SNHG17	SULF2
HM13-AS1	SNORA71B	LINC01522
ID1	SNORA71A	LINC01523
MIR3193	SNORA71C	LINC00494
COX4I2	SNORA71D	PREX1
BCL2L1	SNHG11	ARFGEF2
ABALON	SNORA71E	CSE1L-AS1
TPX2	SNORA60	CSE1L
MYLK2	RALGAPB	STAU1
FOXS1	MIR548O2	DDX27
DUSP15	ADIG	ZNFX1
TTLL9	ARHGAP40	ZFAS1
PDRG1	SLC32A1	SNORD12C
XKR7	ACTR5	SNORD12B
CCM2L	PPP1R16B	SNORD12
HCK	FAM83D	KCNB1
TM9SF4	DHX35	PTGIS
TSPY26P	LINC01734	B4GALT5
PLAGL2	LINC01370	SLC9A8
POFUT1	MAFB	MIR12122
MIR1825	SNORD154	SPATA2
KIF3B	LOC100128988	LOC105372653
ASXL1	TOP1	RNF114
NOL4L	PLCG1-AS1	SNAI1
LOC101929698	PLCG1	TRERNA1
NOL4L-DT	MIR6871	UBE2V1
C20orf203	ZHX3	PEDS1-UBE2V1
COMMD7	LPIN3	PEDS1
DNMT3B	EMILIN3	LINC01273
MAPRE1	CHD6	CEBPB-AS1
EFCAB8	PTPRT	CEBPB
SUN5	LOC101927159	PELATON

Chr20p11.1 deletion	
DEFB125	PLCB4
DEFB126	LAMP5-AS1
DEFB127	LAMP5
DEFB128	PAK5
DEFB129	PARAL1
DEFB132	SNAP25-AS1
C20orf96	ANKEF1
ZCCHC3	SNAP25
NRSN2-AS1	MKKS
SOX12	SLX4IP
NRSN2	JAG1
TRIB3	MIR6870
RBCK1	LINC01752
TBC1D20	LOC101929413
CSNK2A1	LINC02871
TCF15	LOC339593
SRXN1	LINC00687
SCRT2	BTBD3
SLC52A3	LINC01722
FAM110A	LOC102606466
ANGPT4	LINC01723
RSPO4	SPTLC3
PSMF1	ISM1
LOC105372493	ISM1-AS1
TMEM74B	TASP1
C20orf202	ESF1
RAD21L1	NDUFAF5
SNPH	SEL1L2
SDCBP2	MACROD2
FKBP1A-SDCBP2	FLRT3
SDCBP2-AS1	MACROD2-IT1
FKBP1A	MACROD2-AS1
MIR6869	LOC613266
NSFL1C	KIF16B
SIRPB2	SNRPB2
SIRPD	OTOR
SIRPB1	PCSK2
SIRPG	BFSP1
SIRPG-AS1	DSTN
SIRPB3P	RRBP1

BPIFB2	PTPRT-AS1	LINC01270
BPIFB6	SRSF6	LINC01271
BPIFB3	L3MBTL1	PTPN1
BPIFB4	SGK2	MIR645
BPIFA2	IFT52	RIPOR3
BPIFA4P	MYBL2	MIR1302-5
BPIFA3	GTSF1L	RIPOR3-AS1
BPIFA1	LINC01728	PARD6B
BPIFB1	TOX2	BCAS4
CDK5RAP1	JPH2	ADNP
SNTA1	OSER1	ADNP-AS1
CBFA2T2	OSER1-DT	DPM1
NECAB3	GDAP1L1	MOCS3
C20orf144	FITM2	KCNG1
ACTL10	R3HDML	NFATC2
E2F1	HNF4A	MIR3194
PXMP4	HNF4A-AS1	ATP9A
ZNF341	MIR3646	SALL4
ZNF341-AS1	LINC01430	LINC01429
CHMP4B	LINC01620	ZFP64
RALY-AS1	TTPAL	LINC01524
RALY	SERINC3	TSHZ2
MIR4755	PKIG	LOC101927770
EIF2S2	ADA	ZNF217
ASIP	LINC01260	LOC105372672
AHCY	KCNK15-AS1	SUMO1P1
ITCH	CCN5	BCAS1
MIR644A	KCNK15	MIR4756
DYNLRB1	RIMS4	CYP24A1
MAP1LC3A	YWHAB	PFDN4
PIGU	PABPC1L	DOK5
TP53INP2	TOMM34	LINC01441
NCOA6	STK4-AS1	LINC01440
HMGB3P1	STK4	CBLN4
GGT7	KCNS1	MC3R
ACSS2	WFDC5	FAM210B
GSS	WFDC12	AURKA
MYH7B	PI3	CSTF1
MIR499A	SEMG1	CASS4
MIR499B	SEMG2	RTF2
TRPC4AP	SLPI	GCNT7
EDEM2	MATN4	FAM209A
MMP24-AS1-EDEM2	RBPJL	FAM209B
PROCR	SDC4	LINC01716
MMP24	SYS1	TFAP2C

LOC100289473	BANF2	
SIRPA	SNX5	
PDYN-AS1	SNORD17	
PDYN	MGME1	
STK35	OVOL2	
LOC388780	PET117	
TGM3	KAT14	
TGM6	ZNF133	
SNRPB	LINC00851	
SNORD119	DZANK1	
ZNF343	POLR3F	
TMC2	MIR3192	
NOP56	RBBP9	
MIR1292	SEC23B	
SNORD110	SMIM26	
SNORA51	DTD1	
SNORD86	DTD1-AS1	
SNORD56	LINC00652	
SNORD57	LINC00653	
IDH3B	SCP2D1-AS1	
EBF4	SCP2D1	
CPXM1	SLC24A3	
C20orf141	SLC24A3-AS1	
TMEM239	RIN2	
PCED1A	NAA20	
VPS16	CRNKL1	
PTPRA	CFAP61	
GNRH2	INSM1	
MRPS26	RALGAPA2	
OXT	LINC00237	
AVP	KIZ	
UBOX5-AS1	KIZ-AS1	
UBOX5	XRN2	
FASTKD5	NKX2-4	
LZTS3	NKX2-2	
DDRGK1	LINC01727	
ITPA	LINC01726	
SLC4A11	PAX1	
C20orf194	LINC01432	
ATRN	LINC01427	
GFRA4	LOC284788	
ADAM33	LINC00261	
SIGLEC1	FOXA2	
HSPA12B	LNCNEF	
C20orf27	LINC01747	

MMP24OS	SYS1-DBNDD2	BMP7
EIF6	TP53TG5	BMP7-AS1
FAM83C-AS1	DBNDD2	MIR4325
FAM83C	PIGT	SPO11
UQCC1	MIR6812	RAE1
GDF5-AS1	LOC105372631	MTRNR2L3
GDF5	WFDC2	RBM38-AS1
MIR1289-1	SPINT3	RBM38
CEP250	WFDC6	CTCFL
C20orf173	EPPIN-WFDC6	PCK1
ERGIC3	EPPIN	ZBP1
FER1L4	WFDC8	PMEPA1
SPAG4	WFDC9	NKILA
CPNE1	WFDC10A	LINC01742
RBM12	WFDC11	C20orf85
NFS1	WFDC10B	ANKRD60
ROMO1	WFDC13	PPP4R1L
RBM39	MIR3617	RAB22A
PHF20	SPINT4	VAPB
SCAND1	WFDC3	APCDD1L
CNBD2	DNTTIP1	APCDD1L-DT
NORAD	UBE2C	LINC01711
EPB41L1	TNNC2	STX16-NPEPL1
LOC100130373	SNX21	STX16
AAR2	ACOT8	NPEPL1
DLGAP4	ZSWIM3	LOC105372695
DLGAP4-AS1	ZSWIM1	MIR296
MYL9	SPATA25	MIR298
TGIF2	NEURL2	GNAS-AS1
TGIF2-RAB5IF	CTSA	GNAS
RAB5IF	PLTP	LOC101927932
SLA2	PCIF1	NELFCD
NDRG3	ZNF335	CTSZ
DSN1	MMP9	TUBB1
SOGA1	SLC12A5-AS1	ATP5F1E
TLDC2	SLC12A5	SLMO2-ATP5E
SAMHD1	NCOA5	PRELID3B
RBL1	CD40	ZNF831
MROH8	CDH22	EDN3
RPN2	SLC35C2	
GHRH	ELMO2	
MANBAL	LOC105372633	
SRC	ZNF663P	
BLCAP	MKRN7P	

SPEF1	SSTR4
CENPB	THBD
CDC25B	CD93
LINC01730	LINC00656
AP5S1	NXT1
MAVS	LINC01431
PANK2	GZF1
MIR103A2	NAPB
MIR103B2	CSTL1
RNF24	CST11
SMOX	CST8
LINC01433	CST13P
ADRA1D	CST9L
PRNP	CST9
PRND	CST3
PRNT	CST4
RASSF2	CST1
SLC23A2	CST2
TMEM230	CST5
PCNA	GGTLC1
PCNA-AS1	LINC01721
CDS2	SYNDIG1
PROKR2	CST7
LINC00658	APMAP
LOC643406	ACSS1
LINC00654	VSX1
LINC01729	LOC284798
GPCPD1	LOC101926889
SHLD1	ENTPD6
CHGB	PYGB
TRMT6	ABHD12
MCM8	GINS1
MCM8-AS1	NINL
CRLS1	NANP
LRRN4	ZNF337-AS1
FERMT1	ZNF337
CASC20	LOC105372582
LINC01713	FAM182B
BMP2	
LINC01428	
LINC01751	
LINC01706	
MIR8062	
HAO1	

NNAT	**ZNF334**	**TMX4**
LINC00489	**OCSTAMP**	**PLCB1**
LOC100287792	**SLC13A3**	**PLCB1-IT1**
CTNNBL1	**TP53RK**	**RNU105B**

Appendix C: Statement of Originality

All experimental data present in this thesis is original and has been generated as part of this specific PhD project. Unless otherwise stated anywhere in this thesis, all work has been performed by the author. This includes but is not limited to:

- The derivation of iPSC lines from PT1 and PT2 primary cells
- The differentiation of these lines to retinal organoid
- Characterisation of these iPSC lines and differentiation retinal organoids via PCR, immunocytochemistry and western blotting.
- Image acquisition, processing and annotation
- Statistical analysis (excluding scRNA-Seq data)
- Troubleshooting and optimisation experiments
- Sequencing data analysis and interpretation via variant prioritisation.
- Validation of putative genomic variants
- Figure generation

A number of elements of this study were collaborative in nature and generally involved sequencing experiments. This includes:

- scRNA-Seq experiments:
    - Retinal organoid dissociation and library preparation was carried out by Dr. Joseph Collin.
    - Sequencing was carried out by the Core Genomics Facility – Dr. John Coxhead & Rafiqul Hussain
    - scRNA-Seq libraries were processed and QC was performed by Dr. Rachel Queen (Bioinformatics Support Unit).
    - All other data processing and handling, validation *in vitro* and figure generation was carried out by the author of this study.

- Whole-genome sequencing:
    - DNA was prepared by the author.
    - Library preparation and sequencing was carried out by Core Genomics Facility (Dr. John Coxhead & Rafiqul Hussain)
    - Raw data processing and filtering by the Bioinformatics Support Unit (Dr. Michael McCorkindale)
    - All further variant prioritisation and validation was carried out by the author.

- Long-read RNA sequencing:
    - Samples were prepared for sequencing by the author.
    - Library preparation and sequencing was carried out by Dr. Andrew Nelson of Northumbria University
    - Raw data was processed and analysed alongside Dr. Luìs Ferrandez and Dr. Ana Conesa at University of Valencia, Spain.